Cerium oxide nanoparticles as nanozymes and for antifouling applications

Dissertation

zur Erlangung des akademischen Grades

„Doktor der Naturwissenschaft"

im Promotionsfach Chemie

Fachbereich 09: Chemie, Pharmazie, Geographie und Geowissenschaften

Johannes Gutenberg-Universität Mainz.

vorgelegt von

Eva Pütz

geboren in Wittlich

Mainz, Februar 2022

Dekanin: XXX

Erster Berichterstatter: XXX
Zweiter Berichterstatter: XXX

Tag der mündlichen Prüfung: _____

EIGENSTÄNDIGKEITSERKLÄRUNG

Die vorliegende Dissertation wurde zwischen Januar 2018 und Februar 2022 unter der Betreuung von XXX am Fachbereich Chemie der Johannes Gutenberg-Universität Mainz angefertigt. Ich erkläre hiermit, dass ich diese Dissertation selbstständig und ohne fremde Hilfe verfasst habe. Alle verwendeten Quellen und Literaturangaben sind vollständig angegeben.

Mainz, den 24. Februar 2022   _____

Eva Pütz

DANKSAGUNG

An erster Stelle möchte ich mich bei XXX für die Möglichkeit bedanken, an einem so spannenden interdisziplinären Thema zu arbeiten, sowie für die Betreuung während der letzten drei Jahre und die vielen fachlichen Diskussionen und hilfreichen Anregungen.

Ich danke Frau XXX für ihre Bereitschaft, das Zweitgutachten für meine Dissertation zu erstellen, obwohl ihr Schreibtisch bereits mit einem Stapel anderer Doktorarbeiten gefüllt ist.

Vielen Dank an XXX, der mir vor allem zu Beginn der Dissertation immer mit Rat und Tat zur Seite stand und für viele anfängliche Probleme ein offenes Ohr hatte. Ein besonderer Dank geht auch an unsere "Katalyse-Crew", bestehend aus XXX, XXX, XXX und XXX. Ihr habt in den letzten Jahren alle zwei Wochen für viele neue konstruktive Diskussionen, Ideen und Anregungen gesorgt, sei es in Präsenz oder über Teams (hier kein Dank an Corona!).

Besonders bedanken möchte ich mich bei XXX, XXX, XXX, XXX und XXX für ihre unkomplizierte Projektzusammenarbeit.
Besonderen Dank möchte ich auch XXX und XXX für die gute Zusammenarbeit aussprechen. Die interdisziplinären Diskussionen über das Design der Bioassays sowie über mögliche Folgeprojekte/Experimente waren immer sehr produktiv und führten zu tollen Ergebnissen. Danke auch für die vielen "Mikrobiologie-für-Dummies"-Erklärungen, die ein kleines Gebiet der Mikrobiologie auch für Chemiker zugänglich gemacht haben.

Danke an XXX, XXX, XXX und XXX für die Röntgenbeugungsmessungen. Dank auch an XXX für die vielen NMR-Messungen, das offene Ohr und die langen Diskussionen, wenn es um NMR-spezifische Probleme ging.

Danke an XXX, die sich in den letzten Jahren um alle organisatorischen Belange gekümmert hat. Du schmeißt den Laden hier! Alle großen und kleinen organisatorischen Probleme konnten dank dir immer schnell gelöst werden!
Außerdem möchte ich mich bei XXX und XXX für ihre wertvolle Unterstützung bei TEM-spezifischen Fragen oder Problemen bedanken. Auch an die immer größer werdende

ZUSAMMENFASSUNG

Die Ansiedlung von Bakterien auf Oberflächen führt zu einer unerwünschten Bildung von Biofilmen, die als Biofouling bezeichnet wird. In der Regel werden Biofilme mit Bioziden bekämpft, die aber eine Gefahr für andere Organismen darstellen. Eine effiziente Alternative zur Vermeidung von Biofouling-Prozessen ist die Anwendung von Ceroxid (CeO_2), das als Katalysator in der Lage ist, die bakteriellen Kommunikation durch oxidative Bromierung zu unterbrechen und somit eine neue Möglichkeit bietet, die Biofilmbildung ohne Biozide oder Toxine zu hemmen.

Der erste Teil dieser Arbeit widmet sich daher den Oberflächeneigenschaften unterschiedlicher CeO_2-Nanopartikel und deren Einfluss auf die katalytische Aktivität in der oxidativen Bromierung von Thymol. Es wurde gezeigt, dass sowohl eine hohe Lewis-Acidität, ein hohes Produkt aus Zeta-Potential und BET-Oberfläche, als auch eine hohe Stabilität des oberflächengebundenen Wasserstoffperoxids zu einer Beschleunigung der Bromierungsreaktion beitragen.

In einer weiteren Studie wird untersucht, inwiefern sich die zuvor untersuchten Oberflächeneigenschaften von CeO_2 durch Variation der Reaktionszeit beeinflussen lassen. Kürzere Reaktionszeiten liefern Nanopartikel mit hohem Zeta-Potential und kleinem Ce^{3+}/Ce^{4+} Verhältnis, längere Reaktionszeiten führen zu Nanopartikeln mit großer BET-Oberfläche und großem Ce^{3+}/Ce^{4+} Verhältnis. Bei Haloperoxidase-ähnlichen Reaktionen sind CeO_2-Nanopartikel mit großem Zeta-Potential für die katalytische Aktivität vorteilhaft, da ein oberflächengebundenes Halogenid auf H_2O_2 oder ein organisches Substrat übertragen werden muss. Im Gegensatz dazu müssen bei der Peroxidase-ähnlichen Reaktion die BET-Oberfläche und das Ce^{3+}/Ce^{4+} Verhältnis erhöht werden, um eine leichtere Elektronenübertragung auf das Substratmolekül zu gewährleisten. Im dritten Kapitel wird die Anwendung optimierter Nanopartikel in Antifouling-Lacken untersucht. Biofilm-Tests zeigen eine deutliche Reduktion des Biofilms von Gramnegativen Bakterien in Anwesenheit der Nanopartikel. Durch die Anwendung des Reporterstamms *A. tumefaciens* A136 konnte die Quorum Quenching Aktivität der CeO_2-Nanopartikel bestätigt werden. In den Überständen der Bakterienkultur *P. aeruginosa* sind die Bromidkonzentration und die Konzentration der Signalmoleküle in Anwesenheit von CeO_2 deutlich reduziert. Zum ersten Mal wurde bromiertes HQNO (2-Heptyl-4-hydroxychinolin-*N*-oxid) in Gegenwart von CeO_2 nachgewiesen, was den postulierten oxidativen Bromierungsmechanismus untermauert. Die CeO_2-Partikel wurden anschließend in Polyurethan-Lacke eingearbeitet, in denen sie immer noch eine signifikante Biofilm-inhibierende Wirkung aufweisen.

Da für alle oxidativen Bromierungsreaktionen das Oxidationsmittel H_2O_2 zur Verfügung stehen muss, wurde im letzten Kapitel untersucht, ob eine *in-situ* H_2O_2 Erzeugung möglich ist. Dazu wurde eine H_2O_2-freisetzende Substanz in eine Polymermatrix eingebettet. Zusätzlich wurde die photochemische Erzeugung von H_2O_2 mittels graphitiertem Kohlenstoffnitrid (g-C_3N_4/BDI) untersucht.

ABSTRACT

The colonization of bacteria on surfaces leads to an undesirable formation of biofilms, which is called biofouling. Generally, biocides are used to control biofilms, but they pose a threat to other organisms. An efficient alternative to prevent biofouling is the application of cerium oxide (CeO_2), which can interrupt bacterial communication by catalyzing the oxidative bromination of signaling compounds, thereby providing a new way to prevent biofilm formation without biocides or toxins. The first part of this work is therefore devoted to the surface properties of different CeO_2 nanoparticles and their effect on the catalytic activity for the oxidative bromination of thymol. A high Lewis acidity, a high product of zeta potential and BET surface area, and a high stability of the surface-bound hydrogen peroxide were shown to accelerate the bromination reaction.

In another study, we investigated to what extent the surface properties of CeO_2 can be influenced by the reaction time. Shorter reaction times yield nanoparticles with high zeta potential and small Ce^{3+}/Ce^{4+} ratio, whereas longer reaction times yield nanoparticles with large BET surface area and large Ce^{3+}/Ce^{4+} ratio. In haloperoxidase-like reactions, CeO_2 nanoparticles with large zeta potential are crucial for catalytic activity, since a surface-bound halide must be transferred to an organic substrate. In contrast, in the peroxidase-like reaction, the BET surface area and Ce^{3+}/Ce^{4+} ratio must be increased to ensure electron transfer to the substrate molecule.

In the third chapter, the application of optimized nanoparticles in antifouling paints was investigated. Biofilm tests showed a significant reduction of the biofilm of Gram-negative bacteria in the presence of the nanoparticles. The application of the reporter strain *A. tumefaciens* A136 confirmed the *quorum quenching* activity of the CeO_2 nanoparticles. In the supernatants of the bacterial culture *P. aeruginosa*, the bromide concentration, as well as the concentration of signaling molecules, was significantly reduced in the presence of CeO_2. For the first time, brominated HQNO (2-heptyl-4-hydroxyquinoline *N*-oxide) was detected in the presence of CeO_2, supporting the proposed oxidative bromination mechanism. The CeO_2 nanoparticles were incorporated subsequently into polyurethane coatings, in which they still exhibit significant biofilm inhibiting activity.

Since the oxidant H_2O_2 must be available for all oxidative bromination reactions, the last chapter investigated whether H_2O_2 generation is possible *in-situ*. This involves embedding an H_2O_2-releasing substance in a polymer matrix. In addition, the photochemical generation of H_2O_2 using graphitized carbon nitride (g-C_3N_4/BDI) was investigated.

GENERAL REMARKS

This work is divided into six chapters. In the introductory chapter, the theoretical background is examined in some detail, followed by the motivation and the scientific goal of this work. Four projects are presented and discussed in the following four chapters. Each chapter is introduced with a short summary, which highlights the scientific goal of the project, as well as the authors' contributions. References and the supporting information are always attached at the end of each chapter.

NMR spectra were analyzed with MestreNova, XPS data was processed using CasaXPS and chemical structures were prepared using ChemDraw Prime 17.0. Matlab R2017b and OriginPro 8 were used for graphical data analysis including plotting and fitting. All Figures were prepared originally using Matlab R2017b, CorelDRAW 2021, PowerPoint and Inkscape if not mentioned otherwise.

LIST OF CONTENT

<div align="right">

1

</div>

THEORETICAL BACKGROUND

1.1. BIOFOULING

From a general point of view, a biofilm is an aggregate of surface-associated bacteria enclosed in a self-produced, protective slimy matrix of carbohydrates. These carbohydrates, also known as extracellular polymeric substances, are responsible for irreversible surface attachment.[1,2]
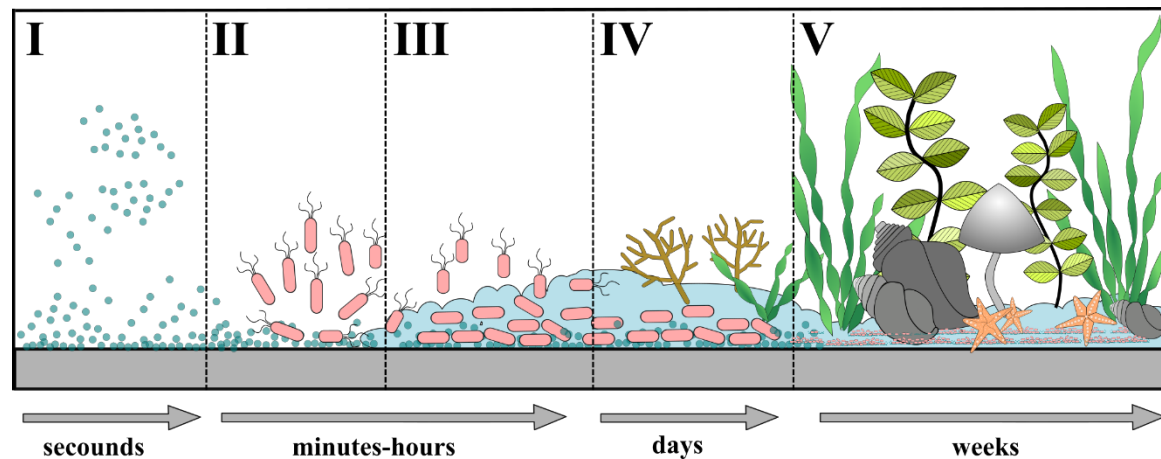
Figure 1-1. Schematic biofilm formation process. (I) Attachment of organic molecules forming a conditioning film. (II) Reversible attachment of bacteria. (III) Formation of extracellular polymeric substance (EPS). (IV) Colonization of small microorganims (V) Attachment of larger organisms.[3]

The undesirable formation of biofilms, so-called biofouling, occurs in many areas of everyday life. Surfaces in an aqueous environment are mainly affected. The dynamic and complex biofilm formation process is shown schematically in Figure 1-1 and consists of five steps. (I) First, adsorption of carbohydrates and proteins on the surface through electrostatic interactions and van der Waals interactions occurs leading to a substrate film ("conditioning film"). The substrate layer serves as a nutrient base for bacteria and other microorganisms. (II) At the beginning the primary colonizers migrate and adhere to the surface, but they are still losely bound. (III) Under optimal conditions, microbial biofilm production starts by forming an extracellular polymeric substance (EPS) and the bacteria

are irreversibly attached ("microfouling"). This polysaccharide-containing hydrogel allows nutrient exchange, enzymatic interactions as well as a protection from external influences, such as biocides and predators. At this stage, the biofilm can no longer be removed without enormous effort. (IV) A more complex community is formed by colonization of small eukaryotes, invertebrates, and microalgae (V) followed by attachment of larger organisms like bivalves, fungi and macroalgae ("macrofouling").[3,4]

1.2. QUORUM SENSING

As described in Section 1.1, bacteria form biofilms in which they live together in protected habitats. To develop such complex biofilms, the bacteria communicate with each other. They can communicate silently with messenger molecules, so called autoinducers (AI). These autoinducers are small diffusible organic molecules produced by other bacteria or the bacteria themselves. The surrounding bacteria can recognize these autoinducers. At a certain concentration of the signaling molecules, the bacteria can initiate transcription processes that determine certain properties such as pathogenicity, biofilm formation or bioluminescence. This silent communication process is called "Quorum Sensing" (QS). Both, Gram-negative and Gram-positive bacteria use Quorum Sensing mechanisms to regulate their group behaviour. However, their autoinducers differ from each other. Gram-negative bacteria use mostly *N*-Acyl-homoserine lactones (AHL, autoinducer-1 (AI-1)), whereas Gram-postive bacteria communicate via small peptides (autoinducer-1 (AI-1)). In addition, bacteria can communicate across species using furanosyl compounds (AI-2).[5,6] Figure 1-2. shows autoinducers isolated from red algae *Delisea pulchra*.[5]
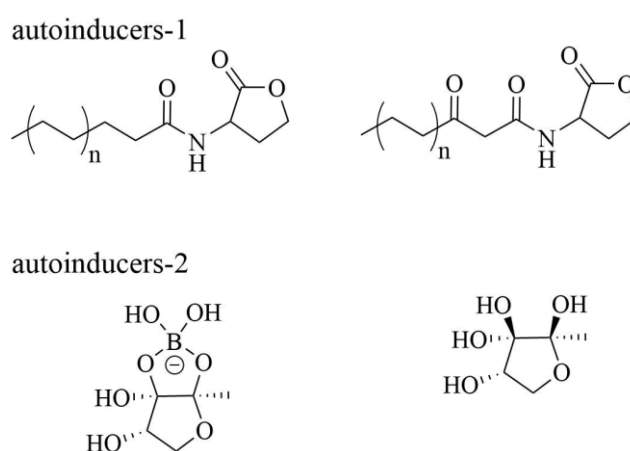
Figure 1-2. Signaling molecules acyl-homoserine lactones and 3-oxo-acyl-homoserine lactones as autoinducers-1 (AI-1) and furanosyl compounds as autoinducers-2 (AI-2) isolated from Gram-negative bacteria *Delisea pulchra*.[5]

Bacterial communication was first discovered in the Gram-negative bacterium *Vibrio fischeri*. Figure 1-3 shows the simplified schematic LuxIR-QS system. *V. fischeri* and other Gram-negative bacteria can produce AHL's (purple and grey) catalyzed by the enzyme LuxI. As the cell population increases, so does the concentration of AHL molecules, which diffuse in and out of bacteria. At a sufficiently high concentration, AHL molecules bind to the receptor LuxR (green) forming a LuxR-autoinducer complex. This complex activates

the expression of genes. In case of *V. fischeri* gene regulation leads to luciferase activity.[6–8] Since the synthesis enzyme LuxI (violet/grey) is also regulated by QS, the production of AHL increases rapidly, resulting in an exponential increase in light production by luciferase. A so-called autoinduction occurs. Quorum sensing based processes change the phenotypic behavior of bacteria at a higher cell density.
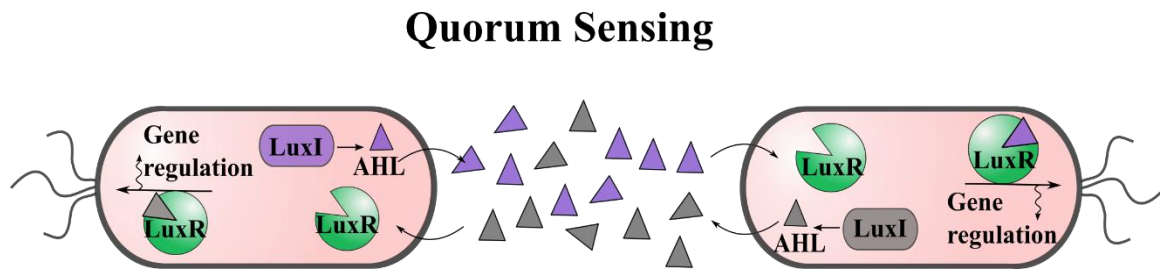
Quorum Sensing

Figure 1-3. Simplified LuxIR based Quorum Sensing system found in Gram-negative bacteria. AHL's (purple and grey) are produced by LuxI enzyme. After binding of AHL to LuxR receptor, the LuxR-autoinducer complex activates gene regulation.[6]

The group behavior of bacteria differs from that of individual bacteria. *V. fischeri* shows bioluminescence only at sufficiently high AHL concentrations due to a certain cell population density, while the single bacterium shows no bioluminescence. It is assumed, that all bacteria communicate *via* Quorum Sensing systems using different autoinducers. In case of Gram-negative bacteria, AHL's differ slightly in length of the hydrophobic side chain. This results in each bacterium speaking its own dialect, which can be partially understood by other bacteria. Moreover, bacteria can also have more than one Quorum Sensing system. The human pathogen *Pseudonomas aeruginosa,* for example, uses two AHL-based systems that interact with each other.[6–8]

1.3. NEGATIVE EFFECTS OF BIOFILMS

The formation of biofilms causes major problems in many industries, such as water management, the food industry and medical technology. Since bacteria in a biofilm matrix are better protected from hostile influences, biofilms make cleaning more difficult, which can lead to hygienic problems. In addition, biofilms can release pathogens and lead to serious infections, especially in a clinical environment. Here, 10–20% of infections in hospitals are caused by *Pseudomonas aeruginosa.*[9,10] *Pseudomonas aeruginosa* is a Gram-negative bacterium that is commonly distributed in natural environment. However, it is an opportunistic pathogen for humans causing infections in wounds, urinary and respiratory tracts.[11,12] Diseases of similar severity can also be caused by *Klebsiella pneumoniae*. As the name implies, this bacterium can cause pneumonias as well as urinary tract infections and pyogenic liver abscesses.[13] According to a report by the Centers for Disease Control (US), the annual costs of healthcare-associated infections (HAI) are $5.7 billion to $6.8 billion, with low cost estimates.[14] Biofilms occur not only in hospitals, but almost on any surface in a moist environment. They can be found on ship hulls, in automotive parts, in steel and paper production, in the food and beverage industry up to water desalination and drinking water treatment.[15,16] Blockages and energy losses due to biofilm formation lead to a significant increase in costs for industry. The presence of biofilms on ship hulls can result in performance losses of up to 86% due to reduced speed and maneuverability. The higher frictional resistance results in enormous costs due to additional fuel consumption. In addition, emissions of greenhouse gases, which have negative ecological effects, increases.[17] Biofouling plays a crucial role also in water treatment processes. Polymer membranes used for purification suffer from biofouling if they are regularly exposed to moisture. The resulting blockage of pores leads to higher hydrodynamic pressure and reduced flux. The membranes suffer a loss of performance and lifetime.[18,19]

1.4. ANTIFOULING STRATEGIES

Many different antifouling strategies were developed in the past decades and centuries. Generally, antifouling strategies are distinguished into two categories: i) surfaces which repel bacteria and inhibit biofilm formation and ii) surfaces capable of killing bacteria. First, methods for killing or destroying adhered microorganisms will be discussed briefly. One possibility to kill bacteria is the design of biocide releasing surfaces. Here, biocides or biocide-forming substances are embedded in a polymeric matrix and released over a certain time period (Figure 1-4 II).These matrices release biocides in a controlled manner and kill bacteria on the surface and in its immediate vicinity.[20,21] Starting around two centuries ago metals like copper, arsenic or mercury where embedded in paint to combat biofilm formation. In the 1960's, the antifouling efficacy of trialkyltin compounds was observed leading to the development of tributyltin (TBT) containing coatings. TBT paints were able to control biofouling on ship hulls for approximately seven years. During this time the coating leaches toxic biocides, which inhibit growth of bacteria on the surface. However, TBT is toxic to marine organisms, leading for example to abnormal shell growth of oysters. From 2008, TBT coatings on vessels were completely banned by the International Maritime Organization (IMO) due to their high toxicity, poor degradability and hormonal effects.[15,17] The substitute product Irgarol® (Cybutryne), which initially seemed promising, has already been banned in some countries too due to its hormonal effect.[22] After banning TBT, copper-based paints were used more frequently again. However, copper paints are also suspected of being harmful to the environment. They are under scrutiny in many countries because copper ions are known to be toxic to bacteria and cells. Copper is known to bind to functional protein groups (such as thiols) and to disrupt the structure and function of enzymes. Metal centers of various enzymes could be replaced by copper ions and alter enzyme functions. In addition, copper can increase the formation of reactive oxygen species (ROS), which exhibit antimicrobial activity due to their attack on diverse targets.[20,23,24] In another strategy, silver is used, generating Ag^+ as antibiofouling species. However, it is considered that organisms can become resistant after a longer time of exposure. All the above-mentioned attempts are based on the embedding of biocides or biocide-generating substances in a carrier matrix. Their antifouling activity is not unlimited due to the finite amount of bactericidal substance incorporated.[21]

Another option is to design surfaces that kill bacteria on contact (Figure 1-4 I). One attempt involves the irreversible binding of antimicrobial compounds to a surface, such as

quaternary ammonium salts, which destroy bacteria after attachment due to electrostatic attractions between R_4N^+ and the phospholipid-based cell wall. In addition, a new approach has been reported using nanopatterned polymers that induce mechanical stress in bacteria. It is believed that nanopatterned surfaces can damage the cell membrane by penetration of the nanopatterns.[21,25]

Killing　　　　　**Repulsion**

I　　　II　　　III　　　IV　　　V

contact biocide　biocide release　electrostatic repulsion　low surface energy　steric repulsion
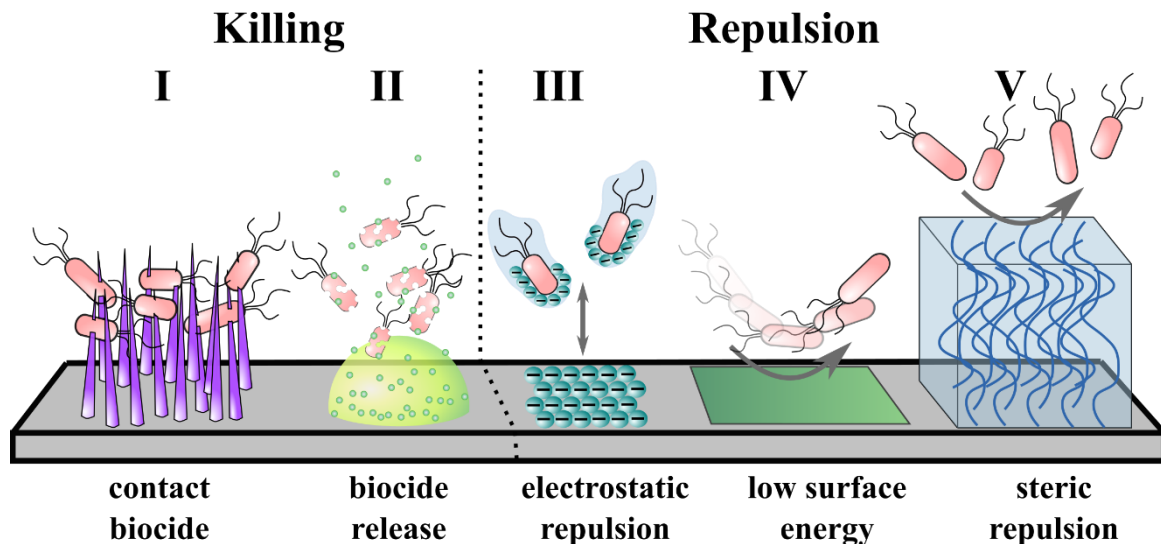
Figure 1-4. Strategies against biofouling based on (I) contact biocide, (II) biocide release, (III) electrostatic repulsion forces, (IV) low surface energy and (V) steric repulsion forces.[21]

Microorganism repellent surfaces that prevent their bacterial attachment are designed in different ways. Superhydrophobic surfaces, for example, exhibit antifouling properties due to their low surface energies (Figure 1-4 IV), which decrease attraction forces between bacteria and surface. Here, researchers have learned a lot from antifouling and self-cleaning surfaces found in nature, such as lotus leaves. Low energy surfaces can be designed using a special chemical composition and a hierarchical micro- to nanometer scale topographie. However, these surfaces only show this behaviour at the interfaces between air and solids, because after immersion in water the surface becomes moist due to the decreasing surface tension.[15,21] In addition to superhydrophobic surfaces, hydrophilic surfaces also exhibit antifouling properties. Hydrophilic surfaces are covered by a thin layer of water, which is tightly connected to the surface by hydrogen bonds. To enhance the antifouling effect of hydrophilic surfaces, hydrophilic polymers such as polyethylene glycol are often applied. Polyethylene glycol functionalized surfaces can prevent the adhesion of bacteria through steric repulsion. On the one hand, the mobile polymer chains make it more difficult for bacteria and proteins to adhere, and on the other hand, these polymer chains have a high

exclusion volume (Figure 1-4 V).[21] Repulsion between bacteria and surface can also be caused by electrostatic forces. Since the cell membrane is in general negatively charged, due to phosphate and carboxyl groups, negatively charged surfaces lead to repulsion and antibiofouling behavior (Figure 1-4 III). Surfaces functionalized with ionic polymers lead to both, electrostatic and steric repulsion.[21]

1.5. QUORUM QUENCHING

Antifouling methods described in Section 1.4 are in part copied from nature but not nearly as efficient. Certain hosts can protect themselves against bacterial attack by chemically altering autoinducers. These produce enzymes which catalyze the degradation of autoinducers. Due to a different chemical structure, autoinducers cannot be any longer recognized by the bacterial receptors, which leads to a disruption in communication. Interruption of bacterial communication is called Quorum Quenching (QQ).[6]
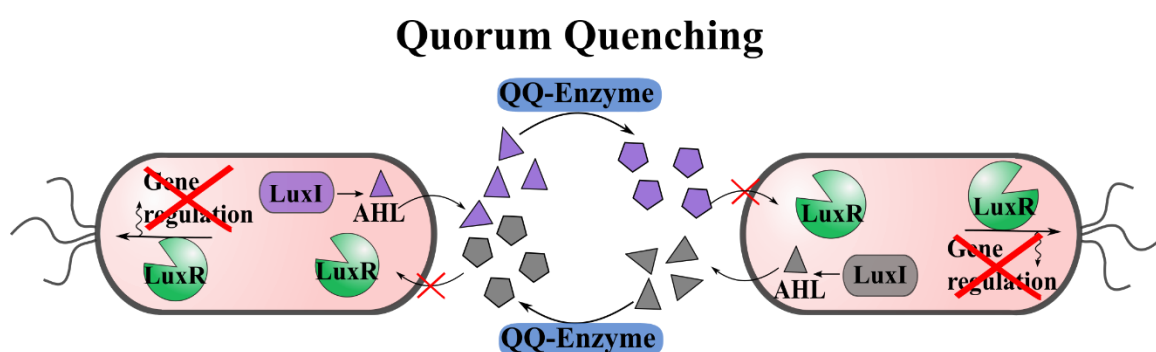
Quorum Quenching

Figure 1-5. Illustration of the disruption of bacterial communication by Quorum Quenching in Gram-negative bacteria. The autoinducers-1, AHLs (triangles), are produced by LuxI enzyme. After diffusion out of the cell, QQ enzymes chemically modify the AHLs (pentagon). The formed compounds cannot bind to LuxR receptor, the LuxR-autoinducer complex is not formed and no gene regulation ocurs.[8]

The mechanism of QQ mechanisms by Gram-negative bacteria is shown schematically in Figure 1-5. AHLs (triangle) produced by LuxI enzyme diffuse out of the cell, where they are chemically altered by an QQ enzyme (pentagon). No LuxR autoinducer complex is formed, and no gene regulation occurs since the modified molecules can no longer bind to the LuxR receptor (green).

AHLs can chemically be altered by a number of different enzymes. Some enzymes degrade them, others modificate their structure. Five different QQ enzymes with their corresponding reaction pathway are shown exemplary in Figure 1-6. Acylase, deaminase and lactonase degradiate the AHL molecule. Acylase splits the AHL molecule forming homoserine lactone (HSL) and a fatty acid. The lactone ring can be split by lactonase, whereas deaminase forms an NH_2-terminated side chain and HSL with the hydroxyl group.[8]
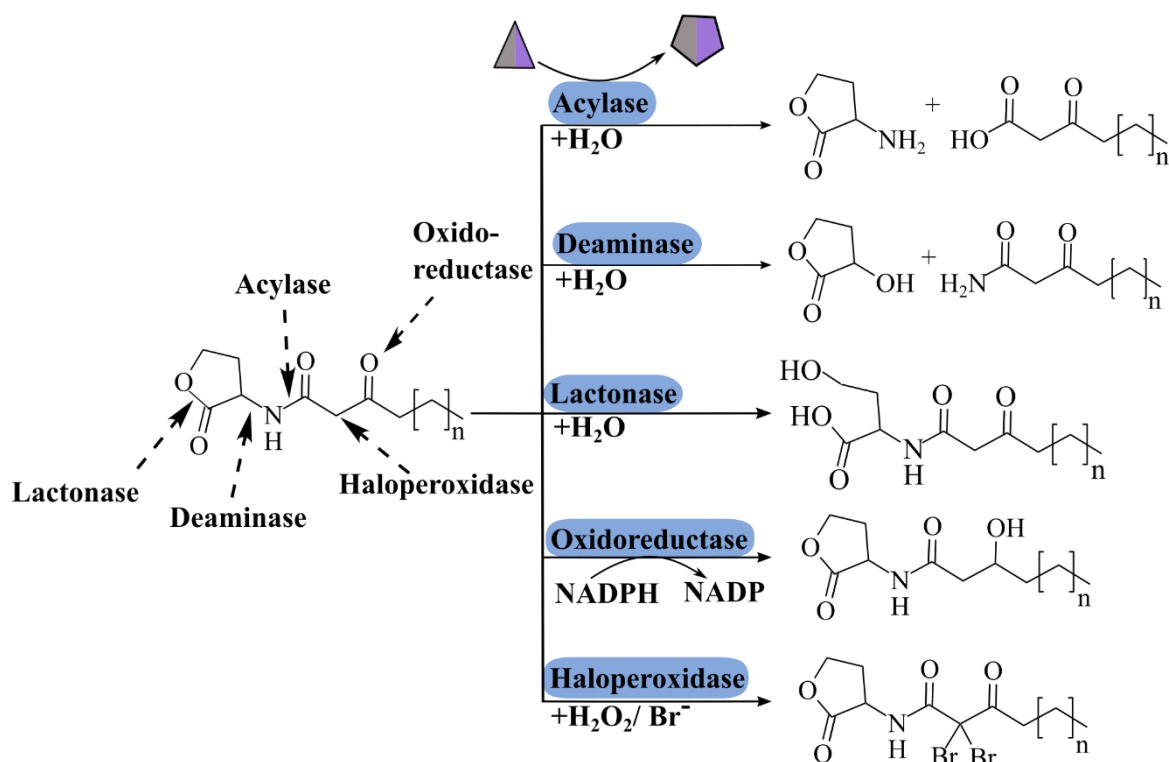
Quorum Quenching Enzymes

Figure 1-6. Enzymatic AHL inactivation by Quorum Quenching enzymes. Degradation (acylase, deaminase, lactonase and modification (oxidoreductase, haloperoxidase) pathways with reaction products.[8]

Two of the QQ enyzmes shown above can inactivate AHLs due to modification. Oxidoreductases can reduce the ketone in the acyl side chain to an alcohol using the nicotinamide adenine dinucleotide phosphate (NADPH/NADP) cofactor. Another mechanism is based on the oxidative halogenation of AHL molecules at the CH-azide site. Enzymes, which can halogenate organic substrates in the presence of hydrogen peroxide and halides are called haloperoxidases.[8,26,27] However, these are attempts to inactivate signaling molecules due to chemical modification or degradation: Blocking the receptor or inhibit AHL synthesis would also be a possibility to inhibit bacterial communication.[8,28]

1.6. DETERMINATION OF QUORUM QUENCHING ACTIVITY

QQ activity of enzymes can be quantified in a bio-assay using reporter strains. These strains express certain genes by detection of AHLs. *Agrobacterium tumefaciens* A136 is one frequently used bacterial strain to prove the QQ activity of enzymes. Since *A. tumefaciens* A136 is genetically modified, it cannot produce AHL molecules by itself. However, long-chained AHLs can be detected by binding to the receptor TraR (pCF218) forming an AHL-

TraR complex. As a result, β-galactosidase production is induced by *traI-lacZ* activation.[8,29] As the β-galactosidase scales with AHL concentration, β-galactosidase activity can be used as a metric for QQ or QS processes. AHL detection pathway in *A. tumefaciens A136* is shown schematically in Figure 1-7.
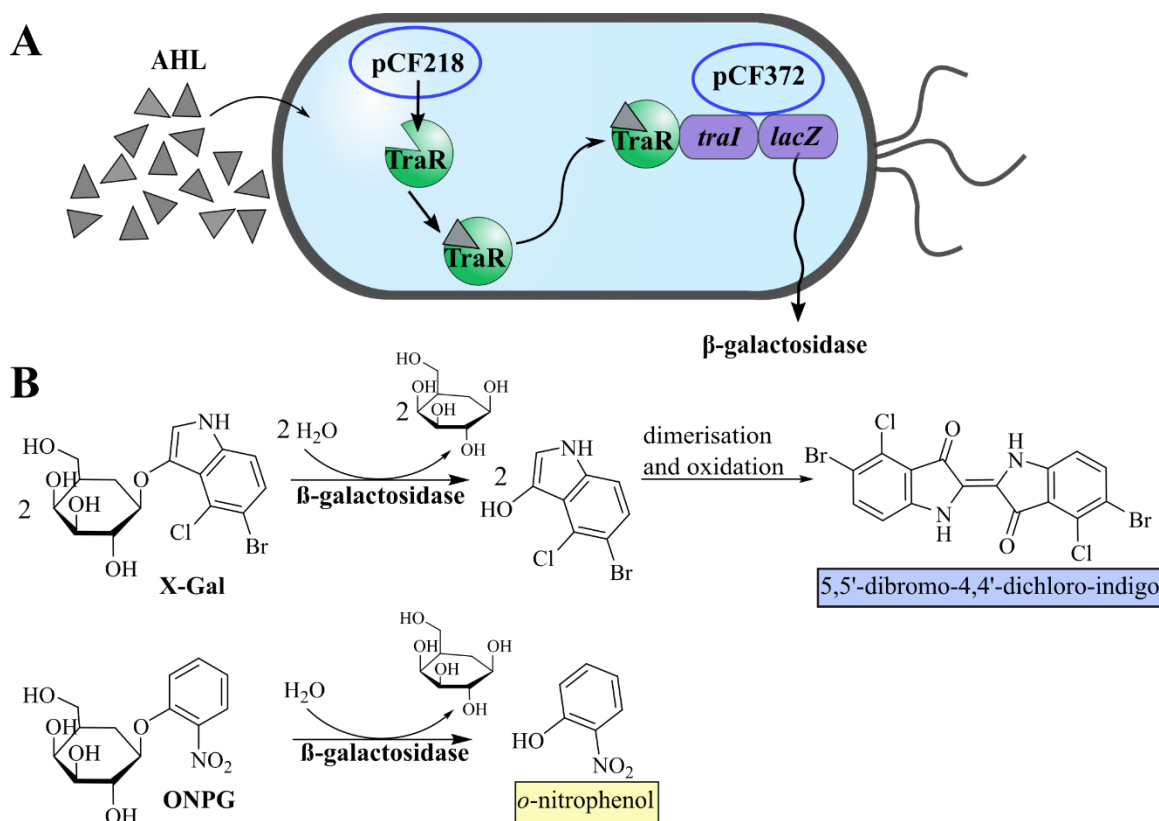

Figure 1-7. (A) Schematically quorum sensing mechanism of *Agrobacterium tumefaciens A136*. AHL detection lead to formation of AHL-TraR complex, which initiates *traI-lacZ* activation and consequently the production of β-galactosidase. (B) Reaction of β-galactosidase with X-Gal (5-bromo-4-chloro-3-indolyl-β-D-galactopyranoside) and ONPG (*o*-nitrophenyl-β-D-galactopyranoside) to form the colored products 5,5'-dibromo-4,4'-dichloroindigo and o-nitrophenol.[8,29,30]

Hydrolysis of ONPG (*o*-nitrophenyl-β-D-galactopyranoside) or X-Gal (5-bromo-4-chloro-3-indolyl-β-D-galactopyranoside) catalyzed by β-galactosidase yields galactose and yellow *o*-nitrophenol or colorless 5-bromo-4-chloro-3-hydroxyindole, respectively. The latter oxidizes and dimerizes spontaneously forming the blue dye 5,5'-dibromo-4,4'-dichloro-indigo.[29,30] Since both ONPG and X-Gal are colorless, formation of the yellow or blue dye indicates β-galactosidase activity, which can be determined photometrically. QQ behavior is demonstrated if the β-galactosidase activity is reduced in the presence of an enzyme with respect to the reference sample.

1.7. HALOGENATION ENZYMES

A large number of enzymes with halogenation activity are known from nature. The halogenated products are of biological interest due to their biological activities.[31] Among other properties, some of the halogenating enzymes exhibit QQ activity because they brominate organic molecules.[26,27] These enzymes halogenate organic substrates oxidatively using halide anions and an oxidizing agent. In this process, hypohalous acid (HOX), the halogenating agent, is formed *in-situ*. Different oxidants are required for HOX production, depending on the enzyme. Haloperoxidases use hydrogen peroxide (H_2O_2), whereas halogenases use oxygen (O_2).[32] Reaction equations for both enzymes are shown in Figure 1-8.

$$R\text{-}H \ + \ X^- \ + \ H_2O_2 \ + \ H^+ \ \xrightarrow[\text{"HOX"}]{\text{Haloperoxidase}} \ R\text{-}X \ + \ 2\,H_2O$$

$$R\text{-}H \ + \ X^- \ + \ O_2 \ + \ H^+ \ \xrightarrow[\text{"HOX"}]{\text{Halogenase}} \ R\text{-}X \ + \ 2\,H_2O$$
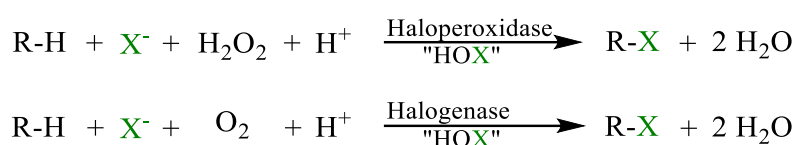
Figure 1-8. General reactions of the enzymes haloperoxidase and halogenase.[33]

Since hydrogen peroxide as a substrate is easier to handle in the laboratory than oxygen, the focus in the following chapter is on haloperoxidase reactions. Haloperoxidase enzymes are divided into two different classes, the i) heme-dependent haloperoxidases and the ii) nonheme vanadium-dependent haloperoxidases. Their active sites are shown in Figure 1-9.

heme-dependent haloperoxidase   vanadium-dependent haloperoxidase
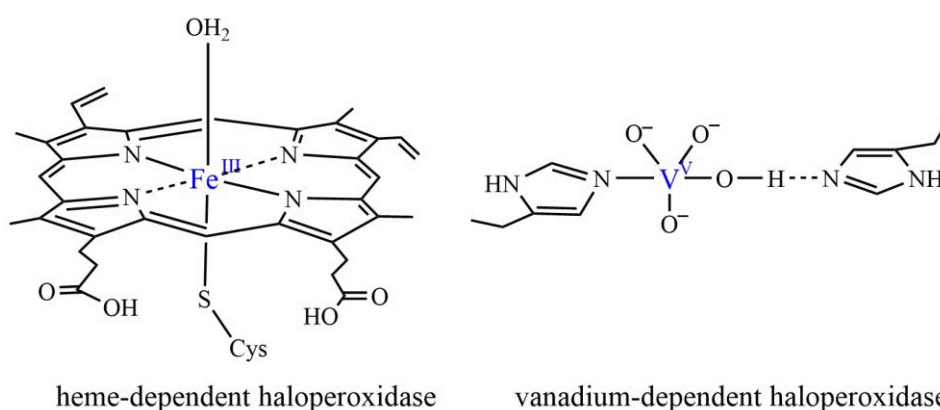
Figure 1-9. Active sites of heme-thiolate chloroperoxidase from fungus *Caldariomyces fumago*[34] and vanadium-dependent bromoperoxidase discovered in *Ascophyllum nodosum*.[31]

In heme-dependent haloperoxidases, the active site is an iron(III) ion which is equatorially coordinated by four nitrogen atoms of protoporphyrin IX. At the axial positions, the

iron(III) center is bound by a cysteine residue and a loosely coordinated water. During the catalytic cycle, the iron site switches between the oxidation states +3 and +4 to form hypohalous acid. The heme thiolate chloroperoxidase can catalyze other reactions besides the haloperoxidase reaction.[34] Catalase-like activity can be detected when neither substrate nor halide is present.[35] In the absence of halide, epoxidation of olefins[36], oxidation of alcohols[37], sulfoxidation[38], or a peroxidase reaction may proceed.[39] Vanadium-dependent haloperoxidases are more common. Vanadium chloroperoxidase (V-ClPO) can be isolated from terrestrial fungi[40], whereas vanadium bromoperoxidase (V-BrPO) is predominantly found in marine environment and can be isolated from algae.[31] Since the vanadium-dependent haloperoxidases exhibit different oxidative ability, they are classified into chloroperoxidases, bromoperoxidases and iodoperoxidases. Chloroperoxidases have the highest oxidative ability, being able to oxidize chloride, bromide and iodide. The oxidative power (redox potential) decreases from chloroperoxidases to bromoperoxidases and finally to iodoperoxidases.[32]
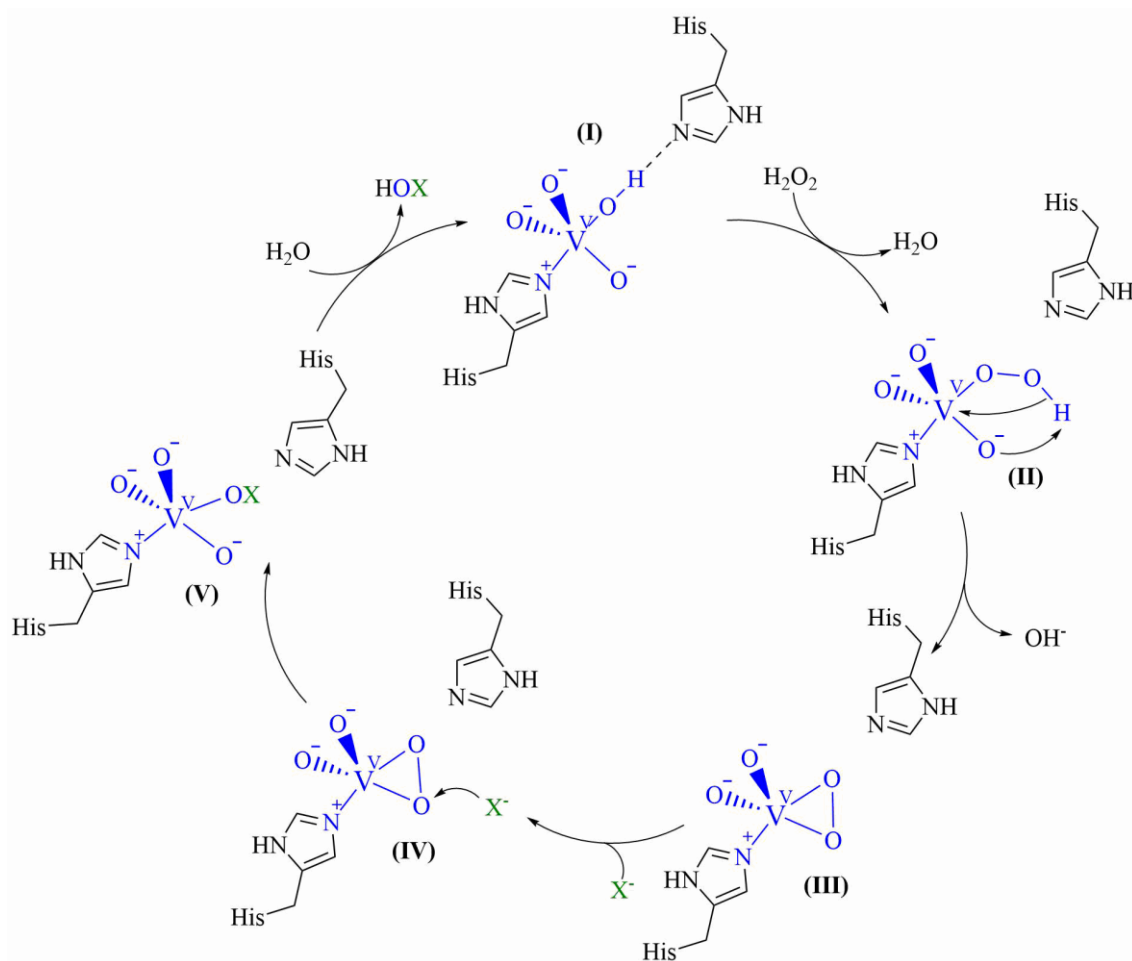

Figure 1-10. Proposed catalytic formation of HOX catalyzed by a vanadium-dependent bromoperoxidase isolated from the brown algae *Ascophyllum nodosum*. [31,33,41,42]

In contrast to heme–dependent haloperoxidases, vanadium does not change its oxidation state during the catalytic reaction cycle as shown in Figure 1-10. Similar to heme–dependent haloperoxidases, several reactions can be catalyzed by vanadium-dependent haloperoxidases. This makes them powerful catalysts in organic synthesis.[43] *In-situ* formation of the halogenating agent HOX can result in various reactions such as halocyclization[44], halohydroxylations[45], oxidative decarboxylation[46], and oxidative bromination.[47] The biosynthesis of halogenated marine products catalyzed by vanadium-dependent haloperoxidases is particulary interesting due to their biological activity.

Algae can to protect themselves against bacterial colonization by producing hypohalous acid, which modify bacterial signaling molecules.[48] This QQ activity was firstly reported for vanadium bromoperoxidase in 2011.[26] Bromination and subsequent hydrolysis of the autoinducer 3-oxo-acyl homoserine lactone by vanadium bromoperoxidase isolated from *Delisea pulchra* is shown schematically in Figure 1-11. The degradation products can no longer bind to the bacterial receptors which leads to an interruption of bacterial communication.
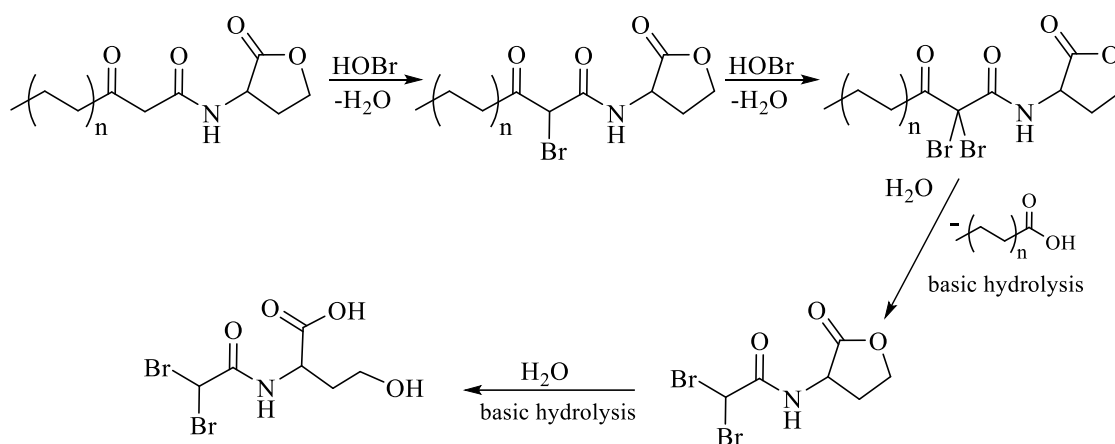
Figure 1-11. Enzymatic degradation pathway of 3-oxo-acylhomoserine lactone. First, double bromination occurs at the α-position, followed by a double basic hydrolysis leading to the cleavage of a fatty acid and the lactone ring.[26,27]

Due to their complex structure, enzymes can bind the desired substrates with a high affinity in favorable spatial proximity to their active catalytic center. There, the catalytic conversion takes place with high efficiency.[49] However, natural enzymes are very expensive and difficult to purify and store.[50] Moreover, they are stable only under mild conditions in a small temperature and pH range. If these conditions are changed, the enzymes denature

easily. Much research has been done in recent years to make artificial enzymes based on nanomaterials to overcome the restrictions of limited stability of natural enzymes.[50]

1.8.   NANOZYMES

Nanomaterials with an intrinsic enzyme-like activity have been dubbed "nanozymes". They have some benefits over natural enzymes and can be used in biocatalysis. They are more resistant to harsh reaction conditions and their production is inexpensive.[51,52] Magnetic Fe_3O_4 nanoparticles were the first reported nanozymes in 2007 showing peroxidase-like activity.[53] Research on artificial enzymes has increased greatly in recent years. The artificial enzymes do not follow any particular structural design but can be of very different types. Organic compounds such as cyclodextrins[54], superbranched polymers[55,56] or fullerenes[57], inorganic nanoparticles (FeO_x[53], V_2O_5[58,59], CeO_2[60–62], Au[63], Ag[64]) as well as hybrid materials like metal-organic frameworks (MOF)[65–67] can be used in various enzymatic reactions. Nanozymes are used mainly as catalysts in peroxidase, oxidase, catalase and superoxide dismutase reactions, as shown in Figure 1-12.
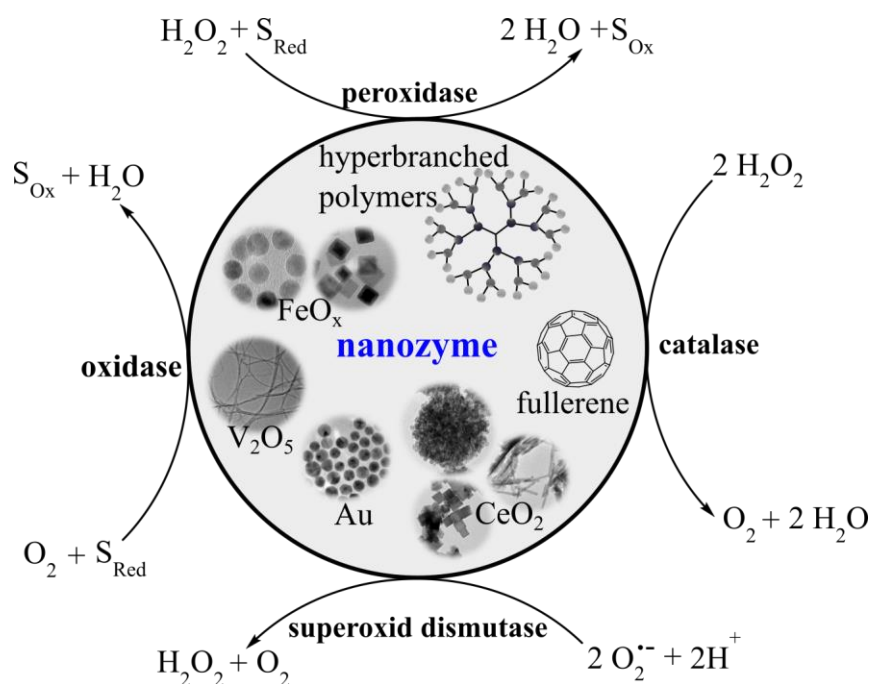
Figure 1-12. A selection of commonly used nanozymes (FeO_x, Au, V_2O_5, CeO_2, hyperbranched polymers and fullerenes), which exhibit enzyme-like activity. General reaction pathways of peroxidase, catalase, superoxide dismutase and oxidase are shown schematically.[68–71]

The reactions enabled by nanozymes lead to a variety of applications. For example, peroxidase-like nanozymes can be used for colorimetric sensing applications to detect

ions[62] or certain compounds.[72,73] Many nanozymes are also capable of degrading organic pollutants, making them suitable for wastewater treatment.[74,75]

The first attempts to use nanozymes with haloperoxidase-like activity were inspired by nature, by using vanadium-containing organometallic compounds and V_2O_5 nanorods.[76–78] However, vanadium compounds form soluble vanadates and polyoxovanadates in aqueous environment by leaching, and their impact on the environment has not been adequately studied.[79] A better, non-toxic and insoluble system with intrinsic haloperoxidase-like activity based on CeO_2 nanorods was presented from Herget *et al.* in 2017.[60,80] Similar to vanadium-dependent haloperoxidases, CeO_2 nanoparticles show QQ behavior due to oxidative bromination of bacterial signaling molecules, which scales with a biofilm inhibitory effect. A significant biofilm reduction for the Gram-negative bacteria *Pseudomonas aeruginosa* and *Phaeobacter gallaeciensis* in the presence of CeO_2 nanoparticles was observed. The activity of this system was significantly improved by the substitution of cerium with bismuth.[81]

1.9. CERIUM DIOXIDE

Cerium dioxide crystallizes in the cubic CaF_2-type structure (space group $Fm3m$), as shown in Figure 1-13 and has a pale yellow color. Since cerium ions can exist in either their +3 or +4 oxidation states ceria is a non-stoichiometric oxygen-deficient compound with composition CeO_{2-x} where oxygen vacancies originate from the presence of Ce^{3+} sites.[82] Reversible transitions between the cerium oxidation states Ce^{3+}/Ce^{4+} lead to the formation of oxygen vacancies in nanoceria enhancing oxygen storage and diffusion capacity.[83] Due to its unique redox properties, CeO_{2-x} is capable of catalyzing a wide range of reactions. Ceria is especially well known for its use in three way catalysts for automotive industry.[83] Additionally, CeO_{2-x} can be used as support in the water-gas shift reaction[84] or for the catalytic oxidation of volatile organic compounds (VOC's).[85] However, the diverse catalytic activity of CeO_{2-x} nanoparticles is not only based on their redox properties but also on their surface acidity/basicity.[86] The Ce^{3+}/Ce^{4+} ratio does not only influence the amount of oxide vacancies, but also the acidity of the nanoceria surface. Since Ce^{3+} and Ce^{4+} are unsaturated Lewis acid sites, adsorption of Lewis bases which donate unpaired electrons to the cerium cations is favored. Since Ce^{4+} is a stronger Lewis acid with respect to Ce^{3+}, chemisorption of electron donor molecules is stronger at Ce^{4+} sites.[87]
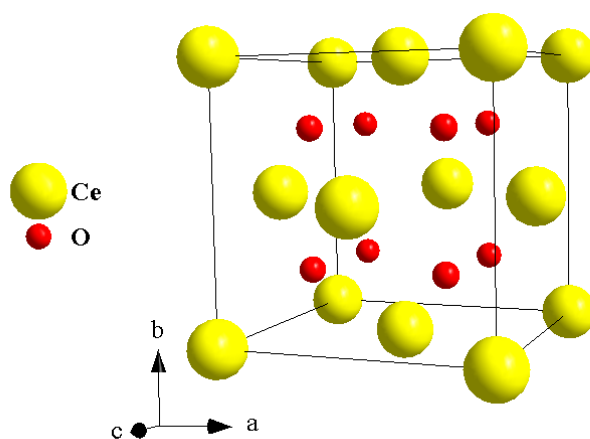
Figure 1-13. Crystal structure of CeO_2 (*Fm3m*) created with Diamond Ver.4.6.5.

Since nanoceria can reduce oxidative stress by scavenging reactive oxygen species (ROS), it exhibits numerous enzyme-mimetic activities. The oxidation states of surface cerium ions play a crucial role for its catalytic activity.[88] A higher Ce^{3+} concentration on the surface improves superoxide dismutase (SOD)[68] and peroxidase (PO)[69] mimetic like activity,

whereas catalase[70] and oxidase-like activity scales with higher Ce^{4+}/Ce^{3+} ratios.[71] Thus, the catalytic activity of ceria is very versatile making CeO_2 a great catalyst in various reactions. Due to its high chemical stability over a wide temperature[89] and pH range[90] and its high insolubility ($K_L = 10^{-60}$)[91], it is superior to enzymes with respect to many reaction conditions. Additionally, cerium oxide exhibits low acute toxicity. For rats, the single oral dose LD_{50} of cerium oxide is greater than >5000 mg·kg^{-1} given as a 50% w/w solution in distilled water.[92]

1.10. REFERENCES

1 Matin, A.; Khan, Z.; Zaidi, S. M. J.; Boyce, M. C. Biofouling in Reverse Osmosis Membranes for Seawater Desalination: Phenomena and Prevention. *Desalination* **2011**, *281* (1), 1–16.

2 Armbruster, C. R.; Parsek, M. R. New Insight into the Early Stages of Biofilm Formation. *Proc. Natl. Acad. Sci.* **2018**, *115* (17), 4317–4319.

3 Müller, W. E. G.; Wang, X.; Proksch, P.; Perry, C. C.; Osinga, R.; Gardères, J.; Schröder, H. C. Principles of Biofouling Protection in Marine Sponges: A Model for the Design of Novel Biomimetic and Bio-Inspired Coatings in the Marine Environment? *Mar. Biotechnol.* **2013**, *15* (4), 375–398.

4 Verderosa, A. D.; Totsika, M.; Fairfull-Smith, K. E. Bacterial Biofilm Eradication Agents: A Current Review. *Front. Chem.* **2019**, *7*.

5 Sandy, M.; Carter-Franklin, J. N.; Martin, J. D.; Butler, A. Vanadium Bromoperoxidase from Delisea Pulchra: Enzyme-Catalyzed Formation of Bromofuranone and Attendant Disruption of Quorum Sensing. *Chem. Commun.* **2011**, *47* (44), 12086.

6 Dominelli, N.; Heermann, R. „Small Talk". *Biol. unserer Zeit* **2020**, *50* (6), 414–423.

7 Miller, M. B.; Bassler, B. L. Quorum Sensing in Bacteria. *Annu. Rev. Microbiol.* **2001**, *55* (1), 165–199.

8 Köse-Mutlu, B.; Ergön-Can, T.; Koyuncu, I.; Lee, C.-H. Quorum Quenching for Effective Control of Biofouling in Membrane Bioreactor: A Comprehensive Review of Approaches, Applications, and Challenges. *Environ. Eng. Res.* **2019**, *24* (4), 543–558.

9 Bodey, G. P.; Bolivar, R.; Fainstein, V.; Jadeja, L. Infections Caused by Pseudomonas Aeruginosa. *Rev. Infect. Dis.* **1983**, *5* (2), 279–313.

10 Parthé, S., Welker, A., Meier, C., Knorr, B., & Schumacher, S. Hygiene & Medizin. **2016**.

11 Yang, L.; Jelsbak, L.; Marvig, R. L.; Damkiaer, S.; Workman, C. T.; Rau, M. H.; Hansen, S. K.; Folkesson, A.; Johansen, H. K.; Ciofu, O.; Hoiby, N.; Sommer, M. O. A.; Molin, S. Evolutionary Dynamics of Bacteria in a Human Host Environment. *Proc. Natl. Acad. Sci.* **2011**, *108* (18), 7481–7486.

12 Fazeli, H.; Akbari, R.; Moghim, S.; Narimani, T.; Arabestani, M. R.; Ghoddousi, A. R. Pseudomonas Aeruginosa Infections in Patients, Hospital Means, and Personnel's Specimens. *J. Res. Med. Sci.* **2012**, *17* (4), 332–337.

13 Chung, P. Y. The Emerging Problems of Klebsiella Pneumoniae Infections: Carbapenem Resistance and Biofilm Formation. *FEMS Microbiol. Lett.* **2016**, *363* (20), fnw219.

14   Scott, R. D. The Direct Medical Costs of Healthcare-Associated Infections in US Hospitals and the Benefits of Prevention. *Cdc* **2009**, No. March, 13.

15   Flemming H.-C. Microbial Biofouling: Unsolved Problems, Insufficient Approaches, and Possible Solutions. In: Flemming H.-C., Wingender J., Szewzyk U. (eds) Biofilm Highlights. Springer Series on Biofilms, Vol 5. Springer, Berlin, Heidelberg 2011, pp. 81-109.

16   Mattila-Sandholm, T.; Wirtanen, G. Biofilm Formation in the Industry: A Review. *Food Rev. Int.* **1992**, *8* (4), 573–603.

17   Dafforn, K. A.; Lewis, J. A.; Johnston, E. L. Antifouling Strategies: History and Regulation, Ecological Impacts and Mitigation. *Mar. Pollut. Bull.* **2011**, *62* (3), 453–465.

18   Baker, J. S.; Dudley, L. Y. Biofouling in Membrane Systems - a Review. *Desalination* **1998**, *118* (1–3), 81–89.

19   Flemming, H.-C. Biofouling Und Biokorrosion - Die Folgen Unerwünschter Biofilme. *Chem-Ing-Tech* **1995**, *67* (11), 1425–1430.

20   Rodríguez-Hernández, J. *Polymers against Microorganisms*; Springer International Publishing: Cham, 2017.

21   Olmo, J. A. Del; Ruiz-Rubio, L.; Pérez-Alvarez, L.; Sáez-Martínez, V.; Vilas-Vilela, J. L. Antibacterial Coatings for Improving the Performance of Biomaterials. *Coatings* **2020**, *10* (2), 1–19.

22   Ittershagen, M. Vom Ersatzstoff Zum Problemfall ? *Umweltbundesamt* **2008**, 1–13.

23   Thurman, R. B.; Gerba, C. P.; Bitton, G. The Molecular Mechanisms of Copper and Silver Ion Disinfection of Bacteria and Viruses. *Crit. Rev. Environ. Control* **1989**, *18* (4), 295–315.

24   Manzl, C.; Enrich, J.; Ebner, H.; Dallinger, R.; Krumschnabel, G. Copper-Induced Formation of Reactive Oxygen Species Causes Cell Death and Disruption of Calcium Homeostasis in Trout Hepatocytes. *Toxicology* **2004**, *196* (1–2), 57–64.

25   Dickson, M. N.; Liang, E. I.; Rodriguez, L. A.; Vollereaux, N.; Yee, A. F. Nanopatterned Polymer Surfaces with Bactericidal Properties. *Biointerphases* **2015**, *10* (2), 021010.

26   Sandy, M.; Carter-Franklin, J. N.; Martin, J. D.; Butler, A. Vanadium Bromoperoxidase from Delisea Pulchra: Enzyme-Catalyzed Formation of Bromofuranone and Attendant Disruption of Quorum Sensing. *Chem. Commun.* **2011**, *47* (44), 12086.

27   Syrpas, M.; Ruysbergh, E.; Blommaert, L.; Vanelslander, B.; Sabbe, K.; Vyverman, W.; De Kimpe, N.; Mangelinckx, S. Haloperoxidase Mediated Quorum Quenching by Nitzschia Cf Pellucida: Study of the Metabolization of N-Acyl Homoserine Lactones by a Benthic Diatom. *Mar. Drugs* **2014**, *12* (1), 352–367.

28	Fetzner, S. Quorum Quenching Enzymes. *J. Biotechnol.* **2015**, *201*, 2–14.

29	Tang, K.; Zhang, Y.; Yu, M.; Shi, X.; Coenye, T.; Bossier, P.; Zhang, X.-H. Evaluation of a New High-Throughput Method for Identifying Quorum Quenching Bacteria. *Sci. Rep.* **2013**, *3* (1), 2935.

30	Lapage, S. P.; Efstratiou, A.; Hill, L. R. The Ortho-Nitrophenol (ONPG) Test and Acid from Lactose in Gram-Negative Genera. *J. Clin. Pathol.* **1973**, *26* (11), 821–825.

31	Butler, A.; Carter-Franklin, J. N. The Role of Vanadium Bromoperoxidase in the Biosynthesis of Halogenated Marine Natural Products. *Nat. Prod. Rep.* **2004**, *21* (1), 180.

32	Timmins, A.; de Visser, S. P. Enzymatic Halogenases and Haloperoxidases; *Adv. Protein Struct. Biol.* **2015**, *100*, pp 113–151

33	Herget, K.; Frerichs, H.; Pfitzner, F.; Tahir, M. N.; Tremel, W. Functional Enzyme Mimics for Oxidative Halogenation Reactions That Combat Biofilm Formation. *Adv. Mater.* **2018**, *30* (36), 1707073.

34	Hofrichter, M.; Ullrich, R. Heme-Thiolate Haloperoxidases: Versatile Biocatalysts with Biotechnological and Environmental Significance. *Appl. Microbiol. Biotechnol.* **2006**, *71* (3), 276–288.

35	Sun, W.; Kadima, T. A.; Pickard, M. A.; Dunford, H. B. Catalase Activity of Chloroperoxidase and Its Interaction with Peroxidase Activity. *Biochem. Cell Biol.* **1994**, *72* (7–8), 321–331.

36	Lakner, F. J.; Hager, L. P. Chloroperoxidase as Enantioselective Epoxidation Catalyst: An Efficient Synthesis of (R)-(−)-Mevalonolactone. *J. Org. Chem.* **1996**, *61* (11), 3923–3925.

37	Baciocchi, E.; Fabbrini, M.; Lanzalunga, O.; Manduchi, L.; Pochetti, G. Prochiral Selectivity in H 2 O 2 -Promoted Oxidation of Arylalkanols Catalysed by Chloroperoxidase. *Eur. J. Biochem.* **2001**, *268* (3), 665–672.

38	Pasta, P.; Carrea, G.; Monzani, E.; Gaggero, N.; Colonna, S. Chloroperoxidase-Catalyzed Enantioselective Oxidation of Methyl Phenyl Sulfide with Dihydroxyfumaric Acid/Oxygen or Ascorbic Acid/Oxygen as Oxidants. *Biotechnol. Bioeng.* **1999**, *62* (4), 489–493.

39	La Rotta Hernandez, C. E.; Lütz, S.; Liese, A.; Bon, E. P. S. Activity and Stability of Caldariomyces Fumago Chloroperoxidase Modified by Reductive Alkylation, Amidation and Cross-Linking. *Enzyme Microb. Technol.* **2005**, *37* (6), 582–588.

40	van Schijndel, J. W. P. M.; Vollenbroek, E. G. M.; Wever, R. The Chloroperoxidase from the Fungus Curvularia Inaequalis; a Novel Vanadium Enzyme. *Biochim. Biophys. Acta - Protein Struct. Mol. Enzymol.* **1993**, *1161* (2–3), 249–256.

41   Weyand, M.; Hecht, H.-J.; Kieß, M.; Liaud, M.-F.; Vilter, H.; Schomburg, D. X-Ray Structure Determination of a Vanadium-Dependent Haloperoxidase from Ascophyllum Nodosum at 2.0 Å Resolution 1 1Edited by R. Huber. *J. Mol. Biol.* **1999**, *293* (3), 595–611.

42   Ligtenbarg, A. Catalytic Oxidations by Vanadium Complexes. *Coord. Chem. Rev.* **2003**, *237* (1–2), 89–101.

43   Höfler, G. T.; But, A.; Hollmann, F. Haloperoxidases as Catalysts in Organic Synthesis. *Org. Biomol. Chem.* **2019**, *17* (42), 9267–9274.

44   Höfler, G. T.; But, A.; Younes, S. H. H.; Wever, R.; Paul, C. E.; Arends, I. W. C. E.; Hollmann, F. Chemoenzymatic Halocyclization of 4-Pentenoic Acid at Preparative Scale. *ACS Sustain. Chem. Eng.* **2020**, *8* (7), 2602–2607.

45   Dong, J. J.; Fernández-Fueyo, E.; Li, J.; Guo, Z.; Renirie, R.; Wever, R.; Hollmann, F. Halofunctionalization of Alkenes by Vanadium Chloroperoxidase from Curvularia Inaequalis. *Chem. Commun.* **2017**, *53* (46), 6207–6210.

46   But, A.; Le Nôtre, J.; Scott, E. L.; Wever, R.; Sanders, J. P. M. Selective Oxidative Decarboxylation of Amino Acids to Produce Industrially Relevant Nitriles by Vanadium Chloroperoxidase. *ChemSusChem* **2012**, *5* (7), 1199–1202.

47   Fernández-Fueyo, E.; van Wingerden, M.; Renirie, R.; Wever, R.; Ni, Y.; Holtmann, D.; Hollmann, F. Chemoenzymatic Halogenation of Phenols by Using the Haloperoxidase from Curvularia Inaequalis. *ChemCatChem* **2015**, *7* (24), 4035–4038.

48   Hille-Rehfeld, A. Halogenierte Naturstoffe. *Chemie unserer Zeit* **2014**, *48* (5), 402–405.

49   Berg, J. M.; Tymoczko, J. L.; Gatto, G. J.; Stryer, L. *Stryer Biochemie*; Springer Berlin Heidelberg: Berlin, Heidelberg, 2018.

50   Wu, J.; Wang, X.; Wang, Q.; Lou, Z.; Li, S.; Zhu, Y.; Qin, L.; Wei, H. Nanomaterials with Enzyme-like Characteristics (Nanozymes): Next-Generation Artificial Enzymes (II). *Chem. Soc. Rev.* **2019**, *48* (4), 1004–1076.

51   Xie, J.; Zhang, X.; Wang, H.; Zheng, H.; Huang, Y.; Xie, J. Analytical and Environmental Applications of Nanoparticles as Enzyme Mimetics. *TrAC Trends Anal. Chem.* **2012**, *39*, 114–129.

52   Hu, X.; Liu, J.; Hou, S.; Wen, T.; Liu, W.; Zhang, K.; He, W.; Ji, Y.; Ren, H.; Wang, Q.; Wu, X. Research Progress of Nanoparticles as Enzyme Mimetics. *Sci. China Physics, Mech. Astron.* **2011**, *54* (10), 1749–1756.

53   Gao, L.; Zhuang, J.; Nie, L.; Zhang, J.; Zhang, Y.; Gu, N.; Wang, T.; Feng, J.; Yang, D.; Perrett, S.; Yan, X. Intrinsic Peroxidase-like Activity of Ferromagnetic Nanoparticles. *Nat. Nanotechnol.* **2007**, *2* (9), 577–583.

54   Kataky, R.; Morgan, E. Potential of Enzyme Mimics in Biomimetic Sensors: A Modified-Cyclodextrin as a Dehydrogenase Enzyme Mimic. *Biosens. Bioelectron.* **2003**, *18* (11), 1407–1417.

55   Kirkorian, K.; Ellis, A.; Twyman, L. J. Catalytic Hyperbranched Polymers as Enzyme Mimics; Exploiting the Principles of Encapsulation and Supramolecular Chemistry. *Chem. Soc. Rev.* **2012**, *41* (18), 6138–6159.

56   Liu, L.; Breslow, R. Dendrimeric Pyridoxamine Enzyme Mimics. *J. Am. Chem. Soc.* **2003**, *125* (40), 12110–12111.

57   Ali, S. S.; Hardt, J. I.; Quick, K. L.; Sook Kim-Han, J.; Erlanger, B. F.; Huang, T. T.; Epstein, C. J.; Dugan, L. L. A Biologically Effective Fullerene (C60) Derivative with Superoxide Dismutase Mimetic Properties. *Free Radic. Biol. Med.* **2004**, *37* (8), 1191–1202.

58   Natalio, F.; André, R.; Hartog, A. F.; Stoll, B.; Jochum, K. P.; Wever, R.; Tremel, W. Vanadium Pentoxide Nanoparticles Mimic Vanadium Haloperoxidases and Thwart Biofilm Formation. *Nat. Nanotechnol. 2012 78* **2012**, *7* (8), 530–535.

59   André, R.; Natálio, F.; Humanes, M.; Leppin, J.; Heinze, K.; Wever, R.; Schröder, H.-C.; Müller, W. E. G. G.; Tremel, W. V2O5 Nanowires with an Intrinsic Peroxidase-Like Activity. *Adv. Funct. Mater.* **2011**, *21* (3), 501–509.

60   Herget, K.; Hubach, P.; Pusch, S.; Deglmann, P.; Götz, H.; Gorelik, T. E.; Gural'skiy, I. A.; Pfitzner, F.; Link, T.; Schenk, S.; Panthöfer, M.; Ksenofontov, V.; Kolb, U.; Opatz, T.; André, R.; Tremel, W. Haloperoxidase Mimicry by CeO2−x Nanorods Combats Biofouling. *Adv. Mater.* **2017**, *29* (4), 1603823.

61   Frerichs, H.; Pütz, E.; Pfitzner, F.; Reich, T.; Gazanis, A.; Panthöfer, M.; Hartmann, J.; Jegel, O.; Heermann, R.; Tremel, W. Nanocomposite Antimicrobials Prevent Bacterial Growth through the Enzyme-like Activity of Bi-Doped Cerium Dioxide (Ce 1−x Bi x O 2−δ). *Nanoscale* **2020**, *12* (41), 21344–21358.

62   Liu, B.; Huang, Z.; Liu, J. Boosting the Oxidase Mimicking Activity of Nanoceria by Fluoride Capping: Rivaling Protein Enzymes and Ultrasensitive F − Detection. *Nanoscale* **2016**, *8* (28), 13562–13567.

63   Lin, Y.; Ren, J.; Qu, X. Nano-Gold as Artificial Enzymes: Hidden Talents. *Adv. Mater.* **2014**, *26* (25), 4200–4217.

64   Jiang, H.; Chen, Z.; Cao, H.; Huang, Y. Peroxidase-like Activity of Chitosan Stabilized Silver Nanoparticles for Visual and Colorimetric Detection of Glucose. *Analyst* **2012**, *137* (23), 5560–5564.

65   Ai, L.; Li, L.; Zhang, C.; Fu, J.; Jiang, J. MIL-53(Fe): A Metal–Organic Framework with Intrinsic Peroxidase-Like Catalytic Activity for Colorimetric Biosensing. *Chem. – A Eur. J.* **2013**, *19* (45), 15105–15108.

66 Huang, Y.; Zhao, M.; Han, S.; Lai, Z.; Yang, J.; Tan, C.; Ma, Q.; Lu, Q.; Chen, J.; Zhang, X.; Zhang, Z.; Li, B.; Chen, B.; Zong, Y.; Zhang, H.; Growth of Au Nanoparticles on 2D Metalloporphyrinic Metal-Organic Framework Nanosheets Used as Biomimetic Catalysts for Cascade Reactions. *Adv. Mater.* **2017**, *29* (32), 1700102.

67 Xiong, Y.; Chen, S.; Ye, F.; Su, L.; Zhang, C.; Shen, S.; Zhao, S. Synthesis of a Mixed Valence State Ce-MOF as an Oxidase Mimetic for the Colorimetric Detection of Biothiols. *Chem. Commun.* **2015**, *51* (22), 4635–4638.

68 Heckert, E. G.; Karakoti, A. S.; Seal, S.; Self, W. T. The Role of Cerium Redox State in the SOD Mimetic Activity of Nanoceria. *Biomaterials* **2008**, *29* (18), 2705–2709.

69 Tian, Z.; Li, J.; Zhang, Z.; Gao, W.; Zhou, X.; Qu, Y. Highly Sensitive and Robust Peroxidase-like Activity of Porous Nanorods of Ceria and Their Application for Breast Cancer Detection. *Biomaterials* **2015**, *59*, 116–124.

70 Pirmohamed, T.; Dowding, J. M.; Singh, S.; Wasserman, B.; Heckert, E.; Karakoti, A. S.; King, J. E. S.; Seal, S.; Self, W. T. Nanoceria Exhibit Redox State-Dependent Catalase Mimetic Activity. *Chem. Commun.* **2010**, *46* (16), 2736.

71 Ju, X.; Hubalek Kalbacova, M.; Šmíd, B.; Johánek, V.; Janata, M.; Dinhová, T. N.; Bělinová, T.; Mazur, M.; Vorokhta, M.; Strnad, L. Poly(Acrylic Acid)-Mediated Synthesis of Cerium Oxide Nanoparticles with Variable Oxidation States and Their Effect on Regulating the Intracellular ROS Level. *J. Mater. Chem. B* **2021**, *9* (36), 7386–7400.

72 Zeng, D.; Luo, W.; Li, J.; Liu, H.; Ma, H.; Huang, Q.; Fan, C. Gold Nanoparticles-Based Nanoconjugates for Enhanced Enzyme Cascade and Glucose Sensing. *Analyst* **2012**, *137* (19), 4435–4439.

73 Wang, T.; Zhu, H.; Zhuo, J.; Zhu, Z.; Papakonstantinou, P.; Lubarsky, G.; Lin, J.; Li, M. Biosensor Based on Ultrasmall MoS2 Nanoparticles for Electrochemical Detection of H2O2 Released by Cells at the Nanomolar Level. *Anal. Chem.* **2013**, *85* (21), 10289–10295.

74 Shahwan, T.; Abu Sirriah, S.; Nairat, M.; Boyaci, E.; Eroĝlu, A. E.; Scott, T. B.; Hallam, K. R. Green Synthesis of Iron Nanoparticles and Their Application as a Fenton-like Catalyst for the Degradation of Aqueous Cationic and Anionic Dyes. *Chem. Eng. J.* **2011**, *172* (1), 258–266.

75 Mu, J.; Li, J.; Zhao, X.; Yang, E. C.; Zhao, X. J. Cobalt-Doped Graphitic Carbon Nitride with Enhanced Peroxidase-like Activity for Wastewater Treatment. *RSC Adv.* **2016**, *6* (42), 35568–35576.

76 Colpas, G. J.; Hamstra, B. J.; Kampf, J. W.; Pecoraro, V. L. A Functional Model for Vanadium Haloperoxidase. *J. Am. Chem. Soc.* **1994**, *116* (8), 3627–3628.

77 Natalio, F.; André, R.; Hartog, A. F.; Stoll, B.; Jochum, K. P.; Wever, R.; Tremel, W. Vanadium Pentoxide Nanoparticles Mimic Vanadium Haloperoxidases and Thwart Biofilm Formation. *Nat. Nanotechnol.* **2012**, *7* (8), 530–535.

78   André, R.; Natálio, F.; Humanes, M.; Leppin, J.; Heinze, K.; Wever, R.; Schröder, H.-C.; Müller, W. E. G.; Tremel, W. V2O5 Nanowires with an Intrinsic Peroxidase-Like Activity. *Adv. Funct. Mater.* **2011**, *21* (3), 501–509.

79   White, D. J.; Levy, L. S. Vanadium: Environmental Hazard or Environmental Opportunity? A Perspective on Some Key Research Needs. *Environ. Sci. Process. Impacts* **2021**, *23* (4), 527–534.

80   Herget, K.; Frerichs, H.; Pfitzner, F.; Tremel, W. Cerdioxid Schützt Vor Marinem Fouling: Biomimetische Biozide. *Chemie Unserer Zeit* **2017**, *51* (4), 278–281.

81   Frerichs, H.; Pütz, E.; Pfitzner, F.; Reich, T.; Gazanis, A.; Panthöfer, M.; Hartmann, J.; Jegel, O.; Heermann, R.; Tremel, W. Nanocomposite Antimicrobials Prevent Bacterial Growth through the Enzyme-like Activity of Bi-Doped Cerium Dioxide (Ce 1−x Bi x O 2−δ). *Nanoscale* **2020**, *12* (41), 21344–21358.

82   Dutta, P.; Pal, S.; Seehra, M. S.; Shi, Y.; Eyring, E. M.; Ernst, R. D. Concentration of Ce 3+ and Oxygen Vacancies in Cerium Oxide Nanoparticles. *Chem. Mater.* **2006**, *18* (21), 5144–5146.

83   Montini, T.; Melchionna, M.; Monai, M.; Fornasiero, P. Fundamentals and Catalytic Applications of CeO 2 -Based Materials. *Chem. Rev.* **2016**, *116* (10), 5987–6041.

84   Andreeva, D.; Idakiev, V.; Tabakova, T.; Ilieva, L.; Falaras, P.; Bourlinos, A.; Travlos, A. Low-Temperature Water-Gas Shift Reaction over Au/CeO2 Catalysts. *Catal. Today* **2002**, *72* (1–2), 51–57.

85   Aouad, S.; Abi-Aad, E.; Aboukaïs, A. Simultaneous Oxidation of Carbon Black and Volatile Organic Compounds over Ru/CeO2 Catalysts. *Appl. Catal. B Environ.* **2009**, *88* (3–4), 249–256.

86   Wang, Y.; Wang, F.; Song, Q.; Xin, Q.; Xu, S.; Xu, J. Heterogeneous Ceria Catalyst with Water-Tolerant Lewis Acidic Sites for One-Pot Synthesis of 1,3-Diols via Prins Condensation and Hydrolysis Reactions. *J. Am. Chem. Soc.* **2013**, *135* (4), 1506–1515.

87   Tan, Z.; Li, G.; Chou, H.-L.; Li, Y.; Yi, X.; Mahadi, A. H.; Zheng, A.; Edman Tsang, S. C.; Peng, Y.-K. Differentiating Surface Ce Species among CeO 2 Facets by Solid-State NMR for Catalytic Correlation. *ACS Catal.* **2020**, *10* (7), 4003–4011.

88   Song, G.; Cheng, N.; Zhang, J.; Huang, H.; Yuan, Y.; He, X.; Luo, Y.; Huang, K. Nanoscale Cerium Oxide: Synthesis, Biocatalytic Mechanism, and Applications. *Catalysts* **2021**, *11* (9), 1123.

89   Ivanov, V. K.; Polezhaeva, O. S.; Baranchikov, A. E.; Shcherbakov, A. B. Thermal Stability of Nanocrystalline CeO2 Prepared through Freeze Drying. *Inorg. Mater.* **2010**, *46* (1), 43–46.

90   Dahle, J. T.; Livi, K.; Arai, Y. Effects of PH and Phosphate on CeO2 Nanoparticle Dissolution. *Chemosphere* **2015**, *119*, 1365–1371.

91   Plakhova, T. V.; Romanchuk, A. Y.; Yakunin, S. N.; Dumas, T.; Demir, S.; Wang, S.; Minasian, S. G.; Shuh, D. K.; Tyliszczak, T.; Shiryaev, A. A.; Egorov, A. V.; Ivanov, V. K.; Kalmykov, S. N. Solubility of Nanocrystalline Cerium Dioxide: Experimental Data and Thermodynamic Modeling. *J. Phys. Chem. C* **2016**, *120* (39), 22615–22626.

92   Lambert, C. E.; Barnum, E. C.; Shapiro, R. Acute Toxicological Evaluation of Cerium Oxide. *J. Am. Coll. Toxicol.* **1993**, *12* (6), 617–617.

2

MOTIVATION AND SCIENTIFIC GOAL

Biofouling causes a variety of problems in many industrial sectors/industries. Generally, bacteria embedded in a biofilm matrix, are better protected from hostile influences, making cleaning and removal much more difficult. Especially in clinical facilities, biofilms can lead to serious infections, due to the release of pathogens. In addition to the infections caused by biofilms and the associated costs in the clinical field, biofilms also lead to major disadvantages in water purification and desalination facilities and in shipping. Blockages or increased friction forces lead to energy losses that drive up costs. In the past, biocide releasing paints were mainly used to prevent the formation of biofilms, which leads to bacterial death. However, these biocides have a toxic effect not only on the bacteria, but also on the settled marine organisms. For this reason, it is particularly important to provide a solution against biofouling that does not contain bactericidal or toxic substances.

One promising approach is to suppress bacterial communication. Prior to the development of a biofilm, the bacteria communicate via small organic signaling molecules. If the number of bacteria and thus the concentration of signaling molecules is sufficiently high, group-coordinated behavior occurs, which controls biofilm formation, virulence and luminescence, among other things. If communication is interrupted at an early stage, biofilm formation can be prevented. Marine algae defend themselves from bacterial colonization using exactly this strategy. They possess enzymes (V-ClPO, V-BrPO) that can oxidatively brominate organic signaling molecules in the presence of a halide and H_2O_2 by producing hypohalous acid (HOX) as halogenating agent.

Cerium oxide (CeO_2) nanoparticles are known for their enzyme-mimetic activity. Being able to scavenge reactive oxygen species (ROS), they can catalyze superoxide dismutase, peroxidase, catalase, and oxidase-like reactions as nanozymes. In 2017, Herget *et al*. have also discovered a haloperoxidase-like activity that makes CeO_2 a promising catalyst for oxidative bromination reactions and in antibiofouling applications. Since CeO_2 has many advantages over natural enzymes, such as low-cost production, thermal stability, stability over wide pH-range and resistance to solvents, the application of CeO_2 as a biofilm inhibitor

is investigated in more detail in the present work. Thus, a main focus of this thesis is the synthesis of functional nanomaterials with antibiofouling activities.
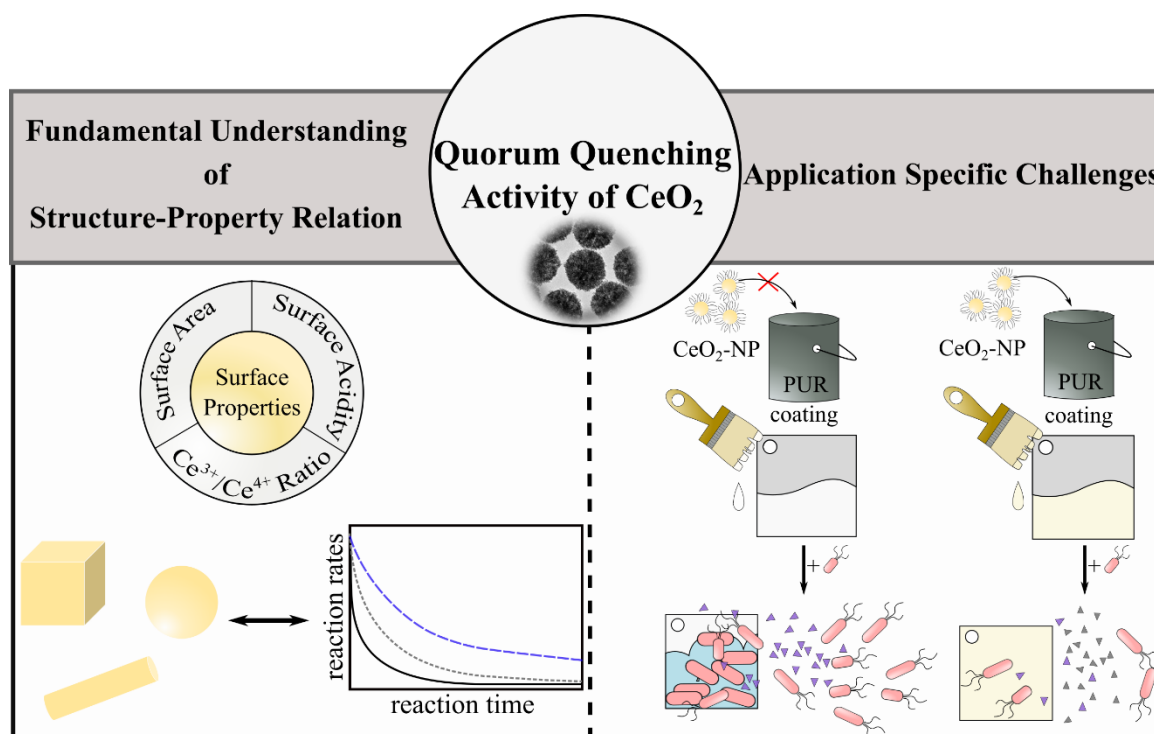

Figure 2-1. Schematic overview of the scientific goals, focusing first on identifying the surface properties that determine reaction rates to develop nanocatalysts with optimal enzyme-like properties and then on using these nanocatalysts in everyday antibiofouling applications.

The first goal of this work is the identification of those surface properties that are responsible for the haloperoxidase-like reaction. For this purpose, nanoparticles with different morphologies are compared with respect to properties such as surface acidity, surface potential and specific surface area. Moreover, the reaction rates of the different nanoparticles on the oxidative bromination of the model substrate thymol are investigated in detail. The correlation of the surface properties with the reaction rates then allows to draw conclusions about the catalytically relevant parameters of the CeO_2 nanoparticles.

In addition, it was investigated whether and how the surface properties of CeO_2 nanoparticles and their performance as catalysts in enzyme-mimetic reactions change with time. The aim is to determine whether the same surface properties are responsible for the catalytic activity in haloperoxidase-like and peroxidase-like reactions. For this purpose, the examination of the nanoparticle growth process by small-angle X-ray scattering, was complemented with detailed surface property studies on aliquots taken after different reaction times.

Since the use of nanoparticles in applications is another major challenge, the insight gained in these fundamental studies was used in the next step to produce CeO_2 composites based on polyurethane coatings. In these composites, CeO_2 should still exhibit a haloperoxidase-like activity to prevent biofouling by quorum quenching mechanisms. To get a better insight into the general mechanism of biofilm inhibition, LC-MS and IC-CD studies were performed in addition to bioassays in collaboration with A. Gazanis and N. Keltsch. The effect of CeO_2 nanoparticles on the concentration of signaling molecules and bromide anions was investigated in more detail. In addition, the degradation of the brominated signal molecules in the bacterial culture and its effect on the biofilm was studied.

Since the haloperoxidase reaction only occurs in the presence of H_2O_2, the last study investigated whether it was possible to circumvent the restriction of adding H_2O_2 externally to the reaction solution. To circumvent this problem, the preparation of H_2O_2 deposits and the *in-situ* generation of H_2O_2 were investigated in more detail. For this purpose, polyvinylidene difluoride/$Bi_{0.2}Ce_{0.8}O_{1.9}$ and polyethersulfone/$Bi_{0.2}Ce_{0.8}O_{1.9}$ composites containing depot substances were prepared and the release of H_2O_2 was studied qualitatively. In addition, it was determined whether g-C_3N_4 doped Biphenyl Diimude (BDI) can generate H_2O_2 photochemically and whether coupling of the haloperoxidase reaction with a CeO_2 catalyst can generate a reaction cascade.

MORPHOLOGY REGULATED OXIDATIVE BROMINATION OF THYMOL WITH CeO$_{2-x}$ NANOCRYSTAL ENZYME MIMICS

3.1. SUMMARY

Cerianite nanoparticles are known to mimic natural enzymes. One of these enzymes is the vanadium-dependent haloperoxidase that catalyzes the oxidative bromination of organic substrates in
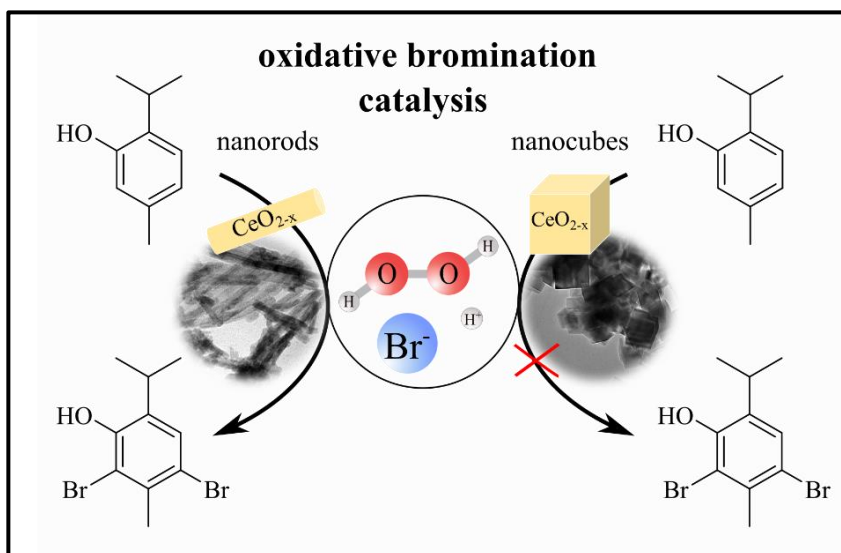
the presence of bromide and hydrogen peroxide, thus serving as a catalyst in organic syntheses. One commonly studied model reaction is the bromination of the phenolic monoterpene thymol. This chapter addresses the question whether synthetic cerianite nanocrystals catalyze the oxidative bromination of thymol and which nanocrystal properties favor catalytic conversion. For this purpose, nanocrystals with three different morphologies (nanorods, nanospheres and nanocubes) were synthesized and added separately to an acidic reaction mixture of thymol, Br$^-$ and H$_2$O$_2$. Since all nanocrystals had the same phase (cerianite), the surface properties of the different morphologies were investigated in order to draw conclusions about catalytic activity. The oxidative bromination of thymol to 4-bromothymol and 2,4-dibromothymol was monitored by ^{1}H-NMR spectroscopy for each nanocrystal morphology. Nanorods showed the highest catalytic activity, while nanospheres were less active and nanocubes showed hardly any conversion. The analysis was done based on specific surface area (S_{BET}), zeta potential (ζ-

potential) and Lewis acidity of the nanocrystals. Surface defect intensities were compared by X-ray photoelectron spectroscopy. The Lewis acidity of the nanocrystals was determined by solid state ^{31}P-NMR spectroscopy using trimethyl phosphine as molecular probe. Based on the ^{31}P signal of trimethyl phosphine, the surface acidity of the cerium oxide was determined to be highest for nanorods, followed by that of nanospheres and lowest for nanocubes. The stability of the surface peroxide or hydroperoxide ligands on the different morphologies was compared by Raman spectroscopy. Since oxidative bromination catalysis likely depends on the stability of the intermediate surface complex, rapid decomposition of H_2O_2 on the nanoparticle surface is detrimental. The overall result of the individual analyses is that the oxidative bromination reaction is favored by a high S_{BET}, a strongly positive ζ-potential, a high Lewis acidity, and surface defects. Based on this study, a deeper insight into the surface chemistry and key features of catalytic oxidative bromination was obtained. The properties of cerianite nanoparticles can be specifically engineered by different synthetic methods to obtain the optimum catalyst for oxidative bromination reactions and thus a powerful haloperoxidase mimic.

Contributions:

Eva Pütz:	Concept development, nanoparticle synthesis, TEM and S_{BET} area measurement, ^{1}H-NMR measurement, manuscript preparation, figure preparation.
XXX:	Concept development, nanoparticle synthesis, TEM images, ζ-potential and ^{1}H-NMR measurement, manuscript preparation, figure preparation.
XXX:	^{31}P-NMR measurement, manuscript correction.
XXX:	PXRD refinements.
XXX:	Deconvolution of ^{31}P-NMR data.
XXX:	HRTEM measurement.
XXX:	HRTEM measurement
XXX:	Raman measurement.
XXX:	XPS measurement.
XXX:	Manuscript correction and scientific supervision.

3.2.   INTRODUCTION

Halogenated organic compounds are important intermediates in chemical,[1] pharmaceutical[2] or agrochemical[3] research, because the carbon-halogen bond is susceptible to nucleophilic attack. This increases biological activity and bioavailability of the corresponding compounds[4] or enables metal-catalyzed cross-coupling reactions.[5] While traditional chemical halogenation methods employ highly reactive reagents and generate harmful waste, nature has evolved a variety of enzymes that halogenate their substrates with Cl^-, Br^-, I^- or even F^- anions and oxygen or peroxide at room temperature in aqueous solution.[6,7] Therefore, these halogenating enzymes, halogenases and haloperoxidases,[8,9] are attractive synthetic tools, as they have additional advantages like regioselectivity and the addressability of electronically disfavored positions. A number of transition metal complexes[10,11], V_2O_5[12] and molybdate anions[13] can act as functional mimics of haloperoxidases ("nanozymes").[14,15] Although enzymatic oxidative halogenation (*via* vanadium bromoperoxidases[16,17] is well explored, mechanistic information on solid state biomimetic models is scarce. The catalytic effect of V-dependent haloperoxidases is related to the formation of a vanadium–peroxido species at the active site due to reaction with hydrogen peroxide[18], which is a stronger oxidant than H_2O_2 itself. The final product is formed from a hypobromite intermediate by reaction with an organic substrate. Reaction with another oxidant molecule leads to its decomposition accompanied by singlet dioxygen formation.[19] The molecular complexes have been reported to form high-valent metal–oxo/peroxido intermediates.[20–23] Likewise, V_2O_5 nanoparticles[24,25] form surface-peroxido species, but they are not stable with time due to the formation of soluble polyoxovanadates.[26]

Ceria nanoparticles are efficient functional mimics of haloperoxidases as well.[27] The formation of stable hydroperoxo/peroxo surface species[27,28] enables the reduction of undesired reactive oxygen species in biological systems.[29] This makes ceria nanoparticles efficient functional mimics of peroxidases[30–32] and haloperoxidases.[33] Since ceria is highly insoluble ($K_L = 10^{-60}$ mol$^3 \cdot$L^{-3}),[34] non-leaching,[35,36] and chemically stable over a wide temperature and pH range (pH 1-13),[35] it exhibits better storage and operational stability with respect to heat, organic solvents, and autoproteolysis compared to natural or recombinant enzymes. Moreover, ceria has low production costs, high catalyst productivity, and it is easy recovered and recycled.

Since cerium is redox active and can cycle between its tetra- and trivalent states ($E° = 1.72$ V)[37], ceria is non-stoichiometric (CeO_{2-x}) every two cation defects Ce^{3+} in ceria are balanced by one oxide-vacancy defect.[38] Its success in chemical reactions (e.g. for HCl oxidation in a Deacon process in order to recover Cl_2)[39] to these unique redox and structural properties associated with oxygen diffusion and oxygen storage/release capacity in combination with its acid/base properties.[38,40] In nanocrystals, the oxygen vacancies may cluster at the particle surface,[41,42] because the ionic radius of Ce^{3+} (128 pm)[43] is more compatible with the undercoordinated surface sites than the 8-fold coordinated sites of Ce^{4+} (115 pm) in the cerianite structure.[27,44]

While the haloperoxidase properties of nanoceria are promising, the design rules for nanocatalysts with optimum halogenating properties are not yet defined. Nanoparticle powders typically expose a range of surfaces with different Ce coordination, defect sites, predominantly low-index surfaces with low surface energies. CeO_{2-x} nanocrystals with specific morphologies have been employed before to study the structure sensitivity of catalytic reactions experimentally[45–47] or theoretically,[48] but almost all studies are concerned with gas-phase reactions at high temperatures.[49] The stability and reactivity of ceria nanoparticles aqueous environment may change significantly, because ion charges and hydration/solvation effects at the metal oxide/water interface come into play.[50,51] Therefore, this work compares the morphology-dependent oxidative bromination reaction catalyzed by CeO_{2-x} nanoparticles using thymol, a monoterpenoid phenolic compound, as model substrate. To investigate the impact of morphology in terms of BET surface area (S_{BET}), ζ-potential and haloperoxidase activity of CeO_{2-x}, we employed CeO_{2-x} particles with defined diameters and morphologies (spheres, cubes, rods).[52] The surface structures of the different morphologies lead to different acid/base properties (and also surface charge) of the respective surfaces, which are essential for the formation of surface hydroperoxo groups and the reaction with negatively charged halide species in aqueous solution.[53,54] Therefore, the Lewis acidity of the surface was studied with trimethylphosphine (TMP) as ^{31}P nuclear magnetic resonance (NMR) probe.[55]

CeO_{2-x} nanorods displayed the highest performance for the bromination of thymol. The catalytic activities for the three morphologies were separated from the effect of active surface area and surface charge (ζ-potential) by determining the S_{BET} by nitrogen physisorption and the ζ-potential by light scattering. In essence, the maximum activity is related to the interplay of the acidity, ζ-potential and the S_{BET} of the CeO_{2-x} nanocrystals.

3.3. RESULTS AND DISCUSSION

TEM/PXRD characterization

Ceria nanorods and cubes were prepared hydrothermally using different NaOH concentrations (rods 4 M, cubes 19 M).[56-58] Spherical ceria particles were prepared by sol-gel chemistry using citric acid as ligand (Figure 3-1B+E).[59,60] Phase composition, morphology and size were determined by powder X-ray diffraction and transmission electron microscopy (TEM), respectively. Figure 3-1A+D shows TEM images of CeO_{2-x} nanorods. The nanorods have a uniform width (5-7 nm) and a broad length distribution (40-200 nm) (Figure S3-1C+D). Increasing the NaOH concentration leads to the formation of well-defined cubes with average sizes of 35 nm. (Figure 3-1C+F, Figure S3-1A) The spherical CeO_{2-x} particles (Figure 3-1B+E, Figure S3-1B) had an average size of 6-7 nm.
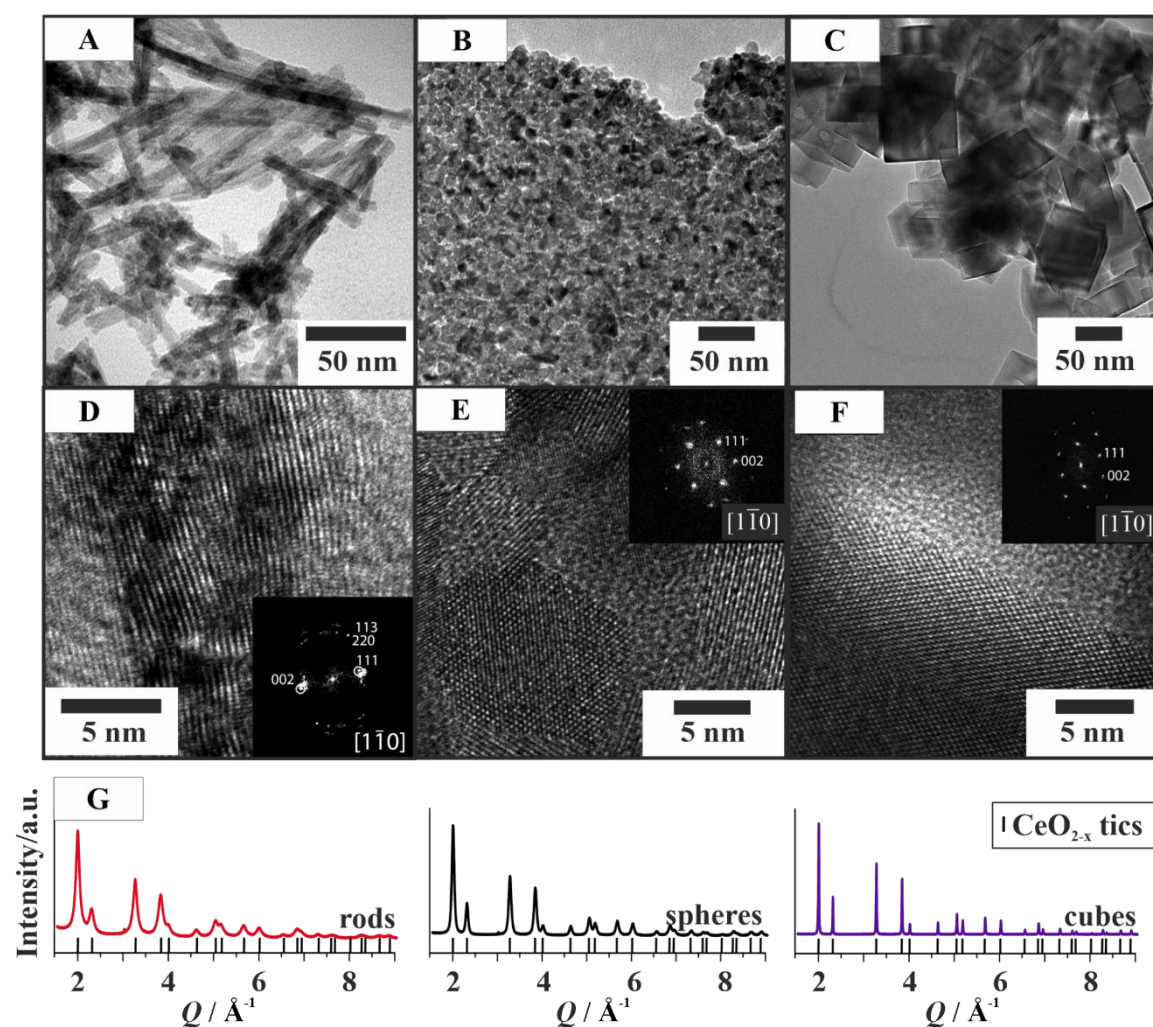
Figure 3-1. TEM (A-C) and high resolution (HR)TEM (D-F) images of CeO_{2-x} nanoparticles with reduced fast-Fourier transformation (FFT). (A, D) nanorods, (B, E) nanospheres, (C, F) nanocubes. (G) Experimental powder X-ray diffraction patterns (PXRD) of CeO_{2-x} nanorods (red line), nanospheres (black line) and nanocubes (purple line). Tics indicate theoretical positions of Bragg intensities.

HRTEM images of all CeO_{2-x} morphologies show the [110] zone axis (Figure 3-1D-F). According to the corresponding fast Fourier transform (FFT) pattern, two sets of reflections were observed for nanocubes and nanospheres, which could be attributed to the (111) and (002) planes. However, the FFT pattern of the nanorods demonstrates a polycrystalline structure with additional (113) and (220) planes. The polycrystallinity of the nanorods was also confirmed by Rietveld refinements. The powder diffraction patterns in Figure 3-1G show that all ceria particles crystallize in the cerianite phase with the space group ($Fm3m$) corresponding to the fluorite (CaF_2) structure. Powder diffraction patterns with Rietveld refinement are shown in Figure S3-6. The reflection half widths of the nanocubes are very narrow, indicating a high crystallinity, low defect density and large crystal domains. The reflections of the pattern of CeO_{2-x} spheres are broader due to small crystallite sizes. The strong reflection broadening of the nanorods is attributed to the presence of grain boundaries and surface defects such as vacancy clusters, pits, and a high degree of surface roughness.[61–63]

Determination of Lewis acidity using TMP

Quantum chemical calculations at various theory levels suggested that the catalytic HOBr formation cycle starts by binding a surface peroxido or hydroperoxido ligand to the CeO_{2-x} facets *via* exchange of surface-bound water molecules. With a Gibbs free energy change ($\Delta G°$) close to zero this exchange was predicted to be unlikely (for typical H_2O_2 concentrations), but to become favorable ($\Delta G°<0$) for a dissociation of H_2O_2 accompanied by a transfer of an oxygen atom to a bromide anion (or HBr molecule) and its subsequent desorption.[27]

Both a replacement of the water ligand nor an oxygen transfer reaction requires a redox activity of Ce, and the haloperoxidase reaction is likely to be dictated by the Lewis acidity of the CeO_{2-x} surfaces. Therefore, the three different CeO_{2-x} nanocrystals were compared with respect to their Lewis acidity, ζ-potential and S_{BET}. ^{31}P solid state NMR spectroscopy was used to study the Lewis acidity of the (amorphous oxygen) deficient CeO_{2-x} surface layer of the ceria nanoparticles with different morphologies.[54] The method is based on the dependence of the ^{31}P chemical shift on the binding strength of the phosphorous donor atom in trimethylphosphine (TMP) on the ceria surface. When a complex between TMP and a Brønsted acidic proton from a hydroxyl surface group is formed, ^{31}P nuclei resonate in a relatively narrow spectral range – from -3 to -5 ppm.[64] This hardly allows a direct correlation between the chemical shift and the different morphologies. However, chemisorbed TMP on the ceria surface acts as a Lewis base by donating the phosphorous lone pair to the cerium cations. Their Lewis acidity varies significantly depending on the morphology. The ^{31}P chemical shifts are detected in the range between -20 ppm and -60 ppm for the different morphologies of ceria nanocrystals, which facilitates their differentiation. Less acidic Ce cations bind only weakly to TMP.[64] At the same time, more acidic Ce cations form stronger bonds, which leads to a shortening of the P-Ce bond length. Consequently, the phosphorous nuclei are more deshielded and the ^{31}P resonance shifts downfield. Figure 3-2 presents the deconvoluted ^{31}P solid state NMR spectra of TMP bound to CeO_{2-x} nanocrystals with different morphologies. The corresponding ^{31}P-NMR spectra show different ^{31}P-NMR shifts indicating Ce sites with Lewis acidities in the order -31.6 ppm (rods, highest acidity) > -41.3 ppm (spheres, intermediate acidity) > -61.5 ppm (cubes, lowest acidity). ^{31}P-NMR spectra of CeO_{2-x} nanocubes show a sharp resonance with a full width of half maximum (fwhm) of 0.183 kHz (1.1 ppm) indicating only a single type of site with low Lewis acidity and uniform size distribution. This is

compatible with the results of powder X-ray diffraction and TEM, where the cube-like nanocrystals showed a high crystallinity.
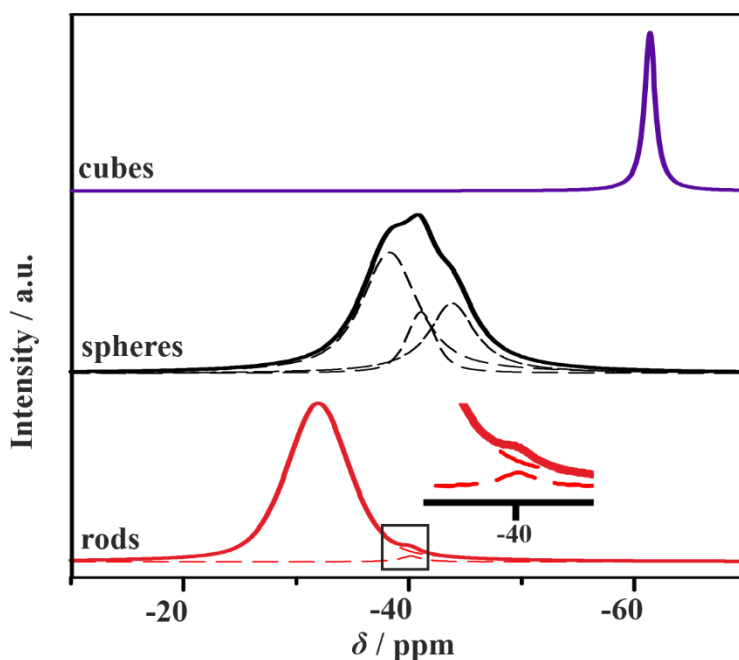
Figure 3-2. ^{31}P-NMR spectra for different CeO$_{2-x}$ morphologies after TMP addition.

The ^{31}P-NMR spectrum of spherical nanoparticles shows a complex signal, which splits after deconvolution into three different resonances at -44.2ppm (0.809 kHz, 5 ppm), -41.4 ppm (0.485 kHz, 3 ppm) and -38.6 ppm (0.971 kHz, 6 ppm) with an integral ratio of 4:1:2. This indicates the presence of three distinguishable sites within a narrow ppm range and Lewis acidities of comparable strength, compatible with a poorly ordered or disordered surface.[54] No well-ordered crystallite surface is formed because of the small crystallite size and the large surface/volume ratio (0.44 nm^{-1}). Thus, different sites with comparable Lewis acidity remain.

Two resonances are observed in the ^{31}P-NMR spectrum of the nanorods: a dominant signal at **-**31.9 ppm (1.054 kHz, 6.5 ppm) and a low intensity peak at **-**40.1 ppm (0.347 kHz, 2.1 ppm) with an integral ratio of 1:0.015. The low intensity signal is comparable with the signal observed for the nanospheres, indicating a disordered surface for the rods, which is consistent with the Raman, PXRD, HRTEM, and XPS data showing a high defect density for the nanorods.

Effect of ζ-potential and S_{BET}

ζ–potential (zeta potential) measurement is an analytical method to determine surface potential of nanoparticles in colloidal systems. The surface charge has an effect on (i) the stability of a colloidal system and (ii) the catalytic behavior due to electrostatic attraction or repulsion forces between a substrate and the catalyst surface. It is known that the addition of fluoride ions causes a negative ζ–potential at CeO_{2-x} surfaces, accelerating oxidase reaction by facilitating electron transfer from the catalyst surface to the substrate TMB.[65] Surface charge is likely to play a crucial role in ceria-catalyzed oxidative bromination reactions in solution, because a negatively charged halide anion must adsorb on the catalyst surface. Surface charge is a key feature of surface acidity because it is the sum of all acidic (as determined by ^{31}P-NMR) and basic surface groups. Therefore, the effect of ζ-potential and S_{BET} on the reaction rate were determined.

The ζ-potential was determined in acidic medium ($HClO_4$ addition, pH=1) to mimic the conditions of thymol bromination.[66] For nanospheres and nanorods ζ-potentials of +31 mV and +25.4 mV were measured, which are in a similar range. Ceria nanocubes showed with +11.8 mV a much lower ζ-potential. The S_{BET} surface area for CeO_{2-x} nanorods was determined by N_2 sorption as 98.4 m^2g^{-1}, the S_{BET} surface areas for nanospheres and -cubes were considerably smaller (44.6 m^2g^{-1} and 16.1 m^2g^{-1}). Since the catalytic activity is determined by both factors, (i) ζ-potential and (ii) surface area S_{BET} in an independent manner, the product of S_{BET} and ζ-potential represents the catalytic activity in a quantitative manner.[44] Table 3-1 shows an overview of ζ-potential, S_{BET} and the product of S_{BET} and ζ-potential for all three morphologies.

Table 3-1. ζ-potential, S_{BET} and the product of S_{BET} and ζ-potential for CeO_{2-x} nanorods, spheres and cubes.

morphology	S_{BET} / m^2g^{-1}	ζ-potential / mV	$S_{BET} \cdot \zeta$-potential / m^2g^{-1}
rods	98.4	25.4 ± 0.6	2500 ± 40
spheres	44.6	31.0 ± 1.0	1383 ± 45
cubes	16.1	11.8 ± 0.7	190 ± 11

Peroxido surface complex on ceria

The binding of H_2O_2 to ceria surfaces is likely the initial step of the oxidative halogenation reaction. H_2O_2 is known to bind to nanoceria surfaces, which catalyze its decomposition to water and oxygen (peroxidase reaction).[29] In a second step, bromide anions must adsorb onto the CeO_{2-x} nanocrystal surface to form hypohalite species. Reactive oxygen intermediates resulting from the reaction of H_2O_2 with ceria nano-powders and the oxidation of organic compounds by a CeO_{2-x}/H_2O_2 system have been studied based on the competitive binding of organic dyes and hydrogen peroxide to Ce surface sites and the subsequent degradation of the organics by pre-formed peroxo species.[67,68]

The binding of H_2O_2 to the facets of ceria nanocrystals give rise to Raman absorption bands (Figure 3-3).[67,69] 2 µL of H_2O_2 (35%) was added to the nanocrystals and spectra were recorded for 5 min each over a period of 20 min. After H_2O_2 addition, an orange powder was obtained. The Raman spectra show a new vibrational band at 840 cm^{-1}, which is in agreement with Raman bands for cerium hydroperoxo species at 842 cm^{-1} and 839 cm^{-1}.[67,70,71] In general, CeO_{2-x} nanocrystals are yellow. Binding of H_2O_2 causes a color change from light yellow to dark orange-brown, which is associated with a ligand to metal charge transfer (LMCT) and deepens with increasing H_2O_2 concentration.[72] Figure 3-3 shows an image of CeO_{2-x} nanopowders (nanorods, nanospheres, nanocubes) after adding H_2O_2 ($c = 11$ M). A significant difference between the peroxo band of different morphologies was observed. The CeO_{2-x} nanorods showed no spectral change at 840 cm^{-1} after 20 min. A clear signal was also detected after 24 h. Spherical particles showed a much weaker peroxide signal that decreased with time. Nanocubes had the weakest signal, which disappeared completely after 20 minutes. This suggests that the persistence of the peroxo complex correlates with the rate constant of thymol bromination. Our hypothesis is that the formation of the surface peroxo complex is essential for HOBr formation and its formation is a key factor for oxidative halogenation catalysis.
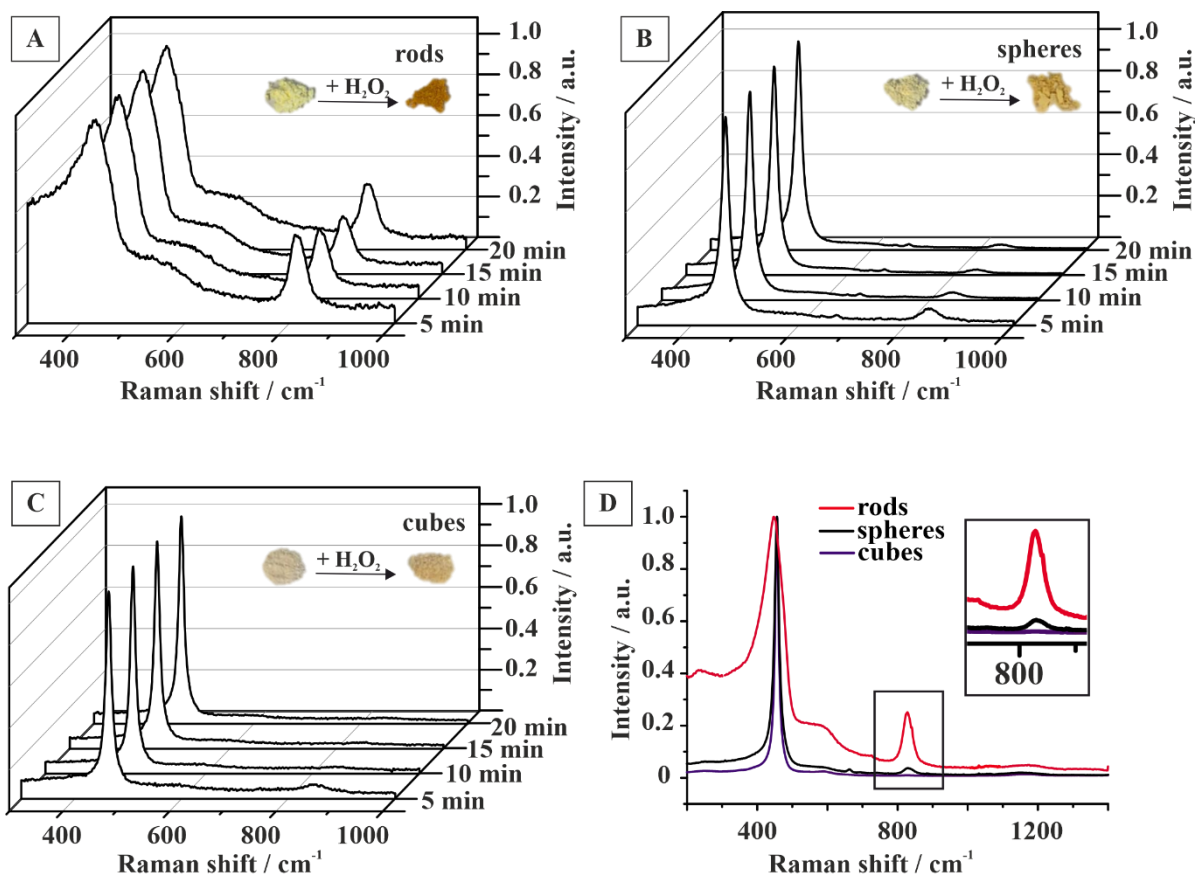
Figure 3-3. Raman spectra of CeO_{2-x} (A) nanorods, (B) nanospheres and (C) nanocubes after H_2O_2 (35%) addition recorded every 5 min over a period of 20 min with a corresponding image of the CeO_{2-x} nanocrystals before and after H_2O_2 addition. (D) Raman spectra 24 h after H_2O_2 addition. The inset shows a magnification of the spectrum in the range of 800-900 nm.

The spectrum of the nanorods shows another special feature with the signal at 595 cm^{-1}, which is assigned to Frenkel-type oxide vacancies.[73] This is further evidence that the nanorods have more defects than nanospheres or -cubes and thus the defects have an important impact on the catalytic rate. Line defects in the HRTEM images confirm this result (Figure S3-2). All Raman spectra show a threefold degenerate band at 464 cm^{-1} (F_{2g} band). This band is associated with the Ce-O stretching vibration.[74] The band of the nanospheres and -cubes is sharp indicating a higher crystallinity. The nanorods, however, show a broad band caused by disorder due to the presence of oxide defects (Figure S3-2).[75] The higher defect concentration of the CeO_{2-x} nanorods is consistent with the results of the XPS spectra (Figure S3-14). As expected from the ionic radii of Ce^{4+} and Ce^{3+}, Ce^{3+} predominantly occurs at the particle surface associated with oxide defects. The XPS survey spectra (Figure S3-13) of CeO_{2-x} nanorods, -spheres and -cubes show only the presence of the elements Ce and O.

The Michaelis-Menten kinetics of the "enzyme" reactions show the affinity of the substrate H_2O_2 to the CeO_{2-x} catalyst for nanocrystal morphologies[54] *via* the Michaelis constants (K_m)[76] in the order nanocubes (K_m=n.a.) < nanospheres (K_m=750 μM) < nanorods (K_m=330 μM). The affinity is reciprocal to the Michaelis-Menten constant K_m. Michaelis-Menten kinetics could not be calculated for the nanocubes because no reaction occurred (Figure S3-7, Equation S3-1). However, Ce promotes H_2O_2 reduction (peroxidase reaction) in reverse order because Ce with lower acidity (or higher electron density) can reduce H_2O_2 easier.

Bromination of thymol

CeO_{2-x} nanocrystals show a robust activity for oxidative halogenation reactions.[77] The catalytic activity of ceria nanoparticles of defined size and morphology (spheres, cubes, rods) was investigated *in-situ* by ^{1}H NMR spectroscopy using the oxidative halogenation of the phenolic monoterpene thymol as a model reaction.[17,78]

A reaction mixture consisting of thymol, KBr, $HClO_4$ and CeO_{2-x} nanocrystals with different morphologies (rods, cubes and spheres) in D_2O/CD_3OD (10% v/v) was prepared and examined *via* ^{1}H-NMR spectroscopy after H_2O_2 addition. An excess of bromide was added. The reaction yielded the monobrominated (4-bromothymol) and, depending on the nanocrystal morphology, also the dibrominated product (2,4-dibromothymol). The progress of the reactions was followed *in-situ* by ^{1}H-NMR spectroscopy after adding H_2O_2 for kinetic analysis. The reaction was monitored every minute for a period of 30 minutes (Figure S3-3, S3-4, S3-5) by following the evolution of the aromatic proton resonances in the spectral region between 6.8 and 7.3 ppm. Figure 3-4A shows stacked spectra of the reaction catalyzed by CeO_{2-x} nanorods. All signals were normalized to the signals of the isopropyl group (at ~1 ppm). The signal at 6.9 ppm corresponds to the aromatic proton of thymol (Figure 3-4A+D: red circle). After only one minute its intensity decreases to 50% which is accompanied by the appearance of a new resonance at 7.1 ppm. The latter corresponds to the proton of 4-bromothymol (Figure 3-4A+D: blue circle) which is formed as a result of the first bromination step. The signal at 7.2 ppm results from the proton of the dibrominated product (Figure 3-4A+D: cyan circle) 2,4-dibromothymol, which begins to form already 2 minutes after H_2O_2 addition. Bromination can be followed based on the change of integrals of aromatic protons highlighted in red, blue and cyan in Figure 3-4B. A fast exponential intensity decrease of the thymol (red) signal at 6.9 ppm was observed in the first 3 minutes. The transformation was complete within 8 minutes, whereas the

intensity of the signal at 7.1 ppm (blue) for the 4-bromothymol increases exponentially up to a maximum value. An additional signal, which is associated with 2,4-dibromothymol (cyan), appears after 2 minutes at 7.2 ppm. An equilibrium between the mono- and di-brominated thymol is reached after 8 min with a respective integral ratio of 1:1.34. The NMR signals could be assigned unambiguously based on the 2D-^{1}H-COSY NMR spectra (Figure S3-8, S3-9, S3-10), in which cross signals appear due to coupling between the aliphatic and aromatic protons. Experimental details are given in the Supporting Information.
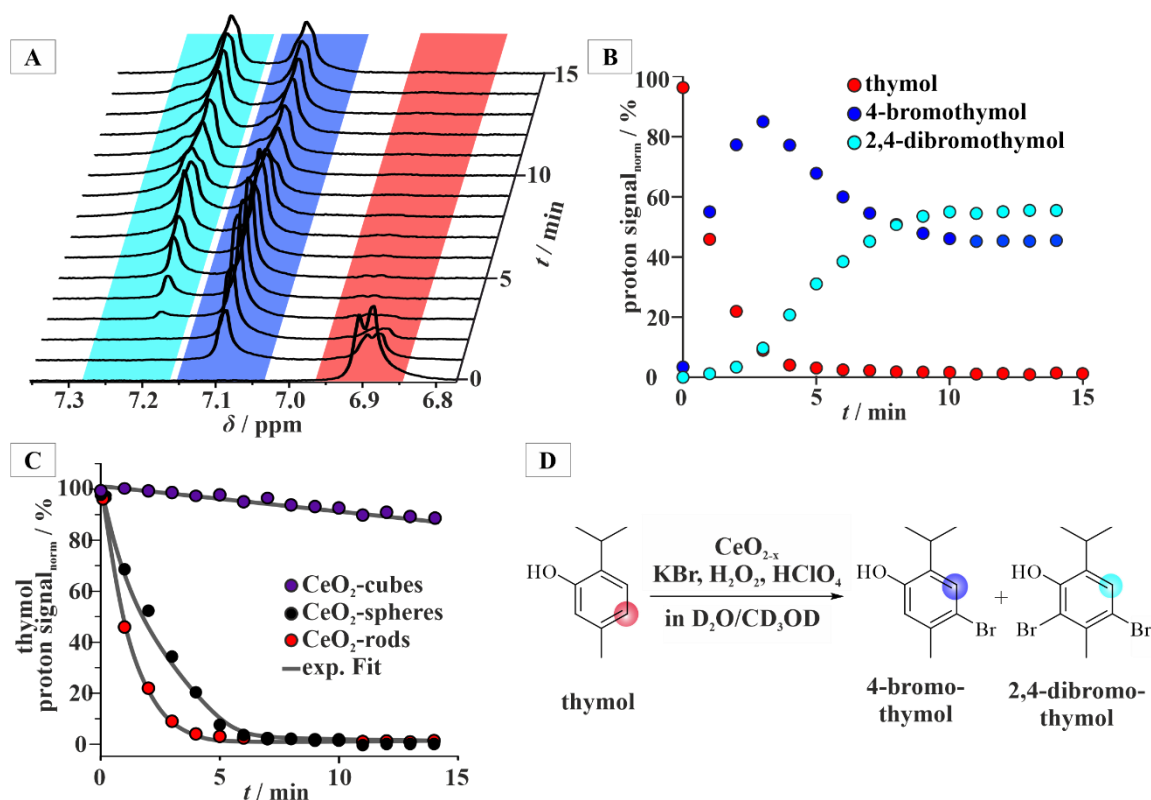
Figure 3-4. (A) Stacked ^{1}H-NMR spectra of oxidative thymol (cyan) bromination to 4-bromothymol (blue) and 2,4-dibromothymol (red) catalyzed by CeO$_{2-x}$ nanorods. (B) Normalized proton signal intensities of thymol (red), 4-bromothymol (blue) and 2,4-dibromothymol (cyan) during the reaction. (C) Decrease of the normalized thymol proton signal during oxidative bromination reaction using CeO$_{2-x}$ nanocubes (violet), nanospheres (black) and nanorods (red) as catalyst over a period of 15 min. (D) Oxidative bromination of thymol to 4-bromothymol and 2,4-dibromothymol.

CeO$_{2-x}$ nanospheres also catalyze the bromination reaction, however more slowly. The equilibrium between the mono- and dibrominated product is reached after ~15 minutes with a final integral ratio of 1:1 for both compounds. Thymol bromination catalyzed by CeO$_{2-x}$ nanocubes results in the formation of the monobrominated product only. Furthermore, 80% of the original thymol remains unreacted after 30 minutes. Figure 3-4C shows the intensity changes of the aromatic protons of thymol for different CeO$_{2-x}$ nanocatalyst morphologies.

The decrease of the proton signals is faster for the nanorods ($k_{rods}=772 \cdot 10^{-3} \pm 19 \cdot 10^{-3}$ min^{-1}) than for the nanospheres ($k_{spheres} = 396 \cdot 10^{-3} \pm 10 \cdot 10^{-3}$ min^{-1}). Almost no reaction ($k_{cubes}=9.6 \cdot 10^{-3} \pm 0.1 \cdot 10^{-3}$ min^{-1}) was observed for CeO$_{2-x}$ nanocubes. A first-order pseudokinetic model was used to compare the conversion rates of thymol (Equation 3-1), where "$a(t)$" indicates the thymol concentration at time t and a_0 was set to 1. Figures S3-3, S3-4, S3-5, and Figure S3-15 show the ^{1}H-NMR spectra for the reaction products in the absence and the presence of the CeO$_{2-x}$ nanocrystals.

$$a(t) = a_0 e^{-k_a \cdot t} \hspace{4cm} \text{(eq 3-1)}$$

To explain the different reaction rates of for the different CeO$_{2-x}$ nanocrystal morphologies, the Lewis acidity and the product of surface area and ζ-potential were compared. Figure 3-5 shows that reaction rate scales with (i) the Lewis acidity, as evaluated by the shift of the ^{31}P-NMR signal of TMP (Figure 3-5A) and (ii) the product $S_{BET} \times \zeta$-potential (Figure 3-5B) in the order nanorods > nanospheres > nanocubes. In essence, the Lewis acidity of the CeO$_{2-x}$ nanocrystals dictates the bromination rate of thymol: The higher the Lewis acidity, the faster the observed bromination rate. A key feature of oxidative halogenation reactions in aqueous environments is that chemical transformations are sensitive toward changes in solvation. High Lewis acidity will allow polar molecules or ion species (like H$_2$O$_2$ or halide anions) to replace solvent molecules at nanocrystal surfaces.
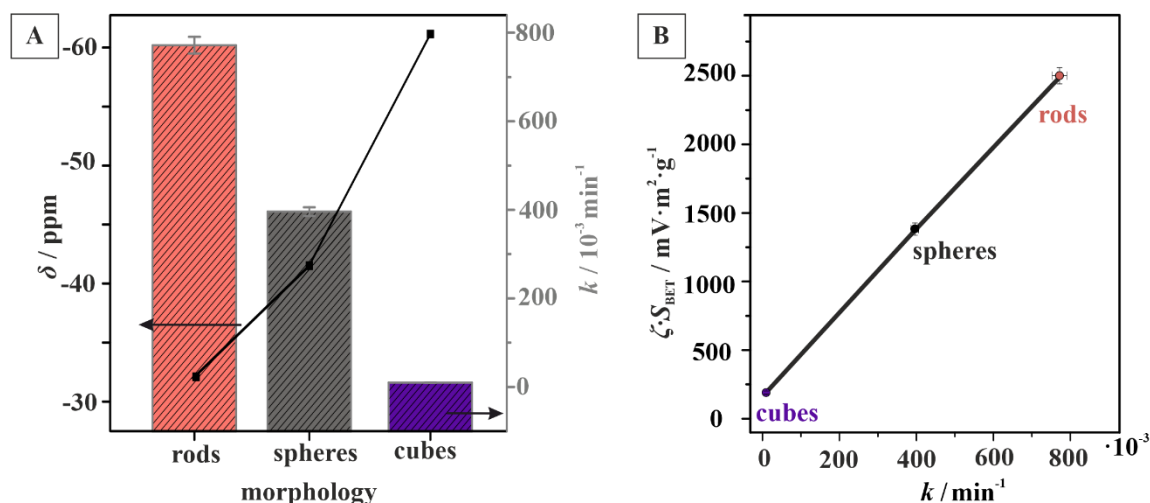
Figure 3-5. (A) Reaction rate (k) scales with the ^{31}P-NMR signal position for different CeO$_{2-x}$ nanocrystal morphologies. (B) Linear correlation of $S_{BET} \times \zeta$-potential and k for three different morphologies.

The experimental results allow to outline the reaction pathway of the halogenation reaction. Halogenation catalysis by nanoceria requires: (i) an active surface, (ii) rapid H$_2$O$_2$ binding (dictated by the surface acidity), (iii) sufficient stability of the Ce-O-O-H surface species with respect to the peroxidase reaction, and (iv) bromide adsorption to be sufficiently fast and strong to allow the transfer of an oxygen atom to bromide anion before a dioxygen molecule can be formed. The surface (i) Lewis acidity and (ii) $S_{BET} \cdot \zeta$-potential of the CeO$_{2-x}$ nanocrystals determine the rate of bromide adsorption.

In essence, the Lewis acidities of the CeO$_{2-x}$ nanocrystals dictate the bromination rate of thymol: *The higher the Lewis acidity, the faster the bromination rate* (Figure 3-5A). A key feature of oxidative halogenation reactions in aqueous environments is that chemical transformations are sensitive to changes in solvation. High Lewis acidity allows polar molecules or ion species (like H$_2$O$_2$ or halide anions) to replace solvent molecules at the nanocrystal surfaces.

3.4.   CONCLUSION

We have shown by a combination of electron microscopy, X-ray diffraction, ^{31}P and ^{1}H-NMR, XPS as well as Raman spectroscopy that the catalytic activity of CeO_{2-x} in oxidative halogenating depends on the combined effects of surface area S_{BET}, surface charge (ζ-potential) and surface acidity. To this end, the kinetics of the oxidative bromination of the model compound thymol, a monoterpene phenol, was studied by ^{1}H-NMR spectroscopy for CeO_{2-x} nanocrystals with well-defined cubic, rod like, and spherical morphologies.

The acid-base properties of CeO_{2-x} nanocrystals (i.e., the catalytic activities in haloperoxidase reactions) are related to its surface structure. The Lewis acidities of CeO_{2-x} nanocrystals, determined by TMP-^{31}P NMR, can be arranged in the order nanorods > nanospheres > nanocubes. Here, the Lewis acidity of CeO_{2-x} nanocrystals is a key factor for the catalytic bromination of thymol. The higher the Lewis acidity, the faster the observed bromination rate. Since the haloperoxidase reaction involves the transfer of an oxygen atom from a surface-bound H_2O_2 oxidant species to a bromide anion, surface charge (controlling bromide adsorption) and stability of the Ce-O-O-H species are essential. The multiplicative combination of these two independent factors, ζ-potential and S_{BET} surface area, provides a reliable measure to describe the rate of the haloperoxidase reaction in the order nanorods > nanospheres > nanocubes. The surface charge is reflected in the product $S_{BET} \times \zeta$-potential, which scales with the experimentally determined surface acidities for the different nanocrystal morphologies. This is consistent with the sequence of surface acidities, H_2O_2 affinity, and reported stability of Ce-O-O-H surface species scaling in the order nanorods > nanospheres > nanocubes. Since the haloperoxidase reaction requires a cleavage of surface-bound O-O units, the peroxidase activity of nanoceria is relevant for the oxidation of bromide *via* transfer of an oxygen atom. CeO_{2-x} has been reported to promote H_2O_2 reduction (peroxidase reaction) with a concomitant release of an oxygen atom in the order nanocubes > nanorods > nanospheres. Thus, the haloperoxidase reaction on CeO_{2-x} is determined by the interplay of cleavage a surface-bound Ce-O-O-H group (peroxidase reaction) and the adsorption of a halide species to which the oxygen resulting from the peroxidase reaction is transferred. Our studies provide new insight into the halogenation catalysis of ceria nanocrystals in aqueous environment and show parallels between heterogeneous surface catalysis and the enzyme-like activity of CeO_{2-x} nanocrystals. Our results show that the surface chemistry of catalysts, including the chemical state and the number of active sites, is key to elucidating catalytic reaction

mechanisms. Given the growing interest in the use of ceria as so-called "nanozymes" and the lack of mechanistic understanding, our results may provide guidance for expanding the scope of application for soluble ceria even beyond aqueous chemistry.

3.5. EXPERIMENTAL SECTION

MATERIAL AND SYNTHESIS

All commercial reagents and solvents were used as received, without further purification. Ceriumnitrate hexahydrate (99.5%) and thymol (98+%) were obtained from Alfa Aesar. Potassium bromide (99+%) and perchloric acid (ca.70% solution in water) were obtained from Acros Organics. Hydrogen peroxide (35%), citric acid (<99.5%, anhydrous) were purchased from Carl Roth. Methanol-d_4 (99.8%) and deuterium oxide (99.9%) were purchased from Deutero. Ammonium hydroxide (25%) was utilized from VWR, and sodium hydroxide from Fisher Scientific. Trimethylphosphine (97%) was obtained from Sigma Aldrich. Ultrapure water (18.2 MΩ cm-1) was used for all experiments.

CeO$_{2-x}$ Nanospheres.[59,60] 1.6 mL of an aqueous 1 M Ce(NO$_3$)$_3$·6H$_2$O solution and 3.2 mL of a 4 M aqueous solution of citric acid were put in a beaker and refilled with Milli-Q water to a total volume of 20 mL. After stirring the resulting sol for 10 min, conc. ammonia solution was added until a pH of 8.5-9 was reached. Then, the solution was stirred for another 10 min and placed in the oven at 100 °C overnight. The resulting gel was heated in an oven with a heat rate of 5 °C/min to 550 °C for 3 h. The product was mortared and analyzed after cooling.

CeO$_{2-x}$ Nanorods.[27] Ce(NO$_3$)$_3$·6H$_2$O (4.86 g, 11 mmol) was used as precursor for the synthesis of CeO$_{2-x}$ nanorods and filled in a Teflon-lined autoclave. 210 mL of a 4 M aqueous NaOH solution was dropped slowly in the Teflon inlay with the precursor while stirring. When the addition was finished, the solution was stirred for another 30 min and autoclaved at 80 °C for 16 h. When the suspension had cooled down, the product was centrifuged for 10 min at 9000 rpm and washed six times with water (until the washing water was neutral). The yellow product was freeze-dried in liquid nitrogen and vacuum dried.

CeO$_{2-x}$ Nanocubes.[58] Ce(NO$_3$)$_3$·6H$_2$O (0.868 g, 2 mmol) and NaNO$_3$ (0.85 g, 1 mmol) were dissolved in 10 mL Milli-Q water. 30 mL of an aqueous NaOH solution (50%) were added and stirred for 30 min. The solution was transferred into a Teflon inlay and heated in a microwave oven to 180 °C for 120 min (heating rate 10 °C/min). After cooling, the product was collected by centrifugation for 10 min at 9000 rpm, washed with water until the supernatant was neutral and dried in vacuum.

Bromination of Thymol. To investigate the oxidative bromination *via* ^{1}H-NMR spectroscopy a reaction medium consisting of nanoparticles (2.85 mg mL^{-1}), thymol

(66 mM), KBr (142 mM), HClO$_4$ (91 mM) and H$_2$O$_2$ (266 mM) in CD$_3$OD was prepared. Firstly, KBr and HOCl$_4$ were dissolved in a CD$_3$OD/D$_2$O (10% v/v) mixture, and the resulting precipitate of KClO$_4$ was separated. Thymol and the CeO$_{2-x}$ nanoparticles were added, followed by ultrasonication for 30 s. The first NMR spectrum was measured without H$_2$O$_2$. The catalysis was started by adding H$_2$O$_2$ to the tube. The first spectrum of the kinetic measurement was recorded after 1 min. The following spectra were recorded every minute. ^{1}H-NMR (400 MHz, CD$_3$OD): 4-bromo-2-isopropyl-5-methylphenol (4-Bromthymol): δ[ppm]= 6.90 (m, J=7.7 Hz, Ar-H), 6.55-6.42 (m, Ar-H), 3.13 (m, J=7.0 Hz, Ar-CH-), 2.13 (s, Ar-CH_3), 1.10 (d, J=6.9 Hz, -CH(CH_3)$_2$). 4,6-Dibromo-2-isopropyl-5-methylphenol. δ [ppm]=7.26 (s, Ar-H), 3.14 (m, Ar-CH-), 2.47 (s, Ar-CH$_3$), 1.16 (d, J=6.9 Hz,-CH(CH_3)$_2$).

Michaelis-Menten Kinetics. The Michaelis-Menten kinetics was determined with various H$_2$O$_2$ concentrations. The kinetic analysis was performed at λ = 592 nm, the absorbance maximum of tetra bromophenol blue. For each measurement, the same stock solution of phenol red (PR) (50 µM) mixed with KBr (25 mM) was used. After adding 62.5 µL of nanoparticle suspension (1 mg/mL), the reaction was left stirring (800 rpm) for 2 min for temperature equilibration (25 °C). Prior to H$_2$O$_2$ addition the absorbance was set to zero. The kinetics were measured for 10 minutes. All data points were linearly fitted in the period of 1-10 minutes.

CHARACTERIZATION

Transmission Electron Microscopy. Samples for transmission electron microscopy (TEM) were prepared by placing a drop of dilute NP dispersion (1 mg·mL^{-1}) in Milli-Q water on a carbon-coated copper grid. TEM images were obtained with a FEI Tecnai 12 TWIN LaB$_6$ at 120 kV together with a Gatan US1000 CCD-camera (16-bit, 2048 x 2048 pixels) using the Gatan Digital Micrograph software.

Nuclear Magnetic Resonance. All solution ^{1}H nuclear magnetic resonance (NMR) spectra were recorded at 295 K on a Bruker Avance DRX 400 MHz spectrometer (Bruker Biospin GmbH, Rheinstetten, Germany) operated at a proton frequency of 400.31 MHz. A commercial Bruker 2 channel 5 mm inverse probe head was used. 8 scans were averaged with a recycle delay of 28 s for the quantitative measurements.

Prior to all solid state NMR measurements, 200 mg CeO$_{2-x}$ nanoparticles were heated in a ground glass vessel at 120 °C under vacuum for 2 h. The vials were transferred into a glove box and 15µL of trimethylphosphine (TMP) was added. TMP adsorption onto the particle

surface was allowed for 20 minutes to reach equilibrium. The sample was transferred into a solid state NMR rotor. Solid state ^{31}P-NMR spectra were recorded on a Bruker Avance DSX 400 MHz spectrometer operating at a ^{1}H and ^{31}P frequencies of 399.87 and 161.87 MHz respectively. A commercial 3 channel Bruker 4 mm probe head was used at a magic angle spinning (MAS) of 10 kHz. Quantitative ^{31}P experiments were conducted using a 30° flip angle pulse and averaging 64 scans with a recycle delay of 15 s with inverse-gated proton decoupling. A two-pulse phase modulation decoupling scheme was used for the experiments. No correction for the frictional heating was conducted. The spectra were referenced to $NH_4H_2PO_4$ at 0.9 ppm as an external standard.

Powder X-ray Diffraction. X-ray diffraction patterns were recorded on a STOE Stadi P diffractometer equipped with a Dectris Mythen 1k detector in transmission mode using Mo Kα1 radiation. Crystalline phases were identified according to the PDF–2 database using Bruker AXS EVA 10.0 software.

Zeta Potentials. ζ-potentials were measured on a Malvern Zetasizer Nano using disposable capillary cells (DTS1070) and single-use polystyrene cuvettes. Data analysis was performed with the Malvern Zetasizer Software 8.01.4906.

BET Surface Area. BET measurements were conducted with 3P Micro 300 gas adsorption instrument using nitrogen as the analysis gas at 77.4 K. The software 3P Surface Area & Pore Size Analyzer System 10.03.02 was used to analyze the recorded data.

X-ray photoelectron spectroscopy. X-ray photoelectron spectroscopy (XPS) measurements were carried out on an Axis Ultra DLD imaging photoelectron spectrometer. Measurements were carried out using the hybrid mode with 10 mA and 15 kV at the Al anode. The analysis area was 700 μm × 300 μm (i.e., X-ray spot size). Survey spectra were measured at a pass energy of 80 eV and elemental spectra at 20 eV pass energy of the analyzer. All spectra were charge corrected to a binding energy of 284.8 eV for the C 1s line corresponding to adventitious aliphatic carbon. Measurements were analyzed using the CasaXPS software plotted with Origin 8.1.

Raman spectroscopy. The Raman spectra were recorded with a Bruker Senterra Microscope operated by the *OPUS* software.

UV/Vis spectroscopy. UV-vis spectra were recorded on an Agilent Cary 3500 spectrophotometer.

3.6.   REFERENCES

1   Sasson, Y. Formation of Carbon–Halogen Bonds (Cl, Br, I). In *Supplement D2; The Chemistry of Halides, Pseudo-Halides and Azides*; John Wiley & Sons, Ltd: Chichester, UK; pp 535–628.

2   Wilcken, R.; Zimmermann, M. O.; Lange, A.; Joerger, A. C.; Boeckler, F. M. Principles and Applications of Halogen Bonding in Medicinal Chemistry and Chemical Biology. *J. Med. Chem.* **2013**, *56* (4), 1363–1388.

3   Jeschke, P. Latest Generation of Halogen-Containing Pesticides. *Pest Manag. Sci.* **2017**, *73* (6), 1053–1066.

4   Gribble, G. Biological Activity of Recently Discovered Halogenated Marine Natural Products. *Mar. Drugs* **2015**, *13* (7), 4044–4136.

5   Tasker, S. Z.; Standley, E. A.; Jamison, T. F. Recent Advances in Homogeneous Nickel Catalysis. *Nature* **2014**, *509* (7500), 299–309.

6   Gkotsi, D. S.; Ludewig, H.; Sharma, S. V.; Connolly, J. A.; Dhaliwal, J.; Wang, Y.; Unsworth, W. P.; Taylor, R. J. K.; McLachlan, M. M. W.; Shanahan, S.; Naismith, J. H.; Goss, R. J. M. A Marine Viral Halogenase That Iodinates Diverse Substrates. *Nat. Chem.* **2019**, *11* (12), 1091–1097.

7   Timmins, A.; de Visser, S. P. Enzymatic Halogenases and Haloperoxidases; Adv. Protein Struct. Biol. 2015, 100, pp 113–151

8   Weichold, V.; Milbredt, D.; van Pée, K.-H. Specific Enzymatic Halogenation-From the Discovery of Halogenated Enzymes to Their Applications In Vitro and In Vivo. *Angew. Chem. Int. Ed.* **2016**, *55* (22), 6374–6389.

9   Hollmann, F.; Opperman, D. J.; Paul, C. E. Biocatalytic Reduction Reactions from a Chemist's Perspective. *Angew. Chem. Int. Ed.* **2021**, *60* (11), 5644–5665.

10   Conte, V.; Floris, B. Vanadium and Molybdenum Peroxides: Synthesis and Catalytic Activity in Oxidation Reactions. *Dalton Trans.* **2011**, *40* (7), 1419–1436.

11   Madaan, N.; Shiju, N. R.; Rothenberg, G. Predicting the Performance of Oxidation Catalysts Using Descriptor Models. *Catal. Sci. Technol.* **2016**, *6* (1), 125–133.

12   Natalio, F.; André, R.; Hartog, A. F.; Stoll, B.; Jochum, K. P.; Wever, R.; Tremel, W. Vanadium Pentoxide Nanoparticles Mimic Vanadium Haloperoxidases and Thwart Biofilm Formation. *Nat. Nanotechnol.* **2012**, *7* (8), 530–535.

13   Sels, B.; De Vos, D.; Buntinx, M.; Plerard, F.; Kirsch-De Mesmaeker, A.; Jacobs, P. Layered Double Hydroxides Exchanged with Tungstate as Biomimetic Catalysts for Mild Oxidative Bromination. *Nature* **1999**, *400* (6747), 855–857.

14   Wei, H.; Wang, E. Nanomaterials with Enzyme-like Characteristics (Nanozymes): Next-Generation Artificial Enzymes. *Chem. Soc. Rev.* **2013**, *42* (14), 6060–6093.

15   Korschelt, K.; Tahir, M. N.; Tremel, W. A Step into the Future: Applications of Nanoparticle Enzyme Mimics. *Chem. – A Eur. J.* **2018**, *24* (39), 9703–9713.

16   Sabuzi, F.; Churakova, E.; Galloni, P.; Wever, R.; Hollmann, F.; Floris, B.; Conte, V. Thymol Bromination - A Comparison between Enzymatic and Chemical Catalysis. *Eur. J. Inorg. Chem.* **2015**, *2015* (21), 3519–3525.

17   Höfler, G. T.; But, A.; Hollmann, F. Haloperoxidases as Catalysts in Organic Synthesis. *Org. Biomol. Chem.* **2019**, *17* (42), 9267–9274.

18   de Boer, E.; Wever, R. The Reaction Mechanism of the Novel Vanadium-Bromoperoxidase. A Steady-State Kinetic Analysis. *J. Biol. Chem.* **1988**, *263* (25), 12326–12332.

19   Everett, R. R.; Soedjak, H. S.; Butler, A. Mechanism of Dioxygen Formation Catalyzed by Vanadium Bromoperoxidase. Steady State Kinetic Analysis and Comparison to the Mechanism of Bromination. *J. Biol. Chem.* **1990**, *265* (26), 15671–15679.

20   Liu, W.; Huang, X.; Cheng, M. J.; Nielsen, R. J.; Goddard, W. A.; Groves, J. T. Oxidative Aliphatic C-H Fluorination with Fluoride Ion Catalyzed by a Manganese Porphyrin. *Science* **2012**, *337* (6100), 1322–1325.

21   Vardhaman, A. K.; Barman, P.; Kumar, S.; Sastri, C. V.; Kumar, D.; de Visser, S. P. Mechanistic Insight into Halide Oxidation by Non-Heme Iron Complexes. Haloperoxidase versus Halogenase Activity. *Chem. Commun.* **2013**, *49* (93), 10926–10928.

22   Galloni, P.; Mancini, M.; Floris, B.; Conte, V. A Sustainable Two-Phase Procedure for V-Catalyzed Toluene Oxidative Bromination with H2O2 –KBr. *Dalton Trans.* **2013**, *42* (33), 11963–11970.

23   Würthner, F.; Stolte, M. Naphthalene and Perylene Diimides for Organic Transistors. *Chem. Commun.* **2011**, *47* (18), 5109–5115.

24   André, R.; Natálio, F.; Humanes, M.; Leppin, J.; Heinze, K.; Wever, R.; Schröder, H. C.; Müller, W. E. G.; Tremel, W. V2O5 Nanowires with an Intrinsic Peroxidase-Like Activity. *Adv. Funct. Mater.* **2011**, *21* (3), 501–509.

25   Wu, C.; Zhang, X.; Dai, J.; Yang, J.; Wu, Z.; Wei, S.; Xie, Y. Direct Hydrothermal Synthesis of Monoclinic VO 2 (M) Single-Domain Nanorods on Large Scale Displaying Magnetocaloric Effect. *J. Mater. Chem.* **2011**, *21* (12), 4509–4517.

26   Greenwood, N. N.; Earnshaw, A.; Press, P. N. N. Greenwood, A. Earnshaw: Chemistry of the Elements. Pergamon Press Oxford 1984, 1542 Seiten, 7 Anhänge Preis: US $ 34.95. ISBN 0–08–022057–6. *Cryst. Res. Technol.* **1985**, *20* (5), 662–662.

27   Herget, K.; Hubach, P.; Pusch, S.; Deglmann, P.; Götz, H.; Gorelik, T. E.; Gural, ya A.; Pfitzner, F.; Link, T.; Schenk, S.; Panthöfer, M.; Ksenofontov, V.; Kolb, U.; Opatz, T.; André, R.; Tremel, W. Haloperoxidase Mimicry by CeO2−x Nanorods Combats Biofouling. *Adv. Mater.* **2017**, *29* (4), 1603823.

28 Fuku, K.; Sayama, K. Efficient Oxidative Hydrogen Peroxide Production and Accumulation in Photoelectrochemical Water Splitting Using a Tungsten Trioxide/Bismuth Vanadate Photoanode. *Chem. Commun.* **2016**, *52* (31), 5406–5409.

29 Karakoti, A.; Singh, S.; Dowding, J. M.; Seal, S.; Self, W. T. Redox -Active Radical Scavenging Nanomaterials. *Chem. Soc. Rev.* **2010**, *39* (11), 4422–4432.

30 Korsvik, C.; Patil, S.; Seal, S.; Self, W. T. Superoxide Dismutase Mimetic Properties Exhibited by Vacancy Engineered Ceria Nanoparticles. *Chem. Commun.* **2007**, *0* (10), 1056–1058.

31 Pirmohamed, T.; Dowding, J. M.; Singh, S.; Wasserman, B.; Heckert, E.; Karakoti, A. S.; King, J. E. S.; Seal, S.; Self, W. T. Nanoceria Exhibit Redox State-Dependent Catalase Mimetic Activity. *Chem. Commun.* **2010**, *46* (16), 2736.

32 Kim, C. K.; Kim, T.; Choi, I. Y.; Soh, M.; Kim, D.; Kim, Y. J.; Jang, H.; Yang, H. S.; Kim, J. Y.; Park, H. K.; Park, S. P.; Park, S.; Yu, T.; Yoon, B. W.; Lee, S. H.; Hyeon, T. Ceria Nanoparticles That Can Protect against Ischemic Stroke. *Angew. Chem. Int. Ed.* **2012**, *51* (44), 11039–11043.

33 Herget, K.; Frerichs, H.; Pfitzner, F.; Tahir, M. N.; Tremel, W. Functional Enzyme Mimics for Oxidative Halogenation Reactions That Combat Biofilm Formation. *Adv. Mater.* **2018**, *30* (36), 1707073.

34 Plakhova, T. V.; Romanchuk, A. Y.; Yakunin, S. N.; Dumas, T.; Demir, S.; Wang, S.; Minasian, S. G.; Shuh, D. K.; Tyliszczak, T.; Shiryaev, A. A.; Egorov, A. V.; Ivanov, V. K.; Kalmykov, S. N. Solubility of Nanocrystalline Cerium Dioxide: Experimental Data and Thermodynamic Modeling. *J. Phys. Chem. C* **2016**, *120* (39), 22615–22626.

35 Dahle, J. T.; Livi, K.; Arai, Y. Effects of PH and Phosphate on CeO2 Nanoparticle Dissolution. *Chemosphere* **2015**, *119*, 1365–1371.

36 Collin, B.; Auffan, M.; Johnson, A. C.; Kaur, I.; Keller, A. A.; Lazareva, A.; Lead, J. R.; Ma, X.; Merrifield, R. C.; Svendsen, C.; White, J. C.; Unrine, J. M. Environmental Release, Fate and Ecotoxicological Effects of Manufactured Ceria Nanomaterials. *Environ. Sci. Nano* **2014**, *1* (6), 533–548.

37 Dahle, J. T.; Arai, Y. Environmental Geochemistry of Cerium: Applications and Toxicology of Cerium Oxide Nanoparticles. *Int. J. Environ. Res. Public Heal.* **2015**, *12* (2), 1253–1278.

38 Montini, T.; Melchionna, M.; Monai, M.; Fornasiero, P. Fundamentals and Catalytic Applications of CeO2-Based Materials. *Chem. Rev.* **2016**, *116* (10), 5987–6041.

39 Li, C.; Sun, Y.; Djerdj, I.; Voepel, P.; Sack, C. C.; Weller, T.; Ellinghaus, R.; Sann, J.; Guo, Y.; Smarsly, B. M.; Over, H. Shape-Controlled CeO2 Nanoparticles: Stability and Activity in the Catalyzed HCl Oxidation Reaction. *ACS Catal.* **2017**, *7* (10), 6453–6463.

40   Korschelt, K.; Schwidetzky, R.; Pfitzner, F.; Strugatchi, J.; Schilling, C.; Von Der Au, M.; Kirchhoff, K.; Panthöfer, M.; Lieberwirth, I.; Tahir, M. N.; Hess, C.; Meermann, B.; Tremel, W. CeO2−x Nanorods with Intrinsic Urease-like Activity. *Nanoscale* **2018**, *10* (27), 13074–13082.

41   Campbell, C. T.; Peden, C. H. F. Oxygen Vacancies and Catalysis on Ceria Surfaces. *Science* **2005**, *309* (5735), 713–714.

42   Esch, F.; Fabris, S.; Zhou, L.; Montini, T.; Africh, C.; Fornasiero, P.; Comelli, G.; Rosei, R. Chemistry: Electron Localization Determines Defect Formation on Ceria Substrates. *Science* **2005**, *309* (5735), 752–755.

43   Shannon, R. D. Revised Effective Ionic Radii and Systematic Studies of Interatomic Distances in Halides and Chalcogenides. *Acta Crystallogr. Sect. A* **1976**, *32* (5), 751–767.

44   Frerichs, H.; Pütz, E.; Pfitzner, F.; Reich, T.; Gazanis, A.; Panthöfer, M.; Hartmann, J.; Jegel, O.; Heermann, R.; Tremel, W. Nanocomposite Antimicrobials Prevent Bacterial Growth through the Enzyme-like Activity of Bi-Doped Cerium Dioxide (Ce1−xBixO2−δ). *Nanoscale* **2020**, *12* (41), 21344–21358.

45   Qiao, Z. A.; Wu, Z.; Dai, S. Shape-Controlled Ceria-Based Nanostructures for Catalysis Applications. *ChemSusChem* **2013**, *6* (10), 1821–1833.

46   Mann, A. K. P.; Wu, Z.; Calaza, F. C.; Overbury, S. H. Adsorption and Reaction of Acetaldehyde on Shape-Controlled CeO2 Nanocrystals: Elucidation of Structure-Function Relationships. *ACS Catal.* **2014**, *4* (8), 2437–2448.

47   Hu, Z.; Liu, X.; Meng, D.; Guo, Y.; Guo, Y.; Lu, G. Effect of Ceria Crystal Plane on the Physicochemical and Catalytic Properties of Pd/Ceria for CO and Propane Oxidation. *ACS Catal.* **2016**, *6* (4), 2265–2279.

48   Guild, C. J.; Vovchok, D.; Kriz, D. A.; Bruix, A.; Hammer, B.; Llorca, J.; Xu, W.; El-Sawy, A.; Biswas, S.; Rodriguez, J. A.; Senanayake, S. D.; Suib, S. L. Water-Gas-Shift over Metal-Free Nanocrystalline Ceria: An Experimental and Theoretical Study. *ChemCatChem* **2017**, *9* (8), 1373–1377.

49   Paunović, V.; Zichittella, G.; Mitchell, S.; Hauert, R.; Pérez-Ramírez, J. Selective Methane Oxybromination over Nanostructured Ceria Catalysts. *ACS Catal.* **2018**, *8* (1), 291–303.

50   Lowry, G. V.; Hill, R. J.; Harper, S.; Rawle, A. F.; Hendren, C. O.; Klaessig, F.; Nobbmann, U.; Sayre, P.; Rumble, J. Guidance to Improve the Scientific Value of Zeta-Potential Measurements in NanoEHS. *Environ. Sci. Nano* **2016**, *3* (5), 953–965.

51   She, Z. W.; Kibsgaard, J.; Dickens, C. F.; Chorkendorff, I.; Nørskov, J. K.; Jaramillo, T. F. Combining Theory and Experiment in Electrocatalysis: Insights into Materials Design. *Science.* **2017**, *355* (6321).

52   Mullins, D. R. The Surface Chemistry of Cerium Oxide. *Surf. Sci. Rep.* **2015**, *70* (1), 42–85.

53   Wang, Y.; Wang, F.; Song, Q.; Xin, Q.; Xu, S.; Xu, J. Heterogeneous Ceria Catalyst with Water-Tolerant Lewis Acidic Sites for One-Pot Synthesis of 1,3-Diols via Prins Condensation and Hydrolysis Reactions. *J. Am. Chem. Soc.* **2013**, *135* (4), 1506–1515.

54   Tan, Z.; Li, G.; Chou, H. L.; Li, Y.; Yi, X.; Mahadi, A. H.; Zheng, A.; Edman Tsang, S. C.; Peng, Y. K. Differentiating Surface Ce Species among CeO2 Facets by Solid-State NMR for Catalytic Correlation. *ACS Catal.* **2020**, *10* (7), 4003–4011.

55   Rothwell, W. P.; Shen, W. X.; Lunsford, J. H. Solid-State Phosphorus-31 NMR of a Chemisorbed Phosphonium Ion in HY Zeolite: Observation of Proton-Phosphorus-31 Coupling in the Solid-State. *J. Am. Chem. Soc.* **1984**, *106* (8), 2452–2453.

56   Ji, Z.; Wang, X.; Zhang, H.; Lin, S.; Meng, H.; Sun, B.; George, S.; Xia, T.; Nel, A. E.; Zink, J. I. Designed Synthesis of CeO2 Nanorods and Nanowires for Studying Toxicological Effects of High Aspect Ratio Nanomaterials. *ACS Nano* **2012**, *6* (6), 5366–5380.

57   Tyrsted, C.; Ornsbjerg Jensen, K. M.; Bøjesen, E. D.; Lock, N.; Christensen, M.; Billinge, S. J. L.; Brummerstedt Iversen, B. Understanding the Formation and Evolution of Ceria Nanoparticles Under Hydrothermal Conditions. *Angew. Chem. Int. Ed.* **2012**, *51* (36), 9030–9033.

58   Fisher, T. J.; Wang, M.; Ibrahim, Y.; Steffensmeier, B.; Cheung, C. L. Effect of Sodium Nitrate on Microwave-Assisted Synthesis of Ceria Nanocubes. *Mater. Lett.* **2016**, *178*, 71–74.

59   Periyat, P.; Laffir, F.; Tofail, S. A. M.; Magner, E. A Facile Aqueous Sol–Gel Method for High Surface Area Nanocrystalline CeO2. *RSC Adv.* **2011**, *1* (9), 1794–1798.

60   Kaspar, J.; Fornasiero, P.; Balducci, G.; Di Monte, R.; Hickey, N.; Sergo, V. Effect of ZrO2 Content on Textural and Structural Properties of CeO2–ZrO2 Solid Solutions Made by Citrate Complexation Route. *Inorg. Chim. Acta* **2003**, *349*, 217–226.

61   Wu, Z.; Li, M.; Howe, J.; Meyer, H. M.; Overbury, S. H. Probing Defect Sites on CeO2 Nanocrystals with Well-Defined Surface Planes by Raman Spectroscopy and O2 Adsorption. *Langmuir* **2010**, *26* (21), 16595–16606.

62   Florea, I.; Feral-Martin, C.; Majimel, J.; Ihiawakrim, D.; Hirlimann, C.; Ersen, O. Three-Dimensional Tomographic Analyses of Ceo2 Nanoparticles. *Cryst. Growth Des.* **2013**, *13* (3), 1110–1121.

63   Yang, C.; Yu, X.; Heißler, S.; Nefedov, A.; Colussi, S.; Llorca, J.; Trovarelli, A.; Wang, Y.; Wöll, C. Surface Faceting and Reconstruction of Ceria Nanoparticles. *Angew. Chem. Int. Ed.* **2017**, *56* (1), 375–379.

64   Chu, Y.; Yu, Z.; Zheng, A.; Fang, H.; Zhang, H.; Huang, S. J.; Liu, S. Bin; Deng, F. Acidic Strengths of Brønsted and Lewis Acid Sites in Solid Acids Scaled by 31P NMR Chemical Shifts of Adsorbed Trimethylphosphine. *J. Phys. Chem. C* **2011**, *115* (15), 7660–7667.

65   Liu, B.; Huang, Z.; Liu, J. Boosting the Oxidase Mimicking Activity of Nanoceria by Fluoride Capping: Rivaling Protein Enzymes and Ultrasensitive F − Detection. *Nanoscale* **2016**, *8* (28), 13562–13567.

66   Li, H.; Vrinat, M.; Berhault, G.; Li, D.; Nie, H.; Afanasiev, P. Hydrothermal Synthesis and Acidity Characterization of TiO2 Polymorphs. *Mater. Res. Bull.* **2013**, *48* (9), 3374–3382.

67   Scholes, F. H.; Hughes, A. E.; Hardin, S. G.; Lynch, P.; Miller, P. R. Influence of Hydrogen Peroxide in the Preparation of Nanocrystalline Ceria. *Chem. Mater.* **2007**, *19* (9), 2321–2328.

68   Ji, P.; Wang, L.; Chen, F.; Zhang, J.; Ji,] P; Wang, L.; Chen, F.; Zhang, J. Ce3+-Centric Organic Pollutant Elimination by CeO2 in the Presence of H2O2. *ChemCatChem* **2010**, *2* (12), 1552–1554.

69   Wang, Y. J.; Dong, H.; Lyu, G. M.; Zhang, H. Y.; Ke, J.; Kang, L. Q.; Teng, J. L.; Sun, L. D.; Si, R.; Zhang, J.; Liu, Y. J.; Zhang, Y. W.; Huang, Y. H.; Yan, C. H. Engineering the Defect State and Reducibility of Ceria Based Nanoparticles for Improved Anti-Oxidation Performance. *Nanoscale* **2015**, *7* (33), 13981–13990.

70   Zhao, H.; Dong, Y.; Jiang, P.; Wang, G.; Zhang, J. Highly Dispersed CeO2 on TiO2 Nanotube: A Synergistic Nanocomposite with Superior Peroxidase-like Activity. *ACS Appl. Mater. Interfaces* **2015**, *7* (12), 6451–6461.

71   Pushkarev, V. V.; Kovalchuk, V. I.; D'Itri, J. L. Probing Defect Sites on the CeO2 Surface with Dioxygen. *J. Phys. Chem. B* **2004**, *108* (17), 5341–5348.

72   Kuchibhatla, S. V. N. T.; Karakoti, A. S.; Baer, D. R.; Samudrala, S.; Engelhard, M. H.; Amonette, J. E.; Thevuthasan, S.; Seal, S. Influence of Aging and Environment on Nanoparticle Chemistry: Implication to Confinement Effects in Nanoceria. *J. Phys. Chem. C* **2012**, *116* (26), 14108–14114.

73   Zhang, Z.; Wang, Y.; Wang, M.; Lü, J.; Li, L.; Zhang, Z.; Li, M.; Jiang, J.; Wang, F. An Investigation of the Effects of CeO2 Crystal Planes on the Aerobic Oxidative Synthesis of Imines from Alcohols and Amines. *Chinese J. Catal.* **2015**, *36* (9), 1623–1630.

74   Sartoretti, E.; Novara, C.; Giorgis, F.; Piumetti, M.; Bensaid, S.; Russo, N.; Fino, D. In Situ Raman Analyses of the Soot Oxidation Reaction over Nanostructured Ceria-Based Catalysts. *Sci. Reports* **2019**, *9* (1), 1–14.

75   Patil, S.; Seal, S.; Guo, Y.; Schulte, A.; Norwood, J. Role of Trivalent La and Nd Dopants in Lattice Distortion and Oxygen Vacancy Generation in Cerium Oxide Nanoparticles. *Appl. Phys. Lett.* **2006**, *88* (24), 243110.

76   Kluenker, M.; Nawaz Tahir, M.; Ragg, R.; Korschelt, K.; Simon, P.; Gorelik, T. E.; Barton, B.; Shylin, S. I.; Panthöfer, M.; Herzberger, J.; Frey, H.; Ksenofontov, V.; Möller, A.; Kolb, U.; Grin, J.; Tremel, W. Pd@Fe2O3 Superparticles with Enhanced Peroxidase Activity by Solution Phase Epitaxial Growth. *Chem. Mater.* **2017**, *29* (3), 1134–1146.

77   Huang, Y.; Ren, J.; Qu, X. Nanozymes: Classification, Catalytic Mechanisms, Activity Regulation, and Applications. *Chem. Rev.* **2019**, *119* (6), 4357–4412.

78   Wischang, D.; Brücher, O.; Hartung, J. Bromoperoxidases and Functional Enzyme Mimics as Catalysts for Oxidative Bromination—A Sustainable Synthetic Approach. *Coord. Chem. Rev.* **2011**, *255* (19–20), 2204–2217.

3.7.   SUPPORTING INFORMATION
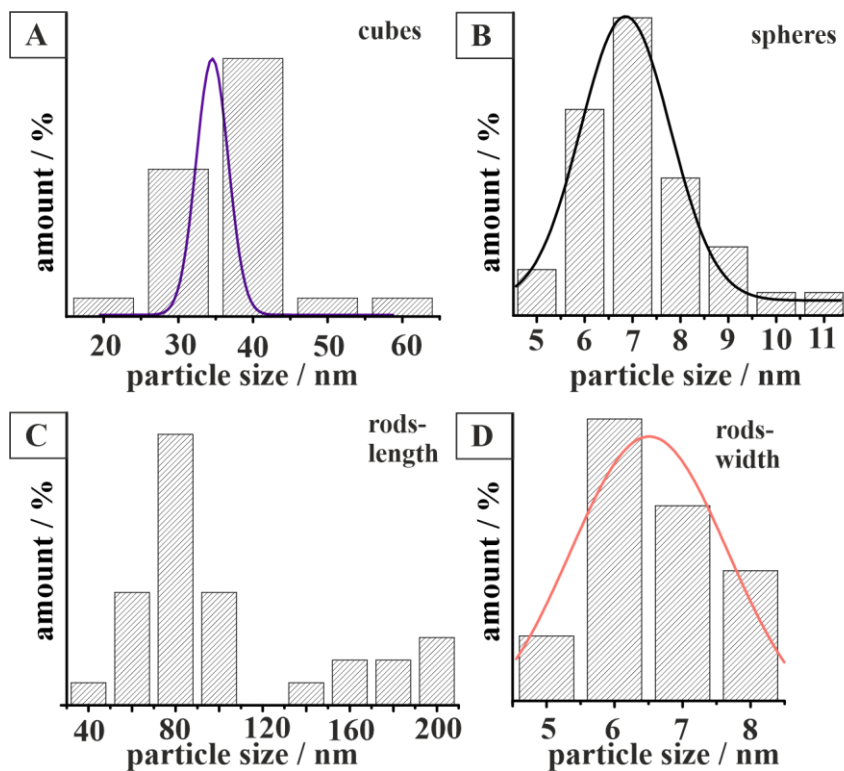
Figure S3-1. Histograms showing the particle size distribution of CeO$_{2-x}$ (A) nanocubes, (B) nanospheres and (C, D) nanorods.
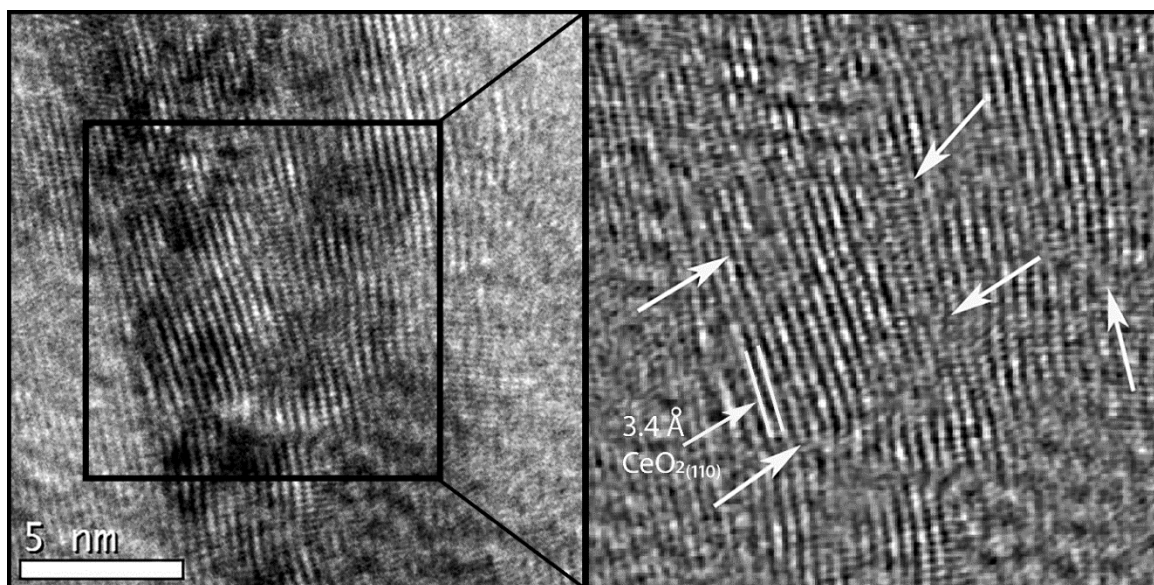
Figure S3-2. HRTEM images of CeO$_{2-x}$ nanorods. The zoomed image shows the presence of line defects.
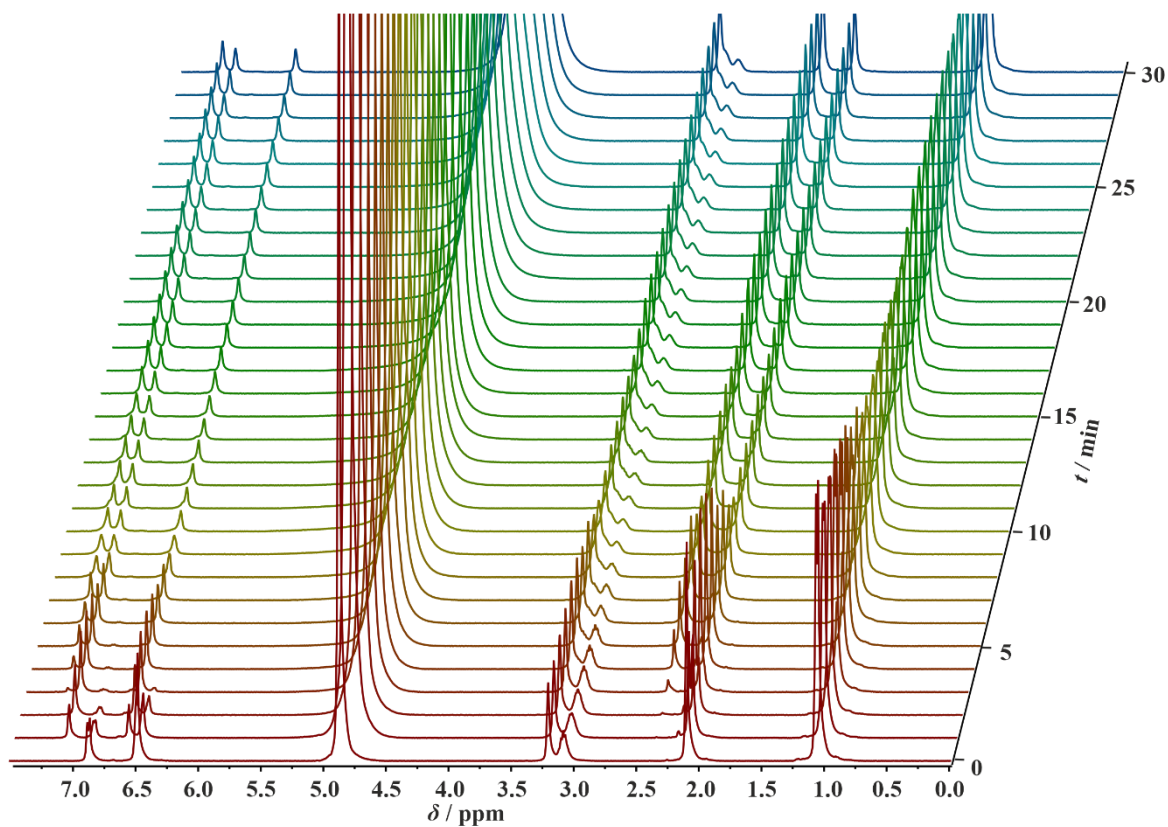
Figure S3-3. Time-resolved (stacked) ^{1}H-NMR spectra of thymol bromination catalyzed by CeO$_{2-x}$ nanorods.
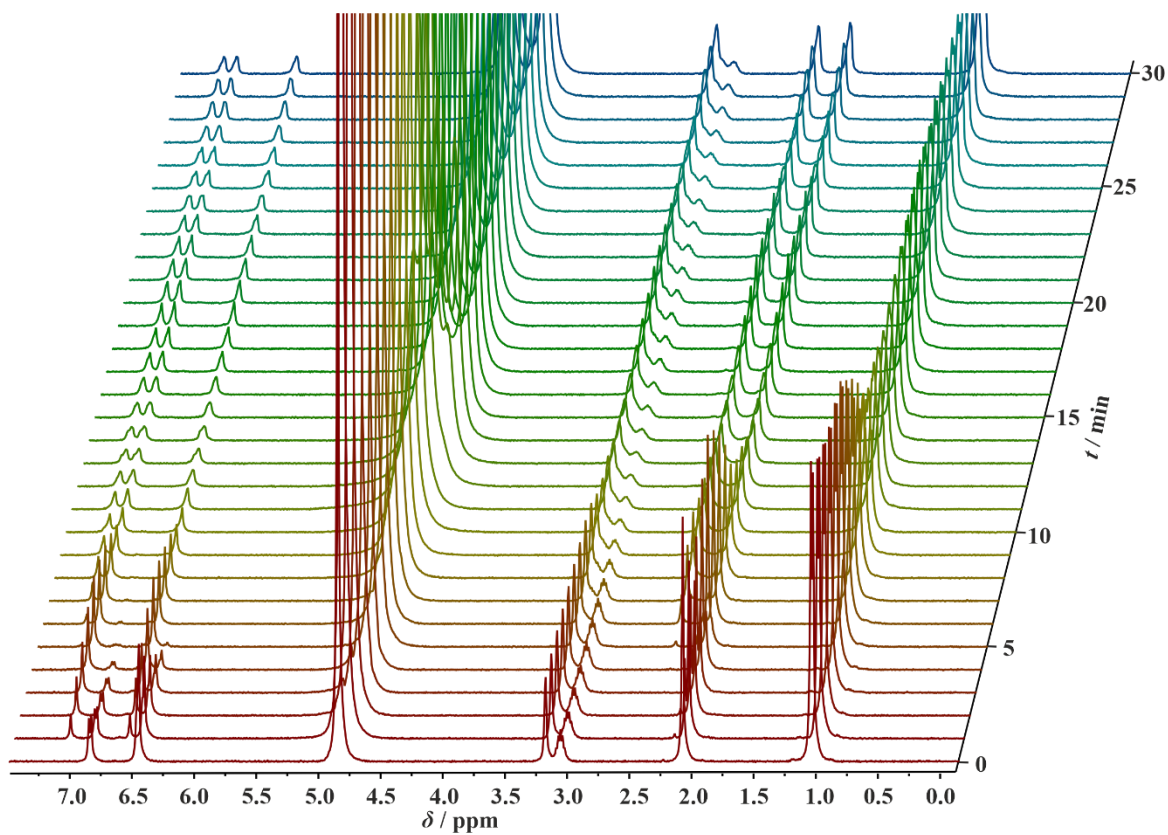
Figure S3-4. Time-resolved (stacked) ^{1}H-NMR spectra of thymol bromination catalyzed by CeO$_{2-x}$ nanospheres.
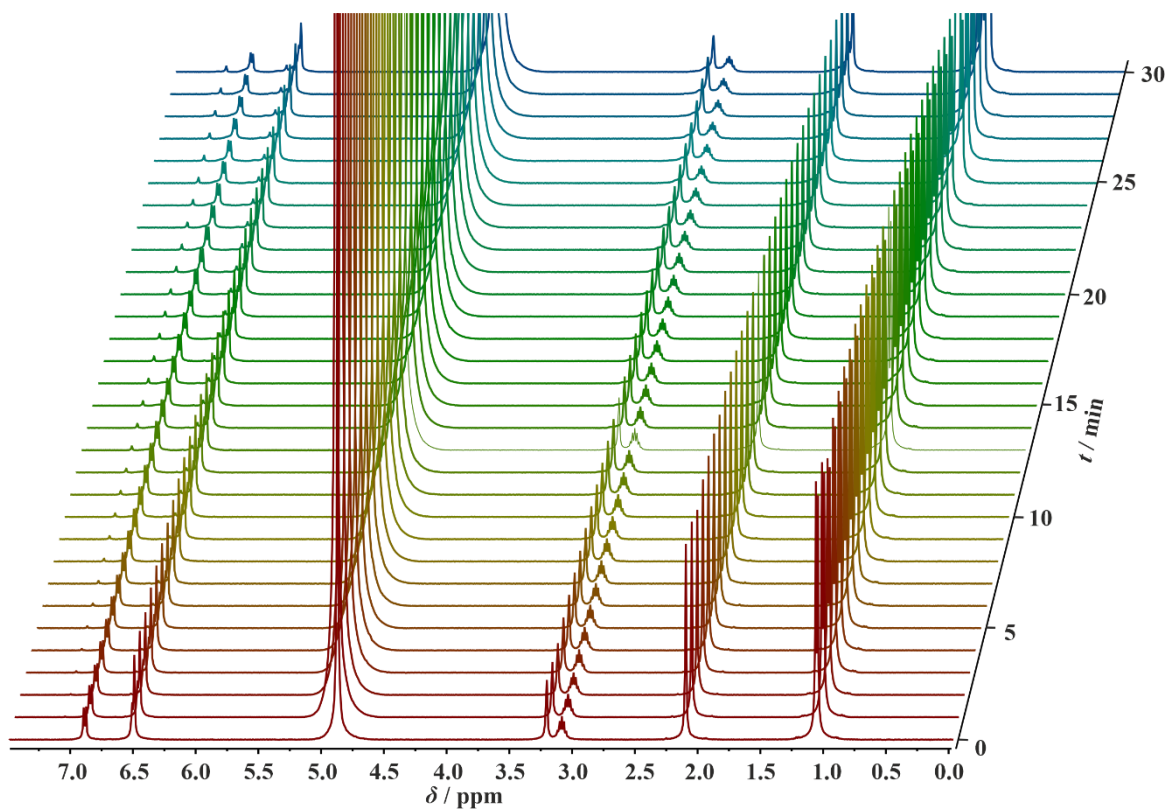
Figure S3-5. Time-resolved (stacked) ^{1}H-NMR spectra of thymol bromination catalyzed by CeO_{2-x} nanocubes.
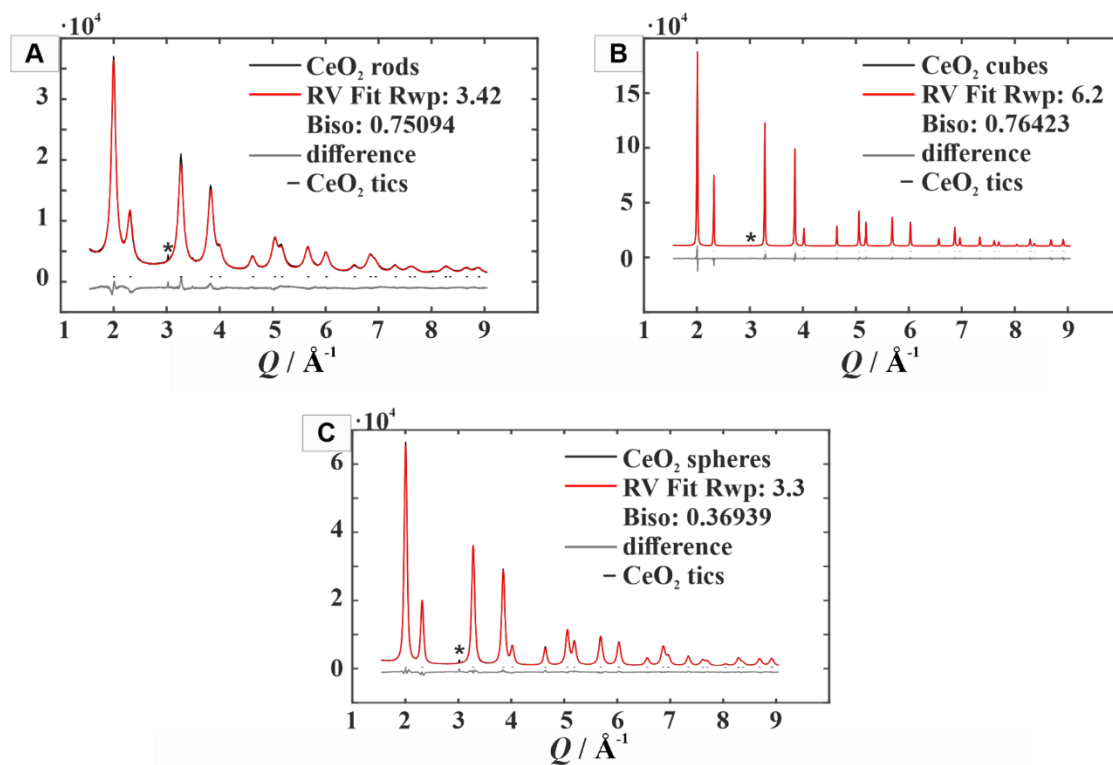
Figure S3-6. Powder diffraction phase analysis with Rietveld refinements of (A) CeO_{2-x} nanorods, (B) nanocubes and (C) nanospheres. Experimental powder pattern (black dots), Rietveld analysis (red lines), difference plots (blue lines). Tick marks show reflection positions of for pure ceria (fluorite structure, $Fm\overline{3}m$). The additional reflections "*" is due to the sample preparation on acetate foil.
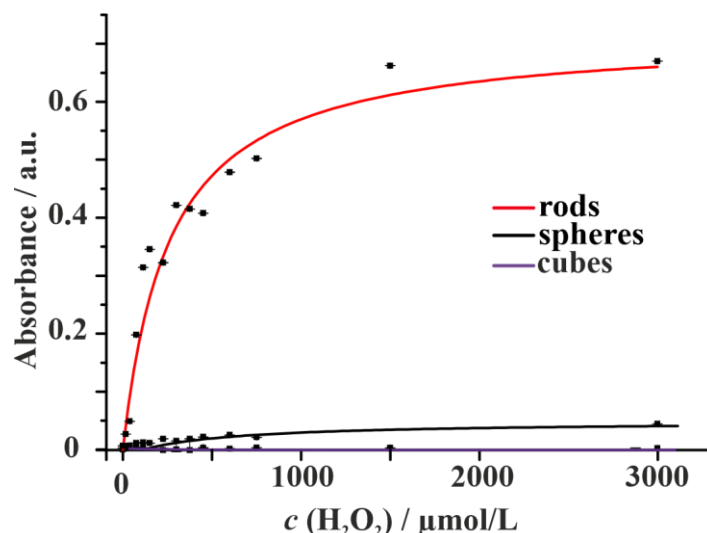
Figure S3-7. Michaelis Menten fit for CeO_{2-x} rods (red), spheres (black) and cubes.

The catalytic activity of CeO_{2-x} nanocrystals is described by their turnover frequencies (*TOF*) or the catalytic constants (k_{cat}).[1] The *TOF* depends on the (i) catalyst surface, (ii) time, and (iii) mass concentration. Brunauer-Emmett-Teller (BET) surface areas of 98.4 $m^2 g^{-1}$ (nanorods), 44.6 $m^2 g^{-1}$ (nanospheres) and 16.1 $m^2 g^{-1}$ (nanocubes) were determined to normalize the reaction rates because the bromination of thymol is surface specific (only the surface of the catalyst is accessible for the substrate). The rate of reaction (*ROR*) is defined by Equation S3-1. Here, the accessible surface area per mass equivalent of the catalyst is expressed through the BET surface area (S_{BET} in $m^2 g^{-1}$), and Equation S3-1 was evaluated based on time (v_{max} / M min^{-1}), surface area (S_{BET} / $m^2 g^{-1}$) and mass concentration ($\beta(Cat)$ / g L^{-1}).

$$\text{TOF} = \frac{v_{max}}{[Cat]_0} \xrightarrow{[Cat]_0 \to S_{BET} \cdot \beta(Cat)} \text{ROR} = \frac{v_{max}}{S_{BET} \cdot \beta(Cat)} \qquad (\text{eq.S3-1})$$

Table S3-1. Overview of v_{max}, K_m, S_{BET} and ROR for all three morphologies.

Sample	v_{max} / µM min^{-1}	K_m/ µM	S_{BET}/$m^2 g^{-1}$	ROR/ µmol m^{-2} min^{-1}
CeO_{2-x} nanorods	0.72±0.04	330±5	98.4	0.29
CeO_{2-x} nanospheres	0.049±0.007	750±24	44.6	0.044
CeO_{2-x} nanocubes	n.a.	n.a.	16.1	n.a.

Experimental procedure to isolate the reaction products

4-Bromothymol: 225 mg (1.5 mmol) Thymol and 140 mg (1.18 mmol) KBr were dissolved in 33 mL of a 10:1 % v/v MeOH/H$_2$O mixture. Subsequently 300 μL conc. H$_2$O$_2$ and 300 μL conc. HClO$_4$ are added to obtain pH=1. 28 mg of CeO$_{2-x}$ nanoparticles (rods) were added. The reaction was stirred for 3 h at room temperature. The reaction solution was diluted with water to 100 mL and extracted five times with 30 mL diethyl ether. The organic phase was dried over sodium sulfate (Na$_2$SO$_4$), filtered and the solvent was evaporated by a rotary evaporator. A yellow oil was received, which was crystallized at -20 °C using 1 mL petrol ether yielding colorless crystals. ^{1}H-NMR (400 MHz, CDCl$_3$): 4-bromo-2-isopropyl-5-methylphenol (4-bromthymol): δ[ppm]= 7.29 (s, 1 H, H-3), 6.64 (s, 1 H, H-6), 3.13 (h, J=6.9 Hz, 1 H, Ar-C$\underline{\text{H}}$-(CH$_3$)$_2$), 2.30 (s, 1 H, Ar-C$\underline{\text{H}}$$_3$, 1.22 (d, J = 6.9 Hz, 6 H, Ar-CH-(C$\underline{\text{H}}$$_3$)$_2$).
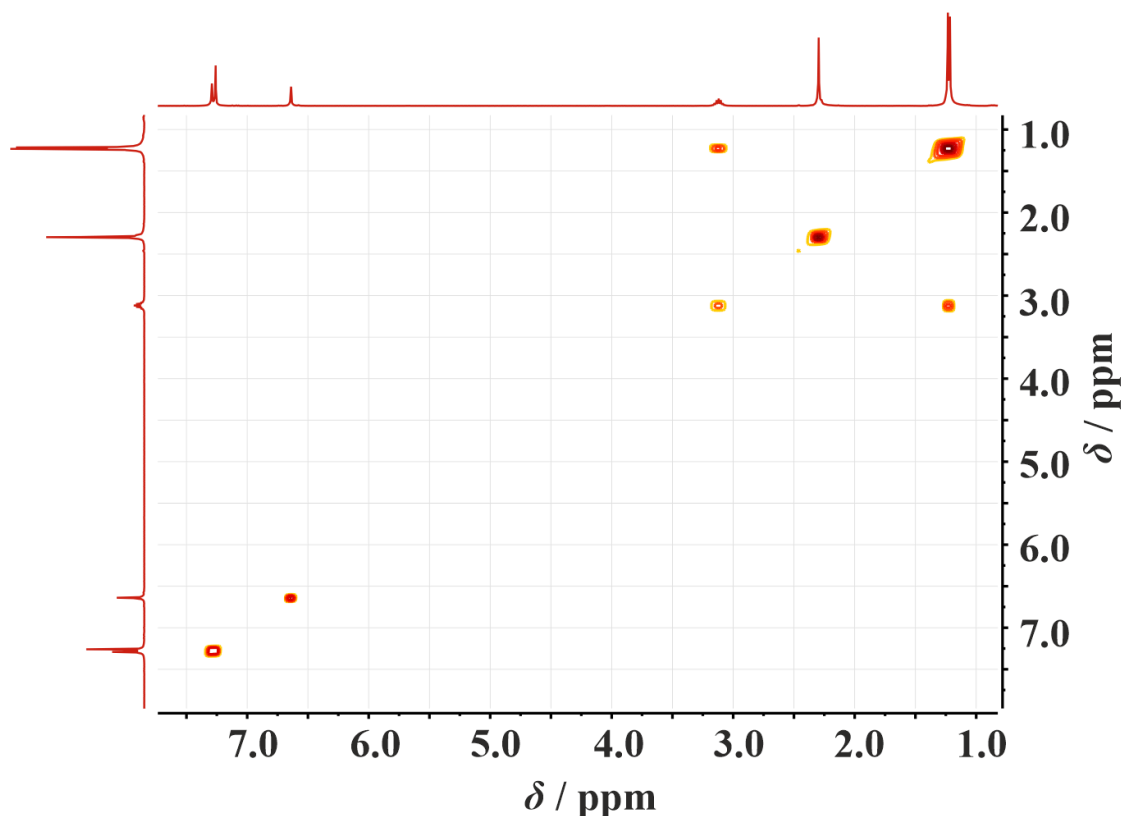
Figure S3-8. COSY spectrum of 4-bromothymol.

2,4-Dibromothymol: 225 mg (1.5 mmol) Thymol and 360 mg (3 mmol) KBr were dissolved in 33 mL of a 10:1 % v/v MeOH/H$_2$O mixture. Subsequently 300 μL conc. H$_2$O$_2$ and 300 μL conc. HClO$_4$ are added to obtain pH=1. 28 mg of CeO$_{2-x}$ nanocrystals (rods) were added. The reaction was stirred for 3 h at room temperature. The reaction solution was diluted with water to 100 mL and extracted five times with 30 mL diethyl ether. The organic phase was dried over sodium sulfate (Na$_2$SO$_4$), filtered and the solvent was evaporated by a rotary evaporator. A yellow oil was received, which purified via column chromatography using a 3:1 mixture of cyclohexane/dichloromethane.

^{1}H-NMR (400 MHz, CDCl$_3$): 2,4-Dibromo-6-isopropyl-3-methylphenol (2,4-dibromthymol): δ[ppm]= 7.31 (s, 1 H, H5), 5.68 (s, 1 H, Ar-O$\underline{H}$), 3.26 (h, J=6.9 Hz, 1 H, Ar-C$\underline{H}$-(CH$_3$)$_2$), 2.52 (s, 3 H, Ar-C$\underline{H}_3$, 1.22 (d, J = 6.9 Hz, 6 H, Ar-CH-(C$\underline{H}_3$)$_2$).
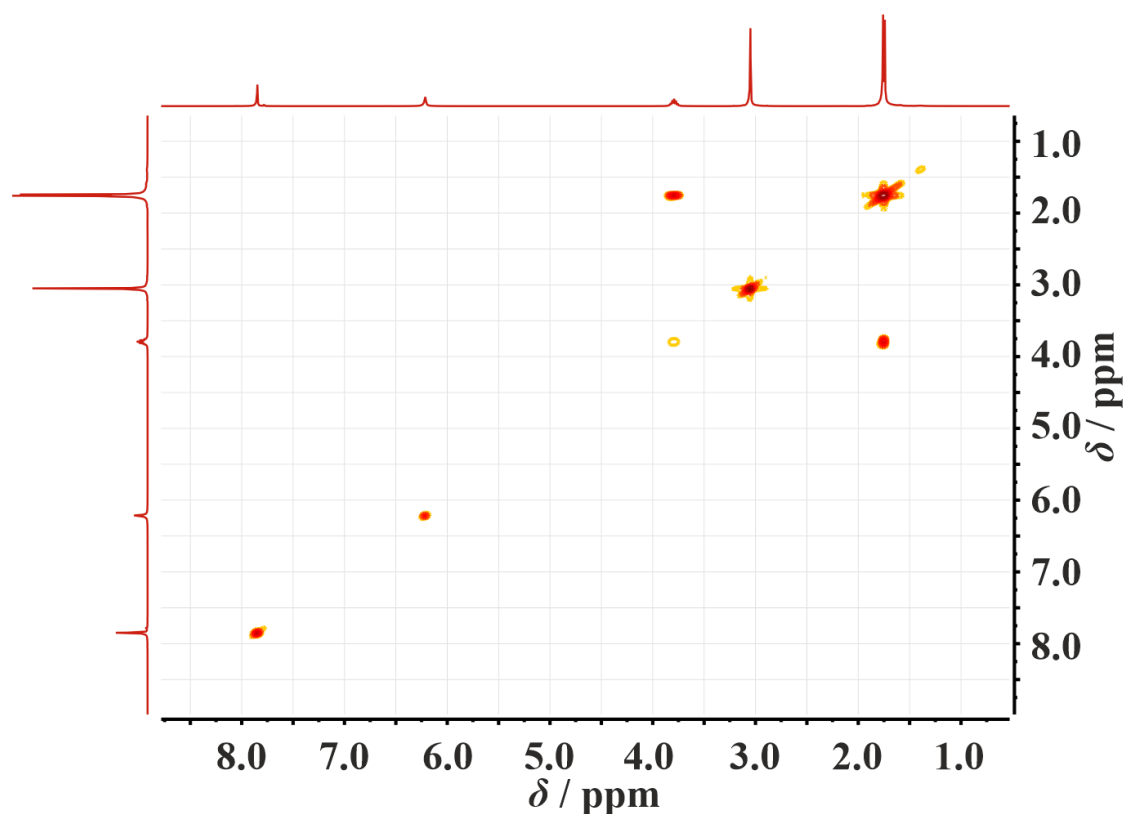
Figure S3-9. COSY spectrum of 2,4-dibromothymol.
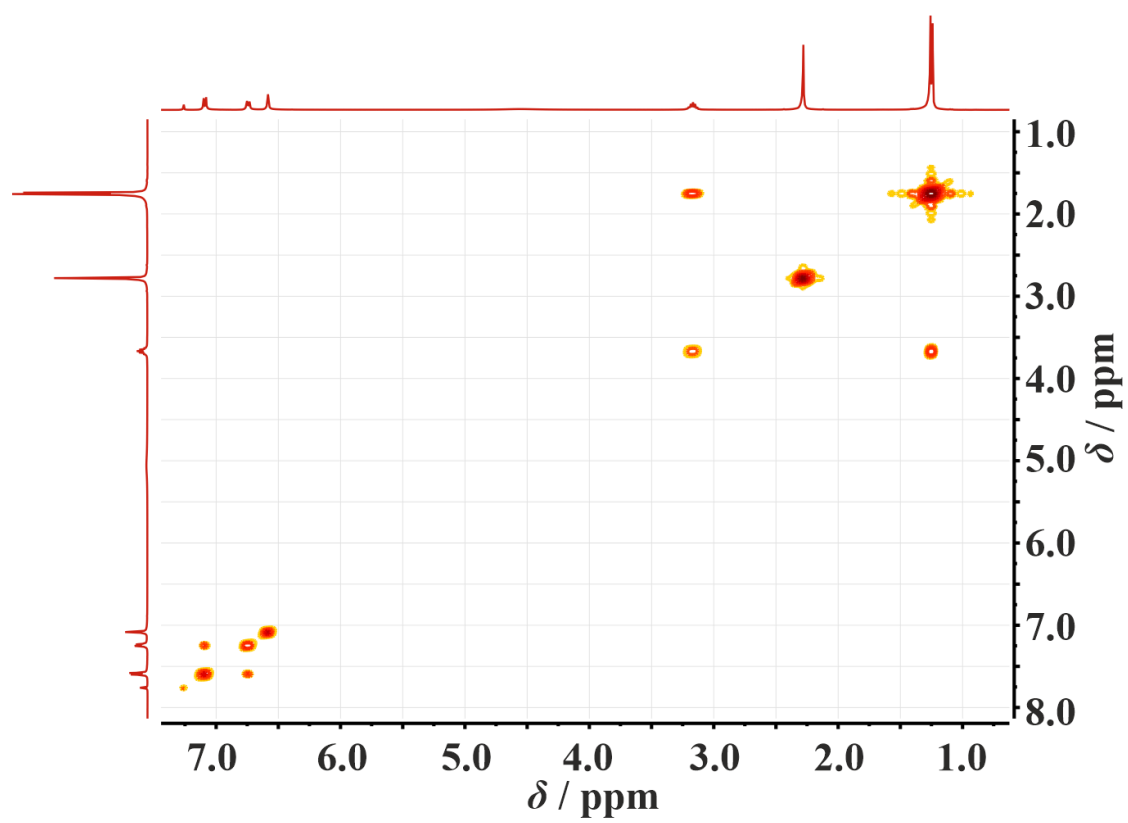
Figure S3-10. COSY spectrum of thymol.
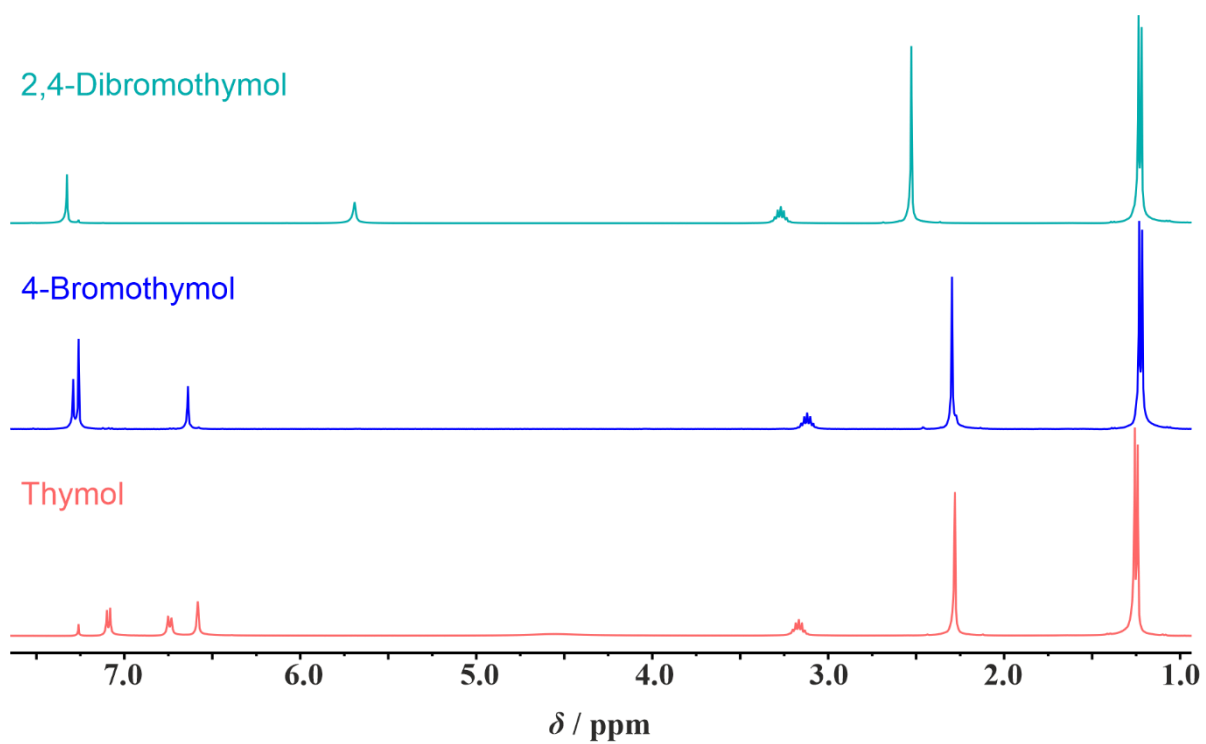
Figure S3-11. Stacked [^1]H-NMR spectra of thymol, 4-bromothymol and 2,4-dibromothymol.
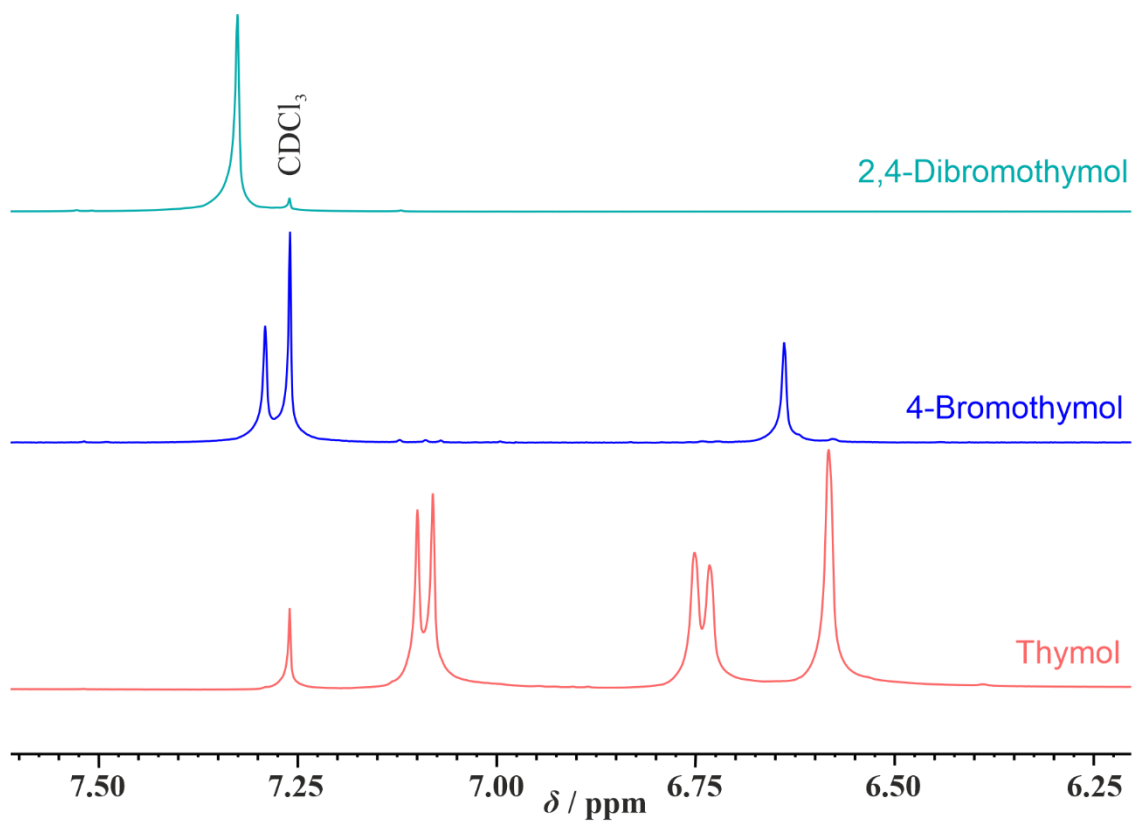
Figure S3-12. Stacked [^1]H-NMR spectra of thymol, 4-bromothymol and 2,4-dibromothymol in the range from 7.5-6.25 ppm.
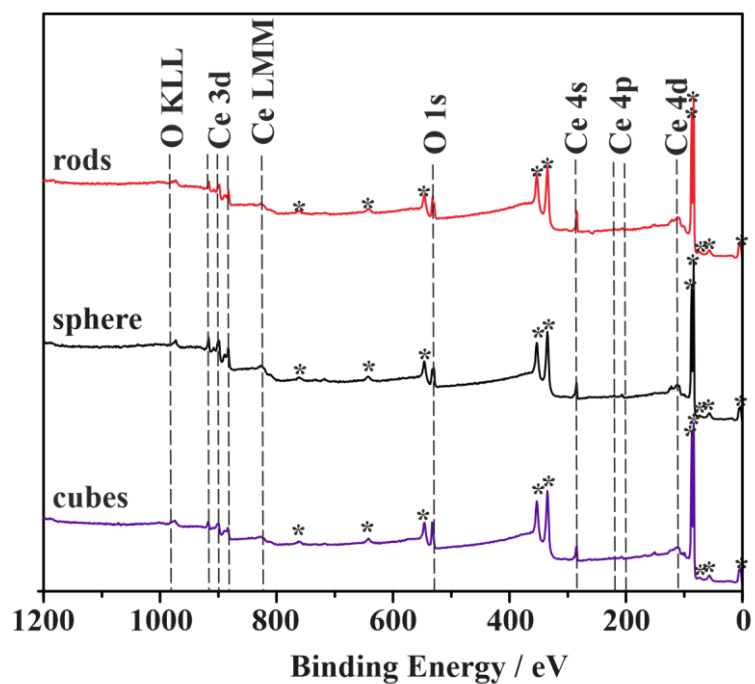
Figure S3-13. XPS survey spectrum of CeO_{2-x} nanorods, -spheres and –cubes using non-monochromatized Al Kα excitation. The detected XPS lines of Ce and O are marked, the additional signals marked with * belong to Au due to sputtering of the sample holders before preparation.
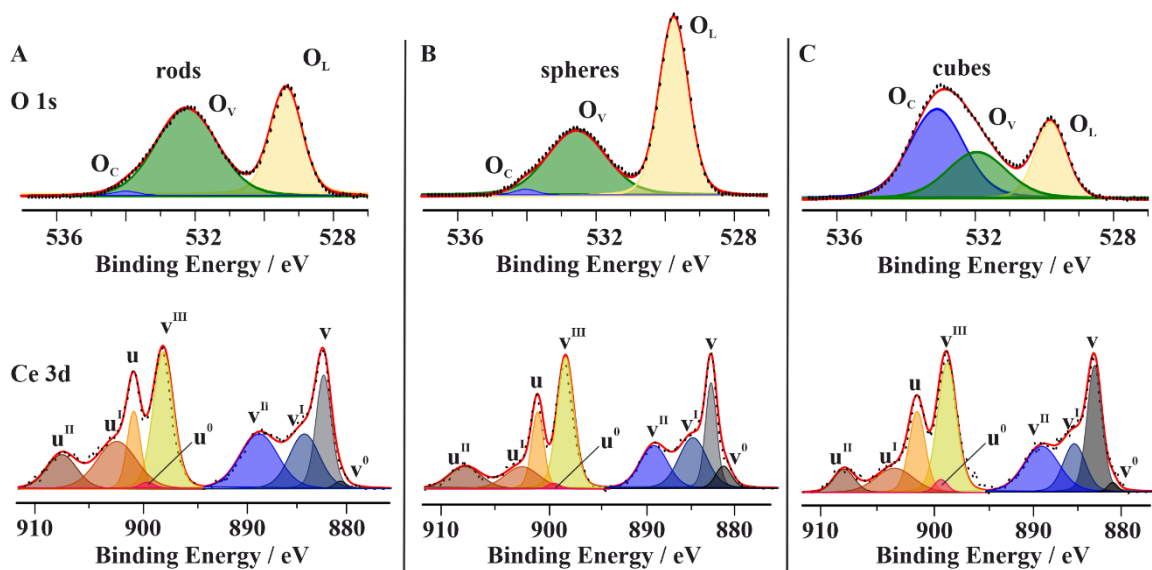
Figure S3-14. XPS spectra of CeO_{2-x} (A) nanorods, (B) -spheres and (C) -cubes. The Ce 3d, O 1s regions confirm the presence of the elements Ce and O.

Figure S3-14 show the Ce and O regions of the XPS spectra of CeO_{2-x} nanorods, -spheres and -cubes. The signals are labeled as v, v^{ll}, v^{lll} and u, u^{ll}, where v and u correspond to $3d_{5/2}$ and $3d_{3/2}$ orbitals of Ce^{4+}, respectively. For Ce^{3+} v^0, v^l and u^0, u^l correspond to $3d_{5/2}$ and $3d_{3/2}$ orbitals revealing mixed oxidation states (4+/3+) for surface Ce in CeO_{2-x}. Deconvolution of the peaks with respect to the $3d_{5/2}$ and $3d_{3/2}$ transitions of Ce^{4+} and Ce^{3+} yielded proportions of approx. 30, 30, and 20% Ce^{3+} surface sites for CeO_{2-x} nanorods, -spheres and -cubes. This shows also that oxygen defects associated with Ce^{3+} predominantly occur at the particle surface (as expected from the ionic radii of Ce^{4+} and Ce^{3+}. However, the Ce^{3+}/Ce^{4+} ratios in nanocubes and –spheres do not differ much from each other. The 1s oxygen signals in Figure 3-14 are assigned to oxide anions in the crystal structure (O_L), oxygen-deficient regions (O_v) and chemisorbed oxygen species (O_c), respectively.[2,3] The oxygen deficient concentration is highest for CeO_{2-x} nanorods which is in harmony with the results of Raman spectroscopy and the XPS spectrum of Ce 3d region (highest Ce^{3+} concentration). Nanocubes exhibit a higher ratio of adsorbed hydroxyl groups (blue) on their surface, whereas nanorods and -spheres only show traces of OH groups. XPS measurements reveal oxygen-deficient regions (green) on the surface for all samples as well as structural oxide ions (yellow). For nanocubes, chemisorbed oxygen species like losely bound hydroxyl groups or water exhibit the highest concentration. The increasing content of hydroxyl surface groups may hinder the activity for oxidative bromination. Attachment of negatively charged Br^- as well as hydrogen peroxide species could be made more difficult.
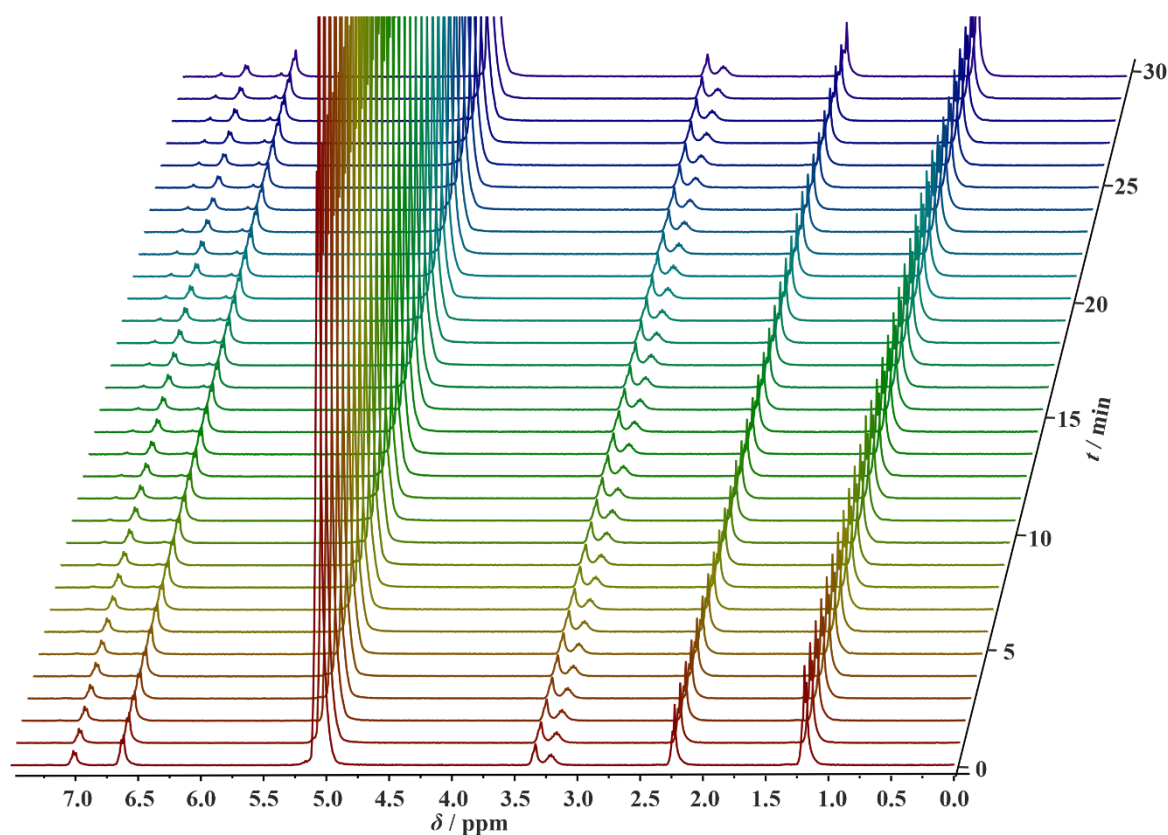
Figure S3-15. Time-resolved (stacked) ^{1}H-NMR spectra of thymol bromination in absence of CeO_{2-x} nanocrystals.

3.7.1. REFERENCES

1   Kozuch, S.; Martin, J. M. L. "Turning Over" Definitions in Catalytic Cycles. *ACS Catal.* **2012**, *2* (12), 2787–2794.

2   Yoon, D. H.; Tak, Y. J.; Park, S. P.; Jung, J.; Lee, H.; Kim, H. J. Simultaneous Engineering of the Interface and Bulk Layer of Al/ Sol -NiO x /Si Structured Resistive Random Access Memory Devices. *J. Mater. Chem. C* **2014**, *2* (30), 6148–6154.

3   Wang, C.; Cui, X.; Liu, J.; Zhou, X.; Cheng, X.; Sun, P.; Hu, X.; Li, X.; Zheng, J.; Lu, G. Design of Superior Ethanol Gas Sensor Based on Al-Doped NiO Nanorod-Flowers. *ACS Sensors* **2016**, *1* (2), 131–136.

4

TUNING CERIA CATALYSTS IN AQUEOUS MEDIA AT THE NANOSCALE: HOW DO SURFACE CHARGE AND SURFACE DEFECTS DETERMINE PEROXIDASE- AND HALOPEROXIDASE-LIKE REACTIVITY

4.1. SUMMARY

As previously shown in chapter 3, cerium dioxide nanoparticles can mimic the vanadium-dependent haloperoxidase because they are able to oxidatively brominate the phenolic monoterpene thymol. However, nanoparticles with different morphologies show completely different
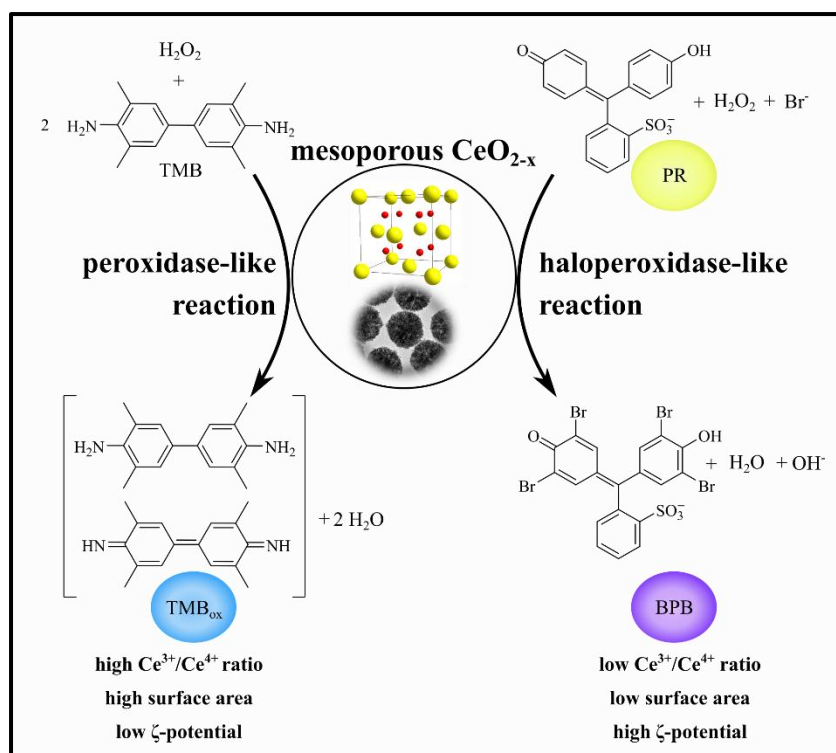
performances in the oxidative bromination reaction due to their varying surface properties. In the following chapter 4 it will be investigated whether these properties can be influenced by varying the reaction time. For this purpose, mesoporous cerianite nanoparticles were prepared by an ethylene glycol based hydrothermal synthesis at different reaction times. Particle formation process was investigated more in detail using small-angle X-ray

scattering. Subsequently, the nanoparticle properties such as particle size, surface area (S_{BET}), zeta potential (ζ-potential) and Ce^{3+}/Ce^{4+} ratio were determined. Finally, the catalytic activity of the resulting nanoparticles was compared in two different enzyme-like reactions. First, their catalytic activity was investigated in i) peroxidase-like activity using the substrate molecule 3,3′,5,5′-tetramethylbenzidine (TMB) and then ii) haloperoxidase-like activity using the substrate molecule phenol red was evaluated. Subsequently, it was concluded which factors are particularly important for a catalyst in the peroxidase-like and in the haloperoxidase-like reaction.

It was observed that the surface properties can be easily tuned by varying the reaction time. Mesoporous CeO_2 produced at longer reaction times exhibit a larger surface area and Ce^{3+}/Ce^{4+} ratio, whereas the zeta potential decreases with increasing reaction time. In the haloperoxidase-like reaction, the nanoparticles prepared at shorter reaction times show a much higher catalytic performance, indicating a large influence of the highly positive zeta potential resulting from a low Ce^{3+}/Ce^{4+} ratio on this type of reaction. In the peroxidase-like reaction, in contrast, the particles prepared at longer reaction times exhibit higher catalytic activity, indicating a strong influence of the larger surface area and the increased Ce^{3+}/Ce^{4+} ratio in this reaction.

In summary, an ethylene glycol-based hydrothermal reaction can be tailored to produce nanoparticles with different surface properties. Thus, they can be selectively optimized for different catalytic applications by a single synthesis.

Contributions:

Eva Pütz:	Concept development, nanoparticle synthesis, TEM, ζ-potential and BET surface area measurement, UV/Vis kinetic measurements, data analysis, manuscript preparation, figure preparation.
XXX:	SAXS measurements and data analysis, manuscript correction.
XXX:	SEM measurement.
XXX:	Manuscript correction and scientific supervision.

4.2. INTRODUCTION

Engineering the size, shape, and surface area of individual particles at the nanometer scale is important for controlling the surface chemistry of metal or metal oxide nanocrystals (NPs), which are key components in catalysis.[1] Ceria (CeO_{2-x}) is a good example of how studies at the nanoscale are a valuable for understanding its catalytic mechanisms, which are crucial for the development of new materials with enhanced properties. CeO_{2-x} is an important material for environmental and energy applications.[2] It is used in heterogeneous catalysis[3], oxygen sensors[4], solar cells[5], photoelectrochemistry[6,7] lithium ion batteries[8], fuel cells[9,10] and other energy-related applications.[11,12]

In aqueous media CeO_{2-x} nanocrystals catalyze H_2O_2 disproportionation in a Fenton-like reaction.[13] Although this fact is known for almost 100 years,[14,15] CeO_{2-x} nanocrystals have recently been used in biomedicine[15] as functional mimics of superoxide dismutases[16] (O_2^- + $2H^+ \rightarrow H_2O_2 + O_2$) and catalases.[17] ($2H_2O_2 \rightarrow 2H_2O + O_2$) Likewise, ceria nanocrystals exhibit peroxidase-like properties (i.e., $XH_2 + H_2O_2 \rightarrow X + 2H_2O$)[18] which allows protecting cells against reactive oxygen species (ROS) such as superoxide and hydrogen peroxide anions or hydroxyl radicals.[18–21]

Likewise, CeO_{2-x} nanocrystals emulate the catalytic activity of haloperoxidases (HPOs),[22,23] a group of enzymes which oxidize halides (X^-) to the corresponding hypohalites at the expense of peroxides ($X^- + H_2O_2 + H^+ \rightarrow HOX + H_2O$).[24–26] These hypohalites are reactive intermediates which are converted in follow-up steps to halogenated organic compounds ($HOX + RH \rightarrow RX + H_2O$).[27] The function of this extracellular enzymatic system is to control bacterial colonization on the surfaces of marine plants by generating HOBr (which is directly bactericidal).[28] Moreover, HOBr reacts in low concentrations with bacterial acyl homoserine lactones (AHLs) which play an important role in bacterial signaling systems. Many bacteria secrete these lactones. AHLs are "inactivated" by bromination with HPO enzymes. The disruption of bacterial signaling via inactive (i.e., brominated) AHLs[29] inhibits the formation of biofilms.[30,31]

However, peroxidase (PO) and HPO-like reactions proceed according to different mechanisms, i.e., nanocrystals for PO-like reactions are not necessarily suitable for HPO-like reactions. The properties of ceria are closely linked to its fluorite crystal structure and its associated defect chemistry. Cation defects, Ce^{3+} (in oxygen-deficient ceria) sit on a Ce^{4+} cubic site with 8-fold oxygen coordination. Every two cation defects in the cerianite structure are balanced by one oxygen-vacancy defect, V_O in a tetrahedral site. The catalytic

properties of ceria nanoparticles can be enhanced through a large BET surface area (e.g., with ultrasmall nano-particles[32,33] or mesoporous structures).[34,35]

The ROS-scavenging activities with neutral (H_2O_2) substrate molecules strongly depend on Ce^{3+}/Ce^{4+} surface ratio, whereas halogenation reactions with surface-bound ionic (X^-) a neutral (H_2O_2) substrates depend on the ζ-surface potential. The ζ-potential of ceria can be changed in two different ways. Surface binding of Pearson-hard[36] (e.g., F^-) anions leads to a negatively charged surface[37], thereby repelling anionic substrates and increasing the oxidase-like activity. Replacing tetravalent Ce^{4+} cation in the CeO_{2-x} structure by trivalent cations (e.g., Bi^{3+} or Ln^{3+})[33,38,39] on the other hand, leads to more positive ζ-potentials, thereby attracting negatively charged substrates which is advantageous for HPO-like reactions.

An understanding of CeO_{2-x} nanocrystal behavior is needed, particularly in aqueous systems where interactions with other soluble compounds can alter their fate and transport. Engineering nanoparticles with large surface area and defined ζ-potential is a tedious and time-consuming task. As a classical oxide ceramic, CeO_{2-x} is prepared by polycondensation chemistry. The condensation process is spontaneous, with a range of smaller oligomers being formed initially.[40] These oligomers grow and serve as nuclei for the formation of stable particles that eventually aggregate/coalesce to form a gel, an aggregate network or crystallites depending on the individual oxide.[41] One difference between the different synthetic approaches is whether the reaction is carried out under equilibrium conditions (e.g. hydro- or solvothermal synthesis)[42–44] or non-equilibrium conditions (e.g. via sonolysis,[45] thermal decomposition of volatile precursors,[46] sol-gel reactions[47,48] or by microfluidics[49–51] Early applications of hydrothermal methods to make CeO_{2-x} nanomaterials date back to the early 1990s,[52] but only a decade later the morphology of ceria nanocrystals was demonstrated by high-resolution transmission electron microscopy (HRTEM).[53] By controlling a few critical reaction variables (pH, temperature, and pressure), it was possible to prepare ceria nanocrystals with rod-like,[54] cube-like[55] or spherical morphologies.[56] Typically, the reactions start from Ce^{3+} salts, which are precipitated initially in alkaline solution as $Ce(OH)_3$. Subsequently, $Ce(OH)_3$ nuclei (with hexagonal structure) can be oxidized to CeO_{2-x} nanocrystals in a topotactic reaction where the anisotropic morphologies may be preserved even for cubic (i.e., isotropic) CeO_{2-x}.[57]

The synthesis of mesoporous oxides typically requires suitable templates that fill the pores during synthesis and are removed afterward.[34,58] A typical example is the use of soft

templates like organic surfactants or block copolymers that co-assemble with metal ions in a sol-gel process and are removed by heating to expose the pores.

We report a template-free approach to synthesize mesoporous crystalline CeO_{2-x} nanocrystals with variable BET surface areas (S_{BET}) and ζ-potentials resulting from different Ce^{3+}/Ce^{4+} ratios. The simplicity of surface engineering of the mesoporous ceria by varying the reaction time makes this synthesis a powerful method for preparing catalytic metal oxides according to individual needs. To evaluate the impact of these different surface characteristics, the enzyme mimetic activities of as synthesized mesoporous CeO_{2-x} nanoparticles in peroxidase and haloperoxidase reaction were compared.

4.3.   RESULTS AND DISCUSSION

Nanoparticle synthesis and characterization

Mesoporous CeO_{2-x} nanocrystals were formed by heating $Ce(NO_3)_3 \cdot 6\ H_2O$ in ethylene glycol, acetic acid and water under hydrothermal conditions.[59] Surface area (S_{BET}), porosity and zeta potential (ζ-potential) were found to depend strongly on the reaction time.
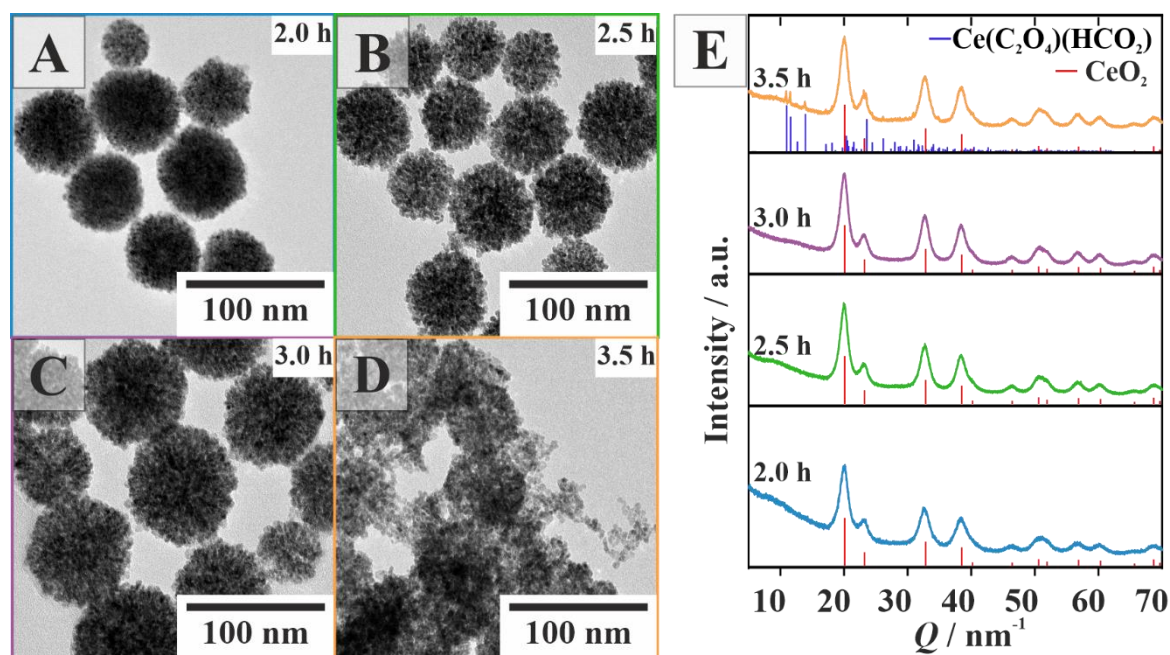
Figure 4-1. TEM images of mesoporous CeO_{2-x} nanoparticles formed after (A) 2.0 h, (B) 2.5 h, (C) 3.0 h and (D) 3.5 h of reaction time. (E) Powder X-ray diffraction patterns of CeO_{2-x} particles formed after 2.0 h, 2.5 h, 3.0 h and 3.5 h. Red ticks indicate the calculated reflection positions for CeO_{2-x} based on structural data from the ICSD data bank (ICSD# 88752). Blue ticks indicate the calculated reflection positions for $Ce(C_2O_4)(HCO_2)$ based on structural data from the ICSD data bank (ICSD# 43450).

Therefore, the reaction products were investigated as a function of the reaction time. Figure 4-1A-D show transmission electron microscopy (TEM) images of reaction products formed after 2.0 h, 2.5 h, 3.0 h and 3.5 h, which are referred to as CeO_2-2.0 h, CeO_2-2.5 h, CeO_2-3.0 h and CeO_2-3.5 h, respectively, below. All TEM images show that large spherical nanoparticle agglomerates in the size range of hundred nanometers have formed, consisting of smaller primary nanoparticles with diameters < 5 nm (Figure 4-1A-D and Figure 4-S1). The growth of these mesoporous nanocrystals proceeds according to a two-step growth model in which primary nanocrystals form in a supersaturated solution and subsequently agglomerate into larger secondary particles.[60,61] The formation mechanism is illustrated schematically in Figure 4-2. Increasing the reaction time leads to an increase in the particle

size of the larger spherical particles. TEM images of the larger spherical particles formed after 2 h reaction time (CeO$_2$-2.0 h) show higher material contrast compared to the particles obtained after longer reaction time (CeO$_2$-2.5 h, CeO$_2$-3.0 h). This indicates a higher packing efficiency of the primary particles within the larger aggregates. In contrast, the images of CeO$_2$-2.5 h and CeO$_2$-3.0 h show less densely packed regions, which is due to porosity of the particles. Further extension of the reaction time to 3.5 h resulted in the degradation of the larger spherical CeO$_{2-x}$ particle aggregates (Figure 4-1D).
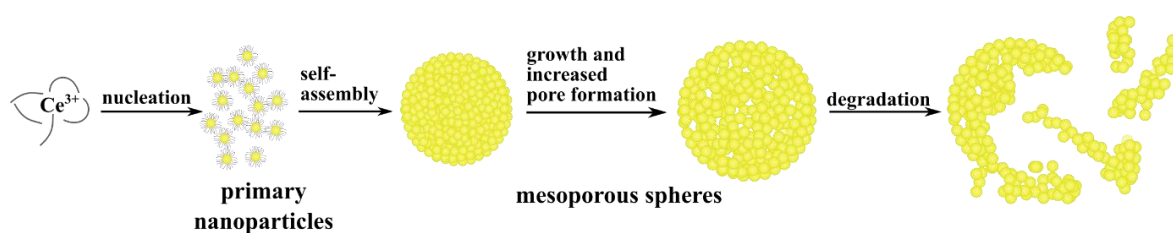
Figure 4-2. Schematic representation of the formation of mesoporous CeO$_{2-x}$ nanoparticles and their degradation.

Figure 4-1E shows the powder X-ray diffraction (PXRD) patterns of the product particles formed after 2.0 h, 2.5 h, 3.0 h and 3.5 h. The diffractogram is compatible with the presence of cubic cerianite (space group Fm$\overline{3}$m). The reflection broadening results from the nano-sized crystallites of the primary particles, in accordance with the TEM images (Figure 4-1A-D). The X-ray diffractograms in Figure 4-1E show that the coordination polymer Ce(C$_2$O$_4$)(HCO$_2$) is formed at longer reaction times (CeO$_2$-3.5 h). This suggests that the particle surfaces are complexed with oxalate and formate ligands. Oxalate and formate may be formed by oxidation of ethylene glycol through nitrate anions under the reaction conditions, where ethylene glycol is first oxidized to aldehyde and then further degraded to oxalic acid and formic acid. The excess of these surface ligands (formed from the solvent) eventually leads to the formation of cerium oxalate formate.[62,63] Phase-pure Ce(C$_2$O$_4$)(HCOO) was formed when the reaction was carried out in an open flask for 120 hours rather than in a sealed autoclave (Figure 4-S2).

Specific surface area, pore size, and pore volume of the mesoporous CeO$_{2-x}$ nanoparticles were determined using N$_2$ sorption measurements. Figure 4-3 shows that a significantly higher surface area (S_{BET}) is obtained with increasing reaction time until the larger spherical particles start to disintegrate (due to the gradual formation of Ce(C$_2$O$_4$)(HCOO)). The calculation of pore size and pore volume shows an inverse trend. While the pore diameter

decreases with reaction time, the pore volume increases. This trend is plausible considering that smaller pore diameters are compatible with a larger number of pores in a given total volume. A larger number of pores also results in a larger exposed S_{BET}. The larger pore volume is evident in the TEM images because of the large number of visible pores and the lower contrast. As the mesoporous spheres disintegrate, the S_{BET}, pore diameter, and pore volume decrease significantly.
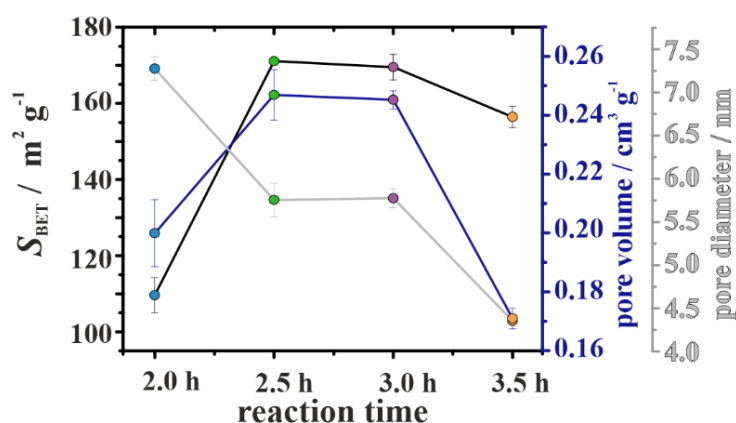
Figure 4-3. Effect of reaction time on specific surface area (S_{BET}), pore diameter and pore volume of CeO$_{2-x}$ nanoparticles.

Particle size distribution

Small angle X-ray scattering (SAXS) measurements were performed to investigate the formation processes in more detail. Figure 4-4A-D show the SAXS data of reaction solutions (Figure S4-3) and derived radii histograms of mesoporous nanoparticles formed at different reaction times. The resulting radii histograms are plotted on a $\log_{10}$ scale and are related to the volume fraction.

For mesoporous CeO$_{2-x}$ nanoparticles up to four different size distributions can be identified in a single sample. Two main regions can be observed for CeO$_2$-2.0 h. Figure 4-4A (inset d) has been assigned to the primary particles with an average radius of 0.8 nm. These small primary nanoparticles with comparable size agglomerate to form larger spherical nanoparticles. The larger spherical mesoporous CeO$_{2-x}$ nanoparticles with an average radius of 33.4 nm are referred to as inset a (Figure 4-4A, inset a). A small distribution of medium-sized objects is also observed (inset b, 13.3 nm), although their relative abundance is very low (Figure 4-4A). As the reaction time increases, the spherical particles grow in size (inset

a+b), resulting in a bimodal size distribution. This can also be observed in the stacked SAXS curves. As the reaction time increases, the SAXS curves shift to smaller Q values, indicating an increase in nanoparticle size (Figure S4-4).
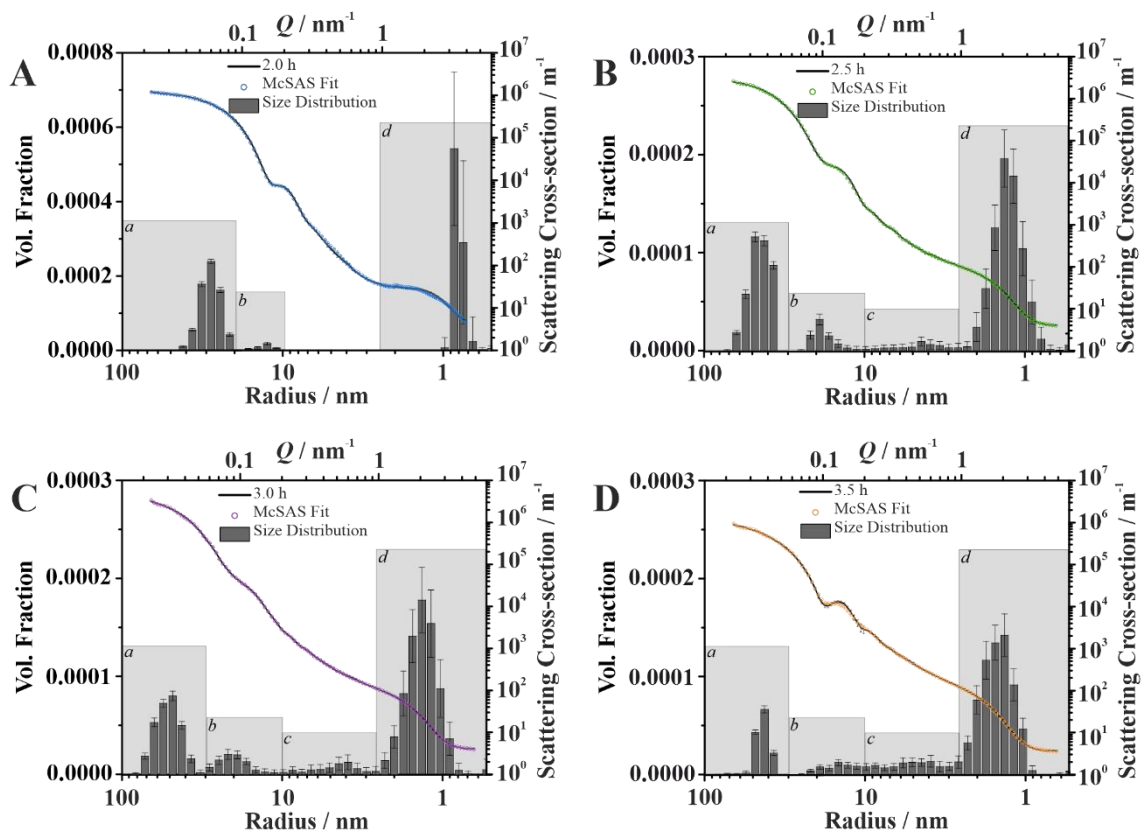
Figure 4-4. Fits of the small angle X-ray scattering data and particle radii histograms for mesoporous CeO$_2$ nanoparticles formed after reaction times of (A) 2.0 h, (B) 2.5 h, (C) 3.0 h and (D) 3.5 h.

This shift occurs both, in the low Q range (larger spherical mesoporous CeO$_{2-x}$ (Figure S4-4B) and in the larger Q range (small primary nanoparticles; Figure S4-4C). Table 4-1 shows the influence of the reaction time on the size of the four determined insets in the histogram. Inset *d* shows that the initially formed primary CeO$_{2-x}$ nanoparticles, which are the basic building blocks for the larger spherical CeO$_{2-x}$ agglomerates, grow larger during the reaction. The same behavior was observed for inset *a+b*, with a maximum size for CeO$_2$-3.0 h The decomposition of the larger particles (CeO$_2$-3.5 h) is evident from the decrease in the average particle size in insets *a+b* and from the lower relative volume fraction of the larger spherical agglomerates (Figure 4-5).

With longer reaction time, the relative amount of the small building block particles (inset *d*) increases from 55 to 70 % of the cumulative abundance, whereas the relative amount of large spherical mesoporous particles decreases from 50 to 15 % throughout the reaction

due to decomposition (Figure 4-5A-D). After 2.5 hours of reaction time, additional particles with a radius of about 10 nm (inset *c*) are formed, which can be attributed to increasing porosity.
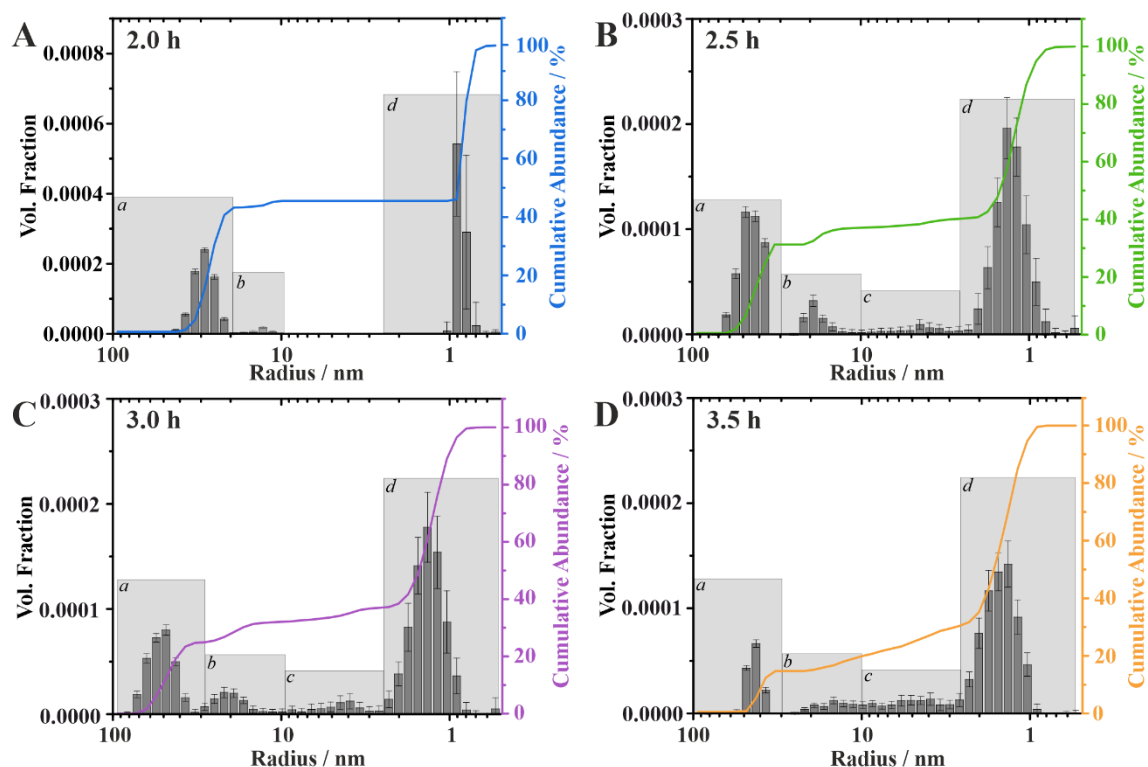
Figure 4-5. Particle radii histograms derived from small angle X-ray scattering data with cumulative abundance (right y-axis) for mesoporous CeO_{2-x} nanoparticles formed after (A) 2.0 h, (B) 2.5 h, (C) 3.0 h and (D) 3.5 h of reaction time.

Table 4-1. Average radii for mesoporous CeO_{2-x} nanoparticles shown in the histograms of the different insets (resultant from Monte Carlo fits) derived from SAXS measurements.

Sample	insets			
	a / nm	*b* / nm	*c* / nm	*d* / nm
CeO_2-2.0 h	33.4 ± 0.1	13.30 ± 0.15	-	0.86 ± 0.01
CeO_2-2.5 h	45.7 ± 0.1	19.13 ± 0.31	5.02 ± 0.30	1.32 ± 0.02
CeO_2-3.0 h	52.3 ± 0.2	20.51 ± 0.73	5.16 ± 0.22	1.39 ± 0.02
CeO_2-3.5 h	43.7 ± 0.2	14.68 ± 0.91	5.62 ± 0.13	1.57 ± 0.01

These results are in harmony with the results of the BET measurements, which show an increase in pore volume over the reaction time. At a reaction time of 3.5 hours, the BET measurement shows a decrease in pore volume that is not consistent with the radius histogram. However, new particles of this size may be formed due to the decomposition of

the larger particles, which are responsible for the corresponding signal from the SAXS data. The SAXS-derived radii for the different insets after various reaction times are shown in Table 4-1.

Ce valence states (X-ray photoelectron spectroscopy)

The catalytic activity of CeO_{2-x} nanocrystals is attributed to oxygen defects, i.e., CeO_{2-x} is non-stoichiometric and multiple oxidation states are possible. The color change from yellow to purple that occurred during the formation of mesoporous CeO_2 nanoparticles indicates a change in the Ce^{3+}/Ce^{4+} ratio during the reaction.[64,65] Therefore, X-ray photoelectron spectroscopy (XPS) was employed to analyze the effect of reaction time on the Ce^{3+}/Ce^{4+} ratio. Figure 4-6A-C show XPS overview spectra, Ce 3d and O 1s XPS core spectra of mesoporous CeO_2 nanoparticles formed after different reaction times. The XPS spectra of the Ce 3d region were used to determine the Ce^{3+} and Ce^{4+} concentrations on the surface of the mesoporous CeO_{2-x} nanoparticles.

The XPS spectra are indeed compatible with mixed oxidation states of cerium. Ce^{4+} forms three doublets labeled v, v^{ll}, v^{lll} and u, u^{ll}, u^{lll} and Ce^{3+} forms a pair of doublets labeled v^0, v^l and u^0, u^l. Here v and u correspond to the orbitals $3d_{5/2}$ and $3d_{3/2}$, respectively.[66,67] The total concentrations of Ce^{3+} and Ce^{4+} were determined using Equation 4-1 and 4-2, and they are listed in Table 4-2, in which $A(Ce^{3+})$ and $A(Ce^{4+})$ are the sums of all integrals of the Ce^{3+} and Ce^{4+} signals obtained after deconvolution.[66]
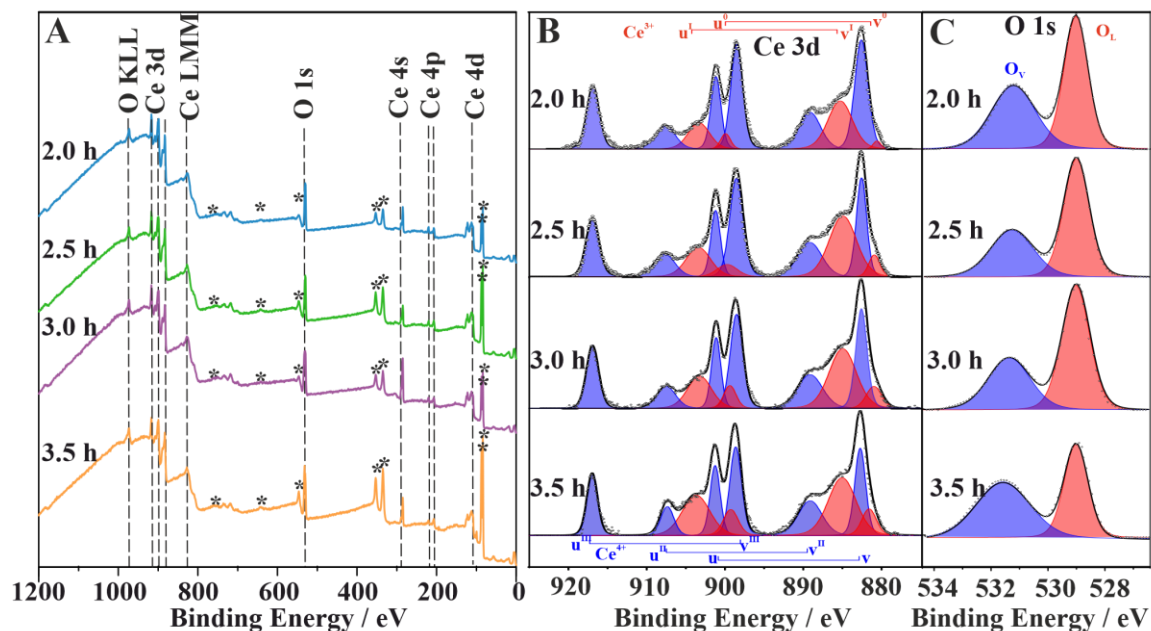
Figure 4-6. (A) XPS survey spectra using non-monochromatized Al Kα excitation for mesoporous CeO_{2-x} nanoparticles formed after different reaction times. The XPS lines of Ce and O are marked. Additional signals marked with * belong to Au, which was brought in by sputtering of the sample holders before preparation. (B) XPS spectra of the Ce 3d and (C) O 1s regions.

$$\%Ce^{3+} = 100\% \cdot \frac{A_{Ce3+}}{A_{Ce3+} + A_{Ce4+}} \qquad \text{(Equation 4-1)}$$

$$\%Ce^{4+} = 100\% \cdot \frac{A_{Ce^{4+}}}{A_{Ce^{3+}} + A_{Ce^{4+}}}$$

<div align="right">(Equation 4-2)</div>

Table 4-2. Ce^{3+}/Ce^{4+} ratios calculated from XPS spectra of Ce 3d region (Figure **4**-6B) for mesoporous CeO_{2-x} nanoparticles formed at different reaction times.

Sample	%Ce^{3+}	%Ce^{4+}	Ce^{3+}/Ce^{4+} ratio
CeO₂-2.0 h	26,3	73,7	0,36
CeO₂-2.5 h	36,1	63,9	0,57
CeO₂-3.0 h	37,5	62,5	0,60
CeO₂-3.5 h	43,3	56,7	0,76

Mesoporous CeO_{2-x} always contains Ce in both, Ce^{3+} and Ce^{4+}, oxidation states. With longer reaction time, the Ce^{3+} fraction increases steadily and finally leads to a Ce^{3+} content of 43%, while the Ce^{4+} concentration decreases from 73% to 56% during the reaction. The O 1s region of all four materials shows two peaks (Figure 4C). The peak at lower binding energy (529 eV) can be assigned to the oxid anions O^{2-} (O_L) of the cubic cerianite structure.[66] The signal at higher binding energies is assigned to oxygen deficient regions (O_V).[68–70] Since Ce^{3+} is coupled to the formation of oxide vacancies, vacancies are formed between the CeO₂-2.5 h and CeO₂-3.5 h stages.[66] Still, the initial oxide vacancy concentration for mesoporous CeO₂-2.0 h is higher than for CeO₂-2.5 h and CeO₂-3.0 h. This may be due to the very small CeO_{2-x} nanoparticles during the initial stages of the reaction, where more defects may form because of the large surface to volume ratio.

Surface potential of mesoporous CeO₂-ₓ particles

ζ-potential measurements were carried out to evaluate the effect of the Ce^{3+}/Ce^{4+} ratio on the surface potential and to obtain information about the stability of the colloidal system and its catalytic activity. Different interactions with the catalyst surface can occur due to electrostatic attraction or repulsion. Depending on the reaction to be catalyzed, the ζ-potential can be changed to increase or decrease the reaction rate. The duration of the hydrothermal reaction allows controlling the ζ-potential as shown in Figure 4-7. The ζ-potential and the Ce^{3+}/Ce^{4+} ratio are likely to be correlated based on the XPS spectra (Figure 4-6 and 4-7) The higher the Ce^{4+} surface concentration, the higher the ζ-potential.

By the same token, an increase in the Ce^{3+} surface concentration leads to a decrease of the ζ-potential.
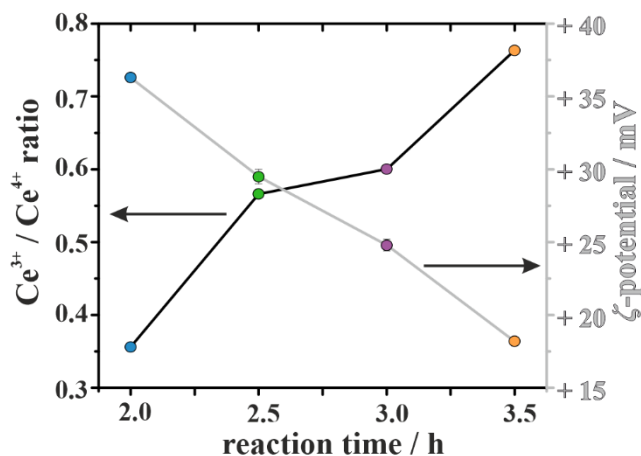
Figure 4-7. Effect of reaction time on the Ce^{3+}/Ce^{4+} ratio and ζ-potential.

With increasing reaction time, the ζ-potential decreases linearly from +36 mV to +18 mV. This simple variation of the zeta potential allows engineering of CeO_{2-x} mesoparticles for a given reaction. Previous methods adjusted the ζ-potential of ceria nanoparticles by (i) adding fluoride anions or (ii) substituting tetravalent Ce^{4+} by trivalent cations such as Bi^{3+}. Fluoride ions bind to surface Ce^{4+} sites, which turns the particle surface negative. This accelerates oxidase-like reactions due to facilitated electron transfer to the model substrate 3,3′,5,5′-tetramethylbenzidine (TMB).[37]

By replacing the cerium with bismuth, on the other hand, the S_{BET} can be selectively altered because Bi^{3+} has a larger ionic radius than Ce^{4+} and is mainly located at the particle surface. Thus, this type of surface engineering leads to an increase in the ζ-potential, which in turn increases the rate of the haloperoxidase-like reaction.[33] However, affecting the zeta potential only by reaction time is much simpler than these the other methods, making it a powerful tool for tailoring the ζ-potential for specific catalytic reactions.

Effect of reaction time or ζ-potential on catalytic activity

The effect of reaction time (2.0 h-3.0 h), or ζ-potential, on catalytic activity was examined with two enzyme-like reactions: (i) Peroxidase-like activity using the model substrate 3,3′,5,5′-tetramethylbenzidine (TMB)[71] and (ii) haloperoxidase-like activity using the model substrate phenolsulfonphthalein (phenol red, PR). CeO_2-3.5 h was not considered because a second phase was formed in addition to CeO_2, which could bias the results of a systematic comparison.
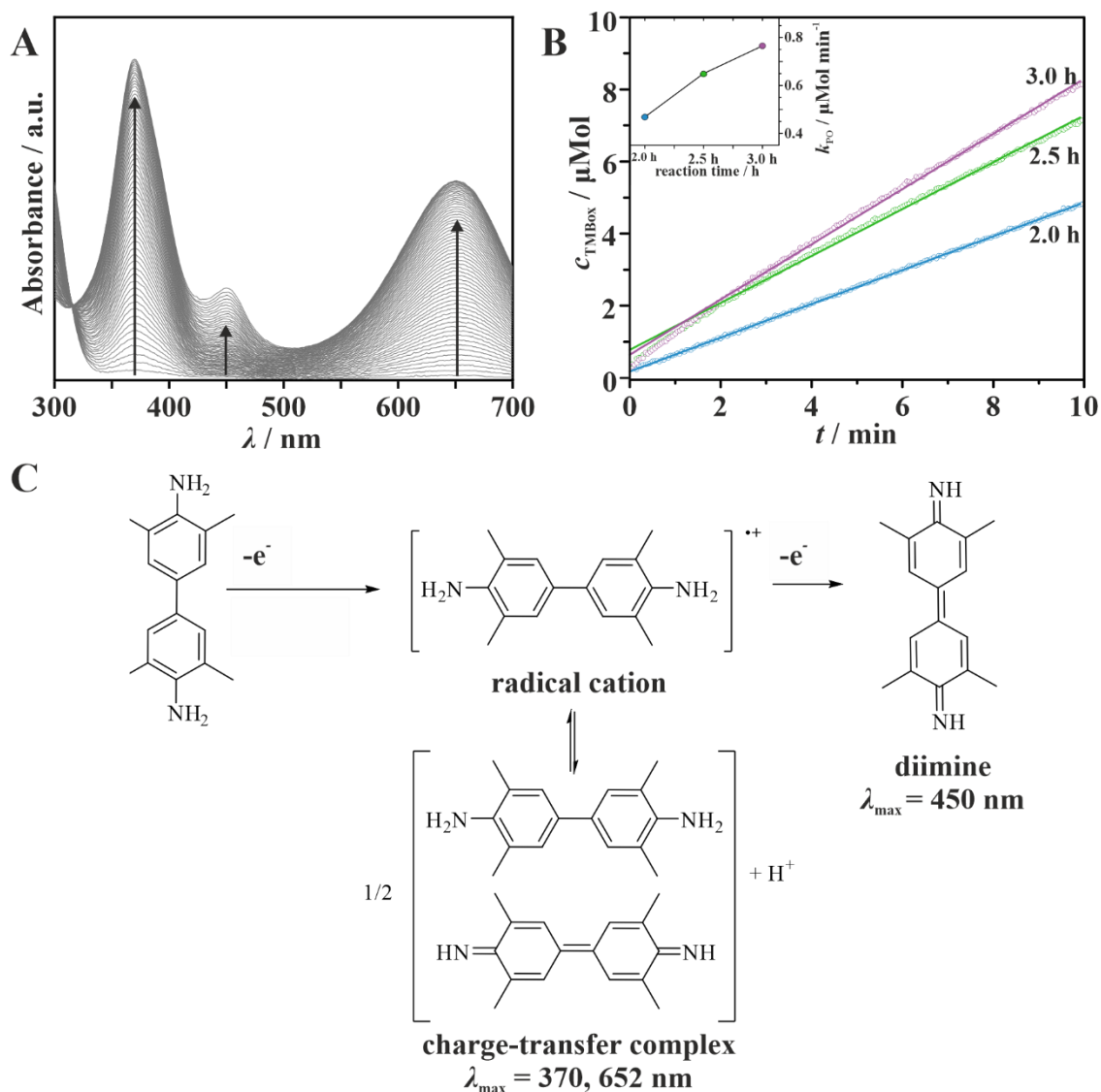
Figure 4-8. TMB-Assay showing the PO-like activity of CeO_{2-x} particles. (A) Time-dependent UV/Vis spectra. Absorption changes are due to oxidation of TMB to TMB_{ox} (B) TMB_{ox} formed over a period of 10 min. Inset: Reaction rates k_{PO} of mesoporous CeO_{2-x} nanoparticles synthesized at different reaction times. (C) Scheme of PO- catalyzed TMB oxidation.

Figure 4-8A shows the time dependent UV/Vis spectra of the TMB oxidation with increasing intensities of the absorption bands at 370 nm and 652 nm. These bands originate

from the TMB oxidation product by charge-transfer.[72] Complete two-electron oxidation resulted in a yellow diimine oxidation product with an absorption maximum at 450 nm, which explains the increasing intensity of the absorbance at this wavelength.[72] TMB reaction pathways are illustrated in Figure 4-8C. The absorbance change at 652 nm was detected over a period of 10 minutes for all four samples. Figure 4-8B shows the effect of reaction time (i.e., ζ-potential) on the peroxidase activity. The formation of the charge-transfer complex using the CeO_2-3.0 h nanoparticles is significantly faster compared to CeO_2-2.0 h nanoparticles. The reaction rates derived from the TMB assay are shown in the inset of Figure 4-8B.
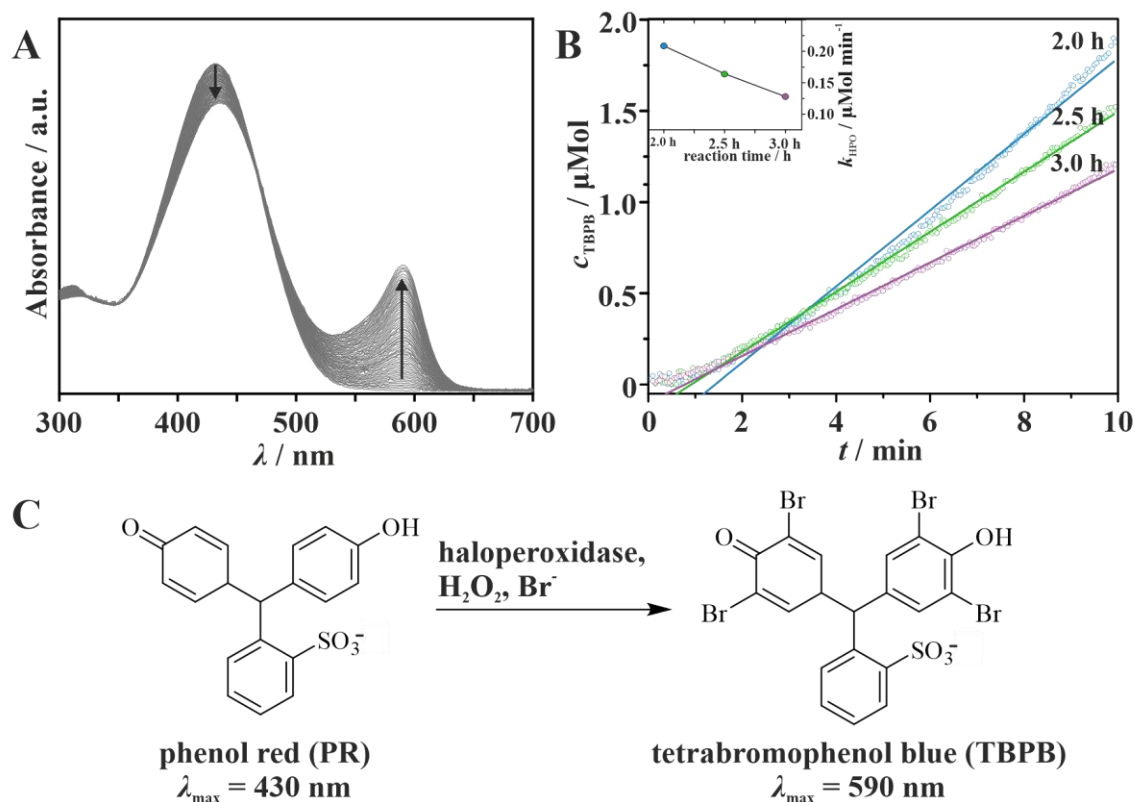
Figure 4-9. Phenol red-Assay showing haloperoxidase-like activity of $CeO_{2\text{-}x}$ particles (A) Time-dependent UV/Vis spectra showing absorption changes displaying oxidative bromination of phenol red (λ_{max}(PR)=430 nm) to bromophenol blue (λ_{max}(TBPB)=590 nm) with $CeO_{2\text{-}x}$. (B) Formed TBPB over a period of 10 min. Inset: Reaction velocities k_{HPO} of mesoporous $CeO_{2\text{-}x}$ nanoparticles synthesized at different reaction times. (C) Scheme of haloperoxidase catalyzed oxidative phenol red bromination.

Figure 4-9A shows the time-dependent UV/Vis spectra for the oxidative bromination of PR using mesoporous $CeO_{2\text{-}x}$ as halogenation catalyst. During the reaction the absorbance at 430 nm decreases due to the bromination of PR to tetrabromophenol blue (TBPB). The reaction equation for the bromination is shown in Figure 4-9C. The formation of TBPB was

monitored at 590 nm for all mesoporous CeO_{2-x} particles (Figure 4-9B).[22] The reaction rates for oxidative bromination now show exactly the opposite trend, i.e., the reaction proceeds fastest with CeO_2-2.0 h (inset, Figure 4-9B).

Surface properties are assumed to be of substantial importance for catalytic activity, because the composition of all nanoparticles is the same (cerianite; Figure 4-1E). Reaction velocities of all nanoparticles in oxidation and oxidative bromination are shown in Table 4-3.

Table 4-3. Reaction rates k_{PO} and k_{HPO} for mesoporous CeO_{2-x} nanoparticles synthesized at different reaction times.

sample	k_{PO} / µMol min^{-1}	k_{HPO} / µMol min^{-1}
CeO$_2$-2.0 h	0.4685 ± 0.0006	0.2086 ± 0.0015
CeO$_2$-2.5 h	0.6500 ± 0.0021	0.1645 ± 0.0007
CeO$_2$-3.0 h	0.7655 ± 0.0019	0.1279 ± 0.0005

The insets of Figure 4-8B and Figure 4-9B demonstrate the contrary impact of reaction time on the catalytic rates of mesoporous CeO_{2-x}. The insets in Figure 8B and Figure 9B show the opposed effect of reaction time or ζ-potential on the reaction rates for mesoporous CeO_{2-x}. Both, surface area and ζ-potential play a crucial role for the activity of mesoporous CeO_{2-x}. A comparison of the rates of peroxidase- and haloperoxidase-like reactions reveals which factor is of higher weight. To this end, the reaction rates were normalized to the S_{BET} or ζ-potential, with the highest value set to 100%. Figure 4-10A shows the reaction rates normalized to the ζ-potential. The normalized reaction rate of the peroxidase-like reaction (PO) still increases by about 60% during the reaction. This shows that the ζ-potential cannot be a rate-determining factor. However, for the haloperoxidase-like reaction, the ζ-potential plays a crucial role. The normalized reaction rates differ only by about 10%. In contrast, the reaction rates normalized to S_{BET} show a different trend.
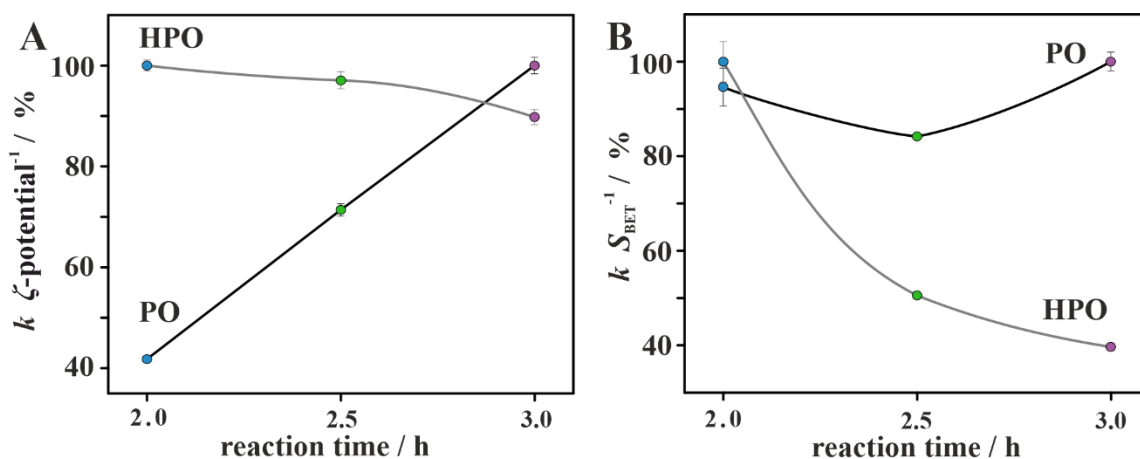
Figure 4-10. Reaction rates of peroxidase and haloperoxidase-like of mesoporous CeO_{2-x} nanoparticles normalized to (A) ζ-potential and (B) S_{BET}. The highest reaction rate was set to 100%.

Here, S_{BET} does not have a significant effect on the rate of the HPO reaction, but it does on that of the PO reaction. After normalization, the reaction rates of the HPO reaction still differ by about 60 %. This indicates that S_{BET} is not the rate-determining factor. In PO-like reactions, where TMB is oxidized by H_2O_2, no ionic substrates are involved in the reaction. Therefore, the surface charge is only of minor importance, the active surface area S_{BET} dictates the catalytic activity much more than the ζ-potential. For the same surface area, the nanoparticles with the lowest zeta potential would show the highest catalytic activity because the negative ζ-potential facilitates electron transfer to the TMB substrate.[37]

In contrast, electrostatic interactions are significant in the haloperoxidase-like reaction, a special type of peroxidase reaction, where a halide is transferred to a substrate *via* oxidative bromination. Here, a high ζ-potential and high Ce^{4+}/Ce^{3+} ratio is required to ensure the binding of the halide to the catalyst surface. The higher the potential, the bigger the attraction forces become. Since the potential has a decisive influence in this case, it is more important than S_{BET} for the catalytic activity. Consequently, in the HPO reaction the S_{BET} can be neglected if the nanoparticles have varying ζ-potential. A positive ζ-potential is of particular importance in this case to favor the reaction of the negative substrate bromide by electrostatic attraction forces. On the contrary, S_{BET} is of greater importance in the peroxidase reaction, where the reaction does not rely on electrostatic interactions.

4.4. CONCLUSION

In summary, mesoporous nanoparticles with different surface properties can be prepared easily by varying the reaction time of a hydrothermal synthesis. In this way, the catalytic properties of CeO_{2-x} nanoparticles could be tailored for different reactions. The chemical activity of CeO_{2-x} nanoparticles in haloperoxidase- and peroxidase-like reactions scales with the surface properties, S_{BET}, ζ-potential, and Ce^{3+}/Ce^{4+} ratio. As the reaction time increases, not only the S_{BET} of the mesoporous CeO_2 nanoparticles changes, but also the Ce^{3+}/Ce^{4+} ratio, which in turn correlates with the ζ-potential.

By comparing the reaction rates of haloperoxidase- and peroxidase-like reactions, the relevant factors for catalysis were determined. Crucial for haloperoxidase-like reactions is the ζ-potential, since a negatively charged halide anion and uncharged H_2O_2 must be adsorbed onto the CeO_{2-x} surface in the catalytic step The adsorption of the halide is favored by a high (positive) ζ-potential. In contrast, the peroxidase-like reaction, in which no charged substrates are adsorbed, is hardly affected by the ζ-potential. Here, the S_{BET} and Ce^{3+}/Ce^{4+} ratio must be increased to provide an effective catalyst for the reaction. Our studies provide new insights into the formation mechanisms, surface properties, and enzyme-like activity of mesoporous CeO_{2-x}.

The straightforward adjustment of the surface properties of mesoporous ceria only by varying the reaction time makes the synthesis a powerful tool for preparing catalytic materials to meet individual needs. Given the increasing interest in the use of ceria as "nanozymes", our results may provide guidance for expanding the scope of CeO_{2-x}-catalyzed reactions.

4.5. EXPERIMENTAL SECTION

MATERIAL AND SYNTHESIS

Chemicals

Cerium nitrate hexahydrate (99.5%, CAS: 10294-41-4) and calcium acetate (CAS: 114460-21-8) were purchased from Alfa Aesar. Hydrogen peroxide (hydrogen peroxide 35% pure, stabilized (34-36-% / CAS: 7722-84-1) as well as ethylene glycol ($\geq$99%, CAS: 107-21-1) were purchased from Roth, phenol red (CAS: 143-74-8) and 3,3′,5,5′-tetramethylbenzidine (TMB, $\geq$99%, CAS: 54827-17-7) from Sigma-Aldrich, acetic acid glacial (HAc: 99.5%, CAS: 64-19-7) from VWR and potassium bromide (99+%, CAS: 7758-02-3) from Acros Organics.

Synthesis of mesoporous CeO$_{2-x}$ nanoparticles. Mesoporous CeO$_{2-x}$ nanoparticles were synthesized hydrothermally with some important variations of a reported method.[59] To this end, 1 g of Ce(NO$_3$)$_3$ $\times$ 6 H$_2$O (2.3 mmol) was transferred into a Teflon inlay and dissolved in 2 mL of a 1:1 mixture of water and acetic acid with stirring. 30 mL of ethylene glycol was added and stirred for another 5 min. The Teflon inlay was transferred to a metal autoclave and heated to 180 °C. After the reaction, the hot autoclaves were removed from the oven and cooled radiatively. The cooled solutions were centrifuged at 9000 rpm for 20 min, the nanoparticle precipitate was washed three times with MQ water and dried in vacuum at 40 °C.

Kinetic measurements

Haloperoxidase-like reaction employing the phenol red assay. The phenol red assay was used to analyze the haloperoxidase like activity of CeO$_{2-x}$ nanoparticles. For this purpose, the oxidative bromination of yellow phenol red (PR) to purple tetrabromophenol blue (TBPB) was observed spectrophotometrically on a Cary 3500 UV/Vis spectrometer from Agilent. The reaction mixture consisted of an aqueous (Milli-Q water, 18.2 MΩ cm^{-1}) dispersion of CeO$_{2-x}$ nanoparticles (25 μg mL^{-1}), H$_2$O$_2$ (300 μM), PR (50 μM) and KBr (25 mM). Before H$_2$O$_2$ addition, the mixture was transferred to a quartz cuvette and stirred for 1 min. The change in absorbance was measured over a period of 10 min. The concentration of TBPB was calculated from the extinction coefficient of 32740 L·mol^{-1}cm^{-1}, which was calculated *via* Lambert-Beers law determined by UV/Vis measurements of different TBPB concentrations.

Peroxidase-like reaction using the TMB assay. The peroxidase-like catalytic activity was determined spectrophotometrically by measuring the formation of the charge-transfer complex of partially oxidized TMB_{ox} at $\lambda = 652$ nm on a Cary 3500 UV/VIS spectrometer. The reaction mixture consisted of a 0.2 M calcium acetate buffered (pH = 4) dispersion of CeO_{2-x} nanoparticles (108 μg mL^{-1}), H_2O_2 (0.97 mM) and TMB (0.11 mM). Before H_2O_2 addition, the mixture was transferred to a quartz cuvette and stirred for 1 min. The absorbance change at $\lambda = 652$ nm was measured over a period of 10 min. The concentration of TMB_{ox} was calculated from the extinction coefficient of 39.000 $L \cdot mol^{-1} cm^{-1}$, which was determined as reported previously.[72]

CHARACTERIZATION

Transmission electron microscopy. For transmission electron microscopy, a FEI Tecnai 12 TWIN with LaB_6 source, at 120 kV was used together with a Gatan US1000 CCD camera (16-bit, 2048 x 2048 pixels) and Gatan Digital Micrograph software. Samples were prepared by dropping a diluted nanoparticle dispersion (1 mg/mL) in water onto a carbon coated copper grid.

Powder X-ray diffraction X-ray diffraction patterns were recorded on a STOE Stadi P diffractometer with a Dectris Mythen 1k detector in transmission mode using Mo $K\alpha 1$ radiation. The crystalline phases were identified according to the PDF-2 database using Bruker AXS EVA 10.0 software.[73]

BET Surface Area. A 3P Micro 300 analyzer was used to determine specific surface area, pore volume and pore size. Nitrogen at 77.4 K was used as analysis gas. The data analysis was performed using the 3P Surface Area & Pore Size Analyzer System 10.03.02 software.

Small-angle X-ray scattering/ wide-angle X-ray scattering. SAXS/WAXS measurements were conducted using a methodology optimization for ultrafine structure exploration (MOUSE) instrument.[74] The X-rays were generated from a monochromatized X-ray tube with Cu $K\alpha$ ($\lambda = 0.154$ nm) radiation. Data collection was performed using an in-vacuum Eiger 1M detector (Dectris, Switzerland), which was placed at multiple distances between 122 and 2507 mm from the sample. Samples and backgrounds were measured in flow-through capillaries. The resulting data have been processed and scaled to absolute intensity using the DAWN software package according to the standardized procedures considering the propagation of errors.[75,76] The analysis of the SAXS data was performed using Monte Carlo simulations with McSAS, a method for the extraction of form-free size distributions.[77]

X-ray photoelectron spectroscopy. An Axis Ultra DLD imaging photoelectron spectrometer was used for X-ray photoelectron spectroscopy measurements. Survey spectra were measured with 80 eV pass energy of the analyzer, whereas for elemental spectra 20 eV were used. All measurements were carried out using the hybrid mode with 10 mA and 15 kV at the Al anode. The analysis area had a size of 700 μm × 300 μm. Resulting data was processed using CasaXPS and plotted with Origin 8.1. All spectra were corrected with respect to the binding energy of aliphatic carbon C 1s at 284.8 eV.

Zeta potential measurements. The ζ-potentials were measured in disposable capillary cells (DTS1070) on a Malvern Zetasizer Nano. Nanoparticle dispersions with concentrations of 0.5 mg/mL were used. The analysis was performed using Malvern Zetasizer software 8.01.4906.

Scanning electron microscopy. A FEI Nova NanoSEM 630 was used to obtain SEM images. The samples were prepared by dropping a diluted nanoparticle dispersion (1 mg/mL) in water onto a silicon wafer, which was attached to an aluminum holder using carbon film pads.

4.6.   REFERENCES

1   Wu, Z.; Overbury, S. H. Catalysis by Materials with Well-Defined Structures, 1st ed; Elsevier, 2015.

2   Montini T., Melchionna M., Monai M., Fornasiero P., Fundamentals and Catalytic Applications of CeO2-Based Materials. Chem. Rev. **2016**, *116*(10), 5987–6041.

3   Ziemba, M.; Schilling, C.; Ganduglia-Pirovano, M. V.; Hess, C. Toward an Atomic-Level Understanding of Ceria-Based Catalysts: When Experiment and Theory Go Hand in Hand. *Acc. Chem. Res.* **2021**, *54* (13), 2884–2893.

4   Primo, A.; Marino, T.; Corma, A.; Molinari, R.; García, H. Efficient Visible-Light Photocatalytic Water Splitting by Minute Amounts of Gold Supported on Nanoparticulate CeO2 Obtained by a Biopolymer Templating Method. *J. Am. Chem. Soc.* **2011**, *133* (18), 6930–6933.

5   Corma, A.; Atienzar, P.; García, H.; Chane-Ching, J. Y. Hierarchically Mesostructured Doped CeO2 with Potential for Solar-Cell Use. *Nat. Mater.* **2004**, *3* (6), 394–397.

6   Lu, X.; Zheng, D.; Zhang, P.; Liang, C.; Liu, P.; Tong, Y. Facile Synthesis of Free-Standing CeO2 Nanorods for Photoelectrochemical Applications. *Chem. Commun.* **2010**, *46* (41), 7721–7723.

7   Hao, Y.; Yang, C. K.; Haile, S. M. Ceria-Zirconia Solid Solutions (Ce1-XZrxO2-δ, x ≤ 0.2) for Solar Thermochemical Water Splitting: A Thermodynamic Study. *Chem. Mater.* **2014**, *26* (20), 6073–6082.

8   Cheng, C.; Chen, F.; Yi, H.; Lai, G. CeO2 Mesoporous Microspheres for High Performance Supercapacitors and Lithium-Ion Batteries. *J. Energy Storage* **2021**, *35*, 102305.

9   Steele, B. C. H.; Heinzel, A. Materials for Fuel-Cell Technologies. *Nature* **2001**, *414* (6861), 345–352.

10   Melchionna M., Fornasiero P., The role of ceria-based nanostructured materials in energy applications. *Mater. Today* **2014**, *17*(7), 349–357.

11   Sun, C.; Li, H.; Chen, L. Nanostructured Ceria-Based Materials: Synthesis, Properties, and Applications. *Energy Environ. Sci.* **2012**, *5* (9), 8475–8505.

12   Schmitt, R.; Nenning, A.; Kraynis, O.; Korobko, R.; Frenkel, A. I.; Lubomirsky, I.; Haile, S. M.; Rupp, J. L. M. A Review of Defect Structure and Chemistry in Ceria and Its Solid Solutions. *Chem. Soc. Rev.* **2020**, *49* (2), 554–592.

13   Heckert, E. G.; Seal, S.; Self, W. T. Fenton-like Reaction Catalyzed by the Rare Earth Inner Transition Metal Cerium. *Environ. Sci. Technol.* **2008**, *42* (13), 5014–5019.

14   Weiss, J. The Catalytic Decomposition of Hydrogen Peroxide on Different Metals. *Trans. Faraday Soc.* **1935**, *31* (0), 1547–1557.

15   Roy, C. B. Catalytic Decomposition of Hydrogen Peroxide on Some Oxide Catalysts. *J. Catal.* **1968**, *12* (2), 129–133.

16   Korsvik, C.; Patil, S.; Seal, S.; Self, W. T. Superoxide Dismutase Mimetic Properties Exhibited by Vacancy Engineered Ceria Nanoparticles. *Chem. Commun.* **2007**, *0* (10), 1056.

17   Pirmohamed, T.; Dowding, J. M.; Singh, S.; Wasserman, B.; Heckert, E.; Karakoti, A. S.; King, J. E. S.; Seal, S.; Self, W. T. Nanoceria Exhibit Redox State-Dependent Catalase Mimetic Activity. *Chem. Commun.* **2010**, *46* (16), 2736–2738.

18   Kim, C. K.; Kim, T.; Choi, I. Y.; Soh, M.; Kim, D.; Kim, Y. J.; Jang, H.; Yang, H. S.; Kim, J. Y.; Park, H. K.; Park, S. P.; Park, S.; Yu, T.; Yoon, B. W.; Lee, S. H.; Hyeon, T. Ceria Nanoparticles That Can Protect against Ischemic Stroke. *Angew. Chem. Int. Ed.* **2012**, *51* (44), 11039–11043.

19   Filippi, A.; Liu, F.; Wilson, J.; Lelieveld, S.; Korschelt, K.; Wang, T.; Wang, Y.; Reich, T.; Pöschl, U.; Tremel, W.; Tong, H. Antioxidant Activity of Cerium Dioxide Nanoparticles and Nanorods in Scavenging Hydroxyl Radicals. *RSC Adv.* **2019**, *9* (20), 11077–11081.

20   Hu, M.; Korschelt, K.; Viel, M.; Wiesmann, N.; Kappl, M.; Brieger, J.; Landfester, K.; Thérien-Aubin, H.; Tremel, W. Nanozymes in Nanofibrous Mats with Haloperoxidase-like Activity to Combat Biofouling. *ACS Appl. Mater. Interfaces* **2018**, *10* (51), 44722–44730.

21   Naha, P. C.; Hsu, J. C.; Kim, J.; Shah, S.; Bouché, M.; Si-Mohamed, S.; Rosario-Berrios, D. N.; Douek, P.; Hajfathalian, M.; Yasini, P.; Singh, S.; Rosen, M. A.; Morgan, M. A.; Cormode, D. P. Dextran-Coated Cerium Oxide Nanoparticles: A Computed Tomography Contrast Agent for Imaging the Gastrointestinal Tract and Inflammatory Bowel Disease. *ACS Nano* **2020**, *14* (8), 10187–10197.

22   Herget, K.; Hubach, P.; Pusch, S.; Deglmann, P.; Götz, H.; Gorelik, T. E.; Gural'skiy, I. A.; Pfitzner, F.; Link, T.; Schenk, S.; Panthöfer, M.; Ksenofontov, V.; Kolb, U.; Opatz, T.; André, R.; Tremel, W. Haloperoxidase Mimicry by CeO 2− x Nanorods Combats Biofouling. *Adv. Mater.* **2017**, *29* (4), 1603823.

23   Herget, K.; Frerichs, H.; Pfitzner, F.; Tahir, M. N.; Tremel, W. Functional Enzyme Mimics for Oxidative Halogenation Reactions That Combat Biofilm Formation. *Adv. Mater.* **2018**, *30* (36), 1707073.

24   Butler A., Sandy M., M. Mechanistic considerations of halogenating enzymes. *Nature* **460**, 848-854 (2009).

25   Wever, R.; Van Der Horst, M. A. The Role of Vanadium Haloperoxidases in the Formation of Volatile Brominated Compounds and Their Impact on the Environment. *Dalton Trans.* **2013**, *42* (33), 11778–11786.

26   Weichold, V.; Milbredt, D.; Van Pée, K. H. Specific Enzymatic Halogenation— From the Discovery of Halogenated Enzymes to Their Applications In Vitro and In Vivo. *Angew. Chem. Int. Ed.* **2016**, *55* (22), 6374–6389.

27   Wever, R.; Tromp, M. G. M.; Krenn, B. E.; Marjani, A.; Van Tol, M. Brominating Activity of the Seaweed Ascophyllum Nodosum: Impact on the Biosphere. *Environ. Sci. Technol.* **2002**, *25* (3), 446–449.

28   Renirie, R.; Dewilde, A.; Pierlot, C.; Wever, R.; Hober, D.; Aubry, J. M. Bactericidal and Virucidal Activity of the Alkalophilic P395D/L241V/T343A Mutant of Vanadium Chloroperoxidase. *J. Appl. Microbiol.* **2008**, *105* (1), 264–270.

29   Borchardt, S. A.; Allain, E. J.; Michels, J. J.; Stearns, G. W.; Kelly, R. F.; McCoy, W. F. Reaction of Acylated Homoserine Lactone Bacterial Signaling Molecules with Oxidized Halogen Antimicrobials. *Appl. Environ. Microbiol.* **2001**, *67* (7), 3174–3179.

30   Waters C. M.,. Bassler B. M, Quorum sensing: cell-to-cell communication in bacteria*. Ann. Rev. Cell Dev. Biol.* **2005**, *21*, 319-346**.**

31   Flemming, H. C.; Wingender, J.; Szewzyk, U.; Steinberg, P.; Rice, S. A.; Kjelleberg, S. Biofilms: an emergent form of bacterial life*. Nat. Rev. Microbiol.* **2016**, *14*, 563-575

32   Stark, W. J.; Stark, W. J. Nanoparticles in Biological Systems. *Angew. Chem. Int. Ed.* **2011**, *50* (6), 1242–1258.

33   Frerichs, H.; Pütz, E.; Pfitzner, F.; Reich, T.; Gazanis, A.; Panthöfer, M.; Hartmann, J.; Jegel, O.; Heermann, R.; Tremel, W. Nanocomposite Antimicrobials Prevent Bacterial Growth through the Enzyme-like Activity of Bi-Doped Cerium Dioxide (Ce 1−x Bi x O 2−δ). *Nanoscale* **2020**, *12* (41), 21344–21358.

34   Hu, M.; Yang, W.; Tan, H.; Jin, L.; Zhang, L.; Kerns, P.; Dang, Y.; Dissanayake, S.; Schaefer, S.; Liu, B.; Zhu, Y.; Suib, S. L.; He, J. Template-Free Synthesis of Mesoporous and Crystalline Transition Metal Oxide Nanoplates with Abundant Surface Defects. *Matter* **2020**, *2* (5), 1244–1259.

35   Gu, D.; Schüth, F. Synthesis of Non-Siliceous Mesoporous Oxides. *Chem. Soc. Rev.* **2014**, *43* (1), 313-344.

36   Pearson, R. G. Hard and Soft Acids and Bases—the Evolution of a Chemical Concept. *Coord. Chem. Rev.* **1990**, *100* (C), 403–425.

37   Liu, B.; Huang, Z.; Liu, J. Boosting the Oxidase Mimicking Activity of Nanoceria by Fluoride Capping: Rivaling Protein Enzymes and Ultrasensitive F − Detection. *Nanoscale* **2016**, *8* (28), 13562–13567.

38   Korschelt, K.; Schwidetzky, R.; Pfitzner, F.; Strugatchi, J.; Schilling, C.; Von Der Au, M.; Kirchhoff, K.; Panthöfer, M.; Lieberwirth, I.; Tahir, M. N.; Hess, C.; Meermann, B.; Tremel, W. CeO2-: X Nanorods with Intrinsic Urease-like Activity. *Nanoscale* **2018**, *10* (27), 13074–13082.

39   Opitz, P.; Jegel, O.; Nasir, J.; Rios-Studer, T.; Gazanis, A.; Pham, D.-H.; Domke, K.; Heermann, R.; Schmedt auf der Günne, J.; Tremel, W. Defect-Controlled Halogenating Properties of Lanthanide-Doped Ceria Nanozymes. *Nanoscale* **2022**, accepted.

40   Hennig, C.; Ikeda-Ohno, A.; Kraus, W.; Weiss, S.; Pattison, P.; Emerich, H.; Abdala, P. M.; Scheinost, A. C. Crystal Structure and Solution Species of Ce(III) and Ce(IV) Formates: From Mononuclear to Hexanuclear Complexes. *Inorg. Chem.* **2013**, *52* (20), 11734–11743.

41   Livage, J.; Henry, M.; Sanchez, C. Sol-Gel Chemistry of Transition Metal Oxides. *Prog. Solid State Chem.* **1988**, *18* (4), 259–341.

42   Tyrsted, C.; Becker, J.; Hald, P.; Bremholm, M.; Pedersen, J. S.; Chevallier, J.; Cerenius, Y.; Iversen, S. B.; Iversen, B. B. In-Situ Synchrotron Radiation Study of Formation and Growth of Crystalline CexZr1−xO2 Nanoparticles Synthesized in Supercritical Water. *Chem. Mater.* **2010**, *22* (5), 1814–1820.

43   Tyrsted, C.; Ornsbjerg Jensen, K. M.; Bøjesen, E. D.; Lock, N.; Christensen, M.; Billinge, S. J. L.; Brummerstedt Iversen, B. Understanding the Formation and Evolution of Ceria Nanoparticles Under Hydrothermal Conditions. *Angew. Chem. Int. Ed.* **2012**, *51* (36), 9030–9033.

44   Slostowski, C.; Marre, S.; Babot, O.; Toupance, T.; Aymonier, C. Near- and Supercritical Alcohols as Solvents and Surface Modifiers for the Continuous Synthesis of Cerium Oxide Nanoparticles. *Langmuir* **2014**, *30*(48)*,* 5965−5972.

45   Wang, H.; Zhu, J. J.; Zhu, J. M.; Liao, X. H.; Xu, S.; Ding, T.; Chen, H. Y. Preparation of Nanocrystalline Ceria Particles by Sonochemical and Microwave Assisted Heating Methods. *Phys. Chem. Chem. Phys.* **2002**, *4* (15), 3794–3799.

46   De Faria, L. A.; Trasatti, S. The Point of Zero Charge of CeO2. *J. Colloid Interface Sci.* **1994**, *167* (2), 352–357.

47   Hirano, M.; Kato, E. Hydrothermal Synthesis of Nanocrystalline Cerium(IV) Oxide Powders. *J. Am. Ceram. Soc.* **1999**, *82* (3), 786–788.

48   Niederberger, M.; Garnweitner, G.; Pinna, N.; Neri, G. Non-Aqueous Routes to Crystalline Metal Oxide Nanoparticles: Formation Mechanisms and Applications. *Prog. Solid State Chem.* **2005**, *33* (2-4 SPEC. ISS.), 59–70.

49   Dunne, P. W.; Munn, A. S.; Starkey, C. L.; Huddle, T. A.; Lester, E. H. Continuous-Flow Hydrothermal Synthesis for the Production of Inorganic Nanomaterials. *Philosophical Transactions of the Royal Society A: Mathematical, Physical and Engineering Sciences*. The Royal Society Publishing December 28, 2015.

50   Stolzenburg, P.; Lorenz, T.; Dietzel, A.; Garnweitner, G. Microfluidic Synthesis of Metal Oxide Nanoparticles via the Nonaqueous Method. *Chem. Eng. Sci.* **2018**, *191*, 500–510.

51   Sarif, M.; Jegel, O.; Gazanis, A.; Hartmann, J.; Plana-Ruiz, S.; Hilgert, J.; Frerichs, H.; Viel, M.; Panthöfer, M.; Kolb, U.; Tahir, M. N.; Schemberg, J.; Kappl, M.;

Heermann, R.; Tremel, W. High-Throughput Synthesis of CeO2 Nanoparticles for Transparent Nanocomposites Repelling Pseudomonas Aeruginosa Biofilms. *Sci. Rep.* **2022**, accepted.

52   Hirano, M.; Kato, E. Hydrothermal Synthesis of Cerium(IV) Oxide. *J. Am. Ceram. Soc.* **1996**, *79* (3), 777–780.

53   Wang, Z. L.; Feng, X. Polyhedral Shapes of CeO2 Nanoparticles. *J. Phys. Chem. B* **2003**, *107* (49), 13563–13566.

54   Vantomme, A.; Yuan, Z. Y.; Du, G.; Su, B. L. Surfactant-Assisted Large-Scale Preparation of Crystalline CeO2 Nanorods. *Langmuir* **2004**, *21* (3), 1132–1135.

55   Mai, H. X.; Sun, L. D.; Zhang, Y. W.; Si, R.; Feng, W.; Zhang, H. P.; Liu, H. C.; Yan, C. H. Shape-Selective Synthesis and Oxygen Storage Behavior of Ceria Nanopolyhedra, Nanorods, and Nanocubes. *J. Phys. Chem. B* **2005**, *109* (51), 24380–24385.

56   Ho, C.; Yu, J. C.; Kwong, T.; Mak, A. C.; Lai, S. Morphology-Controllable Synthesis of Mesoporous CeO2 Nano- and Microstructures. *Chem. Mater.* **2005**, *17* (17), 4514–4522.

57   Tang, C.; Bando, Y.; Liu, B.; Golberg, D. Cerium Oxide Nanotubes Prepared from Cerium Hydroxide Nanotubes. *Adv. Mater.* **2005**, *17* (24), 3005–3009.

58   Ren, Y.; Ma, Z.; Bruce, P. G. Ordered Mesoporous Metal Oxides: Synthesis and Applications. *Chem. Soc. Rev.* **2012**, *41* (14), 4909–4927.

59   Liang, X.; Xiao, J.; Chen, B.; Li, Y. Catalytically Stable and Active CeO 2 Mesoporous Spheres. *Inorg. Chem.* **2010**, *49* (18), 8188–8190.

60   Libert, S.; Gorshkov, V.; Goia, D.; Matijević, E.; Privman, V. Model of Controlled Synthesis of Uniform Colloid Particles: Cadmium Sulfide. *Langmuir* **2003**, *19* (26), 10679–10683.

61   Ge, J.; Hu, Y.; Biasini, M.; Beyermann, W. P.; Yin, Y. Superparamagnetic Magnetite Colloidal Nanocrystal Clusters. *Angew. Chem. Int. Ed.* **2007**, *46* (23), 4342–4345.

62   Gondolini, A.; Mercadelli, E.; Sanson, A.; Albonetti, S.; Doubova, L.; Boldrini, S. Effects of the Microwave Heating on the Properties of Gadolinium-Doped Cerium Oxide Prepared by Polyol Method. *J. Eur. Ceram. Soc.* **2013**, *33* (1), 67–77.

63   Jiao, Y.; Wang, F.; Ma, X.; Tang, Q.; Wang, K.; Guo, Y.; Yang, L. Facile One-Step Synthesis of Porous Ceria Hollow Nanospheres for Low Temperature CO Oxidation. *Microporous Mesoporous Mater.* **2013**, *176*, 1–7.

64   Zhou, X.-D. Processing and Characterization of Nanocrystalline Ceria, University of Missouri-Rolla, 2001.

65   Zhou, X. D.; Huebner, W.; Anderson, H. U. Room-Temperature Homogeneous Nucleation Synthesis and Thermal Stability of Nanometer Single Crystal CeO2. *Appl. Phys. Lett.* **2002**, *80* (20), 3814–3816.

66   Soni, S.; Vats, V. S.; Kumar, S.; Dalela, B.; Mishra, M.; Meena, R. S.; Gupta, G.; Alvi, P. A.; Dalela, S. Structural, Optical and Magnetic Properties of Fe-Doped CeO2 Samples Probed Using X-Ray Photoelectron Spectroscopy. *J. Mater. Sci. Mater. Electron.* **2018**, *29* (12), 10141–10153.

67   Suresh, R.; Ponnuswamy, V.; Mariappan, R. Effect of Annealing Temperature on the Microstructural, Optical and Electrical Properties of CeO2 Nanoparticles by Chemical Precipitation Method. *Appl. Surf. Sci.* **2013**, *273*, 457–464.

68   Dupin, J.-C. C.; Gonbeau, D.; Vinatier, P.; Levasseur, A. Systematic XPS Studies of Metal Oxides, Hydroxides and Peroxides. *Phys. Chem. Chem. Phys.* **2000**, *2* (6), 1319–1324.

69   Agasti, N.; Astle, M. A.; Rance, G. A.; Alves Fernandes, J.; Dupont, J.; Khlobystov, A. N. Cerium Oxide Nanoparticles Inside Carbon Nanoreactors for Selective Allylic Oxidation of Cyclohexene. *Nano Lett.* **2020**, *20* (2), 1161–1171.

70   Sreeremya, T. S.; Thulasi, K. M.; Krishnan, A.; Ghosh, S. A Novel Aqueous Route to Fabricate Ultrasmall Monodisperse Lipophilic Cerium Oxide Nanoparticles. *Ind. Eng. Chem. Res.* **2012**, *51* (1), 318–326.

71   Marquez, L. A.; Dunford, H. B. Mechanism of the Oxidation of 3,5,3',5'-Tetramethylbenzidine by Myeloperoxidase Determined by Transient- and Steady-State Kinetics. *Biochemistry* **1997**, *36* (31), 9349–9355.

72   Josephy, P. D.; Eling, T.; Mason, R. P. The Horseradish Peroxidase-Catalyzed Oxidation of 3,5,3',5'-Tetramethylbenzidine. Free Radical and Charge-Transfer Complex Intermediates. *J. Biol. Chem.* **1982**, *257* (7), 3669–3675.

73   EVA 10.0 Rev. 1, Bruker AXS, Madison (WI) US (2003). https://www.bruker.com/en/products-and-solutions/diffractometers-and-scattering-systems/x-ray-diffractometers/diffrac-suite-software/diffrac-eva.html

74   Smales, G. J.; Pauw, B. R. The MOUSE Project: A Meticulous Approach for Obtaining Traceable, Wide-Range X-Ray Scattering Information. *J. Instrum.* **2021**, *16* (6), P06034.

75   Filik, J.; Ashton, A. W.; Chang, P. C. Y.; Chater, P. A.; Day, S. J.; Drakopoulos, M.; Gerring, M. W.; Hart, M. L.; Magdysyuk, O. V.; Michalik, S.; Smith, A.; Tang, C. C.; Terrill, N. J.; Wharmby, M. T.; Wilhelm, H. Processing Two-Dimensional X-Ray Diffraction and Small-Angle Scattering Data in DAWN 2. *J. Appl. Crystallogr.* **2017**, *50* (3), 959–966.

76   Pauw, B. R.; Smith, A. J.; Snow, T.; Terrill, N. J.; Thünemann, A. F. The Modular Small-Angle X-Ray Scattering Data Correction Sequence. *J. Appl. Crystallogr.* **2017**, *50* (6), 1800–1811.

77   Bressler, I.; Pauw, B. R.; Thünemann, A. F. McSAS: Software for the Retrieval of Model Parameter Distributions from Scattering Patterns. *J. Appl. Crystallogr.* **2015**, *48* (3), 962–969.

4.7. SUPPORTING INFORMATION
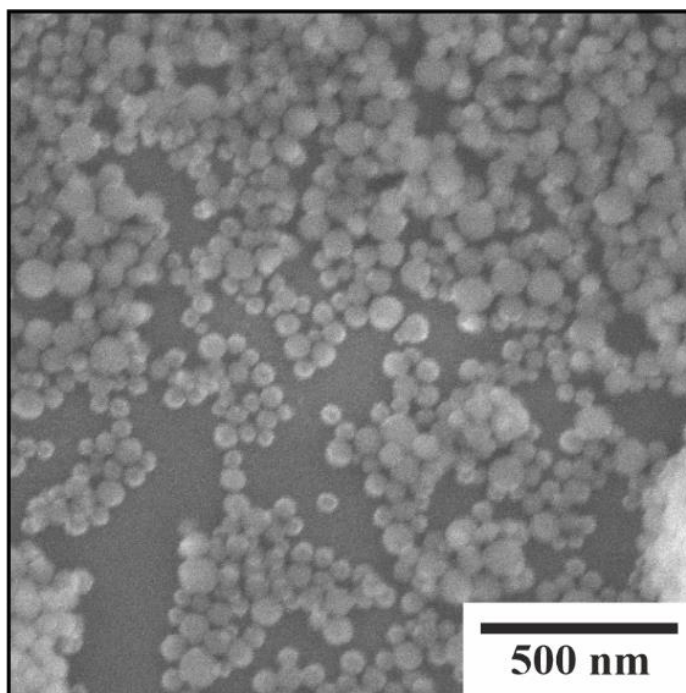
Figure S4-1. Scattering electron microscope (SEM) images of mesoporous CeO_2 nanoparticles formed after 2.0 h.
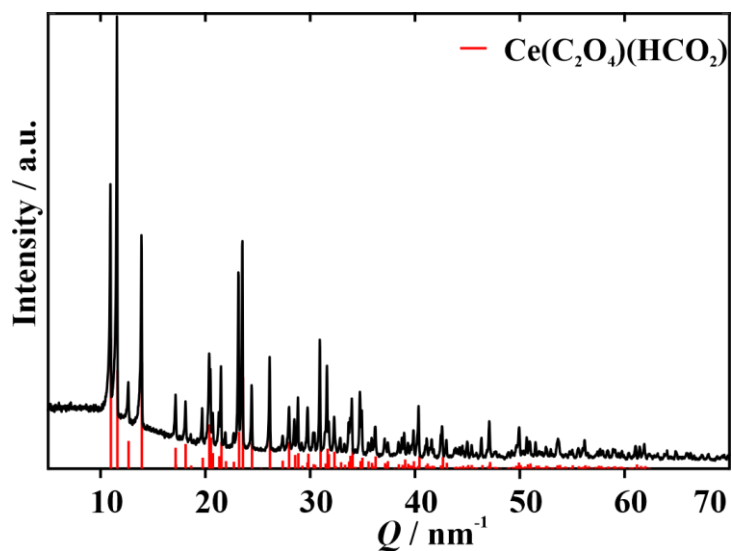
Figure S4-2. X-ray powder diffraction pattern of $Ce(C_2O_4)(HCO_2)$ formed after 120 h in a flask reaction. Red ticks indicate the calculated reflection positions for $Ce(C_2O_4)(HCO_2)$ based on structural data from the ICSD data bank (ICSD# 43450).
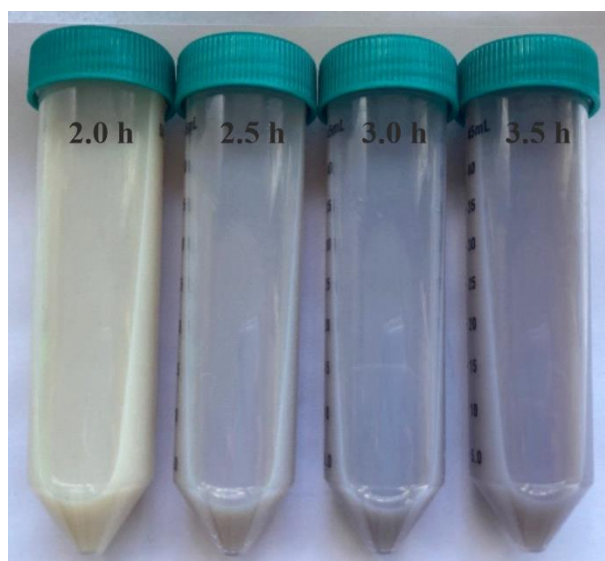
Figure S4-3. Image of the reaction solutions after 2.0 h, 2.5 h, 3.0 h and 3.5 h.
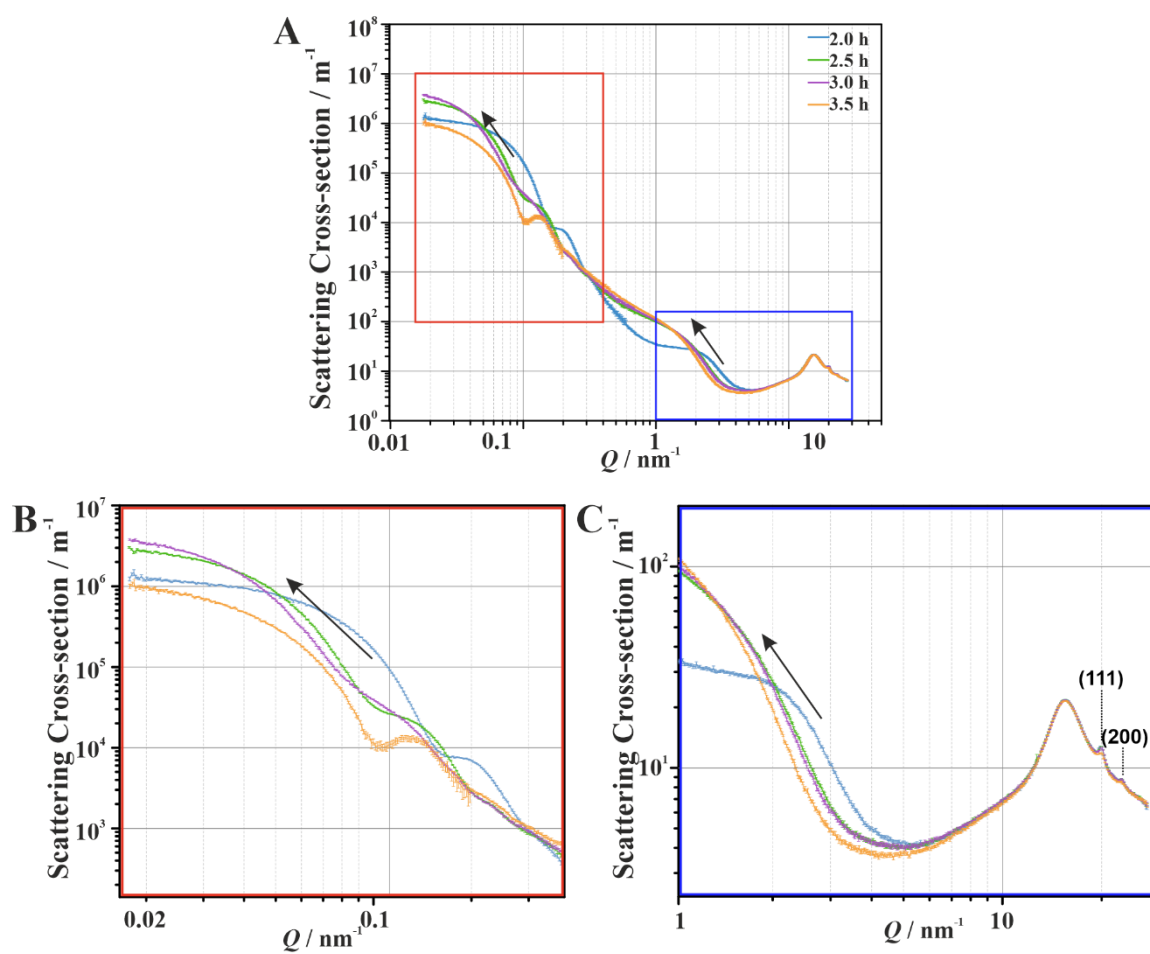
Figure S4-4. (A)SAXS measurements of mesoporous CeO_2 nanoparticles formed after 2.0 h (light blue), 2.5 h (green), 3.0 h (violet) and 3.5 h (orange) of reaction time with magnification at (B) lower Q values (red) and (C) higher Q values (dark blue).

5

BROAD-SPECTRUM BIOFILM INHIBITION DUE TO QUORUM QUENCHING INDUCED BY CeO$_2$ CONTAINING LACQUERS

5.1.   SUMMARY

In this chapter, the knowledge gained in chapters 3 and 4 was applied to prepare CeO$_2$ nanoparticles that best mimic the natural enzyme haloperoxidase and thus catalyze oxidative bromination reactions efficiently. These nanocrystals should be functionalized to allow a facile incorporation
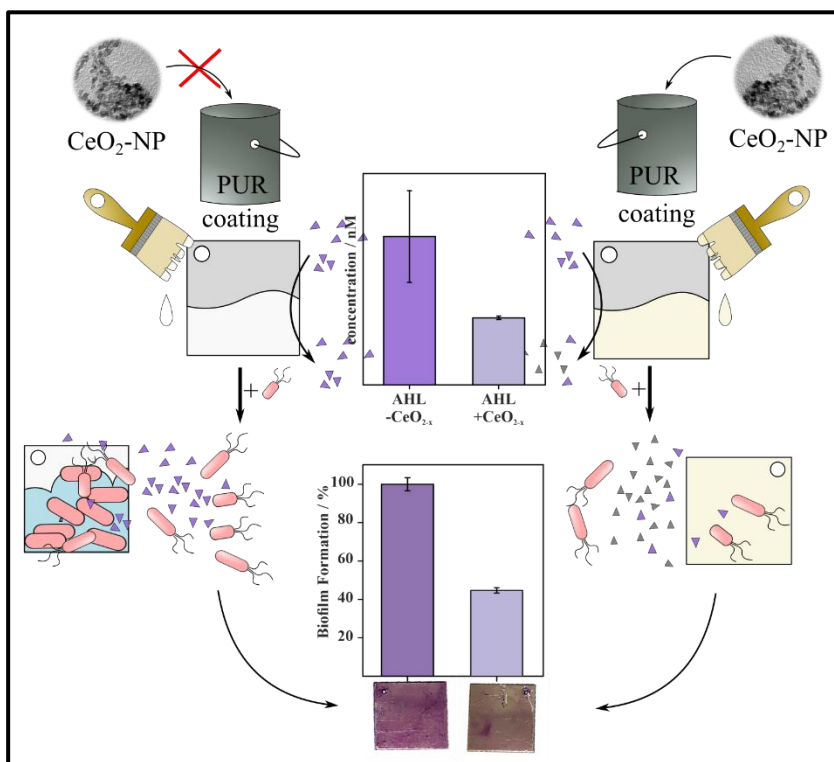
into oil-based coatings. To this end, catalytically highly active, monodisperse and non-agglomerated CeO$_2$ nanocrystals were synthesized at ultra-large scale (12 g/batch in 20 min) in n-butyl acetate by a new solvothermal approach. Previously, it was only known phenomenologically that CeO$_2$ exhibited antifouling activity. However, the explanation of the mode of action of this activity has been merely speculative. We provide here, for the first time, experimental results that, through separation and unambiguous analytical identification, allow identification of the bacterial response to CeO$_2$-catalyzed halogenation in the presence of a multitude of possible competing reactions in aquatic environments.

For this purpose, established bioassays as well as LC-MS methods were applied. Using a developed high-sensitive LC-MS/MS method and the reporter strain *Agrobacterium tumefaciens* A136, it was shown that the concentration of the signaling molecules 3-oxo-C_{12}-HSL and C_4-HSL in the supernatant of *Pseudomonas aeruginosa* decreased significantly in the presence of CeO_2 nanocrystals. Moreover, the bromide concentration in the supernatants decreased, indicating a consumption of bromide in favor of other brominated substrates. No brominated homoserine lactones (3-oxo-C_{12}-HSL and C_4-HSL) could be identified in the supernatants *via* LC-MS analysis, as they were degraded by the bacteria. The hypothesis of oxidative bromination using CeO_2 nanocatalysts was supported by the discovery of brominated 2-heptyl-1-hydroxyquinolin-4(1*H*)-one (HQNO) which is another molecule present in *Pseudomonas aeruginosa* and responsible for biofilm formation. These results support the hypothesis that CeO_2 exerts a quorum quenching effect on Gram-negative bacteria that disrupts their communication and resulting gene expression that controls, for example, biofilm formation and bacterial pathogenicity. CeO_2 nanocrystals embedded in the coatings still exhibit a high haloperoxidase-like activity, resulting in a successful biofilm inhibition by quorum quenching of up to ~60%, ~70%, ~80% and ~60% for *Klebsiella pneumoniae, Methylobacterium mesophilicum, Phaeobacter gallaeciensis* and *Pseudomonas aeruginosa*, respectively. Surfaces with antibacterial activity even without adding toxins or biocides represent a new innovative approach. Bactericidal behavior of CeO_2 was excluded, since the coating does not prevent a reversible attachment of individual bacteria, but only inhibits biofilm development by interfering with cell-cell communication.

Contributions:

Eva Pütz:	Concept development, nanoparticle synthesis, production of composite, plasma treatment, synthesis of homoserine lactone hydrobromide and N-α,α-dibromoacetyl homoserine lactones. TEM, ^{1}H-NMR measurement, ζ-potential and BET surface area measurement, UV/Vis kinetic measurements, data analysis, manuscript preparation, figure preparation.
XXX:	Concept development, biofilm inhibition testing and CLSM measurements, quorum quenching tests using *Agrobacterium tumefaciens A136*, data analysis, manuscript preparation, figure preparation.
XXX:	Concept development, LC-MS analysis with sample preparation, method development, mass spectra acquisition (data generation; methods application), data processing of measured data (suspect screening; "non-target analytics"), data analysis, manuscript preparation, figure preparation.
XXX:	Cell experiments with CLSM measurements.
XXX:	SEM/EDX measurements.
XXX:	Nanoparticle synthesis.
XXX:	Scientific supervision
XXX:	Scientific supervision
XXX:	Manuscript correction and scientific supervision.

5.2. INTRODUCTION

Colonization of surfaces in medical facilities, on work benches, household appliances, on packaging or contact surfaces such as railings, door handles, armatures, toys or electronic devices by microorganisms is an urging problem. Pathogenic microorganisms can lead to accidental infections, and they are a leading cause of death worldwide, killing 17 million people annually.[1] Due to the increasing antibiotic resistance of pathogens[2] there is a strong demand to explore innovative surface coatings with new antibacterial agents to combat the antimicrobial resistance of pathogens.[3] There are currently two main strategies to solve this problem. Considerable efforts are made to inactivate the pathogenic microorganisms or to kill them by application of antibiotics.[4,5] Silver nanocrystal-based systems are still the most popular platform for antibacterial agents[6], but the toxic effects[7,8] and low abundance are good reasons why there is a need for alternatives. The second strategy for controlling pathogenic infections is to prevent the settlement, growth, and colonization of microorganism on biorelevant surfaces, e.g., by surface modification with polymers[9–12] or by coating with photocatalysts (e.g., TiO_2 or SnO_2) which form reactive oxygen species (ROS) upon exposure to sunlight.[13] Since $^•OH$ or $^1O_2$ cannot be detoxified enzymatically these oxides and other photocatalysts act as efficient biocides.[14] Each of these methods has its advantages and limitations. Polymer coated surfaces suffer from mechanical weakness, poor substrate adhesion, non-uniform coating, or insufficient long-term stability. Shortcomings of antimicrobial coatings are leaching of toxins and low biocompatibility. A simple, sustainable, and inexpensive method to prepare durable surfaces, which repel a variety of microorganisms, has immediate relevance in many applications that suffer from the above issues.

Nature also uses biotoxins and antibiotics for "chemical warfare" to kill foreign organisms, or enzymes that convert viscous biogenic adhesives of the biofilm into wash-off solutions. Another strategy is to disturb "bacterial talk". Biofilm formation is regulated by cell-to-cell communication.[15,16] Biofilms develop when microorganisms form synergistic communities. To this end, bacteria have developed specific communication channels. Bacteria use small molecules for communication, which they release into their environment. As the number of cells increases, the concentration of these signaling molecules increases. Once the bacterial cell number or the concentration of signaling molecules reaches a threshold (a quorum), gene expression is switched on and phenotypes are formed that are important for biofilm formation. This process is called "quorum

sensing" (QS).[17,18] Under QS control are e.g., phenotypes that are crucial for a symbiotic, but also for a pathogenic way of bacterial life. In recent years, molecular mechanisms of bacterial communication have been unraveled, and even new bacterial "languages" and "dialects" have been discovered.[19] The first system described consisted of a regulator protein (LuxR) that detected an acyl homoserine lactone (AHL) produced by a cognate synthase (LuxI).[20] AHLs consist of a lactone ring modified with a fatty acid side chain.[20] The hydrophobic AHLs are membrane-permeable and thus accumulate in the environment of the cells. After reaching a threshold concentration, bacteria sense AHL *via* a receptor, LuxR, localized in the cytoplasm. After interaction with the AHL, LuxR receptors bind to specific regions of DNA, thereby activating or repressing the expression of downstream localized genes. A defense mechanism in nature against biofilm formation is to disrupt cell-to-cell communication of bacteria. This is done with haloperoxidases (HPOs), a group of enzymes that form oxidizing halonium species (HOX) as short-lived reactive intermediates in the presence of halides ($X^- = Cl^-$, Br^-, I^-) and H_2O_2 (formed in daylight at micromolar concentration). They can be used in the synthesis of halogenated organic compounds such as bromofuranone, which are known to disrupt QS, or brominated AHLs.[21–25] The halogenated AHL signaling compounds bind to their receptors, but they are physiologically ineffective. The resulting disruption of bacterial communication ("quorum quenching") prevents the formation of biofilms. Our approach to biofilm-inhibiting surfaces is inspired by nature. Nanozymes[26–28] are functional enzyme mimics, which can catalyze the oxidation of halides (Cl^- and Br^-) with hydrogen peroxide (H_2O_2) to hypohalous acids (HOCl and HOBr)[29]. Some metal complexes[30–32], V_2O_5[33] and CeO_2[34] or $Ce_{1-x}M_xO_{2-x/2}$ nanocrystals (NCs)[35] can mimic the catalytic activity of HPOs under ambient conditions. The advantage over conventional antifouling systems is that CeO_2 NCs act only as a catalyst. It is therefore not necessary to continuously release any biocides or synthetic signaling compounds. Although a promising bacteria repellent activity of the CeO_2 HPO mimetics has been demonstrated in classical antifouling tests with CeO_2-coated plates in river water, the mechanism of action of their antibacterial activity is still poorly understood. Studies of alternative systems have also yielded phenomenological results - some of them very startling - but the details are not at all clear.[36] Here we monitor the signaling molecules and the produced halogenated compounds which could induce the interruption of cell-cell communication and inhibit development of a *Pseudomonas aeruginosa* biofilm on samples coated with a lacquer containing embedded CeO_2 HPO mimics. The reactivity of CeO_2 NCs strongly depends on the particle diameter and the resulting surface area. In addition,

manufacturing transparent dispersions requires monodisperse and non-agglomerated NCs for next-generation applications. For these monodisperse NCs to be used, an economical mass-production method needs to be developed. In most syntheses reported so far, only sub-gram quantities of monodisperse NCs were produced. Here, we report on the ultra-large-scale synthesis of monodisperse NCs using inexpensive and non-toxic metal salts as starting compounds. We could synthesize as much as 12 g of monodisperse NCs in 20 minutes in a single batch, without a size-sorting process. By using liquid chromatography coupled with mass spectrometry (LC-MS) we are able to identify the formation of bacteria-specific signaling compounds and their reduction by CeO_2 NCs. The quorum quenching activity was demonstrated using the reporter strain *Agrobacterium tumefaciens* A136. In presence of CeO_2 NCs, AHL as well as bromide concentration decrease indicating a successful bromination of organic substrates.

However, no brominated AHLs could be detected because they are degraded by bacteria. Still, it was possible to identify a brominated 2-heptyl-4-hydroxyquinoline N-oxide (HQNO). HQNO is a substrate from the quinolone group which is known to increase biofilm formation and antibiotic resistance not only in *Pseudomonas aeruginosa* but also *Staphylococcus aureus* biofilms.[37] This analytical finding supports the hypothesis that the catalytic bromination of bacterial signaling molecules leads to a significant reduction in biofilm formation. This makes the CeO_2 nanocomposite an alternative "green" catalyst that offers high environmental benefits compared to biocidal or toxin-releasing substances.

5.3.   RESULTS AND DISCUSSION

Nanoparticle synthesis and characterization

Non-agglomerated CeO_2 nanocrystals (CeO_2 NCs) with large active surface area and diameters of less than one-tenth of the wavelength of visible light (< 20-30 nm) are required in thin film polymer systems to engineer the antimicrobial properties while maintaining visible transparency. Since *n*-butyl acetate is a standard solvent in oil-based coatings that impart color and texture to countless objects to enhance their appearance, NCs had to be soluble in *n*-butyl acetate. This could be achieved with an ultra-large-scale microwave-assisted solvothermal synthesis in *n*-butyl acetate using inexpensive and non-toxic metal salts as reactants. However, unlike in aqueous solution[38,39], the low dipole moment of *n*-butyl acetate prevented sufficient energy transfer between solvent and solute. This problem could be overcome by using HalSiC (recrystallized silicon carbide) heating rods. With the help of the heating rods, the autoclaves are heated uniformly, which enables good temperature control.(Figure S5-1) Compared to a classical solvothermal synthesis, the reaction times could be significantly reduced because the entire reaction volume is heated simultaneously.[40] If reaction is performed without HalSiC-R heating rods, only one microwave autoclave can be used because the microwave device stops the reaction if the temperatures in the autoclaves differ too much and the energy uptake is not sufficient. With HalSiC-R heating rods the reactions could be parallelized so that 12 reactions could be carried out simultaneously.
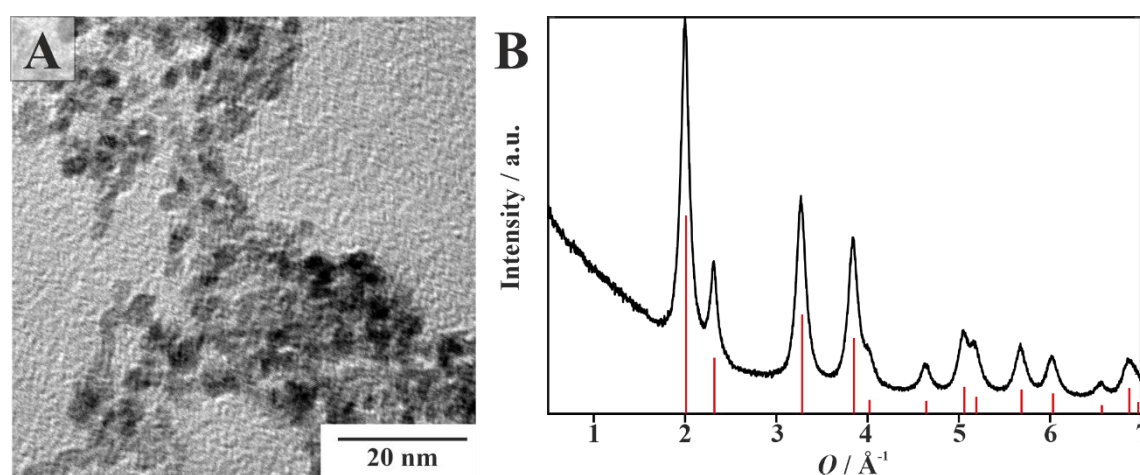
Figure 5-1. (A) TEM images of CeO_2 NCs and (B) X-ray powder diffraction pattern of a CeO_2 sample. Due to the small crystallite sizes in the nanometer range, the reflections are broadened. Red ticks indicate the calculated reflection positions for CeO_2 based on structural data from the ICSD data bank (ICSD# 88752).

This permitted the synthesis of uniform and non-agglomerated CeO$_2$ NCs in large yields (12 g/20 min) in a single batch without a size-sorting process and enabled the production of paint dispersions in large quantities. The CeO$_2$ NCs were phase-pure (cerianite structure, space group $Fm3m$) (Figure 5-1A) with an average diameter of 3.5 nm (Figure 5-1B, Figure S5-3A), confirmed by powder X-ray diffraction (PXRD) and transmission electron microscopy (TEM). They possess a large specific surface area (116 m$^2 \cdot$g^{-1}) and a high ζ-potential of +36 ±1 mV. Thermogravimetric analysis showed a content of about 10% organic compounds, i.e., the CeO$_2$ NCs contained n-butyl acetate as weakly bound capping ligand. Therefore, they could be dispersed easily in polyurethane-based coatings (2K-PUR), which is a basic requirement for smooth surfaces after painting. Solvothermal reactions in the absence of HalSiC-R heating rods yielded only CeO$_2$ microparticles (MP) with diameters of several hundred nanometers (as shown by PXRD and TEM in Figure S5-2A+B), and a specific surface area of 88 m$^2 \cdot$g^{-1}. These microparticles were not dispersible in n-butyl acetate.

Oxidative bromination catalysis

Virulence mechanism such as sporulation or biofilm formation can be blocked by quorum quenching, i.e., silencing bacteria by deactivating their signal molecules with specific enzymes (e.g., halogenation with HPOs or HPO mimics) or blocking their receptors (e.g. the AHL receptor) with antagonists.[41] Quorum quenching due to the intrinsic HPO activity of the CeO$_2$ NCs was demonstrated by the HPO (phenol red, PR) photometric assay.

In the PR assay the phenol sulfonphtalein (PR) is brominated in the presence of Br$^-$ anions and H$_2$O$_2$ to bromophenol blue (TBPB). The reaction can be monitored photometrically[42] thorough the change of the absorption bands of phenol red λ_{max}(PR) = 430 nm and bromophenol blue λ_{max}(TBPB) = 590 nm or by NMR spectroscopy.[35] Figure 5-2A shows the time dependent change in absorption during oxidative bromination of phenol red to bromophenol blue. By varying the H$_2$O$_2$ concentration, the constants K_m and v_{max} were determined from Michaelis-Menten kinetics using the Hill equation for CeO$_2$ NCs and MP (Figure 5-2B, Equation S5-1).
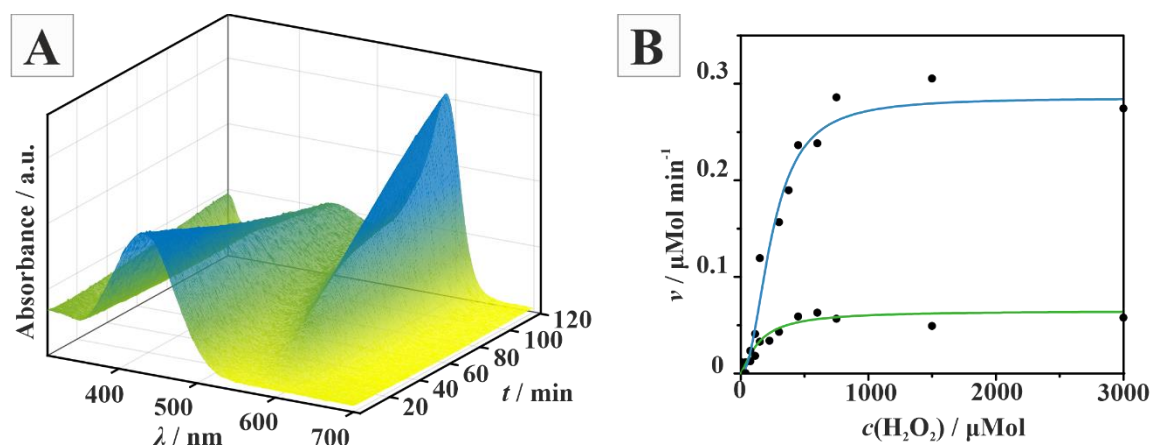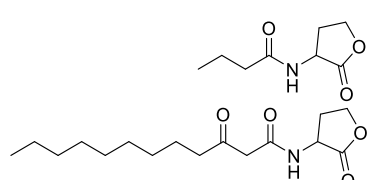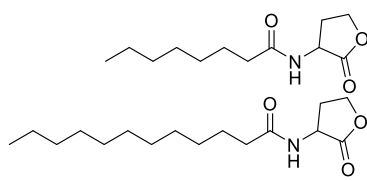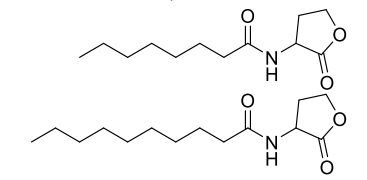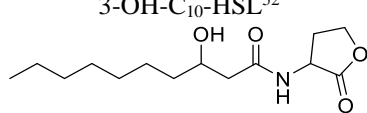
Figure 5-2. HPO-like activity of CeO$_2$ NCs using phenol red assay. (A) Time-dependent UV/Vis spectra showing absorption changes of λ_{max}(PR) = 430 nm and λ_{max}(TBPB) = 590 nm displaying the oxidative bromination of phenol red (PR) to tetrabromophenol blue (TBPB) with CeO$_2$ NC. (B) Michaelis-Menten kinetics with Hill-Fit of the CeO$_2$ NCs (blue) and MPs (green). The reaction rates for the CeO$_2$ NCs was significantly higher due to their larger BET surface area compared to CeO$_2$ MPs.

The catalytic activity of the CeO$_2$ NCs and MPs was quantified by determining the rates of reaction (*ROR*) from the maximum rates v_{max} and the active surface areas S_{BET} (Equation S5-2, Table S5-1). The results revealed an ~3.5-fold higher catalytic activity of CeO$_2$ NCs (*ROR*(CeO$_2$ NC) = 0.098 µmol m^{-2} min^{-1}) compared to CeO$_2$ MP (*ROR*(CeO$_2$ MP) = 0.029 µmol m^{-2} min^{-1}) due to the higher BET surface area of the CeO$_2$ NCs.

Biofilm inhibition of CeO₂ NCs

The biofilm inhibiting activity of the CeO$_2$ NCs was tested for the adherent bacteria *P. aeruginosa, Klebsiella pneumoniae, Methylobacterium mesophilicum, Phaeobacter gallaeciensis* and *Staphylococcus aureus*. Biofilms of these pathogens are protected by a slimy extracellular polymeric substance (EPS) and become more difficult to remove. Encapsulated in the biofilm, the bacteria exhibit greater resistance towards mechanic stress and antibiotic treatment.[43] 10-20% of infections in hospitals originate from *P. aeruginosa*, one of the most prominent water-associated infectious pathogens.[44,45] Infections with *K. pneumoniae* can cause serious diseases such as pneumonia, urinary tract infections, and pyogenic liver abscesses.[46]

Table 5-1. Signaling molecules produced by the bacterial strains *P. aeruginosa, K. pneumoniae, M. mesophilicum, P. gallaeciensis and S. aureus*.

Bacterial strain	Quorum sensing molecules
P. aeruginosa	3-oxo-C$_{12}$-HSL, C$_4$-HSL[49]
K. pneumoniae	C$_8$-HSL, C$_{12}$-HSL[50]
M. mesophilicum	C$_8$-HSL, C$_{10}$-HSL[51]
P. gallaeciensis	3-OH-C$_{10}$-HSL[52]

M. mesophilicum occurs in natural environments, i.e., on leaf surfaces or in soils. Pink colonies are formed when incubated in the laboratory. This opportunistic pathogen has been isolated frequently from tap water[47], where it can cause care-associated infections

especially in immunocompromised hosts.[48] The bacterium *P. gallaeciensis* is a marine species. Freshly submerged surfaces are mainly inhabited by these initial colonizers.[49,50] Both, Gram-positive and Gram-negative bacteria use quorum sensing mechanisms to regulate virulence or biofilm formation. Many Gram-negative bacteria communicate *via* AHLs, but each bacterial strain produces/recognizes different individual AHL molecules in its QS pathways. Table 5-1 provides an overview of the AHLs of all tested Gram-negative strains involved in corresponding QS-systems.

Biofilm formation for the Gram-negative (*P. aeruginosa, K. pneumonia, M. mesophilicum* and *P. gallaeciensis*) and AHL producing bacteria was clearly reduced in the presence of CeO_2 NCs, KBr and H_2O_2. Figure 5-3 displays the total biofilm formed in absence (left bar) and presence (right bar) of CeO_2 NC. Significant reductions of the biofilm formation ranging from 30% (*P. gallaeciensis*) to 58% (*P. aeruginosa*) were achieved indicating a broad spectrum of biofilm inhibition activity. Controls using either CeO_2 NCs, KBr or H_2O_2 alone showed no biofilm inhibitory effect. (Figure S5-4).
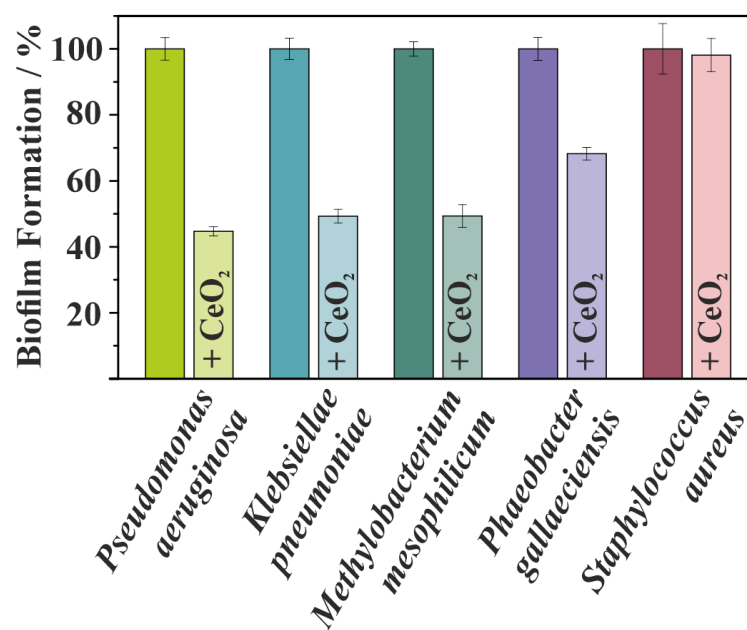
Figure 5-3. Quantification of the biofilm formation from different bacteria (*P. aeruginosa, K. pneumoniae, M. mesophilicum, P. gallaeciensis* and *S. aureus*) in the absence (left) an in the presence of CeO_2 NCs, KBr and H_2O_2 (right) *via* a crystal violet staining assay. Each experiment was performed in triplicate. Controls (left boxes) using only KBr and H_2O_2 showed no inhibitory effects.

The inhibitory effect on biofilm formation is proposed due to the oxidative halogenation process and an influence of the AHL system, which prevents them from being recognized by surrounding bacteria. As a result, biofilm formation, which is regulated by AHLs, cannot

proceed unhindered. Thus, CeO$_2$ NCs may suppress the group behavior of Gram-negative bacteria without killing them. In contrast, Gram-positive bacteria such as *S. aureus* use peptides as autoinducer.[55] Thus, Figure 5-3 shows no inhibition of biofilm formation of *S. aureus* in the presence of CeO$_2$ NCs. CeO$_2$ NCs show no toxic effects on the tested bacteria. In summary, this demonstrates that CeO$_2$ NCs show biofilm inhibition activity only for Gram-negative bacteria (AHL-based QS) and no activity for Gram-positive bacteria (peptide-based QS).

Quorum quenching activity

The quorum quenching activity can further be proved with the reporter strain *Agrobacterium tumefaciens* A136. Long-chain AHLs bind to the AHL-responsive transcription factor *TraR* (*pCF218*) of *A. tumefaciens* which expresses β-galactosidase (encoded by *lacZ*). To observe the quorum quenching activity CeO$_2$ NCs were mixed with 3-oxo-C$_{12}$-HSL, KBr and H$_2$O$_2$. After 8 h, 500 µL of the mixture was added to the biosensor strain solution with 5-bromo-4-chloro-3-indolyl-β-D-galactopyranoside (X-Gal).

For ortho-nitrophenyl-β-galactoside (ONPG) the procedure was described in material and methods. Both compounds consist of a galactose linked to a dye. The produced enzyme β-galactosidase initiates a bond cleavage of ONPG or X-Gal, which leads to the formation of *o*-nitrophenol and 5-bromo-4-chloro-3-hydroxyindole, which forms the blue dye 5,5-dibromo-4,4'-dichloroindogo after oxidation[56] as a result of enzyme-catalyzed hydrolysis. The dye concentrations are determined photometrically, which allows conclusions about the AHL concentration in solution. A 10 µM 3-oxo-C$_{12}$-HSL solution was used as positive control, and a solution with an equivalent concentration was treated with CeO$_2$ NCs, H$_2$O$_2$ and KBr. After 8 h, the 3-oxo-C$_{12}$-HSL solutions were added to the reporter strains and dye formation was analyzed. LB medium in case of X-Gal and Buffer Z in case of ONPG without 3-oxo-C$_{12}$-HSL was used as negative control. Figure 5-4A+C shows dye formation of the 3-oxo-C$_{12}$-HSL solution with and without prior treatment with CeO$_2$ NCs In X-Gal and ONPG, dye production decreases by up to 40%, caused by lower expression of *lacZ* due to lower 3-oxo-C$_{12}$-HSL concentration. The conversion to Miller Units was done according to Equation S5-3. Figure 5-4 shows that the Miller units decrease by 40% from 4600 to 2831. The biofilm inhibition from CeO$_2$ NCs could therefore be based of their potential quorum quenching activity.
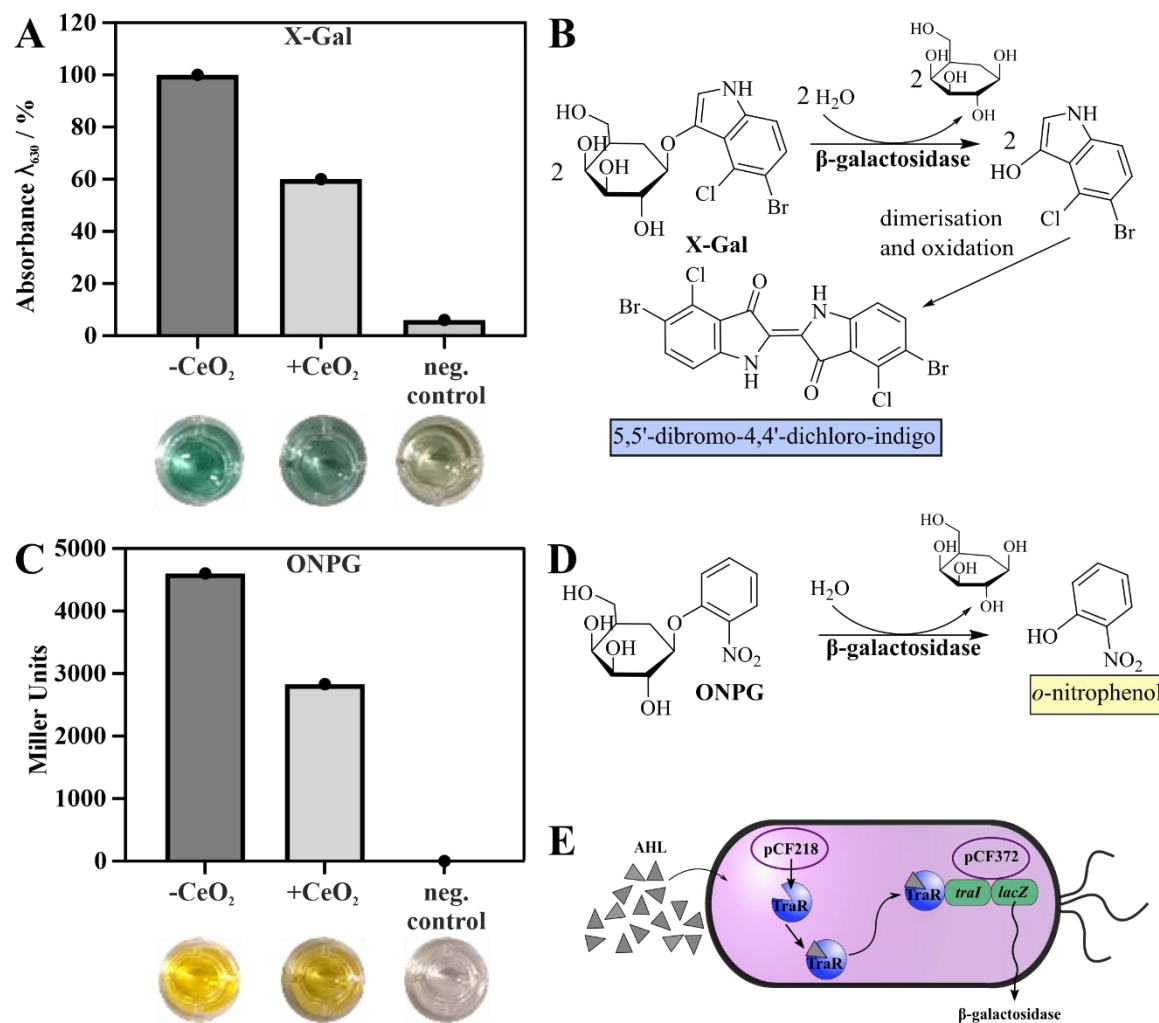
Figure 5-4. Detection of long chain AHLs using *A. tumefaciens* A136 as biosensor strain expressing β-galactosidase. (A) Reporter strain after 8 h of reaction with 10μM 3-oxo-C_{12}-HSL (positive control), 10μM 3-oxo-C_{12}-HSL with CeO_2 NCs, KBr and H_2O_2, LB medium (negative control) in the presence of X-Gal producing the blue dye 5,5'-dibromo-4,4'-dichloro indigo. (B) Hydrolytic cleavage of X-Gal by β-galactosidase. (C) Reporter strain after 8 h of reaction time with 3-oxo-C_{12}-HSL (positive control), with AHL and CeO_2 NCs, KBr and H_2O_2, buffer Z (negative control) in the presence of ONPG producing yellow o-nitrophenol. (D) Hydrolytic cleavage of ONPG by β-galactosidase (E) Expression of β-galactosidase after AHL detection of *A. tumefaciens* 136.

The concentration of the signaling molecules C_4-HSL and 3-oxo-C_{12}-HSL in the supernatants of *Pseudomonas aeruginosa* was analyzed using a newly developed liquid chromatography/mass spectrometry (LC-MS/MS). The measurements showed in the supernatants of *P. aeruginosa* a decrease in concentration of C_4-HSL and 3-oxo-C_{12}-HSL in the presence of CeO_2 NCs (Figure S5-5), which supports the results from the reporter strains in Figure 5-4. The decrease could be explained by reduced biofilm growth, but also by degradation processes caused by catalytically formed free active bromine, e.g., hypobromous acid as known from the natural enzyme bromoperoxidases, which could explain the observed quorum quenching process. However, it is unclear what happened to

the signaling molecules and whether bromination processes like the haloperoxidase assay also occur in bacterial media.

Determination of bromide concentrations by ion chromatography -conductivity detection (IC-CD)

Bromide concentration may be affected by processes such as halogenation. The addition of a 30 mM of sodium bromide did not result in a significant reduction due to the high excess in the bacterial supernatant. This indicates that the bromide concentration does not have a limiting effect on the reaction and biofilm inhibition. However, to observe the reduction of bromide concentration by the addition of H_2O_2 and CeO_2 nanocrystals due to a bromination of organic molecules in the bacterial supernatant, the bromide concentration was adjusted to 30 µM.
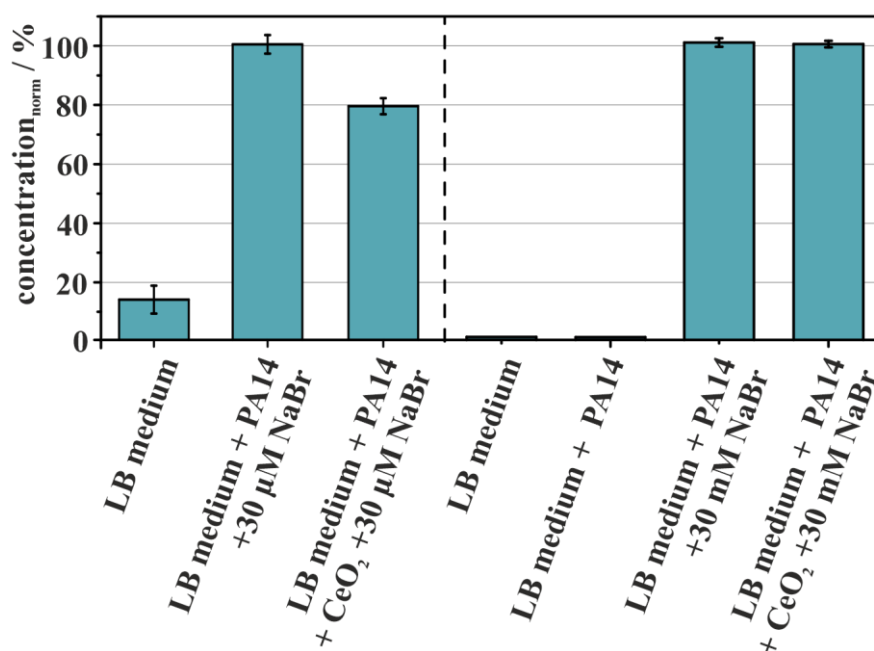
Figure 5-5. Normalized bromide concentrations in bacterial supernatant and the effect of nanoparticle catalyst on bromide concentration after addition of 30 µM and 30 mM sodium bromide.

The reduction of bromide concentration in samples with a bromide concentration of 30 µM (approximately 20%, Figure 5-5) gives a first hint that oxidation of bromide occurs also in bacterial media, and that free active bromide is formed. These reactive species like hypobromous acid can react with quorum sensing molecules and thus have an effect on the quorum quenching process.[25,57]

Degradation of *N*-acyl-homoserine lactone

To get a deeper insight into the degradation processes of quorum sensing molecules by CeO$_2$ NC, different signaling molecules used by the bacteria from this study were selected to investigate their degradability. Degradation studies of C$_4$-HSL, 3-OH-C$_{10}$-HSL and 3-oxo-C$_{12}$-HSL, were performed in MilliQ-water and in presence of H$_2$O$_2$, sodium bromide and CeO$_2$ NCs.
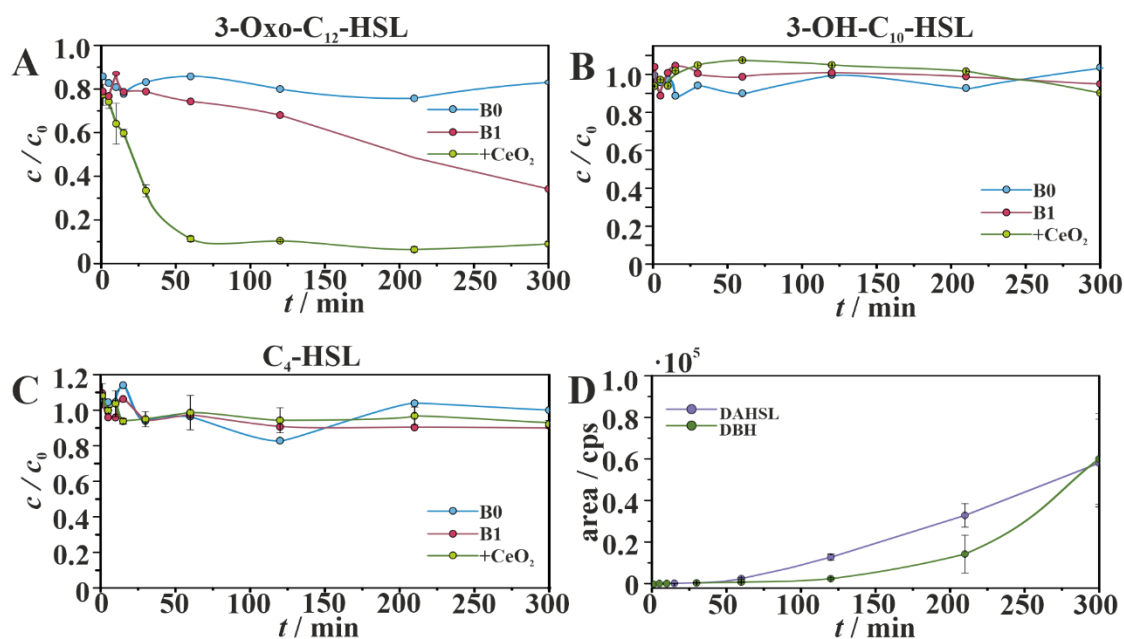
Figure 5-6. Degradation curves of different signal molecules in MilliQ-water with CeO$_2$ nanocrystals, sodium bromide and H$_2$O$_2$ addition. The actual concentration (*c*) at the discrete time interval was divided by the initial concentration (*c$_0$*). Blank reaction B0 shows the substrates in MilliQ-water without any addition and B1 with addition of H$_2$O$_2$ and sodium bromide. Degradation curves of (A) C$_4$-HSL (B) 3-OH-C$_{10}$-HSL (C) 3-oxo-C$_{12}$-HSL and (D) time-trend from the produced DAHSL and DAHS from 3-oxo-C$_{12}$-HSL degradation experiment.

Degradation curves of the signaling molecules are presented in Figure 5-6. The three signaling molecules represent the main groups of *N*-acyl-homoserine lactones. The degradation experiments showed that only 3-oxo-C$_{12}$-HSL was degraded. Similar results were already reported[55] and an antimicrobial effect through this reaction was assumed. In high-resolution mass spectrometer data, two transformation products could be detected for 3-oxo-C$_{12}$-HSL. Since the alpha position of the 1,3-diketone is electron-rich, it serves as a target for the reactive species of (catalytically formed) hypobromous acid, resulting in bromination. Moreover, hydrolysis of the alkyl chain was observed for 3-oxo-C$_6$-HSL.[56] In this study, N-α,α-dibromoacetylhomoserine lactone (DAHSL) and the hydrolyzed transformation product (DAHS) were monitored and verified against pure DAHSL as

reference standard. (Figure S5-7). It was assumed that the brominated transformation products not only "silence the signal" but also have effects on growth behavior and biofilm formation.

Biofilm inhibition experiments with signaling molecules and DAHSL

In another set of experiments, we investigated whether 3-oxo-C_{12}-HSL, C_4-HSL, and DAHSL, formed by degradation of the bacterial signaling molecule 3-oxo-C_{12}-HSL, affect the growth behavior and biofilm formation of *P. aeruginosa*. For this purpose, bacteria were incubated with different concentrations (1 nm-10 μM) of 3-oxo-C_{12}-HSL, C_4-HSL, or DAHSL.
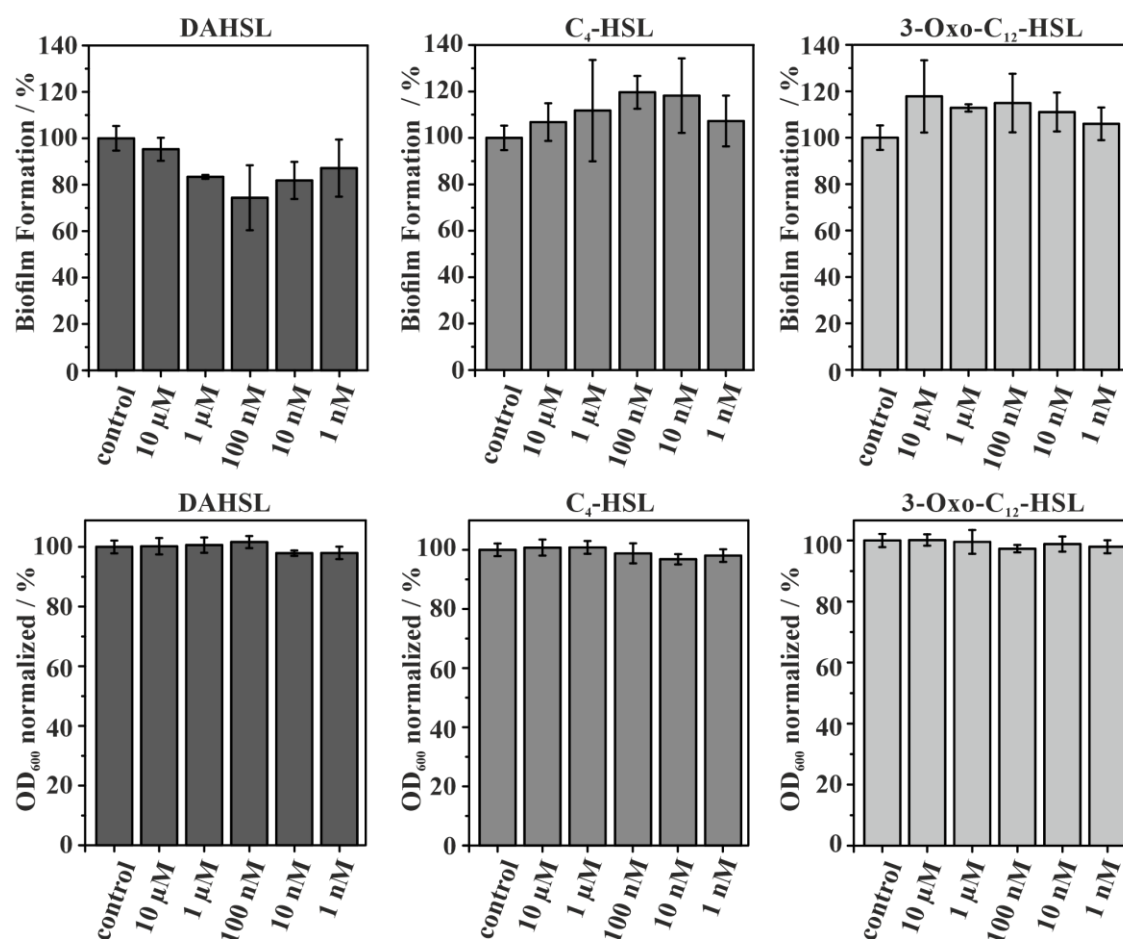
Figure 5-7. Effect of 3-oxo-C_{12}-HSL, C_4-HSL and DAHSL (1 nM-10 μM) on biofilm formation and growth behavior measured at OD_{600}. All values are normalized to a control without CeO_2 NCs, Br^- and H_2O_2.

The normalized OD_{600} values and biofilm formation were compared after 72 h (Figure 5-7). The addition of signaling molecules (3-oxo-C_{12}-HSL, C_4-HSL) leads to increased biofilm

formation, while DAHSL reduces biofilm formation to a small extent. In a simple picture, DAHSL may be considered as "background noise" that affects the communication between bacteria. Bacteria can recognize their autoinducers, but communication is effectively disrupted only when the signal molecules are chemically modified. This is achieved with the HPO mimic CeO_2 NCs in the presence of the reactants Br^- and H_2O_2. Neither the presence of DAHSL alone nor of 3-oxo-C_{12}-HSL and C_4-HSL affect the growth of bacteria monitored at OD600.

Attempt to detect DAHSL and DBH in bacterial supernatant

In order to detect the brominated products that appeared in the degradation experiments also in the bacterial supernatants, a sensitive LC-MS/MS method was developed for these products using the pure reference standard (Figure S5-7). The extracts were measured with LC-MS/MS and liquid chromatography/high resolution mass spectrometry (LC-HRMS).
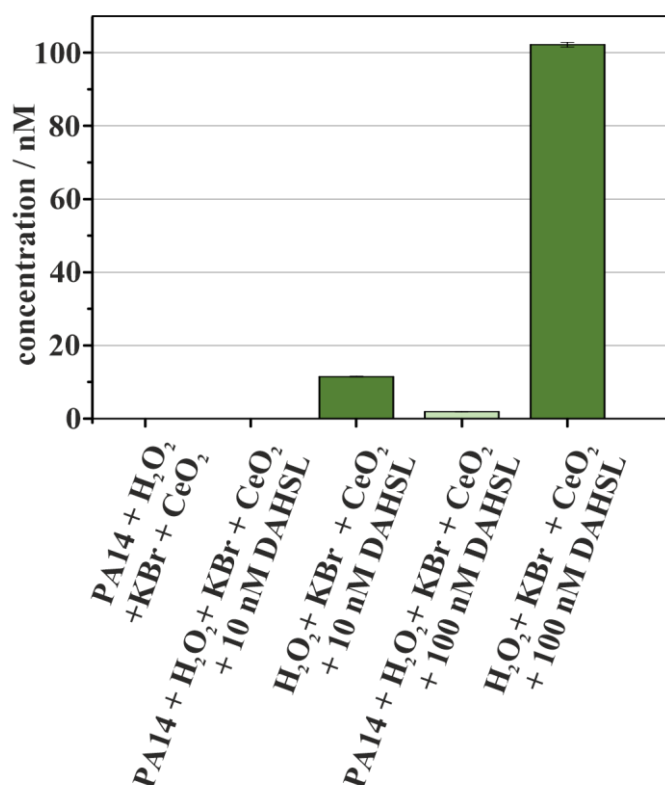
Figure 5-8. Spike Experiments with DAHSL in *Pseudomonas aeruginosa* (PA14) supernatant. Different recoveries of DAHSL measured after 24 h incubation of samples with several variations and combinations of PA 14, H_2O_2, CeO_2 NSs and DAHSL solutions (10 nM and 100 nM) are shown.

Since the transformation products (DAHSL and DBH) could not be detected in bacterial supernatant, spike experiments with DAHSL were performed to clarify their fate. The spike experiments in Figure 5-8 showed that DAHSL and DBH could not be detected in bacterial supernatant but were stable in pure solutions of CeO_2 NC, H_2O_2 and sodium bromide. This indicates that the concentration or presence of these transformation products is affected by biodegradation.

Screening for bromated products in bacterial supernatant and degradation of HQNO

Since neither DAHSL nor DBH could be detected in the extracts, other brominated compounds were searched for to determine the fate of the bromine and to determine the total bromine balance. A brominated compound with the exact mass of 338.07502 Da was detected in the positive ion mode (Figure 5-9B). From the isotope pattern the presence of one bromine atom and a chemical formula $C_{16}H_{21}BrNO_2$ (-0.9 ppm) was determined. The fragment spectra from this compound showed quinolone-specific fragments and in the negative ion mode specific bromine fragments (79.91/80.91). (Figure S5-8).
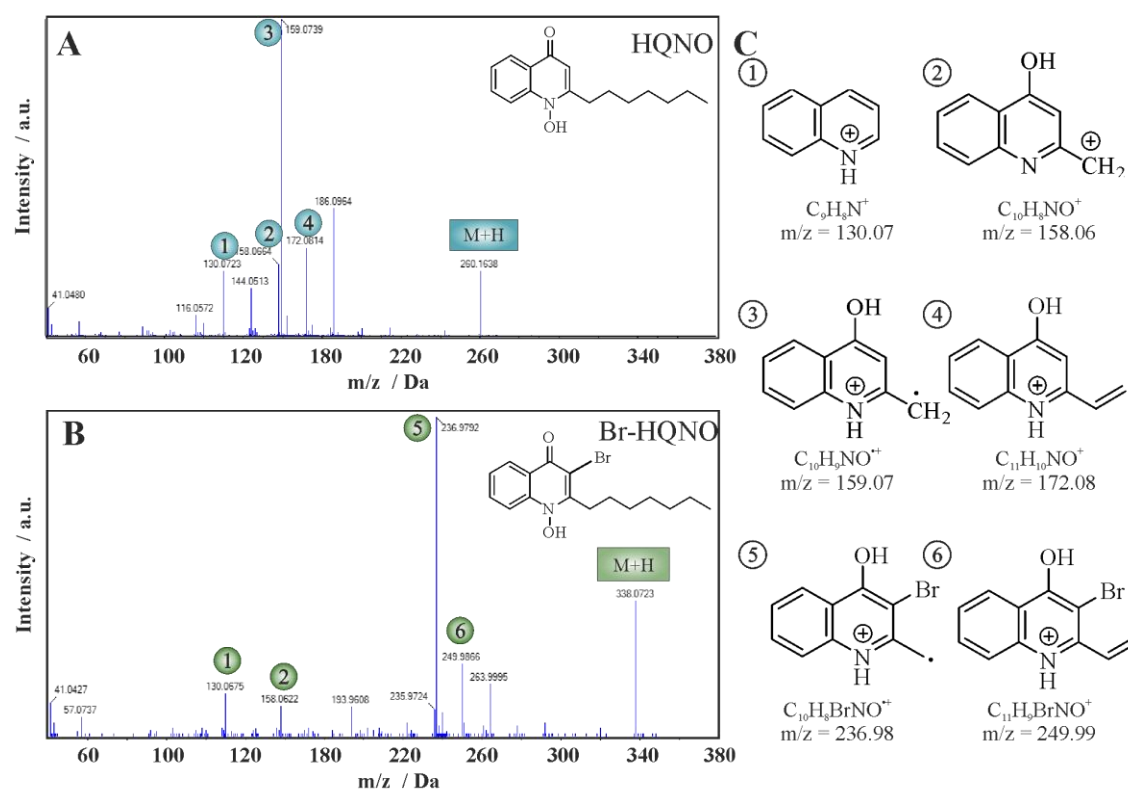
Figure 5-9. (A, C) Fragment spectra of HQNO in positive ion mode with proposed structures for the fragments. (B, C) Fragment spectra of Br-HQNO in positive ion mode with proposed structures for the fragments

122

Figure 5-9 shows the fragment spectra of the purchased reference HQNO and the unknown brominated compound with the proposed structures of the observed fragments. The monitored fragments indicate the bromination of 2-heptyl-1-hydroxyquinolin-4-one (HQNO) to Br-HQNO which was already shown for various alkyl quinolones by a vanadium-dependent haloperoxidase.[59] Although HQNO does not function as a signaling molecule in *P. aeruginosa*, it is regulated by the *Pseudomonas* quinolone signal (PQS) quorum sensing system and acts as a cytochrome inhibitor for prokaryotic and eukaryotic cells.[60,61] Furthermore, previous studies have shown that HQNO is responsible for increased biofilm formation and concomitant increased antibiotic tolerance.[37,62] Therefore, it seems plausible that bromination of the HQNO will result in reduced biofilm formation in *P. aeruginosa*. In addition, studies have shown that HQNO is also responsible for increased biofilm formation and aminoglycoside tolerance in *S. aureus*.[63,64] Both bacteria are opportunistic pathogens and can form a polymicrobial biofilm in cystic fibrosis patients.[65] When *S. aureus* is exposed to HQNO, the formation of so-called small-colony-variants (SCV) occurs. SCV is a phenotype that grows more slowly than the wild type due to the switch to fermentative growth. This phenotype can occur if the electron chain is inhibited.[66] The danger of these SCV is that they are often not recognized at diagnosis and thus the symptoms cannot be identified as *S. aureus* infection.[64] Bromination of HQNO may therefore not only inhibit biofilm formation in *P. aeruginosa*, but also make it easier to treat undetected *S. aureus* infections due to a dual-species or polymicrobial biofilm. The observed Br-HQNO explains biofilm reduction and the concomitant decrease in bromide concentration in *Pseudomonas aeruginosa* since HQNO is known to increase biofilm formation and resistance to antibiotics.[37] However, additional studies are necessary to fully understand communication mechanisms and biofilm formation process in the other Gram-negative bacteria, since they were also influences by CeO_2 NCs. Still, even bacteria that do not communicate *via* 3-oxo-C_n-HSL and do not produce HQNO like *Methylobacterium mesophilicum*, showed biofilm inhibition (Figure 5-3). The intermediate halonium species HOX may act as a disinfectant,[22] and it can undergo a variety of reactions with organic substrates, only a few of which were uncovered here. Moreover, *Methylobacterium mesophilicum* was reported to exhibit resistance to disinfectants like chlorine and *Staphylococcus aureus* showed no significant biofilm inhibition.[67] This supports the idea that there is an interference with the quorum-sensing system of Gram-negative bacteria by the reactive HOBr intermediate.

Application and performance of CeO_2 nanocrystals in lacquer coatings

CeO_2 NCs were embedded in PUR (polyurethane) coatings to produce antimicrobial surfaces. Since the as-synthesized CeO_2 NCs contain weakly surface-bound *n*-butyl acetate, they are highly dispersible in PUR lacquers. Different amounts of a stock solution containing 100 mg/mL CeO_2 in *n*-butyl acetate were added to PUR lacquers to produce coatings with different CeO_2 loadings. For this purpose, cleaned steel plates, LEGO bricks and quartz slides were coated with the lacquers by dip-coating process. The plates were subsequently dried for 2 hours at room temperature and later at 80 °C in an oven. The painted steel plates were examined by scanning electron microscopy (SEM) to demonstrate the incorporation of CeO_2 NCs in the coating. The images in Figure 5-9A show no differences between uncoated and coated specimens apart from a higher roughness of the uncoated surfaces (Figure S5-9).
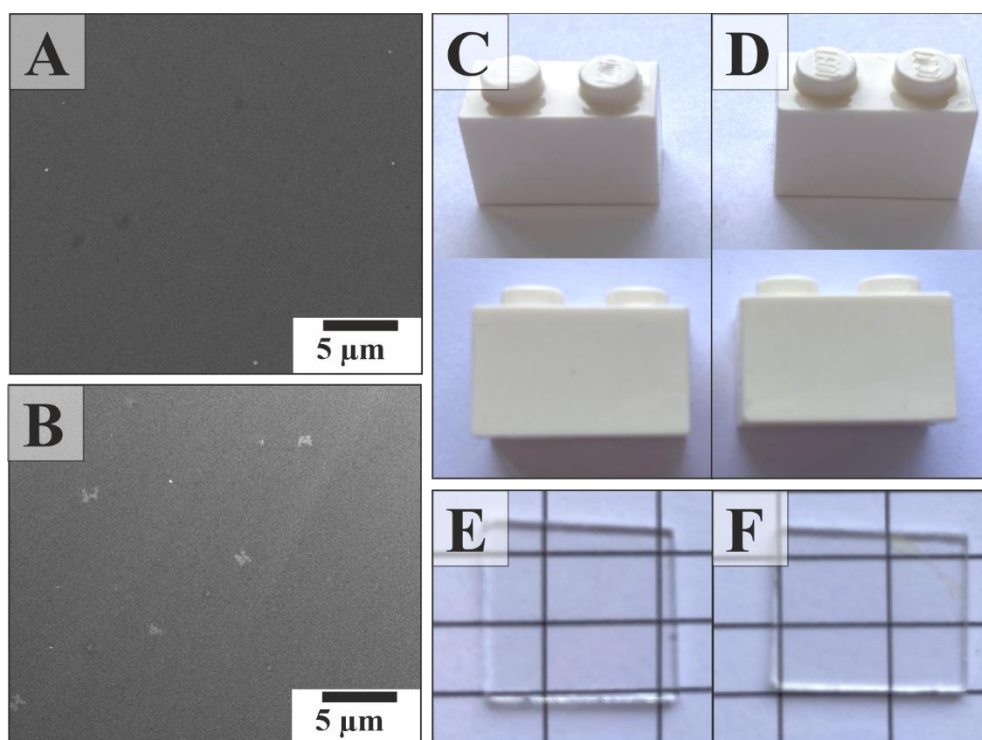
Figure 5-10. SEM image of steel plates painted with (A) PUR lacquer and (B) PUR lacquer containing incorporated CeO_2 NCs. Digital images of LEGO bricks (C, D) and quartz slides (E, F) painted with a PUR lacquer (C, E) and a PUR lacquer containing incorporated CeO_2 NCs (D, F).

The surface coating with incorporated CeO_2 NCs shows spots with higher material contrast (Figure 5-10B), corresponding to the areas with the lanthanide element cerium. Energy dispersive X-ray (EDX) mapping analysis clearly showed the presence of CeO_2 (Figure S5-10). Only small amounts of cerium were observed by EDX analysis as a very

low cerium oxide concentration was used for the coatings. Coatings with and without cerium oxide were both transparent (Figure 5-10C-F).
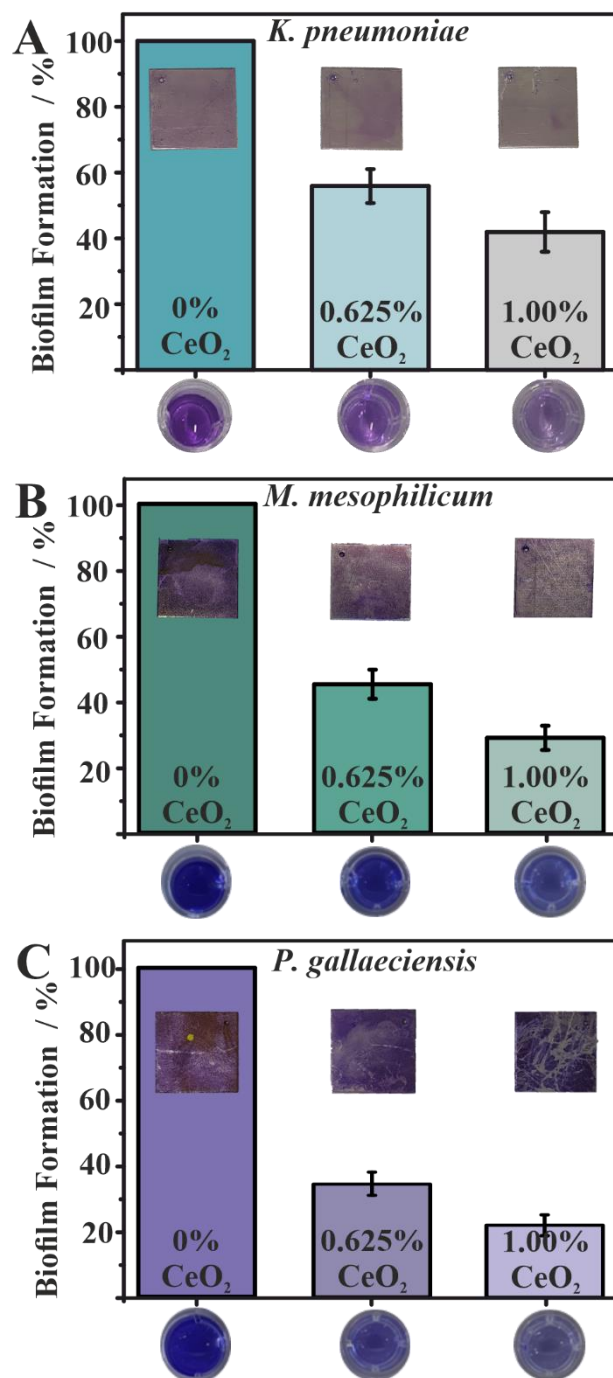
Figure 5-11. Quantification of the biofilm formation of (A) *K. pneumonia*, (B) *M. mesophilicum* and (C) *P. gallaeciensis* incubated for 72 h with steel plates coated with lacquers containing 0% (left), 0.625% (middle) and 1% (right) of CeO_2 NCs by a crystal violet staining assay. Each experiment was performed in triplicate.

To test the biofilm inhibiting effect of the specimens coated with lacquer containing embedded CeO_2 NCs, the lacquered steel plates were incubated with bacteria of the strains

K. pneumonia, M. mesophilicum and *P. gallaeciensis*. The plates were removed after 72 h and the adherent biofilms of *K. pneumonia, M. mesophilicum* and *P. gallaeciensis* were stained with crystal violet. The steel plates coated with PUR lacquer without (0%) CeO_2 NCs (positive control) showed for all bacteria a significantly higher amount of attached biomass compared to their counterparts coated with PUR lacquer containing 0.625 wt% and 1wt% of CeO_2 NCs. Figure 5-11A-C shows a strong reduction in biofilm formation for specimens coated with PUR lacquer containing 1% CeO_2 NCs. Biofilm inhibition of ~60%, ~70% and ~80% could be achieved for *K. pneumonia, M. mesophilicum* and *P. gallaeciensis,* respectively. The incubation assays show consistently that a higher proportion of embedded CeO_2 NCs results in higher inhibition levels.

The antibacterial activity of all plates coated with PUR lacquer containing no (0%) CeO_2 NCs (positive control) and 0.625 wt% and 1 wt% was quantified by confocal laser scanning microscopy (CLSM). Biofilm formation of *P. aeruginosa* on lacquer surfaces containing no CeO_2 NCs (0%, positive control) was compared with biofilm formation on surfaces coated with PUR lacquer containing 0.625 wt% and 1 wt% of CeO_2 NCs. For this purpose, a *P. aeruginosa* culture was allowed to grow for 72 h at 30 °C on steel samples in 6-well plates. Attached bacteria were stained with SYTO 9 and propidium iodide after removing the planktonic cells. SYTO 9 permeates into all cells, while propidium iodide diffuses only into dead cells. The measured fluorescence represents the sum of live and dead cells.[68] The fluorescence-labelled cells were imaged by three-dimensional confocal laser scanning microscopy (3D CLSM). Figure 5-12 shows the scanned areas (left) and the biofilm thicknesses (right). The steel plate painted with PUR lacquer without CeO_2 NCs (0%, positive control) shows a homogeneous green fluorescence, compatible with a fully developed biofilm having an average thickness > 60 μm. Steel plates coated with PUR lacquer containing 0.625 wt% and 1 wt% of CeO_2 NCs showed a strongly reduced biofilm growth. White areas indicate the absence of attached cells. The amount of the attached biofilms is up to 38% (0.625% CeO_2) and 66% (1% CeO_2) lower than those of the control, i.e., higher CeO_2 NCs loadings lead to enhanced biofilm inhibition, in harmony with the results of the staining tests. To demonstrate the difference in biofilm formation, the painted plastic building blocks and glass plates were also incubated with *P. aeruginosa* for 24 h, and the biofilm formed was stained with crystal violet showing a deep violet deposition on all materials coated with a lacquer without CeO_2 NCs. (Figure 5-12B+C)
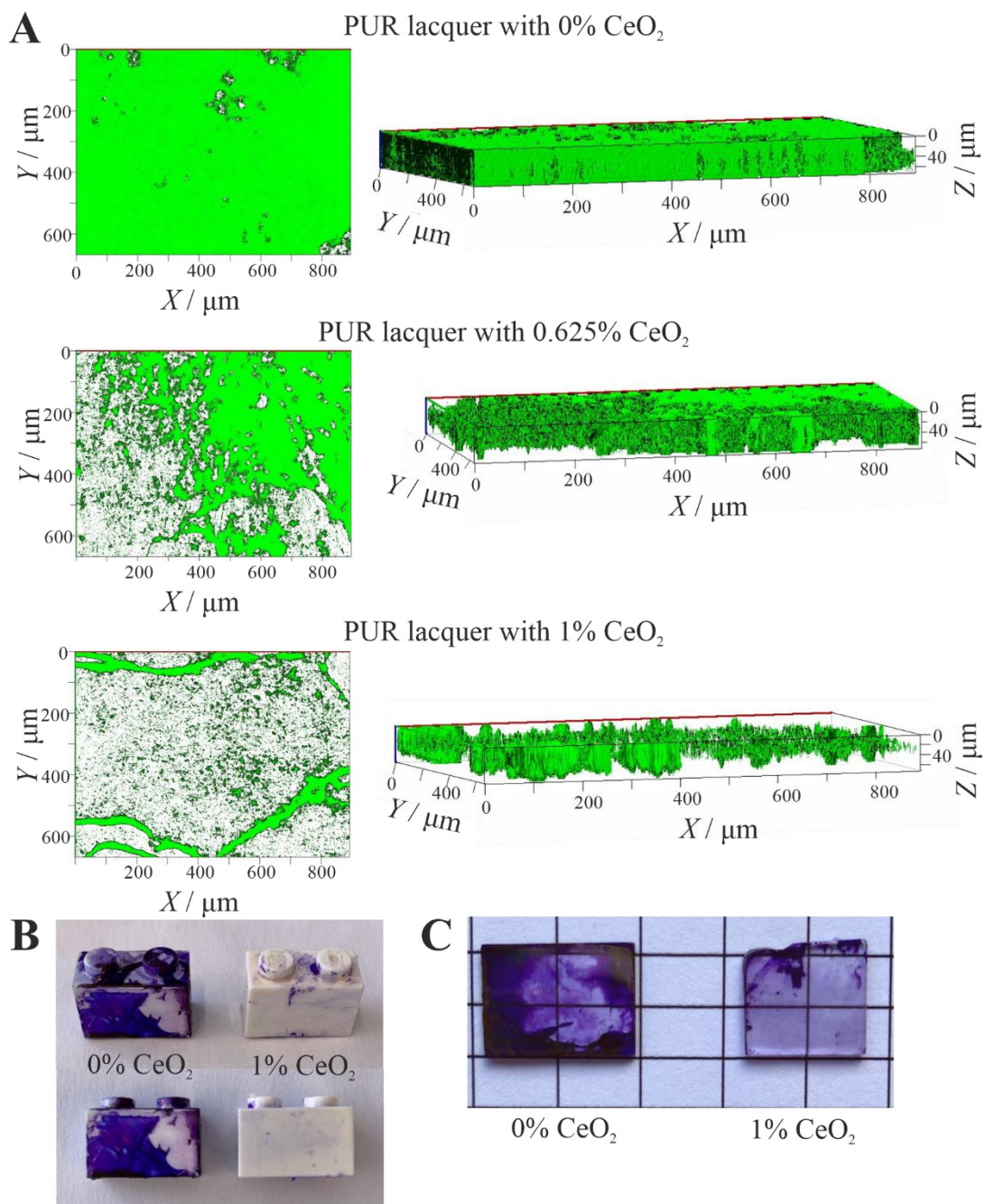
Figure 5-12. (A) CLSM images of *P. aeruginosa* biofilms grown on steels plates coated with PUR lacquer containing 0% (positive control), 0.625 wt% and 1 wt% CeO_2 NCs in LB medium. The scanned surface is shown on the left, and the thickness of the corresponding biofilms on the right. (B) Image of crystal violet stained biofilm (*P. aeruginosa*) grown after 72 h incubation on coated (B) coated children's LEGO toys and (C) quartz glass slides.

P. aeruginosa biofilms were analyzed by scanning electron microscopy (SEM) after 72 h of incubation at 30 °C. Figure 5-13A+D show a thick biofilm adhering to a lacquer coating without CeO_2 NCs. Since bacterial communication was not inhibited by oxidative halogenation, the slimy extracellular polymeric substance (EPS) could form. Therefore, a coherent biofilm formed during the cultivation process as the bacteria proliferate on the surface. On surfaces coated with lacquer containing 0.625 wt% (Figure 5-13B+E) and 1 wt% (Figure 5-13C+F) CeO_2 NCs, respectively, a less dense biofilm was formed. Some isolated bacteria adhered to the surface that were not enclosed by the EPS. Although a reversible attachment of individual bacteria cannot be prevented, disruption of cell-cell communication by biomimetic halogenation clearly inhibits biofilm proliferation.
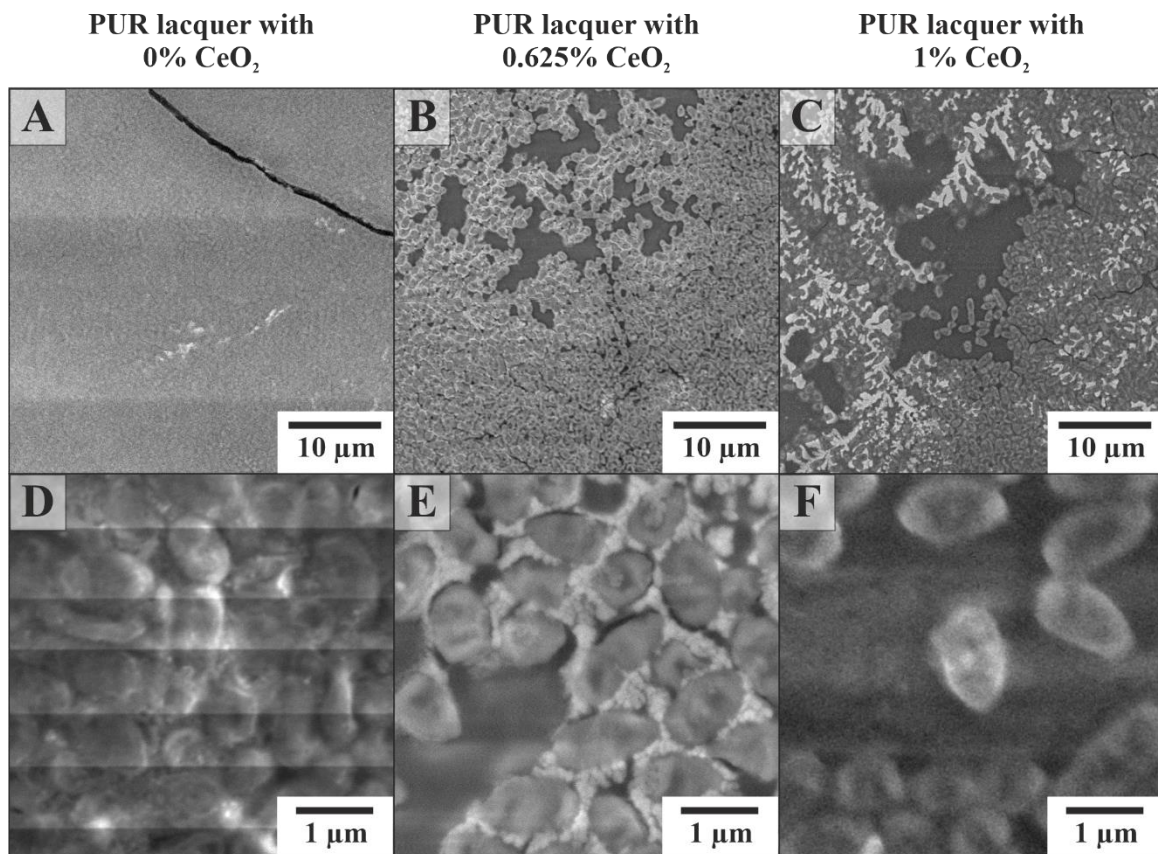
Figure 5-13. SEM image of a *P. aeruginosa* biofilm grown on steel plates coated with PUR lacquer containing (A, D) 0% (positive control), (B, E) 0.625 wt% and (C, F) 1 wt% CeO_2 NCs. *P. aeruginosa* was cultured in LB medium at 30 °C for 72 h. The white substance between bacteria is crystallized salt from the culture medium.

The as-prepared glass slides (Figure 5-10E+F) show that coating with CeO_2-loaded lacquer does not affect transparency. For this purpose, green-fluorescent osteoblasts (MG-63 GFP) were seeded on PUR-coated quartz slides containing 0% and 1 wt% CeO_2 NCs and

incubated at 37 °C under 5 vol% CO_2. Analysis was performed by fluorescence imaging after 24 and 72 h using 2D CLSM (Figure 5-14). As a control, cell growth was also examined on cell-adherent Petri dishes. Cells show adherent cell growth (prolonged cell morphology) after 24 h on the PUR-coated silica slides both with and without CeO_2 NCs. This is consistent with the control experiment and demonstrates the minor effect of the PUR lacquer and CeO_2 NCs on cell adhesion. Moreover, the increasing fluorescence intensity shows a significant increase in cell growth after 72 h, indicating good cell viability in all three experiments with no apparent effect of the lacquer and the CeO_2 NCs.
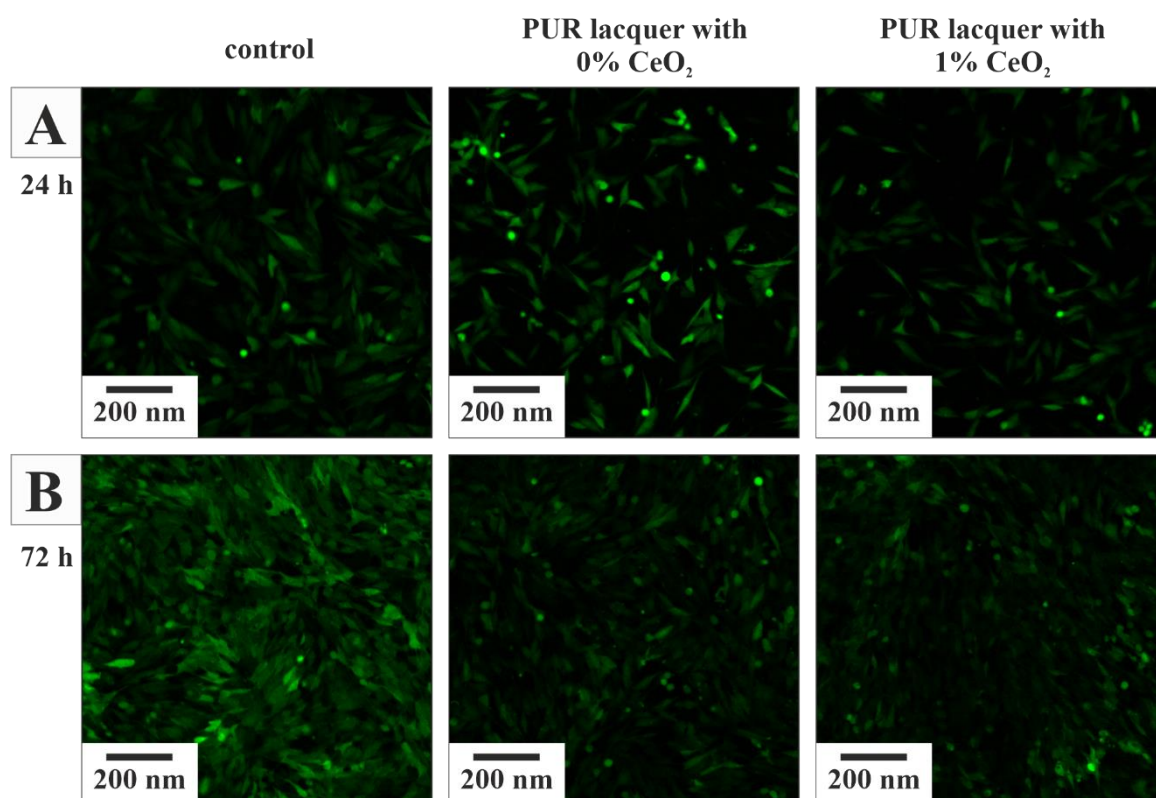
Figure 5-14. CLSM imaging of green-fluorescent cells (MG-63 GFP) grown on cell-adhesive Petri dishes (control) and on PUR lacquer coated quartz glass slides containing 0% and 1% CeO_2 NC. Imaging was performed after (A) 24 h and (B) 72 h.

5.4. CONCLUSION

Colonization of surfaces by bacteria is a common phenomenon with implications for the environment and human health. Thus, antibacterial agents without the drawbacks of traditional antibiotics are highly desirable. CeO_2 nanocrystals have been proposed as environmentally benign antimicrobials. They act like naturally occurring HPOs that prevent biofilm formation by catalyzing the formation of oxidizing halonium species such as hypobromous acid in the presence of halides and H_2O_2, but the molecular mechanism of their antimicrobial activity is still poorly understood.

Therefore, this work analyzes on a molecular level the reaction cascade that proceeds when biofilm formation in a culture of *P. aeruginosa* is inhibited due to the HPO activity of CeO_2 nanocrystals embedded in polyurethane lacquer. The CeO_2-loaded lacquers are applied to everyday objects such as metal parts, plastic building blocks or glass plates.

Monodisperse and non-agglomerated CeO_2 nanocrystals for the coatings were obtained by an ultra-large scale of 12 g per batch from non-toxic and low-cost reagents without further size-sorting in any of the dispersants desired for the coatings. When the reactors are set up in parallel, kilogram amounts of monodisperse nanocrystals can readily be obtained. The solvent molecules weakly bound to the CeO_2 particle surfaces allow easy dispersion in paints. The paints are transparent due to the small particle size and the particles are still catalytically highly active. The HPO activity of the CeO_2 nanocrystals was evaluated in a standardized manner with BET surface area measurements and phenol red enzyme assays. Gram-negative bacteria communicate *via* AHLs, where each bacterial strain uses different individual AHL molecules in its quorum sensing pathways. HQNO, another substrate molecule from the quinolone family, increases *P. aeruginosa* biofilm and its resistance to antibiotics. Using LC-MS trace analysis we could isolate and identify non-halogenated and halogenated compounds in *P. aeruginosa* bacterial cultures "at work" in nanomolar concentrations. This shows that the hypohalous acids or halonium species formed by CeO_2 further react to form halogenated bacterial signaling molecules Br-HQNO in a subsequent reaction, especially in the presence of a large number of possible competing reactions under natural growth conditions. This shows that the hypohalogenated acids or halonium species formed by CeO_2 surface catalysis react further to form halogenated signal molecules (Br-HQNO, DAHSL). These can only be partially detected in bacterial supernatants as they are metabolized to some degree by the bacteria. Detection of brominated HQNO, indicating that oxidative bromination mechanism takes places and explains reduction of biofilm in

presence of CeO_2 NC's. This demonstrated the catalytic involvement of CeO_2 enzyme mimetics in the quorum quenching mechanism of biofilm inhibition at the molecular level. The inhibition of biofilm formation is most likely not due to the photocatalytic formation of reactive oxygen species (such as singlet oxygen or superoxide radicals).

The role of the CeO_2 nanocrystal HPO mimics in disrupting bacterial quorum sensing, the biological feedback mechanism by which bacteria can sense a sufficient cell density of themselves was further demonstrated with the reporter strain *Agrobacterium tumefaciens* A136.

Although a reversible attachment of individual bacteria cannot be prevented, disruption of cell-cell communication by biomimetic halogenation of signaling molecules clearly inhibits biofilm proliferation. Biofilm formation of *P. aeruginosa* on PUR lacquer surfaces containing only 0.625 wt% and 1 wt% of CeO_2 nanocrystals was reduced by up to 60% s shown by CLSM and SEM. Likewise, a biofilm inhibition of ~60%, ~70% and ~80% could be achieved for *K. pneumonia, M. mesophilicum and P. gallaeciensis,* respectively. The incubation assays show consistently that a higher proportion of embedded CeO_2 NCs results in higher inhibition levels. Development of new functional antifouling surfaces using CeO_2 is a new attempt to reduce biofouling without using biocides or toxins. The design of a green catalyst against biofouling has a promising future, as conventional methods do not offer a long-term solution due to the development of microbial resistance and limited lifetime.

5.5. EXPERIMENTAL SECTION

Chemicals

Cerium nitrate hexahydrate (99.5%, CAS: 10294-41-4) was purchased from Alfa Aesar. Bromoacetic acid (98+%, CAS: 10035-10-6), hydrogen bromide (33 wt%) in glacial acetic acid (CAS: 79-08-3), ethyl acetate (99.9%, CAS: 141-78-6), potassium bromide (99+%, CAS: 7758-02-3), magnesium sulfate (99%, CAS: 22189-08-8) and petroleum ether (CAS: 64742-49-0) were obtained from Acros Organics. Phenol red (CAS: 143-74-8), as well as dibromoacetic acid (97% / CAS: 631-64-1), (L)-methionine (98%, CAS: 63-68-3), triethylamine ($\geq$99%, CAS: 121-44-8) and $NaHCO_3$ (99.5-100.5%, CAS: 144-55-8) were purchased from Sigma-Aldrich. Sodium chloride (CAS: 7647-14-5), isopropanol (CAS: 67-63-0) and acetic acid glacial (HAc; 99.5%, CAS: 64-19-7) were obtained from VWR. N-Butyl acetate ($\geq$99% CAS: 123-86-4) and hydrogen peroxide (hydrogen peroxide 35% pure, stabilized (34-36-% / CAS: 7722-84-1) were obtained from Roth and 1-ethyl-3-(3-dimethyl aminopropyl) carbodiimide hydrochloride (EDC, $\geq$99%, CAS: 25952-53-8) from Carbolution. Polyurethan lacquers (PUR) were provided by lacolor Lackfabrikation GmbH. Ethanol (99%, CAS: 164-17-5), tryptone (CAS: 91079-40-2), yeast extract (CAS: 8013-01-2), NaCl (7647-14-5), soy peptone (CAS: 91079-46-8), meat extract (CAS: 68990-09-0), H_2O_2 (35 % CAS: 7722-84-1), KBr (CAS: 7758-02-3), NaBr (CAS: 7647-15-6), tetracycline (CAS: 64-75-5), spectinomycine (CAS: 22189-32-8), Na_2HPO_4 (CAS: 10028-24-7), NaH_2PO_4 (CAS: 10049-21-5), $MgSO_4$ (CAS: 22189-08-8), 2-Mercaptoethanol (CAS: 60-24-2), Chloroform (CAS: 67-66-3), ONPG (CAS: 369-07-3), SDS (CAS: 151-21-3), Na_2CO_3 (CAS: 497-19-8) and X-Gal (CAS: 7240-90-6) were purchased from Carl Roth. The marine medium 2216 (CAS: 10043-52-4) was purchased by Thermo Fisher Scientific.

Inorganic synthesis, characterization and analytics

Synthesis of CeO₂ nanocrystals. CeO_2 nanoparticles were synthesized using a method. In a typical procedure $Ce(NO_3)_3 \cdot 6H_2O$ (1.5 g, 3.5 mmol) was added to 25 mL n-butyl acetate (190 mmol) and transferred into a Teflon autoclave (110 mL) equipped with Halsic-R heating rods (recrystallized silicon carbide, 1 cm length). Within two minutes, the n-butyl acetate was heated to 180°C with a power of up to 1800 W in a Mars 6-mircowave from CEM. The temperature was maintained for additional 15 min. After cooling down to room temperature, autoclaves were opened in the fume hood allowing nitrous gases to be

released. The CeO$_2$ NCs were washed each with *n*-butyl acetate, ethanol and water (9000 rpm, 10 min) 2 times each. For further processing into PUR coatings, the particles were again washed with ethanol and redispersed in *n*-butyl acetate to a final concentration of 100 mg·L^{-1}.

Preparation of CeO$_{2-x}$ coated steel plates. Steel plates with a size of 2x2 cm were washed washed with MilliQ-water and ethanol to remove surface contaminants. In addition, the plates were treated with Argon plasma to remove further interfering organic compounds. The treated plates were immersed in PUR coating with different additions of CeO$_{2-x}$ NCs (0%, 0.625%, 1% with respect to PUR coating) at an immersion speed of 70 mm/min. After complete dipping in the lacquer, the steel plates were pulled out using the same speed. The painted steel plates were dried in an oven at 80°C for 16 h to remove the organic volatiles.

Haloperoxidase Assay. The haloperoxidase activity of CeO$_2$ NCs was analyzed via the so-called phenol red assay. Using a Cary 3500 UV/Vis from Agilent, the oxidative bromination of yellow phenol red to violet bromophenol blue was observed spectrophotometrically. The reaction mixture was an aqueous (MilliQ-water, 18.2 MΩ cm^{-1}) dispersion of CeO$_2$ NCs (25 µg mL^{-1}), H$_2$O$_2$ (300 µM), PR (50 µM) and KBr (25 mM). Prior to H$_2$O$_2$ addition, the mixture was transferred into a quartz cuvette and stirred for 1 min to achieve an adsorption/desorption equilibrium. The absorbance change was observed over a period of 2 h.

Michaelis Menten Kinetics. Different amounts of H$_2$O$_2$ were added to a stirred solution of phenol red, KBr and the CeO$_2$ NCs to determine Michaelis-Menten kinetics. 2 mL of a 50 µM phenol red and 25 mM bromide solution were added to a quartz cuvette, 62.5 µL of a NC dispersion (1 mg mL^{-1}) was added and stirred for 1 min. All reactions were maintained at 25 °C: Before addition of 50 µL H$_2$O$_2$ (different concentrations), the adsorption was set to zero. Change in absorbance were measured at a wavelength of λ = 590 nm over a period of 10 minutes. All data points were linearly fitted at an interval of 2-8 min receiving a linear relationship. The concentration of bromophenol blue was calculated from Lambert-Beers law, and the extinction coefficient was determined as 32740 L·mol^{-1}cm^{-1} (measured for different bromophenol blue concentrations in a 1 cm quarz cuvette).

IC-CD (Ion chromatography-conductivity detector). The bromide concentrations were measured with a 940 Professional IC Vario ion chromatography (Metrohm, Herisau,

Switzerland) coupled with a conductivity detector (CD). The separation was performed by a Metrosep A Supp 7 (250/4.0) column and the flow rate was set to 700 µL/min. The column temperature was 50 °C and 50 µL of each sample were injected. A 3.6 mM Na_2CO_3 solution was used as eluent, and a 250 mM H_3PO_4 solution as suppressant/suppression solution. The switching time was at 30 and 45 min and the total running time was 50 min. All samples were diluted 1 to 100 in MilliQ-water.

Transmission Electron Microscopy. Transmission electron microscopy (TEM) samples were prepared by placing a drop of NC dispersion ($1mg\cdot mL^{-1}$) in MilliQ-water on a carbon coated copper grid. TEM images were acquired with an FEI Tecnai 12 TWIN LaB_6 at 120 kV along with a Gatan US1000 CCD camera (16-bit, 2048 x 2048 pixels) using Gatan Digital Micrograph software.

Powder X-ray Diffraction. X-ray diffraction patterns were recorded using a STOE Stadi P diffractometer equipped with a Dectris Mythen 1k detector in transmission mode with Mo Kα1 radiation.

Zeta Potentials. Zeta potentials were measured on a Malvern Zetasizer Nano using disposable capillary cells (DTS1070). Data analysis was performed using Malvern Zetasizer software 8.01.4906.

BET Surface Area. BET measurements were performed using the 3P Micro 300 gas adsorption instrument at 77.4 K with nitrogen as the analysis gas. 3P Surface Area & Pore Size Analyzer System 10.03.02 software was used to analyze the recorded data.

Thermogravimetric analysis. TGA measurement was performed using a Mettler-Toledo TGA/SDTA 851^e thermogravimetric analyzer. 11 mg sample were weight into an Al_2O_3 crucible and heated from 25 to 900°C at a heating rate of 2°C min^{-1} under nitrogen atmosphere.

Scanning Electron Microscopy. The steel plates for scanning electron microscopy (SEM) were attached to aluminum holders with carbon film pads. SEM images were acquired using an FEI Nova NanoSEM 630 equipped with an EDAX-Pegasus X4M instrument (for EDX measurements). Acceleration voltages of 15 or 20 keV were used for EDX analysis.

Plasma Treatment. The plates were treated with argon using Plasma Cleaner PC 2000 from South Bay Technologies. Argon treatment was conducted at 175 mT and 20 W for 5 min.

Organic synthesis, characterization and analytics

Synthesis of Homoserine Lactone Hydrobromide (1) [69] 100 mL of a MilliQ-water-isopropanol-acetic acid mixture (5:5:2 v:v) was added to 10 g (*L*)-methionine (0.067 mol) and 10.2 g bromoacetic acid (0.073 mol). The solution was stirred at reflux for 18 h. The solvent was removed under reduced pressure resulting in an orange oil. 50 mL of a isopropanol : 30% hydrogen bromide in acetic acid mixture (4:1 v:v) was added where a white precipitate was formed. The white compound was collected by vacuum filtration and dried at reduced pressure, mp 226–229 °C (lit.[70] mp 226–228 °C).

Synthesis of *N*-α,α-Dibromoacetyl Homoserine Lactones (DAHSL) [69] 364 mg (2 mmol) compound **1** was dissolved in 4 mL water. 278 µL (2 mmol) triethylamine and 653 mg (3 mmol) dibromo acetic acid were added while stirring. After addition of 575 mg (3 mmol) 1-ethyl-3-(3-dimethylaminopropyl) carbodiimide hydrochloride (3 mmol) the solution was stirred at room temperature overnight. The aqueous phase was extracted three times with ethyl acetate (20 mL). The organic phase was washed with saturated aqueous $NaHCO_3$ solution, brine and dried with $MgSO_4$. After filtration, the solvent was removed under reduced pressure resulting in a white product. Via column chromatography on silica gel the product was purified (Ethyl acetate:petroleum ether 4:1).

^{1}H NMR (400 MHz, $CDCl_3$): δ (ppm) = 2.16-2.30 (1H, m); 2.88-2.98 (1H, m); 4.33 (1H, ddd, *J* = 11.3 Hz, 9.4 Hz, 5.8 Hz); 4.47–4.59 (2H, m); 5.85 (1H, s); 6.96 (1H, s). (Figure S5-7)

^{1}H-NMR. For all measurements solution NMR measurements, a commercial Bruker 2 channel 5 mm inverse probe head was used. Measurements were conducted at 295 K on a Bruker Avance DRX 400 MHz spectrometer (Bruker Biospin GmbH, Rheinstetten, Germany) operating at a proton frequency of 400.31 MHz.

LC-MS/MS. The LC system consisted of an Agilent 1260 Infinity Series (Waldbronn, Germany) equipped with an isocratic pump, switching valve to cut off the first two, and last seven minutes of each LC run. The separation was achieved with a Poroshell 120 C18 column (3 x 50 mm, 2.7 µm, Agilent) using a flow rate of 0.3 mL·min^{-1}. The temperature of the column oven was set to 40 °C and the injection volume was 10 µL. For elution, MilliQ-water and acetonitrile/MilliQ-water (90/10 v/v) with 2 mM ammonium formate and 0.1% formic acid were used. The generic LC gradient from Nürenberg *et al*. was applied.[71] For detection, a triple-quadrupole mass spectrometer system (QqQ-LIT-MS, API 6500+

QTrap, Sciex, Darmstadt, Germany) was used with electrospray ionisation (ESI) in positive ion mode for C_4-HSL and 3-oxo-C_{12}-HSL. The multiple reaction monitoring (MRM) parameters were summarized in Table 5-2. For negative ion mode measurements (DAHSL and DAHS) the eluents were used without ammonium formate and 100% acetonitrile for eluent B.

Table 5-2. Selected MRM parameter of the Targets for LC-MS/MS.

Analyte	Precursor	Fragment	CE [V]	DP [V]	CXP [V]
DBHL	299.9	126	-14	-20	-16
		79	-45	-20	-10
		81	-47	-20	-10
		173	-24	-20	-16
		98	-22	-20	-17
		70	-27	-20	-10
Hyd-DBH	317.9	79	-17	-20	-10
		81	-17	-20	-10
		156	-14	-20	-20
		128	-25	-20	-12
		144	-21	-20	-16
		300	-15	-20	-10
C_4-HSL	172.0	102	14	18	8
		74	19	18	11
3-oxo-C_{12}-HSL	298	102	19	43	8
		197	20	43	16

LC-HRMS. For high resolution measurements the same LC method as for the LC-MS/MS measurements was used. However, the eluents were adapted from the method of Nürenberg *et al.* 2015 to obtain a more general LC method.[71] Briefly, 100% MilliQ-water for Eluent A and 100% acetonitrile for Eluent B (both with 0.1% formic acid) were used. For detection, a TripleTOF 6600 (Sciex, Darmstadt, Germany) equipped with an ESI source was used. Calibration was done by a calibrant delivery system (CDS) after every five samples. Every sample was measured in positive and negative ion mode and MS^2 spectra were recorded for the eight most intense ions from the survey scans. More details on the source and fragmentation parameters for this method reported in Nürenberg *et al.* 2015.[71]

Degradation Experiments. Degradation was performed in batch experiments in triplicate with blank reactions. The reaction medium was MilliQ-water with additives of 30 mM NaBr, 25 µg·mL^{-1} CeO_2 NCs suspension and 5 µM substrate. A six-fold excess of H_2O_2 (30 µM; controlled by Hach Lange, LCW 058) was spiked into the stirred solution to start the reaction. The samples were taken as aliquots at discrete time intervals and the reaction was

stopped with an excess of sodium thiosulfate (20-fold excess compared to reactive agents). All samples were centrifuged (18 000 rpm, 15 min, 4 °C; Mikro 220R Hetterich) before injection to remove the NCs in solution. Quantification was performed by external calibration with 5 calibration points in a range from 0.5 µM to 5 µM using C_6-d_3-HSL (100 nM) as an internal standard to compensate matrix effects and intensity variations during measurements. The measurements were performed with the LC-HRMS method to detect substrate and formed reaction products. However, the MS system was a Triple TOF 5600 system (Sciex, Darmstadt, Germany) instead of the Triple TOF 6600 system (Sciex, Darmstadt, Germany).

Biological characterization and experiments

Confocal Laser scanning Microscopy (Cell Tests). Confocal Laser Scanning Microscopy (CLSM) images of cell viability were acquired on a Leica TCS-SP8 AOBS SMD microscope with an HCPL APO CS2 10 × /0.40 DRY objective. Cells expressing GFP were excited with an argon laser (488 nm); fluorescence was detected between 500 and 600 nm using a PMT2 detector. Transmission was detected using a PMT Trans detector.

Confocal Laser Scanning Microscopy (bacteria). *P. aeruginosa* PA14 was cultivated in LB medium over night at 30 °C. The cultures were diluted in LB, in a volume of 3 mL per well of a 6-well polystyrene microtiter plate (Sarstedt, Nürnbrecht) at a final OD_{600} of 0.5. Additionally, KBr (Roth, Karlsruhe, Germany) and H_2O_2 (Roth, Karlsruhe, Germany) at a final concentration of 32 mM and 0.8 mM, respectively, were added to the wells. The blank steel plates containing only PUR lacquer and the plates containing nanoparticle lacquer were then added to the wells. The microtiter plate was then incubated for 72 h under gentle shaking (150 rpm) at 30 °C. Every 24 h H_2O_2 was added at a final concentration of 0.8 mM. Then, the plates were rinsed with water to remove the planktonic cells. Afterwards, the plates were placed in 3 mL of a combined SYTO 9 and propidium iodide solution (Thermo Fisher, Pittsburgh, USA) and incubated for 30 minutes at 30 °C. Then, the plates were rinsed again with water and mounted on microscopy slides. Biofilm samples were microscopically analyzed on an Axio Imager 2 fluorescence microscope, which is especially designed for material surface analysis (Carl Zeiss, Jena, Germany). The fluorophore SYTO 9 was visualized with an excitation of 470 nm while propidium iodide was visualized with an excitation of 558 nm. The emission settings for the used filters were

509 nm for SYTO 9 and 570 nm for propidium iodide. The images were then processed using the ZEN 3.3 blue software. The combined fluorescence intensities within the different field of views were then quantified and set into correlation using ImageJ software (Version: 2.0.0-rc-69/1.52n).

Bacterial Strains and Growth Conditions. In this study the following bacteria were used: *P. aeruginosa* PA14, *K. pneumoniae* DSM 4270, *M. mesophilicum* DSM 1708, *P. gallaeciensis* DSM 26640, *S. aureus* DSM 11823 and *A. tumefaciens A136*. *P. aeruginosa*, *K. pneumoniae* and *S. aureus* were aerobically cultivated in LB medium [1% (w/v) NaCl; 1% (w/v) tryptone; 0.5% (w/v) yeast extract] at 30 °C. *M. mesophilicum* was cultivated aerobically in M1 medium [0,5 % (w/v) soy peptone; 0,3 % meat extract; pH=7.0]. *P. gallaeciensis* was cultivated aerobically in 2216 marine broth (Thermo Fisher Scientific). A. tumefaciens A136 was cultivated aerobically in LB medium supplemented with spectinomycine (50 $\mu g \cdot mL^{-1}$) and tetracycline (10 $\mu g \cdot mL^{-1}$). For preparation of agar plates, 1.5% (w/v) agar was added to the medium.

Biofilm Assays with single CeO2 nanoparticles. For quantification of bacterial biofilm production, a modified method of already published protocols was used.[72,73] Briefly, *P. aeruginosa*, *K. pneumoniae*, *S. aureus*, *M. mesophilicum* and *P. gallaeciensis* were cultivated in LB medium, M1 medium and marine broth 2216, respectively, over night at 30 °C. Then, the cultures were diluted in the respective medium in the presence or absence of 28 $\mu g \ mL^{-1}$ CeO_2, in a volume of 135 µl per well of a 96-well polystyrene microtiter plate (Sarstedt, Nümbrecht) at a final OD_{600} of 0.5. Additionally, KBr (Roth, Karlsruhe, Germany) and H_2O_2 (Roth, Karlsruhe, Germany) at a final concentration of 32 mM and 0.8 mM respectively were added to the wells. The microtiter plate was then incubated for 72 h under gentle shaking (150 rpm) at 30 °C. Every 24 h H_2O_2 was added at a final concentration of 0.8 mM. Then, the liquid phase of the culture was removed by turning the plate. The planktonic cells were removed by gently submerging the plate two times in a water tub. After drying for 5 min, 135 µl of 1% (w/v) crystal violet (Merck, Darmstadt) was added to the wells. After 15 min incubation at room temperature, unbound crystal violet was removed by gently submerging the plate for two times in water. The plate was then air-dried over-night at room temperature. For quantification, 135 µl of 30% (v/v) acetic acid (Roth, Karlsruhe) was added to solubilize the crystal violet from the biofilm. After 15 min of incubation at room temperature, absorbance was quantified in a plate reader (Tecan, Salzburg) at 575 nm.

Biofilm Assays with CeO₂-painted objects. For quantification of bacterial biofilm production, a modified method of previously published protocols was used.[72,73] Briefly, *P. aeruginosa*, *K. pneumoniae*, *M. mesophilicum* and *P. gallaeciensis* were cultivated in LB medium, M1 medium and marine broth 2216, respectively, over night at 30 °C . The cultures were then diluted in their respective medium in a volume of 3 mL per well of a 6-well polystyrene microtiter plate (Sarstedt, Nürnbrecht) at a final optical density at 600 nm (OD_{600}) of 0.5. Additionally, KBr (Roth, Karlsruhe, Germany) and H_2O_2 (Roth, Karlsruhe, Germany) were added to the wells at final concentration of 32 mM and 0.8 mM, respectively. Then, the blank objects and CeO₂-containing composites were immersed. Subsequently, the microtiter plate was incubated for 72 h under gentle shaking (150 rpm) at 30°C. H_2O_2 was added stepwise at a final concentration of 0.8 mM every 24 h. Then, the objects were rinsed with water to remove the planktonic cells. After drying for 5 min, 3 mL of 1% (w/v) crystal violet (Merck, Darmstadt) was added to the wells containing the samples. After 30 min incubation at room temperature, unbound crystal violet was removed by gently submerging the samples two times in water. The objects were then air-dried over-night at room temperature. For quantification, 3 mL of 30% (v/v) acetic acid (Roth, Karlsruhe) was added to the samples to solubilize the crystal violet from the biofilm. After 15 min of incubation at room temperature, absorbance was quantified in a plate reader (Tecan, Salzburg) at 575 nm.

Biofilm Assays with addition of homoserine lactones and DAHSL. For quantification of bacterial biofilm production, a modified method of previously published protocols was used.[72,73] Briefly, *P. aeruginosa* was cultivated in LB medium over night at 30 °C. Then, the culture was diluted in LB medium in the presence or absence of different concentrations of C₄-HSL, 3-oxo-C₁₂-HSL and DAHSL respectively, in a volume of 135 µl per well of a 96-well polystyrene microtiter plate (Sarstedt, Nümbrecht) at a final OD_{600} of 0.5. Subsequently, the microtiter plate was incubated for 72 h under gentle shaking (150 rpm) at 30°C. Before the biofilm staining, the OD_{600} was quantified in a plate reader in order to observe effects on the bacterial cell densitiy (Tecan, Salzburg). Then, the liquid phase of the culture was removed by turning the plate. The planktonic cells were removed by gently submerging the plate two times in a water tub. After drying for 5 min, 135 µl of 1% (w/v) crystal violet (Merck, Darmstadt) was added to the wells. After 15 min incubation at room temperature, unbound crystal violet was removed by gently submerging the plate for two times in water. The plate was then air-dried over-night at room temperature. For

quantification, 135 μl of 30% (v/v) acetic acid (Roth, Karlsruhe) was added to solubilize the crystal violet from the biofilm. After 15 min of incubation at room temperature, absorbance was quantified in a plate reader (Tecan, Salzburg) at 575 nm.

Bromide concentration assay. *P. aeruginosa* was grown over night in LB medium at 30 °C. The culture was then diluted in LB medium at a final OD_{600} of 0.5. Additionally, several variations and combinations of CeO_2, H_2O_2 and NaBr were tested. Furthermore, different NaBr concentrations (30 μM and 30 mM) were added to the bacteria. The bacteria were then incubated for 24 h at 30 °C. Afterwards, the samples were centrifuged at 4500 x g for 20 min. The bacterial supernatant was then filtered (0,22 μm, Merck, Darmstadt).

Cell Experiments. Osteoblasts (MG-63 GFP) in DMEM (10% FBS, 1% Gl., 1% P/S) were cultured at 37 °C and 5% CO_2 in 9.4 cm diameter petri dishes. At a population density of approximately 80%, cells were detached from the culture vessel (trypsin-EDTA) and resuspended in 5 mL DMEM (10% FBS, 1% Gl, 1% P/S). For cell experiments, cells were diluted to a concentration of 1.6×10^5 cells mL^{-1}. Control experiments were performed in cell-adhesive petri dishes, whereas non-cell-adhesive Petri dishes were used for experiments on coated quartz glass slides. Cell viability was monitored by confocal laser scanning microscopy at 24 and 72 h. GFP-expressing cells were excited with an argon laser (488 nm) to measure fluorescence between 500 and 600 nm.

Bacteria Samples for LC-MS. *P. aeruginosa* PA14 was kept aerobically in LB medium like "Bacterial strains and Growth Condition" and 32 mM NaBr, 0.8 mM H_2O_2 and 28 μg·mL^{-1} CeO_2 NCs was added. The culture was incubated 24 h under gentle shaking (150 rpm) at 30°C. For supernatants the culture was centrifuged at 5000 x g for 20 min and the culture supernatant was filtered (pore size 0.22 μm, Merck, Darmstadt, Germany). The supernatants were extracted with ethyl acetate three times and evaporated to dryness. The residue was re-dissolved with methanol and MilliQ-water (50/50 v/v). For spike experiments with DAHSL 100 nM were added to the bacteria with same condition together with various blank reactions. All experiments were performed in triplicate.

Biosensor assay. External 3-oxo-C_{12}-HSL (10 μM) was incubated in presence or absence of 28 μg·mL^{-1} CeO_2 NC´s for 8 h at RT. Additionally, KBr and H_2O_2 were added at a final concentration of 32 mM and 0,8 mM, respectively. The reaction mixtures (500 μl) were then added to an *A. tumefaciens* A136 culture, which was adjusted to an OD_{600} of 0.5. Two different substrates were used (5-Brom-4-chlor-3-indoxyl-β-D-galactopyranosid (X-Gal)

and o-Nitrophenyl-β-D-galactopyranosid (ONPG)). After the addition of 250 µg·mL^{-1} X-gal (5-Brom-4-chlor-3-indoxyl-β-D-galactopyranosid), the cultures were incubated at 30 °C for 8 h. Finally, the cultures were transferred to 1.5 mL tubes and were centrifuged at 10.000 x g for 5 min. The supernatant was then transferred to 96-well plates and the absorbance at 630 nm was measured using a plate reader (Tecan, Switzerland). For the ONPG assay, the reaction mixtures were also added to the *A. tumefaciens* A136, which was adjusted to an OD$_{600}$ of 0.5. Afterwards the cultures were incubated at 30 °C for 8 h. 1 mL of each culture was then collected and centrifuged at 5000 x g for 5 min. The supernatant was then discarded, and the cells were resuspended in 1 mL buffer Z [60 mM Na$_2$HPO$_4$; 40 mM NaH$_2$PO$_4$; 1 mM MgSO$_4$; 50 mM beta-Mercapto-EtOH]. Only buffer Z served as a negative control. The OD$_{600}$ of the cultures was then measured. By adding 100 µl Chloroform and 50 µl 0.1% SDS and shaking, the cells were lysed. The samples were then incubated for 30 min at 30 °C. 160 µl of fresh prepared 4 mg·mL^{-1} ONPG solution was then added to each sample. Time was stopped until samples turned yellow. The reaction was then stopped by adding 500 µl of 1 M Na$_2$CO$_3$. The cell fractions were then spinned down at 16000 x g for 2 min. The absorbance at 420 nm and 550 nm was then measured in a plate reader (Tecan, Salzburg. Miller units could then be calculated using the equation S3.)

5.6.   REFERENCES

1   Murray, C. J.; Ikuta, K. S.; Sharara, F.; Swetschinski, L.; Robles Aguilar, G.; Gray, A.; Naghavi, M. Global Burden of Bacterial Antimicrobial Resistance in 2019: A Systematic Analysis. *Lancet* **2022**, *399* (10325), 629–655.

2   Sharma, D.; Misba, L.; Khan, A. U. Antibiotics versus Biofilm: An Emerging Battleground in Microbial Communities. *Antimicrob. Resist. Infect. Control* **2019**, *8*, 76.

3   Tillotson, G. S.; Zinner, S. H. Burden of Antimicrobial Resistance in an Era of Decreasing Susceptibility. *Expert Rev. Anti-Infecti. Ther.* **2017**, *15* (7) 663–676.

4   Ling, L. L.; Schneider, T.; Peoples, A. J.; Spoering, A. L.; Engels, I.; Conlon, B. P.; Mueller, A.; Schäberle, T. F.; Hughes, D. E.; Epstein, S.; Jones, M.; Lazarides, L.; Steadman, V. A.; Cohen, D. R.; Felix, C. R.; Fetterman, K. A.; Millett, W. P.; Nitti, A. G.; Zullo, A. M.; Chen, C.; Lewis, K. A New Antibiotic Kills Pathogens without Detectable Resistance. *Nature* **2015**, *517* (7535), 455–459.

5   Lewis, K. Platforms for Antibiotic Discovery. *Nat. Rev. Drug Discov*. **2013**, 12(5), 371-387.

6   Martinez-Gutierrez, F.; Boegli, L.; Agostinho, A.; Sánchez, E. M.; Bach, H.; Ruiz, F.; James, G. Anti-Biofilm Activity of Silver Nanoparticles against Different Microorganisms. *Biofouling* **2013**, *29* (6), 651–660.

7   Chernousova, S.; Epple, M. Silver as Antibacterial Agent: Ion, Nanoparticle, and Metal. *Angew. Chem. Int. Ed.* **2013**, *52* (6), 1636–1653.

8   Quevedo, A. C.; Lynch, I.; Valsami-Jones, E. Silver Nanoparticle Induced Toxicity and Cell Death Mechanisms in Embryonic Zebrafish Cells. *Nanoscale* **2021**, *13* (12), 6142–6161.

9   Banerjee, I.; Pangule, R. C. R. S.; Kane, R. S.; Banerjee, I.; Pangule, R. C. R. S.; Kane, H. P. Antifouling Coatings: Recent Developments in the Design of Surfaces That Prevent Fouling by Proteins, Bacteria, and Marine Organisms. *Adv. Mater.* **2011**, *23* (6), 690–718.

10 Hasan, J.; Crawford, R. J.; Ivanova, E. P. Antibacterial Surfaces: The Quest for a New Generation of Biomaterials. *Trends Biotechnol.* **2013**, *31* (5), 295–304.

11 Zander, Z. K.; Becker, M. L. Antimicrobial and Antifouling Strategies for Polymeric Medical Devices. *ACS Macro Lett.* **2018**, *7* (1), 16–25.

12 Teisala, H.; Butt, H. J. Hierarchical Structures for Superhydrophobic and Superoleophobic Surfaces. *Langmuir* **2019**, *35* (33), 10689–10703.

13 Schneider, J.; Matsuoka, M.; Takeuchi, M.; Zhang, J.; Horiuchi, Y.; Anpo, M.; Bahnemann, D. W. Understanding TiO2 Photocatalysis: Mechanisms and Materials. *Chem. Rev.* **2014**, *114* (19), 9919–9986.

14 Das, K.; Roychoudhury, A. Reactive Oxygen Species (ROS) and Response of

Antioxidants as ROS-Scavengers during Environmental Stress in Plants. *Front. Environ. Sci.* **2014**, *2*, 53.

15   Bassler, B. L.; Losick, R. Bacterially Speaking. *Cell* **2006**, *125* (2), 237–246.

16   Camilli, A.; Bassler, B. L. Bacterial Small-Molecule Signaling Pathways. *Science* **2006**, *311* (5764), 1113–1116.

17   Fuqua, W. C.; Winans, S. C.; Peter Greenberg2, E. MINIREVIEW Quorum Sensing in Bacteria: The LuxR-LuxI Family of Cell Density-Responsive Transcriptional Regulatorst. *J. Bacteriol.* **1994**, *176* (2), 269–275.

18   Papenfort, K.; Bassler, B. L. Quorum Sensing Signal–Response Systems in Gram-Negative Bacteria. *Nat. Rev. Microbiol.* **2016**, *14* (9), 576–588.

19   Brameyer, S.; Bode, H. B.; Heermann, R. Languages and Dialects: Bacterial Communication beyond Homoserine Lactones. *Trends Microbiol.* **2015**, *23* (9), 521–523.

20   Galloway, W. R. J. D.; Hodgkinson, J. T.; Bowden, S. D.; Welch, M.; Spring, D. R. Quorum Sensing in Gram-Negative Bacteria: Small-Molecule Modulation of AHL and AI-2 Quorum Sensing Pathways. *Chem. Rev.* **2010**, *111* (1), 28–67.

21   Butler, A.; Sandy, M. Mechanistic Considerations of Halogenating Enzymes. *Nature* **2009**, *460* (7257), 848–854.

22   Wever, R.; Van Der Horst, M. A. The Role of Vanadium Haloperoxidases in the Formation of Volatile Brominated Compounds and Their Impact on the Environment. *Dalton Trans.* **2013**, *42* (33), 11778–11786.

23   Weichold, V.; Milbredt, D.; Van Pée, K. H. Specific Enzymatic Halogenation—From the Discovery of Halogenated Enzymes to Their Applications In Vitro and In Vivo. *Angew. Chem. Int. Ed.* **2016**, *55* (22), 6374–6389.

24   Agarwal, V.; Miles, Z. D.; Winter, J. M.; Eustáquio, A. S.; El Gamal, A. A.; Moore, B. S. Enzymatic Halogenation and Dehalogenation Reactions: Pervasive and Mechanistically Diverse. *Chem. Rev.* **2017**, *117* (8), 5619–5674.

25   Sandy, M.; Carter-Franklin, J. N.; Martin, J. D.; Butler, A. Vanadium Bromoperoxidase from Delisea Pulchra: Enzyme-Catalyzed Formation of Bromofuranone and Attendant Disruption of Quorum Sensing. *Chem. Commun.* **2011**, *47* (44), 12086.

26   Wei, H.; Wang, E. Nanomaterials with Enzyme-like Characteristics (Nanozymes): Next-Generation Artificial Enzymes. *Chem. Soc. Rev.* **2013**, *42* (14), 6060–6093.

27   Korschelt, K.; Tahir, M. N.; Tremel, W. A Step into the Future: Applications of Nanoparticle Enzyme Mimics. *Chem. Eur. J.* **2018**, *24* (39), 9703–9713.

28   *Nanozymology*; Yan, X., Ed.; Nanostructure Science and Technology; Springer Singapore: Singapore, 2020.

29   Herget, K.; Frerichs, H.; Pfitzner, F.; Tahir, M. N.; Tremel, W. Functional Enzyme Mimics for Oxidative Halogenation Reactions That Combat Biofilm Formation. *Adv. Mater.* **2018**, *30* (36), 1707073.

30   Sels, B.; De Vos, D.; Buntinx, M.; Plerard, F.; Kirsch-De Mesmaeker, A.; Jacobs, P. Layered Double Hydroxides Exchanged with Tungstate as Biomimetic Catalysts for Mild Oxidative Bromination. *Nature* **1999**, *400* (6747), 855–857.

31   Conte, V.; Floris, B. Vanadium and Molybdenum Peroxides: Synthesis and Catalytic Activity in Oxidation Reactions. *Dalton Trans.* **2011**, *40* (7), 1419–1436.

32   Madaan, N.; Shiju, N. R.; Rothenberg, G. Predicting the Performance of Oxidation Catalysts Using Descriptor Models. *Catal. Sci. Technol.* **2016**, *6* (1), 125–133.

33   Natalio, F.; André, R.; Hartog, A. F.; Stoll, B.; Jochum, K. P.; Wever, R.; Tremel, W. Vanadium Pentoxide Nanoparticles Mimic Vanadium Haloperoxidases and Thwart Biofilm Formation. *Nat. Nanotechnol.* **2012**, *7* (8), 530–535.

34   Herget, K.; Hubach, P.; Pusch, S.; Deglmann, P.; Götz, H.; Gorelik, T. E.; Gural'skiy, I. A.; Pfitzner, F.; Link, T.; Schenk, S.; Panthöfer, M.; Ksenofontov, V.; Kolb, U.; Opatz, T.; André, R.; Tremel, W. Haloperoxidase Mimicry by CeO2−x Nanorods Combats Biofouling. *Adv. Mater.* **2017**, *29* (4), 1603823.

35   Frerichs, H.; Pütz, E.; Pfitzner, F.; Reich, T.; Gazanis, A.; Panthöfer, M.; Hartmann, J.; Jegel, O.; Heermann, R.; Tremel, W. Nanocomposite Antimicrobials Prevent Bacterial Growth through the Enzyme-like Activity of Bi-Doped Cerium Dioxide (Ce 1−x Bi x O 2−δ). *Nanoscale* **2020**, *12* (41), 21344–21358.

36   Chen, Z.; Wang, Z.; Ren, J.; Qu, X. Enzyme Mimicry for Combating Bacteria and Biofilms. *Acc. Chem. Res.* **2018**, *51* (3), 789–799.

37   Maura, D.; Rahme, L. G. Pharmacological Inhibition of the Pseudomonas Aeruginosa MvfR Quorum-Sensing System Interferes with Biofilm Formation and Potentiates Antibiotic-Mediated Biofilm Disruption. *Antimicrob. Agents Chemother.* **2017**, *61* (12).

38   Dos Santos, M. L.; Lima, R. C.; Riccardi, C. S.; Tranquilin, R. L.; Bueno, P. R.; Varela, J. A.; Longo, E. Preparation and Characterization of Ceria Nanospheres by Microwave-Hydrothermal Method. *Mater. Lett.* **2008**, *62* (30), 4509–4511.

39   Yang, H.; Huang, C.; Tang, A.; Zhang, X.; Yang, W. Microwave-Assisted Synthesis of Ceria Nanoparticles. *Mater. Res. Bull.* **2005**, *40* (10), 1690–1695.

40   Yang, G.; Park, S. J. Conventional and Microwave Hydrothermal Synthesis and Application of Functional Materials: A Review. *Materials.* **2019**, *12* (7), 1177.

41   Köse-Mutlu, B.; Ergön-Can, T.; Koyuncu, I.; Lee, C.-H. Quorum Quenching for Effective Control of Biofouling in Membrane Bioreactor: A Comprehensive Review of Approaches, Applications, and Challenges. *Environ. Eng. Res.* **2019**, *24* (4), 543–558.

42   Holloway, P.; Trevors, J. T.; Lee, H. A Colorimetric Assay for Detecting Haloalkane Dehalogenase Activity. *J. Microbiol. Methods* **1998**, *32* (1), 31–36.

43   Hall-Stoodley, L.; Costerton, J. W.; Stoodley, P. Bacterial Biofilms: From the Natural Environment to Infectious Diseases. *Nat. Rev. Microbiol.* **2004**, *2* (2), 95–108.

44   Bodey, G. P.; Bolivar, R.; Fainstein, V.; Jadeja, L. Infections Caused by Pseudomonas Aeruginosa. *Rev. Infect. Dis.* **1983**, *5* (2), 279–313.

45   Parthé, S., Welker, A., Meier, C., Knorr, B., & Schumacher, Application study on aerosol-reducing hygienic siphons for control of a 4MRGN Pseudo-monas aeruginosa outbreak on a neurological early stage rehabilitation ward. *Hyg. Med.* **2016**, *41*(12), E194–E199.

46   Chung, P. Y. The Emerging Problems of Klebsiella Pneumoniae Infections: Carbapenem Resistance and Biofilm Formation. *FEMS Microbiol. Lett.* **2016**, *363* (20), 219.

47   Falkinham, J. O.; Williams, M. D.; Kwait, R.; Lande, L. Methylobacterium Spp. as an Indicator for the Presence or Absence of Mycobacterium Spp. *Int. J. Mycobacteriology* **2016**, *5* (2), 240–243.

48   Kovaleva, J.; Degener, J. E.; Van Der Mei, H. C. Methylobacterium and Its Role in Health Care-Associated Infection. *J. Clin. Microbiol.* **2014**, *52* (5), 1317–1321.

49   Thole, S.; Kalhoefer, D.; Voget, S.; Berger, M.; Engelhardt, T.; Liesegang, H.; Wollherr, A.; Kjelleberg, S.; Daniel, R.; Simon, M.; Thomas, T.; Brinkhoff, T. Phaeobacter Gallaeciensis Genomes from Globally Opposite Locations Reveal High Similarity of Adaptation to Surface Life. *ISME J.* **2012**, *6* (12), 2229–2244.

50   de Carvalho, C. C. C. R. Marine Biofilms: A Successful Microbial Strategy with Economic Implications. *Front. Mar. Sci.* **2018**, *5* (4), 126

51   Hentzer, M.; Riedel, K.; Rasmussen, T. B.; Heydorn, A.; Andersen, J. B.; Parsek, M. R.; Rice, S. A.; Eberl, L.; Molin, S.; Høiby, N.; Kjelleberg, S.; Givskov, M. Inhibition of Quorum Sensing in Pseudomonas Aeruginosa Biofilm Bacteria by a Halogenated Furanone Compound. *Microbiology* **2002**, *148* (1), 87–102.

52   Yin, W. F.; Purmal, K.; Chin, S.; Chan, X. Y.; Koh, C. L.; Sam, C. K.; Chan, K. G. N-Acyl Homoserine Lactone Production by Klebsiella Pneumonia Isolated from Human Tongue Surface. *Sensors* **2012**, *12* (3), 3472–3483.

53   Poonguzhali, S.; Madhaiyan, M.; Sa, T. Production of Acyl-Homoserine Lactone Quorum-Sensing Signals Is Wide-Spread in Gram-Negative Methylobacterium. *J. Microbiol. Biotechnol.* **2007**, *17* (2), 226–233.

54   Berger, M.; Neumann, A.; Schulz, S.; Simon, M.; Brinkhoff, T. Tropodithietic Acid Production in Phaeobacter Gallaeciensis Is Regulated by N-Acyl Homoserine Lactone-Mediated Quorum Sensing. *J. Bacteriol.* **2011**, *193* (23), 6576.

55   M. B. Miller, B. L. Bassler, Quorum Sensing in Bacteria. *Ann. Rev. Microbiol.* **2003**,

55, 165–199.

56   Tang, K.; Zhang, Y.; Yu, M.; Shi, X.; Coenye, T.; Bossier, P.; Zhang, X. H. Evaluation of a New High-Throughput Method for Identifying Quorum Quenching Bacteria. *Sci. Rep.* **2013**, *3* (1), 1–9.

57   Michels, J. J.; Allain, E. J.; Borchardt, S. A.; Hu, P.; McCoy, W. F. Degradation Pathway of Homoserine Lactone Bacterial Signal Molecules by Halogen Antimicrobials Identified by Liquid Chromatography with Photodiode Array and Mass Spectrometric Detection. *J. Chromatogr. A* **2000**, *898* (2), 153–165.

58   Borchardt, S. A.; Allain, E. J.; Michels, J. J.; Stearns, G. W.; Kelly, R. F.; McCoy, W. F. Reaction of Acylated Homoserine Lactone Bacterial Signaling Molecules with Oxidized Halogen Antimicrobials. *Appl. Environ. Microbiol.* **2001**, *67* (7), 3174–3179.

59   Ritzmann, N. H.; Mährlein, A.; Ernst, S.; Hennecke, U.; Drees, S. L.; Fetzner, S. Bromination of Alkyl Quinolones by Microbulbifer Sp. HZ11, a Marine Gammaproteobacterium, Modulates Their Antibacterial Activity. *Environ. Microbiol.* **2019**, *21* (7), 2595–2609.

60   Heeb, S.; Fletcher, M. P.; Chhabra, S. R.; Diggle, S. P.; Williams, P.; Cámara, M. Quinolones: From Antibiotics to Autoinducers. *FEMS Microbiol. Rev.* **2011**, 35 (2), 247–274.

61   Rampioni, G.; Falcone, M.; Heeb, S.; Frangipani, E.; Fletcher, M. P.; Dubern, J. F.; Visca, P.; Leoni, L.; Cámara, M.; Williams, P. Unravelling the Genome-Wide Contributions of Specific 2-Alkyl-4-Quinolones and PqsE to Quorum Sensing in Pseudomonas Aeruginosa. *PLoS Pathog.* **2016**, *12* (11), e1006029.

62   Hazan, R.; Que, Y. A.; Maura, D.; Strobel, B.; Majcherczyk, P. A.; Hopper, L. R.; Wilbur, D. J.; Hreha, T. N.; Barquera, B.; Rahme, L. G. Auto Poisoning of the Respiratory Chain by a Quorum-Sensing-Regulated Molecule Favors Biofilm Formation and Antibiotic Tolerance. *Curr. Biol.* **2016**, *26* (2), 195–206.

63   Fugère, A.; Séguin, D. L.; Mitchell, G.; Déziel, E.; Dekimpe, V.; Cantin, A. M.; Frost, E.; Malouin, F. Interspecific Small Molecule Interactions between Clinical Isolates of Pseudomonas Aeruginosa and Staphylococcus Aureus from Adult Cystic Fibrosis Patients. *PLoS One* **2014**, *9* (1), e86705.

64   Xu, J.; Saunders, C. W.; Hu, P.; Grant, R. A.; Boekhout, T.; Kuramae, E. E.; Kronstad, J. W.; DeAngelis, Y. M.; Reeder, N. L.; Johnstone, K. R.; Leland, M.; Fieno, A. M.; Begley, W. M.; Sun, Y.; Lacey, M. P.; Chaudhary, T.; Keough, T.; Chu, L.; Sears, R.; Yuan, B.; Dawson, T. L. Dandruff-Associated Malassezia Genomes Reveal Convergent and Divergent Virulence Traits Shared with Plant and Human Fungal Pathogens. *Proc. Natl. Acad. Sci. U. S. A.* **2007**, *104* (47), 18730–18735.

65   Hotterbeekx, A.; Kumar-Singh, S.; Goossens, H.; Malhotra-Kumar, S. In Vivo and In Vitro Interactions between Pseudomonas Aeruginosa and Staphylococcus Spp. *Front. Cell. Infect. Microbiol.* **2017**, *7*, 106.

66   Proctor, R. A.; von Eiff, C.; Kahl, B. C.; Becker, K.; McNamara, P.; Herrmann, M.; Peters, G. Small Colony Variants: A Pathogenic Form of Bacteria That Facilitates Persistent and Recurrent Infections. *Nat. Rev. Microbiol.* **2006**, *4*, 295–305.

67   Hiraishi, A.; Furuhata, K.; Matsumoto, A.; Koike, K. A.; Fukuyama, M.; Tabuchi, K. Phenotypic and Genetic Diversity of Chlorine-Resistant Methylobacterium Strains Isolated from Various Environments. *Appl. Environ. Microbiol.* **1995**, *61* (6), 2099–2107.

68   Deng, Y.; Wang, L.; Chen, Y.; Long, Y. Optimization of Staining with SYTO 9/Propidium Iodide: Interplay, Kinetics and Impact on Brevibacillus Brevis. *Biotechniques* **2020**, *69* (2), 89–99.

69   Syrpas, M.; Ruysbergh, E.; Blommaert, L.; Vanelslander, B.; Sabbe, K.; Vyverman, W.; De Kimpe, N.; Mangelinckx, S. Haloperoxidase Mediated Quorum Quenching by Nitzschia Cf Pellucida: Study of the Metabolization of N-Acyl Homoserine Lactones by a Benthic Diatom. *Mar. Drugs* **2014**, *12* (1), 352–367.

70   Persson, T.; Hansen, T. H.; Rasmussen, T. B.; Skindersø, M. E.; Givskov, M.; Nielsen, J. Rational Design and Synthesis of New Quorum-Sensing Inhibitors Derived from Acylated Homoserine Lactones and Natural Products from Garlic. *Org. Biomol. Chem.* **2005**, *3* (2), 253–262.

71   Nürenberg, G.; Schulz, M.; Kunkel, U.; Ternes, T. A. Development and Validation of a Generic Nontarget Method Based on Liquid Chromatography - High Resolution Mass Spectrometry Analysis for the Evaluation of Different Wastewater Treatment Options. *J. Chromatogr. A* **2015**, *1426*, 77–90.

72   O'Toole, G. A. Microtiter Dish Biofilm Formation Assay. *J. Vis. Exp.* **2010**, No. 47, 10–11.

73   O'Toole, G. A.; Kolter, R. Initiation of Biofilm Formation in Pseudomonas Fluorescens WCS365 Proceeds via Multiple, Convergent Signalling Pathways: A Genetic Analysis. *Mol. Microbiol.* **1998**, *28* (3), 449–461.

5.7. SUPPORTING INFORMATION
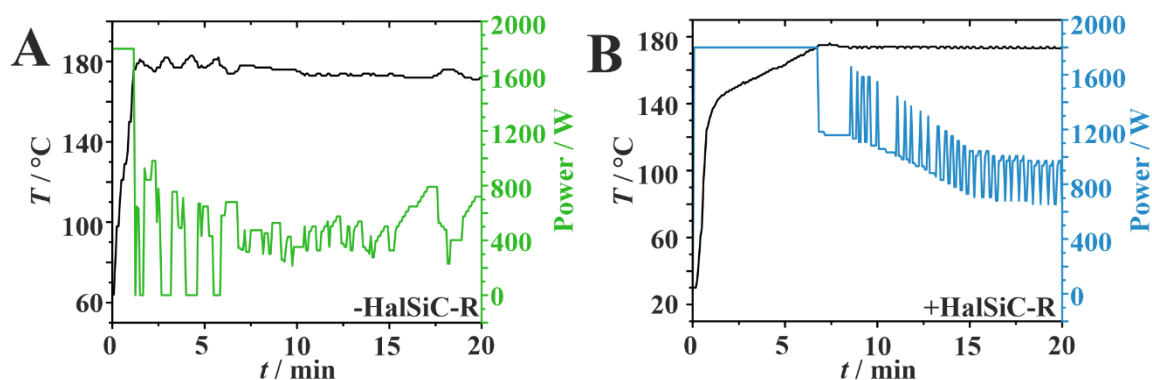
Figure S5-1. Temperature profile and power consumption during microwave assisted solvothermal synthesis (A) without and (B) with HalSiC-R heating rods (right). In the absence of HalSiC-R heating rods only one reaction could be carried out. With HalSiC-R rods, 12 reaction vessels were heated simultaneously.
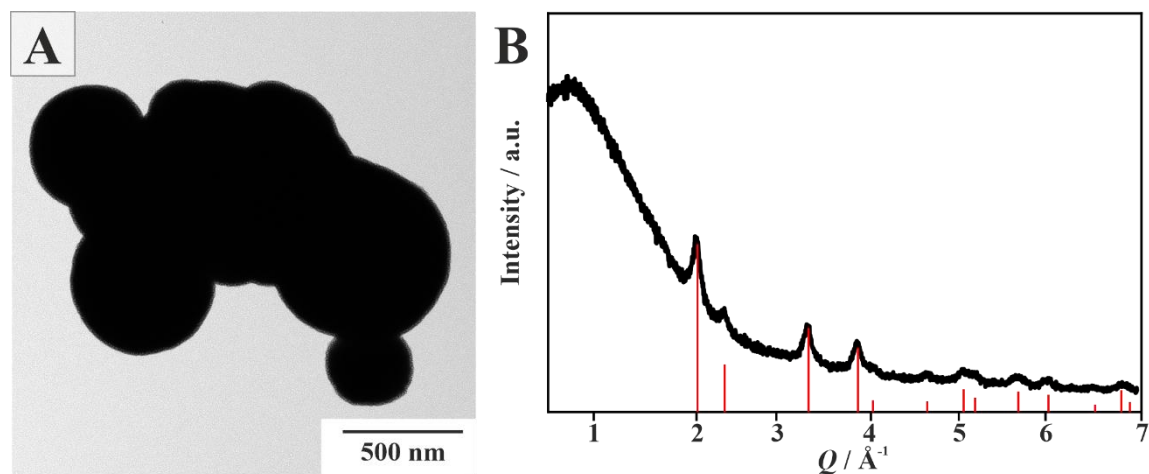
Figure S5-2. (A) TEM images and (B) X-ray powder diffraction pattern of CeO_2 MP synthesized without HalSiC-R heating rods. Red ticks indicate the calculated reflection positions for CeO_2 based on structural data from the ICSD data bank (ICSD# 88752).
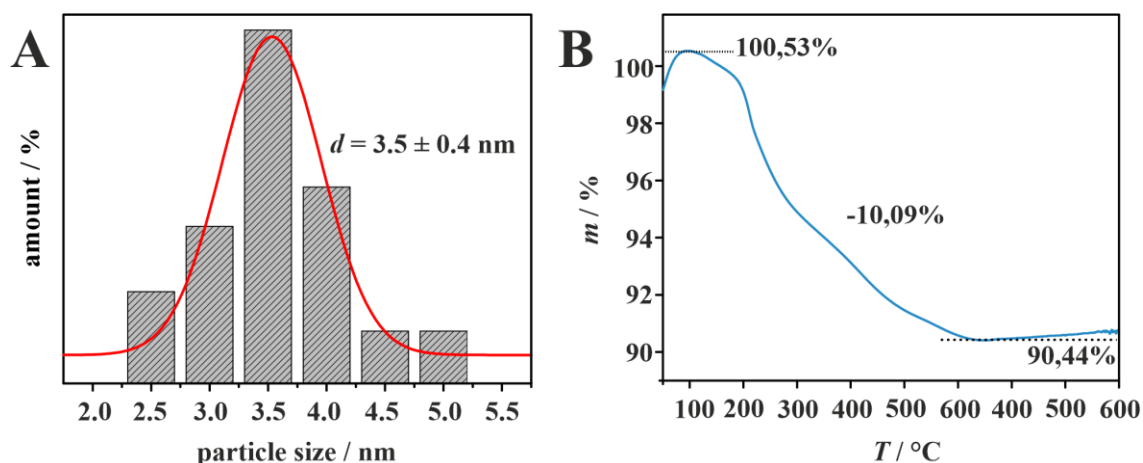
Figure S5-3. (A) Histogram of CeO_2 NCs and (B) thermogravimetric analysis of CeO_2 NCs indicating an organic amount of about 10%.

Hill equation (Equation S5-1)

$$v = \frac{v_{max} \cdot [S]_0{}^n}{K_m{}^n + [S]_0{}^n}$$ (eq.S5-1)

Rate of reaction (Equation S5-2)

$$TOF = \frac{v_{max}}{[Cat]_0} \xrightarrow{[Cat]_0 \rightarrow S_{BET} \cdot \beta_{Cat}} ROR = \frac{v_{max}}{S_{BET} \cdot \beta_{Cat}}$$ (eq.S5-2)

The turnover frequency (*TOF*) describes the catalytic activity of a substance, which is dependent on the surface area (S_{BET} ·), mass concentration (β_{Cat}) and reaction time (v_{max}). In order to determine the reaction velocities standardized to the surface, the rate of reaction *(ROR)* is calculated.[1]

Miller Units of β-galactosidase activity (Equation S5-3)

$$\text{Miller Units} = \frac{(OD_{420} - 1.75\, OD_{550})}{t \cdot V \cdot OD_{600}}$$ (eq.S5-3)

Where *t* is reaction time (min), *V* reaction volume (mL) and OD_λ the optical density at the mentioned wavelength (420, 550 or 600 nm)[2]

Table S5-1. Overview of Michaelis-Menten parameter K_m, v_{max}, Hill coefficient (*n*) and rate of reaction (*ROR*) for CeO$_2$ NC and MP respectively.

	v_{max} / μMol min^{-1}	K_m / μM	*n*	*ROR* / μmol m^{-2} min^{-1}
CeO₂ NC	0.286 ± 0.008	243 ± 30	2.1 ± 0.3	0.098
CeO₂ MP	0.065 ± 0.009	142 ± 50	1.3 ± 0.5	0.029
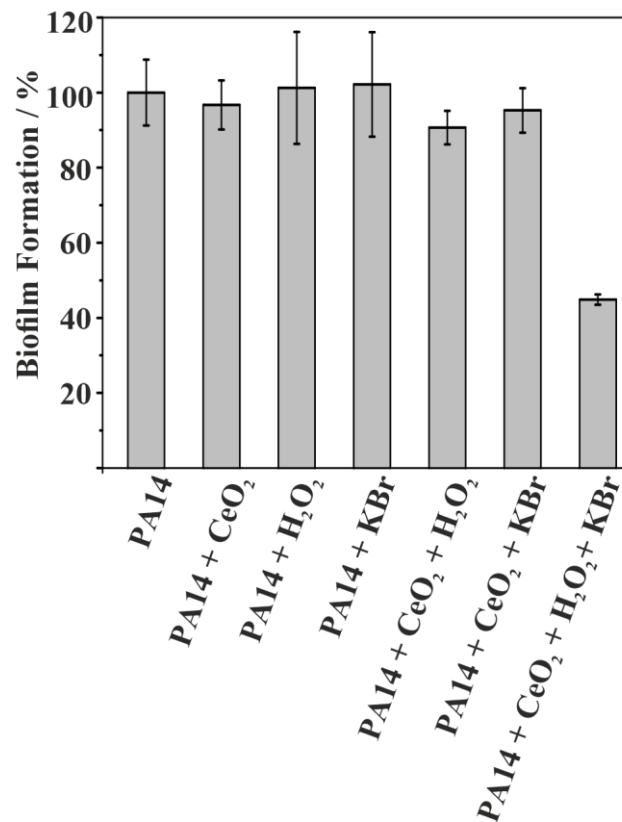
Figure S5-4. Quantification of the biofilm formed from *P. aeruginosa* (PA14) using a crystal violet staining assay. Bacteria were incubated with CeO_2 NCs, KBr and H_2O_2 in different variations to exclude HPO-like activity of the individual components. Each experiment was performed in triplicate.
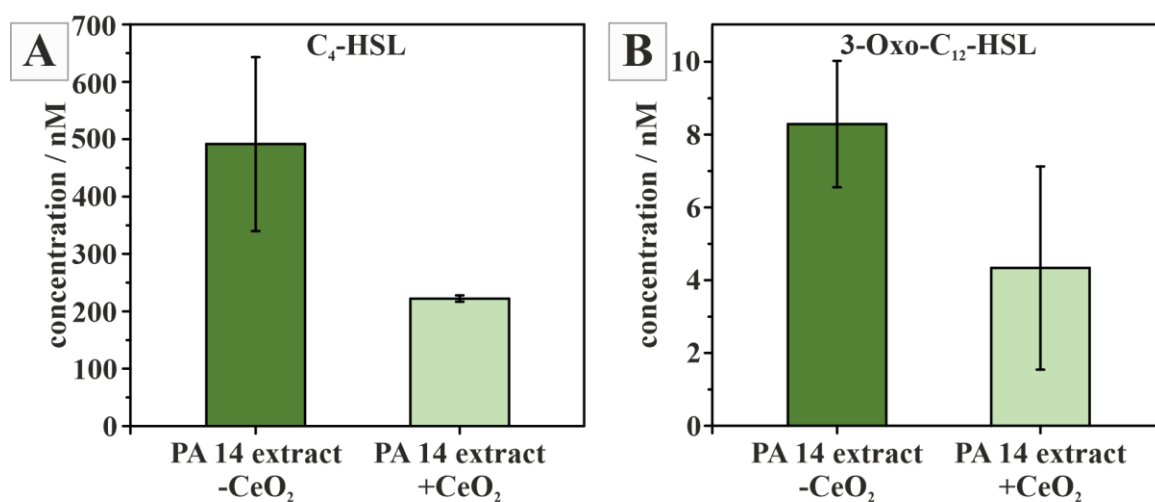
Figure S5-5. Concentration of the signaling molecules C_4-HSL and 3-oxo-C_{12}-HSL in supernatant of *P. aeruginosa (PA14)* in the presence and the absence of CeO_2 NC. Each experiment was performed in triplicate.
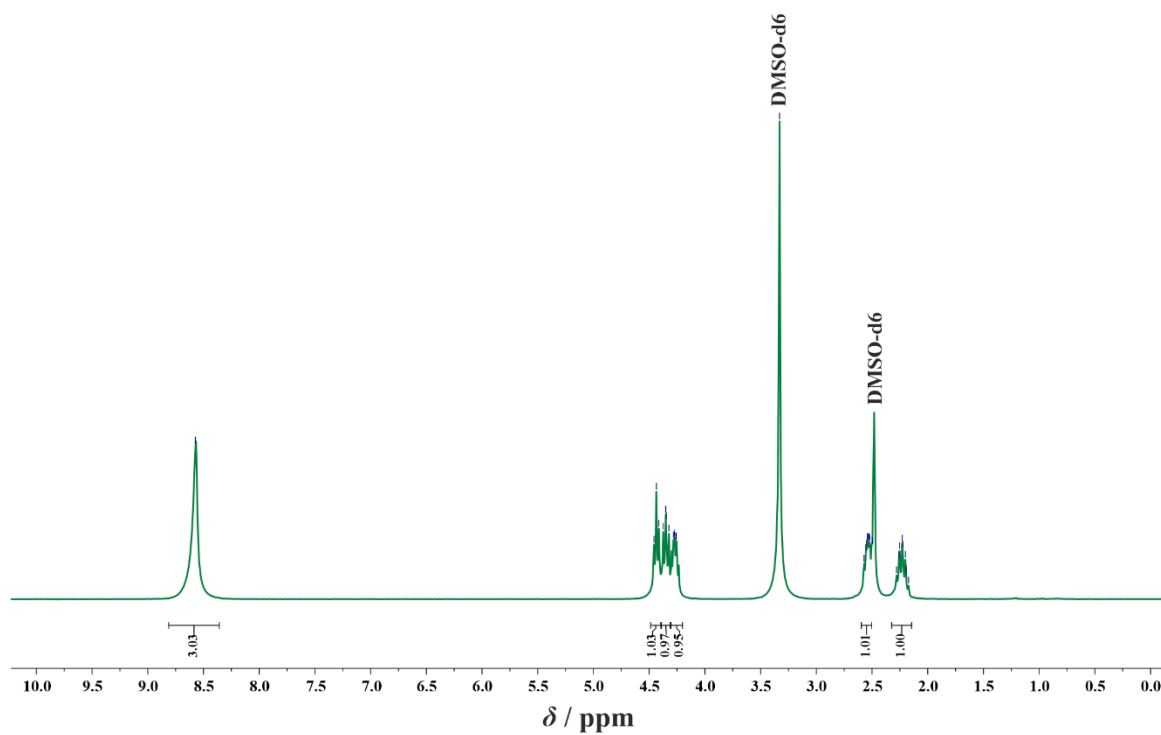
Figure S5-6. ^{1}H-NMR of homoserine lactone hydrobromide (1).

Figure S5-7. ^{1}H-NMR of *N*-α,α-dibromoacetyl homoserine lactones (DAHSL).

| Summenformel: $C_{16}H_{21}BrNO_2$ | Exakte Masse: 338.07502 | Error in ppm: -0.9 | Error in mmu: -0.31 | RDB: 7.0 |
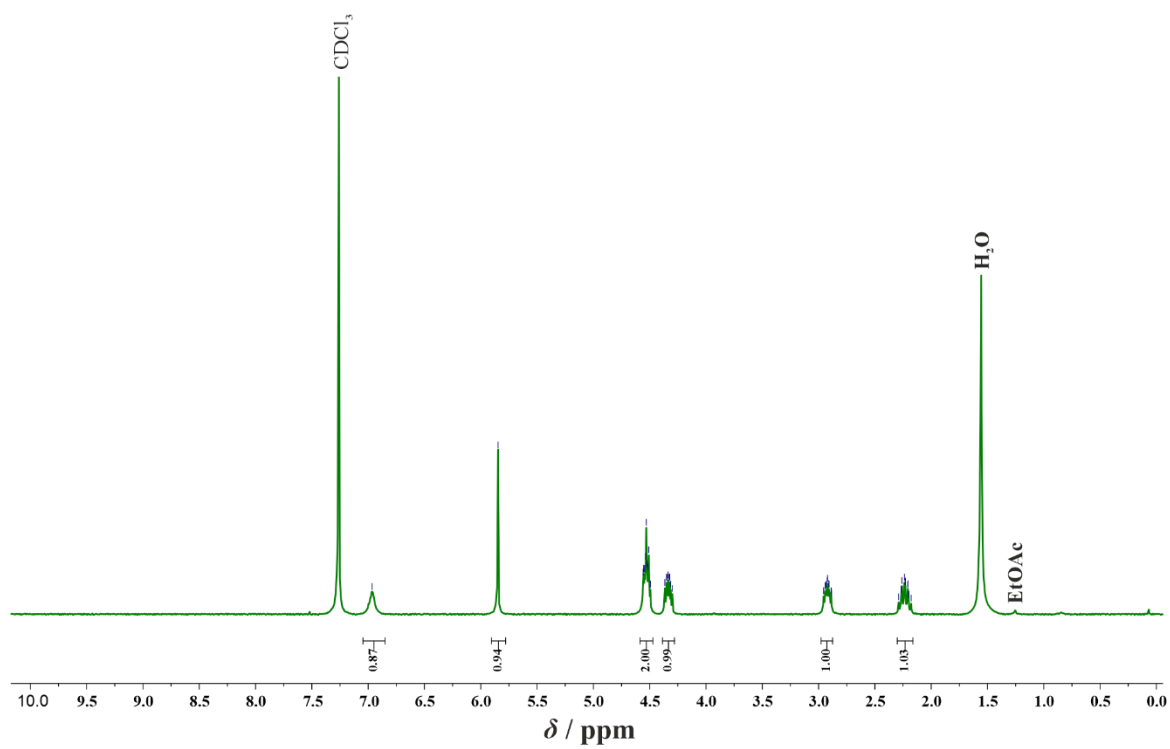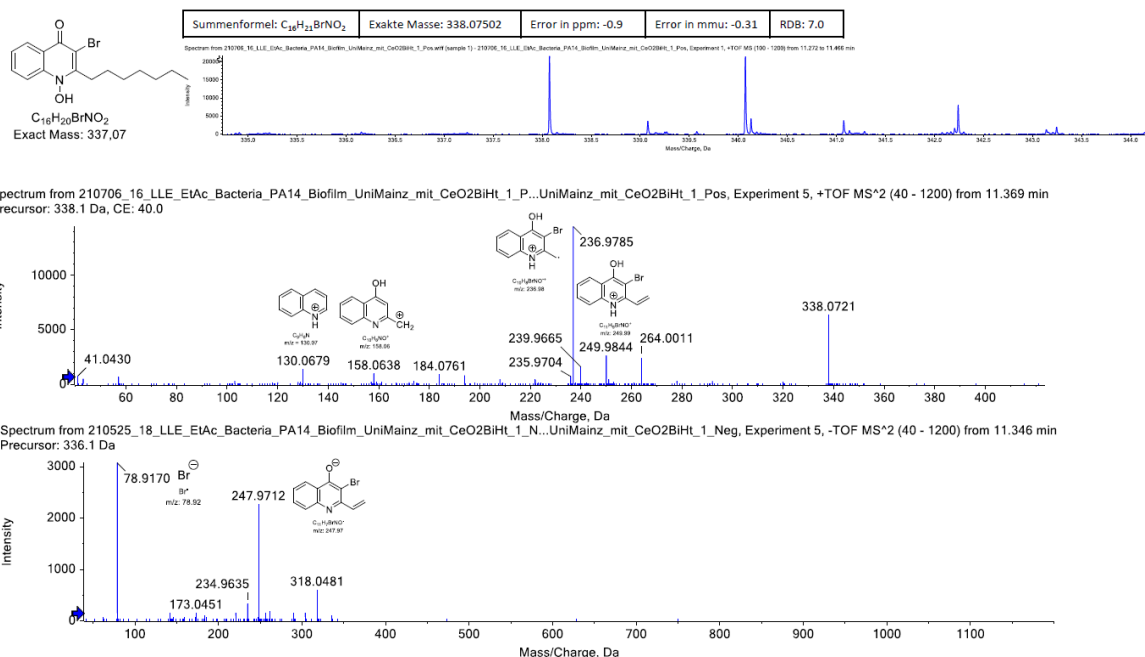
Figure S5-8. LC-HRMS data from the unknown compound with the exact mass of 337.07 (A) Full scan data in positive ion mode with calculated chemical formula (B) Fragment spectra in positive ion mode with proposed structure for the fragments (C) Fragment spectra in negative ion mode with proposed structure for the fragments.
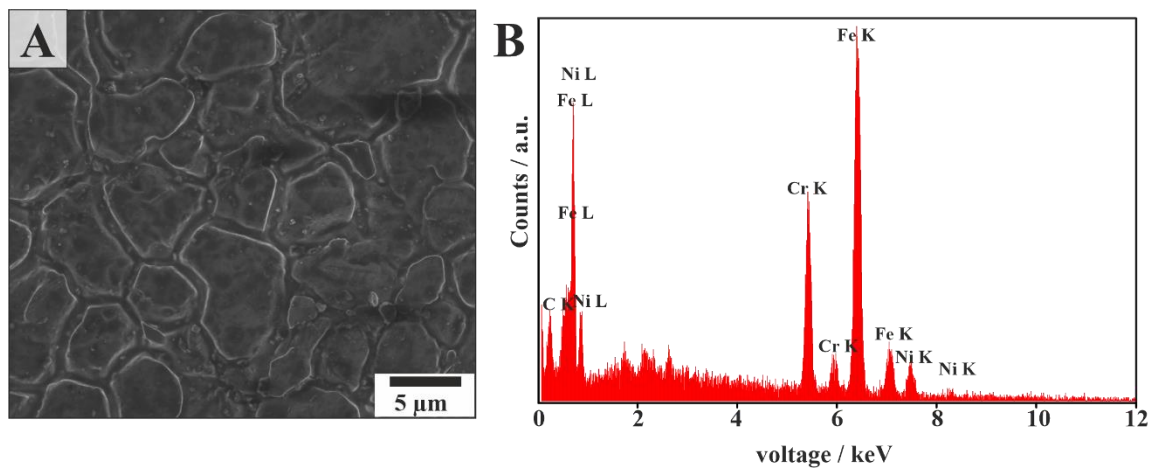
Figure S5-9. (A) SEM image and (B) EDX analysis of uncoated steel plates.
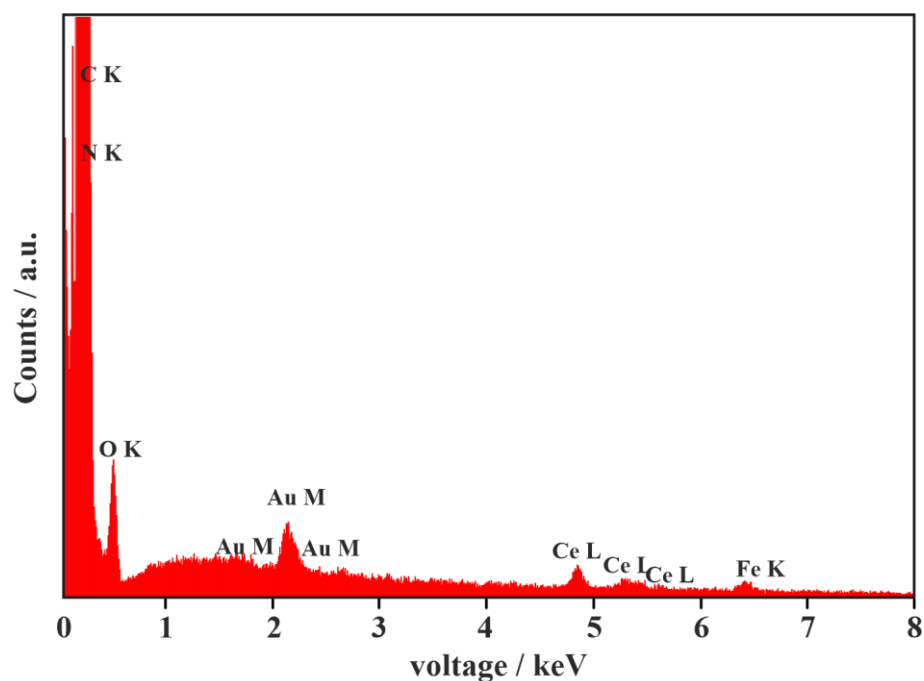
Figure S5-10. EDX analysis of painted steel plates with PUR lacquer containing 1% CeO_2 NCs. The additional gold signal is due to gold sputtering prior measuring

5.7.1. REFERENCES

1   Frerichs, H.; Pütz, E.; Pfitzner, F.; Reich, T.; Gazanis, A.; Panthöfer, M.; Hartmann, J.; Jegel, O.; Heermann, R.; Tremel, W. Nanocomposite Antimicrobials Prevent Bacterial Growth through the Enzyme-like Activity of Bi-Doped Cerium Dioxide (Ce 1−x Bi x O 2−δ). *Nanoscale* **2020**, *12* (41), 21344–21358.

2   Li, W.; Zhao, X.; Zou, S.; Ma, Y.; Zhang, K.; Zhang, M. Scanning Assay of β-Galactosidase Activity. *Appl. Biochem. Microbiol.* **2012**, *48* (6), 603–607.

<div style="text-align: right; font-size: 4em;">6</div>

IN-SITU GENERATION OF H_2O_2 USING DEPOT SUBSTANCES AND HETEROGENEOUS CATALYSIS

6.1. SUMMARY

Cerium dioxide displays several enzyme-like activities, but for both, haloperoxidase- and peroxidase-like reactions (chapters 3-5), addition of H_2O_2 is required to initiate the catalysis. Here, we investigated to what
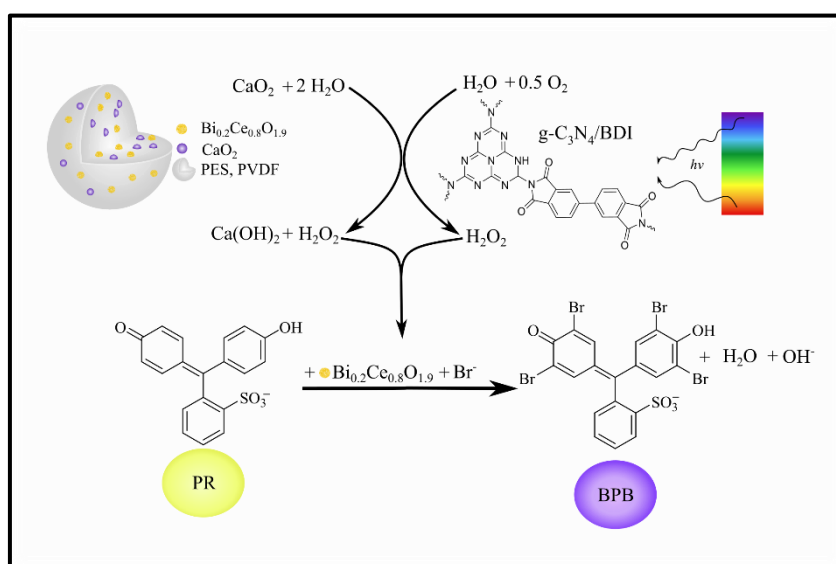
extent *in-situ* H_2O_2 generation can be realized to expand the scope of applications for cerium dioxide. For this purpose, two different approaches were taken. First, a H_2O_2 depot was prepared by embedding a H_2O_2 releasing substance (CaO_2) together with mesoporous $Bi_{0.2}Ce_{0.8}O_{1.9}$ nanoparticles in a polymer matrix. PES and PVDF were selected as polymer matrices because they are used in water treatment membranes or in medical applications and both suffer from biofouling. The generation of H_2O_2 by the polymer depot was investigated qualitatively using phenol red assays in the presence of KBr. Furthermore, bismuth-doped mesoporous ceria of the composition $Bi_{0.2}Ce_{0.8}O_{1.9}$ was prepared, since the performance of ceria is significantly improved when Ce^{4+} ions are partially replaced by Bi^{3+} ions. In addition, the effect of reaction time on the nanoparticles´ surface properties was investigated using specific surface area (S_{BET}) and zeta potential (ζ-potential) measurements to develop an optimum catalyst for the haloperoxidase-like reaction. In

addition, photochemical H_2O_2 formation by heterogeneous catalysis was investigated. For this purpose, a modified graphitized carbon nitride (g-C_3N_4/BDI) catalyst was prepared and its H_2O_2 generating effect was determined by a FOX assay. Finally, it was investigated whether it is possible to couple two heterogeneous catalysts. For this purpose, H_2O_2 was generated photochemically by the g-C_3N_4/BDI catalyst. The photogenerated H_2O_2 could brominate the substrate molecule phenol red oxidatively in the presence of mesoporous $Bi_{0.2}Ce_{0.8}O_{1.9}$ and KBr, producing violet bromophenol blue.

Contributions:

Eva Pütz:	Concept development, nanoparticle synthesis, TEM and BET surface area measurement, IR measurement, manuscript preparation, figure preparation.
XXX:	Nanoparticle synthesis, ζ-potential, IR and UV/Vis measurements, depot production.
XXX:	SEM measurement and concept development.

6.2. INTRODUCTION

Many industrial branches suffer from problems caused by biofilm formation. Biofilms cause damage to health and enormous costs due to friction losses or blockages.[1–4] Marine algae, as natural aquatic organisms, protect themselves from bacterial attack by inhibiting bacterial communication *via* natural products whose synthesis involves so-called haloperoxidase enzymes.[5,6] These enzymes brominate bacterial signaling molecules and thus make them "silent" (i.e., unrecognizable) for other bacteria of the same strain. In recent years, intensive research has been conducted on artificial enzymes, as they often exhibit higher stability than their natural counterparts. CeO_2 showed haloperoxidase-like properties and can therefore be used as a haloperoxidase mimic against bacterial growth.[7] The catalytic performance of ceria can significantly be improved by partially replacing Ce^{4+} ions with Bi^{3+} ions.[8] For this reason, bismuth-doped mesoporous cerium oxide of composition $Bi_{0.2}Ce_{0.8}O_{1.9}$ was used as haloperoxidase nanozyme in this chapter. However, as the haloperoxidase-like reaction can be carried out only in the presence of halide and hydrogen peroxide (H_2O_2), that form hypohalous acid (HOX) as reactive intermediate the application of these nanozymes is confined to aqueous media. To initiate the reaction, the presence of H_2O_2 is required.[9] In the wild environment, H_2O_2 is generated photochemically by sunlight. For indoor use, H_2O_2 must be added synthetically to allow the reaction to occur. To circumvent the problem of external H_2O_2 addition, this study investigated *in-situ* H_2O_2 generation using two different approaches: (i) Embedding of a H_2O_2-generating depot substance and (ii) *in-situ* formation of H_2O_2 by heterogeneous photocatalysis. The released H_2O_2 was consumed directly by the haloperoxidase-like reaction using the model substrate phenol red to initiate a reaction cascade.

In the first approach, CaO_2 was chosen as the depot substance, because it generates H_2O_2 and $Ca(OH)_2$ in aqueous solution.[10,11] $CaO_2/Bi_{0.2}Ce_{0.8}O_{1.9}/polyethersulfone$ nanocomposites were prepared,[8] because their antibiofouling activity has been reported previously. In addition, $CaO_2/Bi_{0.2}Ce_{0.8}O_{1.9}/poly(vinylidene fluoride)$ composites were prepared, since poly(vinylidene fluoride) (PVDF) is commonly used in medical applications and membranes, which are known to suffer from biofouling.[12,13] H_2O_2 formation was detected qualitatively using a haloperoxidase assay with the model substrate phenol red and $Bi_{0.2}Ce_{0.8}O_{1.9}$.

In addition to the depot substance, photochemical *in-situ* H_2O_2 formation by heterogeneous catalysis was investigated. Modified graphitic carbon nitride (g-C_3N_4) was used as

photocatalyst for H_2O_2 production. g-C_3N_4 is capable of photocatalytic H_2O_2 production from water and molecular oxygen (O_2) in aqueous solution.[14,15] Subsequently, an attempt was made to use H_2O_2 that was generated photochemically by irradiation of g-C_3N_4 for the catalytic oxidative bromination of phenol red in the presence of KBr and $Bi_{0.2}Ce_{0.8}O_{1.9}$. The coupling these two reactions by heterogeneous catalysis eliminates the need for external addition of H_2O_2 and may open spectrum of new applications for CeO_2 nanoparticles and substituted variant such as $Bi_{0.2}Ce_{0.8}O_{1.9}$.

6.3. RESULTS AND DISCUSSION

Synthesis and characterization of mesoporous $Bi_{0.2}Ce_{0.8}O_{1.9}$ nanoparticles

Mesoporous $Bi_{0.2}Ce_{0.8}O_{1.9}$ nanoparticles were prepared via hydrothermal reaction in ethylene glycol, acetic acid and water as already discussed in chapter 4. Bi-substituted CeO_2 was used, because it has been shown to enhance the reactivity of haloperoxidase-like reactions. The effect of reaction time on zeta potential (ζ-potential) and surface area (S_{BET}) was investigated for $Bi_{0.2}Ce_{0.8}O_{1.9}$.
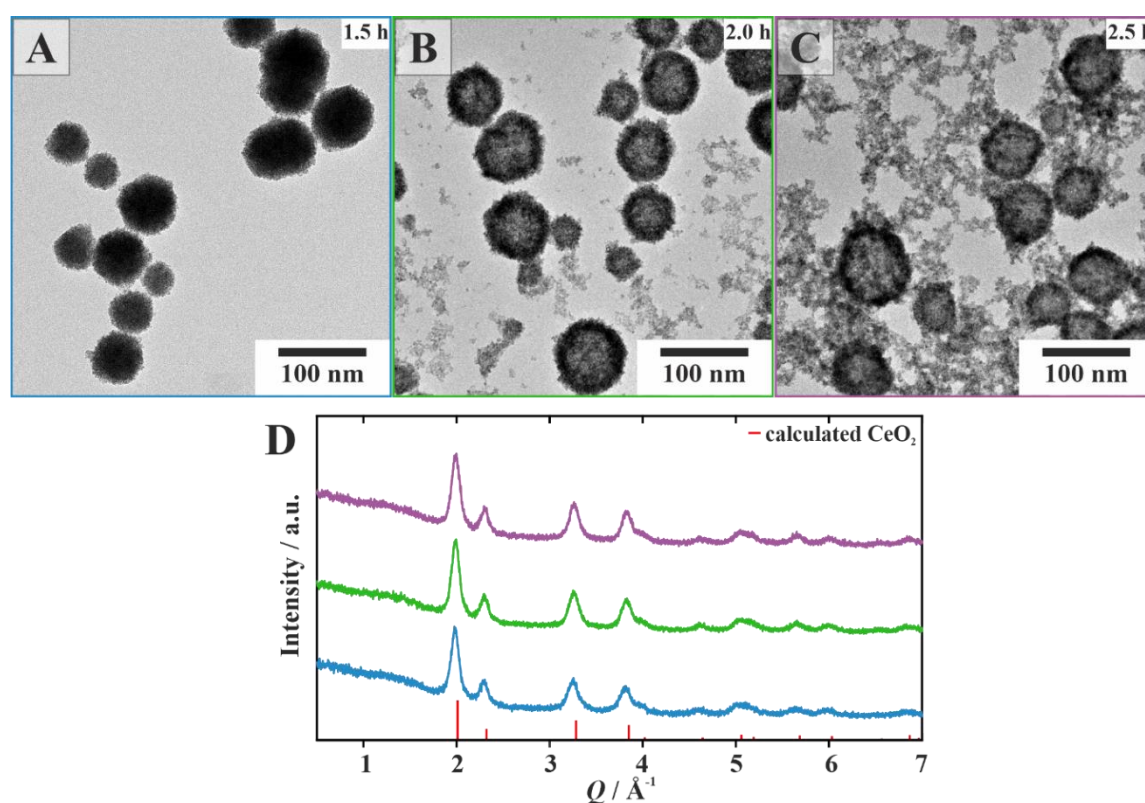
Figure 6-1. TEM images of mesoporous $Bi_{0.2}Ce_{0.8}O_{1.9}$ nanoparticles formed after (A) 1.5 h, (B) 2.0 h and (C) 2.5 h of reaction time. (D) Powder X-ray diffraction pattern (PXRD) of mesoporous $Bi_{0.2}Ce_{0.8}O_{1.9}$ at different reaction times. Red ticks indicate the calculated reflection positions for CeO_2 based on structural data from the ICSD data bank (ICSD# 88752).

Figure 6-1A-D shows the diffraction patterns of $Bi_{0.2}Ce_{0.8}O_{1.9}$ reaction products formed after 1.5 h, 2.0 h and 2.5 h (referred to as BiCe-1.5 h, BiCe-2.0 h and BiCe-2.5 h). $Bi_{0.2}Ce_{0.8}O_{1.9}$ nanoparticles exhibit a similar morphology as mesoporous CeO_2 nanoparticles, except that the reaction time was shorter and mesoporous $Bi_{0.2}Ce_{0.8}O_{1.9}$ nanoparticles formed already after 1.5 h. These $Bi_{0.2}Ce_{0.8}O_{1.9}$ particles are made up of small primary nanoparticles (diameter ~5 nm) that form mesoporous spheres with diameters of up to 80 nm due to aggregation. Similar as for CeO_2 mesoparticles (chapter 4) partricle growth is assumed to occur *via* two-step growth where very small primary particles (~5 nm)

are formed in the first step from a supersaturated solution. They agglomerate in a second step to larger mesoporous particles.[16,17] TEM images of BiCe-1.5 h show a high contrast, indicating a higher packing efficiency of the primary particle building blocks within the larger spheres. At longer reaction times (BiCe-2.0 h and BiCe-2.5 h), hollow nanospheres were formed, possible by decomposition of the larger mesoparticles (Figure 6-1B,C). Such a decomposition process may lead to many small, non-agglomerated nanoparticles which are also present in the sample. Figure 6-1D shows the powder X-ray diffraction patterns (PXRD) of BiCe-1.5 h, BiCe-2.0 h and BiCe-2.5 h. The broadened reflections are attributed to the small crystallite sizes in the nanometer range as shown in the TEM images (Figure 6-1A-C). The observed reflections can be assigned to a cubic cerianite phase (red ticks). However, all reflections are slightly shifted to smaller Q values, indicating a lattice expansion due to Bi^{3+} substitution. Since the ionic radius of Bi^{3+} ($r(Bi^{3+}) = 131.0$ pm, CN = 8) is larger than that of Ce^{4+} ($r(Ce^{4+}) = 111.0$ pm, CN = 8), the unit cell dimensions increase. Due to the larger Bi^{3+}radii, it can be assumed that Bi^{3+} substation occurs preferentially close to the surface.[18]

Catalyst activity

The haloperoxidase-like activity of mesoporous $Bi_{0.2}Ce_{0.8}O_{1.9}$ nanoparticles formed after different reaction times were compared. Catalytic oxidative bromination of phenol red was chosen as model reaction for determining oxidative bromination activity.
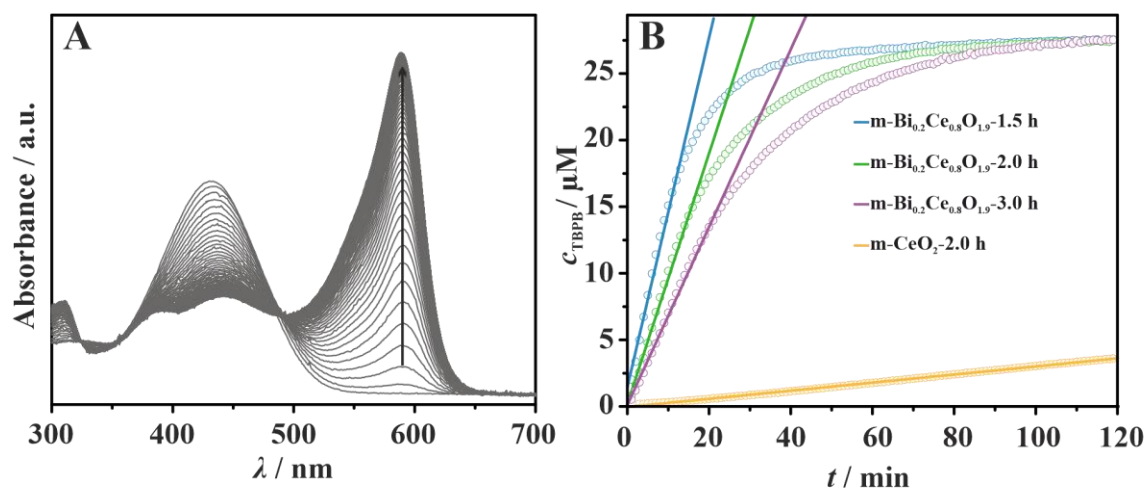
Figure 6-2. (A) Time-dependent UV/Vis spectra of a haloperoxidase-assay showing absorption changes due to oxidative bromination of phenol red (λ_{max}(PR)=430 nm) to tetrabromophenol blue (λ_{max}(TBPB) = 590 nm) with BiCe-1.5 h. (B) Tetrabromophenol blue (TBPB) for due to catalysis of BiCe-1.5 h, BiCe-2.0 h, BiCe-2.5 h and mesoporous CeO_2 over a period of 2 h.

Figure 6-2A shows the corresponding UV/Vis spectra for the halogenation reaction using BiCe-1.5 h particles. Tetrabromophenol blue (TBPB) with an absorption maximum at λ=590 nm was formed during the reaction. Absorption changes at λ_{max}(BPB)=590 nm were fitted to calculate reaction rates of TBPB formation. Figure 6-2B shows the concentration of TBPB generated in the presence of different nanoparticles over a period of 120 min. Linear fits were used to determine the reaction rates (k_{HPO}). Similar to m-CeO$_2$, Bi-doped nanoparticles isolated after shorter reaction times have higher catalytic activity. In addition, all Bi-substituted samples show up to 40-fold higher reaction rates in TBPB formation compared to pure m-CeO$_2$ particles. The calculated reaction rates are compiled in Table 6-1.

Table 6-1. Reaction rates (k_{HPO}) of mesoporous Bi$_{0.2}$Ce$_{0.8}$O$_{1.9}$ nanoparticles isolated at different reaction times derived from the absorbance changes at λ_{max}(TBPB)=590 nm.

Catalyst	k_{HPO} / µMol min^{-1}
BiCe-1.5 h	1.31 ± 0.05
BiCe-2.0 h	0.94 ± 0.02
BiCe-2.5 h	0.67 ± 0.01
m-CeO$_2$-2.0 h	0.0304 ± 0.0001

Surface properties

The effect of reaction time on the surface properties zeta potential (ζ-potential) and specific surface area (S_{BET}) was evaluated. Since haloperoxidase-like reactions are controlled by electrostatic interactions between halide ions and CeO_2 particle surfaces, the ζ-potential of the CeO_2 colloids is a key factor for their catalytic activity.[8] The ζ-potential can be adjusted from +41 mV to +28 mV by varying the reaction time for the synthesis of the nanoparticles (Figure 6-3). Similar to mesoporous ceria prepared under analogous conditions without Bi^{3+} substitution, the ζ-potential decreases with the reaction time, while the surface area (S_{BET}) increases from 56 to 102 m^2g^{-1}. Figure 6-3 displays the effect of reaction time on ζ-potential and S_{BET}.
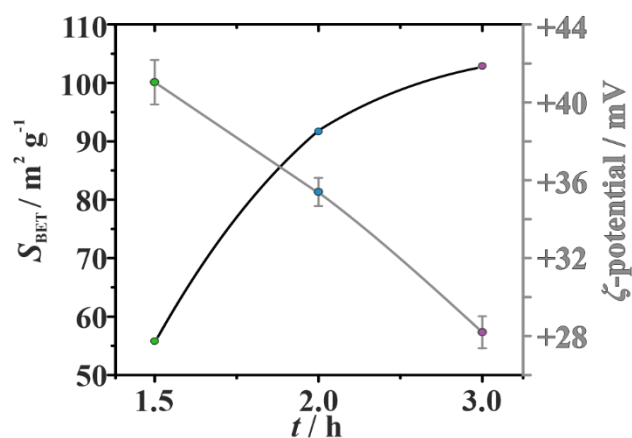
Figure 6-3. Effect of reaction time on specific surface area (S_{BET}) and zeta potential (ζ-potential).

S_{BET} can be neglected in the haloperoxidase-like reaction, since electrostatic interactions play a dominant role. Therefore, a high ζ-potential is crucial for a good catalyst. Since BiCe-1.5 h has the highest catalytic activity and ζ-potential, these nanoparticles were used for the preparation of the composites.

Synthesis and characterization of PES and PVDF nanoparticle composites

BiCe-1.5 h nanoparticles were embedded in different polymer matrices, and the activity of the composites was evaluated. Poly(ethersulfone) (PES) and poly(vinylidene fluoride) (PVDF) were used as solid matrix-forming materials, while poly(vinylidene pyrrolidone) (PVP) was used as a pore-forming agent. To this end, the polymers were first dissolved in 1-methylpyrrolidin-2-one (NMP), the Bi-substituted ceria particles (2wt% related to PES or PVDF respectively) were dispersed in the polymer solution and coagulated in a mixture of 7:3 v/v (H_2O/EtOH).
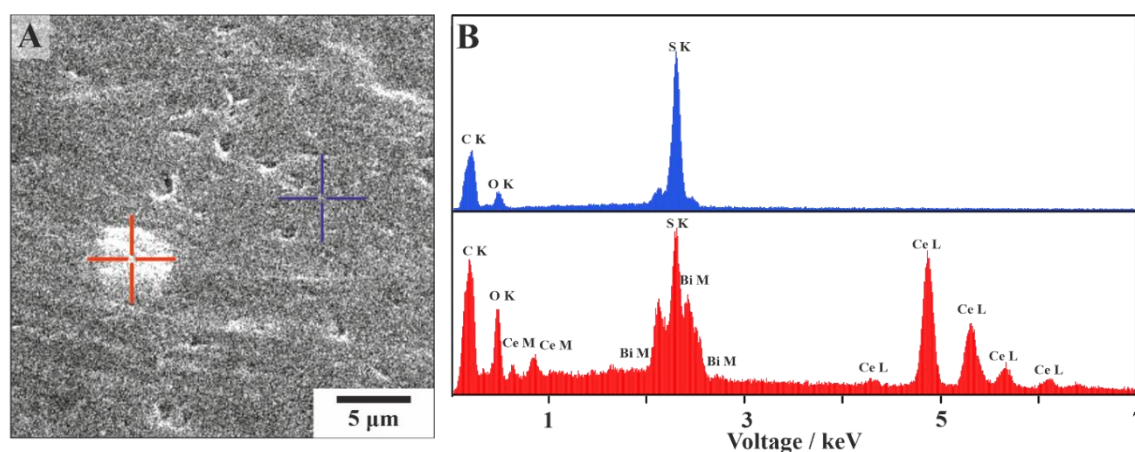
Figure 6-4. (A) SEM image of PES-BiCe spheres and EDX mapping at the (B) blue spot and the (C) brighter red spot.

Scanning electron microscopy (SEM) of BiCe-1.5 h revealed the formation of the PES-BiCe spheres. The SEM images of the PES spheres show a porous structure (Figure S6-1). Figure 6-4A show the surface of PES spheres with embedded BiCe-1.5 h particles that show a slightly higher contrast that the polymer matric due to their higher electron and mass density. EDX analysis (blue mark in Figure 6-4B blue) revealed mainly carbon, oxygen and sulfur, resulting from the elemental composition of PES. The brighter spot (red mark) shows the elements bismuth and cerium besides the elements of PES, indicating the incorporation of $Bi_{0.2}Ce_{0.8}O_{1.9}$ nanoparticles into the polymer matrix (Figure 6-4B red). IR spectra of the composite beads (Figure 6-5A-B) show no difference between polymers with and without embedded BiCe-1.5 h. This indicates that the addition of BiCe-1.5 h nanoparticles had no effect on the polymer matrix, i.e., the polymer was not chemically degraded or modified. Since the vibrational band at 1500 cm^{-1}, which originates from the pore-forming agent PVP (Figure S6-2), is still present after coagulation, we conclude that this component was not completely removed from the particles during coagulation.
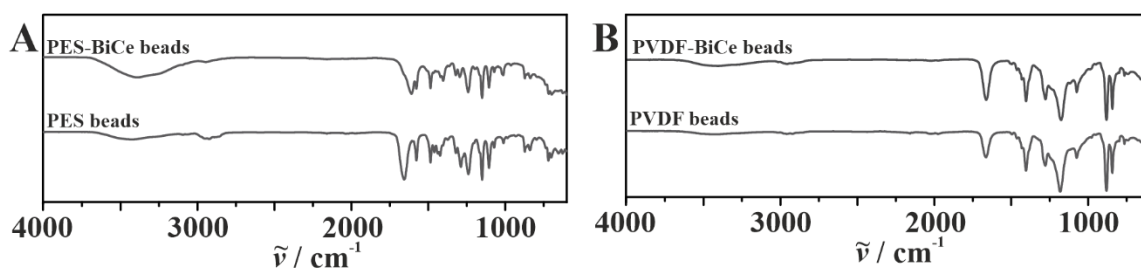
Figure 6-5. FTIR spectra of the coagulated (A) PES based and (B) PVDF based composites.

The oxidative bromination activity of the polymer containing mesoporous $Bi_{0.2}Ce_{0.8}O_{1.9}$ nanoparticles is shown with the the phenol red assay. The composites with incorporated BiCe-1.5 h are referred to as PES-BiCe and PVDF-BiCe in the sequel.
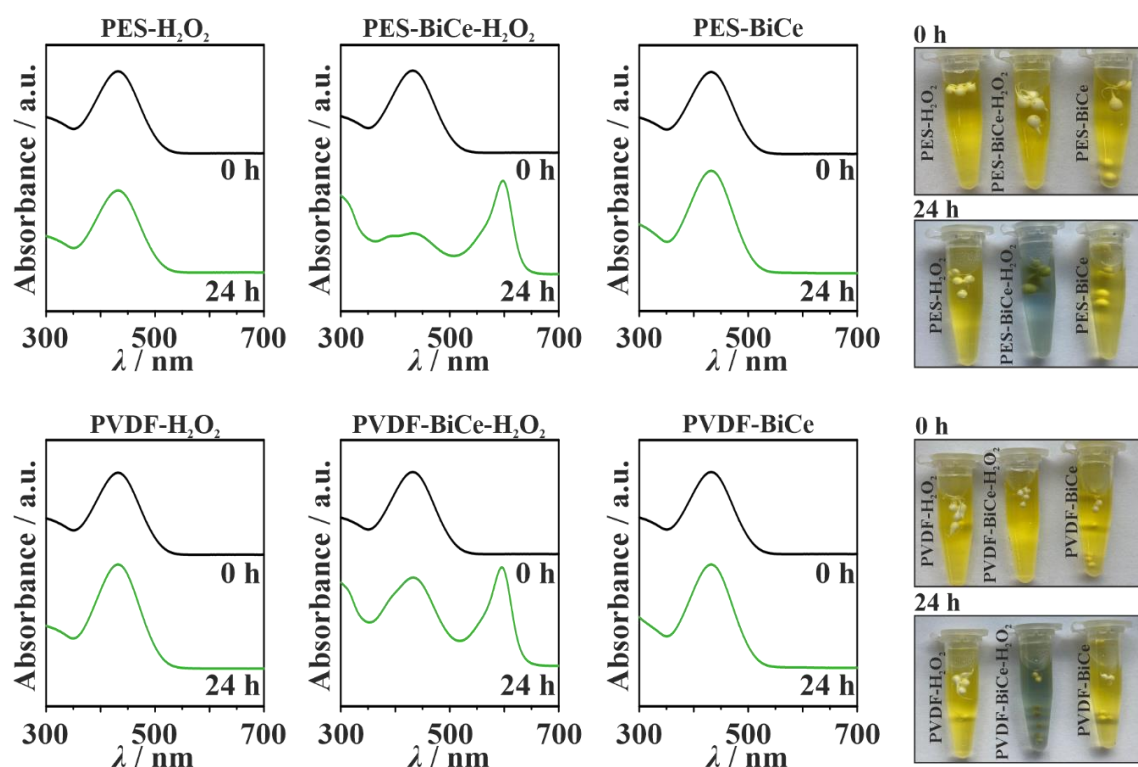
Figure 6-6. UV/Vis spectra of a phenol red assay in the presence of PES and PVDF, PES-BiCe and PVDF-BiCe composites in the absence and in the presence of H_2O_2 together with images of the reaction mixtures after 0 h and 24 h.

Coagulated polymer particles with and without BiCe-1.5 h were added to a mixture of phenol red and KBr. The reaction was initiated by addition of H_2O_2. After 24 hours of reaction time, tetrabromophenol blue had formed as indicated by a change in absorbance UV/Vis spectra and the color change of the supernatants after 0 h and 24 h (Figure 6-6).

These changes in color and absorption were observed only for PES-BiCe and PVDF-BiCe composites in the presence of H_2O_2. Pure PES and PVDF beads did not show a color change due to the formation of tetrabromophenol blue after adding H_2O_2. No oxidative bromination occurred in the absence of H_2O_2, i.e., peroxide is essential to initiate the reaction.

Effect of CaO_2 on oxidative bromination reaction

Since oxidative bromination with BiCe-1.5 h requires the presence of peroxides, the preparation of depot systems liberating H_2O_2 is essential for future applications. Calcium peroxide (CaO_2) is a promising candidate because it dissolves in aqueous environment to form $Ca(OH)_2$ and H_2O_2.[10,11] The release of H_2O_2 from an aqueous 30 mM CaO_2 solution was evaluated in comparison to a 30 mM H_2O_2 solution using the phenol red assay. Freshly prepared solutions of H_2O_2 or CaO_2 were added to a mixture of phenol red, KBr and BiCe-1.5 h to initiate the reaction. Figure 6-7A shows absorbance spectra of a phenol red assay after 120 min in the presence of H_2O_2, CaO_2 and in the absence of any oxidant. The reaction rate in the presence of CaO_2 was slower than in the presence of H_2O_2 (phenol red assay, Figure 6-7B) because the hydrolysis of CaO_2 to $Ca(OH)_2$ and H_2O_2 is a rate-determining step. However, the slow release of H_2O_2 makes CaO_2 a promising compound for depot formation. Due to the slow H_2O_2 release, the incorporation of CaO_2 into the polymer matrix is possible even in aqueous media despite the coagulation process, since the CaO_2 dissolves only slighty during the manufacturing process. In addition, the slow release of H_2O_2 extends the lifetime of the depot.
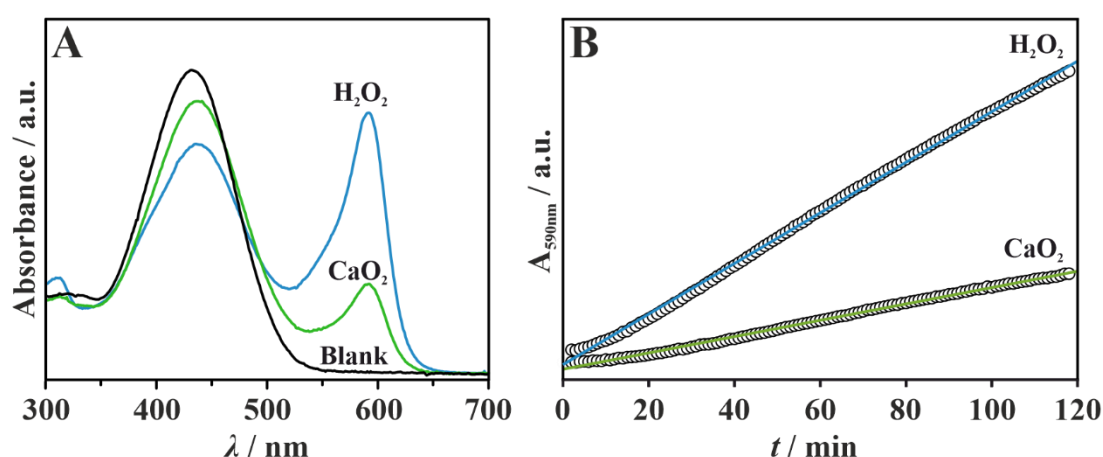
Figure 6-7. (A) UV/Vis spectra of the haloperoxidase-assay using BiCe-1.5 h as catalyst in the absence of H_2O_2 addition (blank), with CaO_2 and H_2O_2 addition after 2.0 h of reaction time. (B) Time-dependent change in absorbance at $\lambda_{max} = 590$ nm after CaO_2 and H_2O_2 addition monitored over a period of 2 h.

Preparation of BiCe composite depots for oxidative bromination

CaO_2 was used as depot substance in polymer beads to generate H_2O_2 because of the promising results in the activity studies. The polymer beads were synthesized using the coagulation method as described before. For this purpose, CaO_2 and BiCe-1.5 h were dispersed together in polymer solutions and coagulated. PES/PVDF beads and PES/PVDF beads containing either CaO_2 or BiCe-1.5 h only were prepared as blank samples.
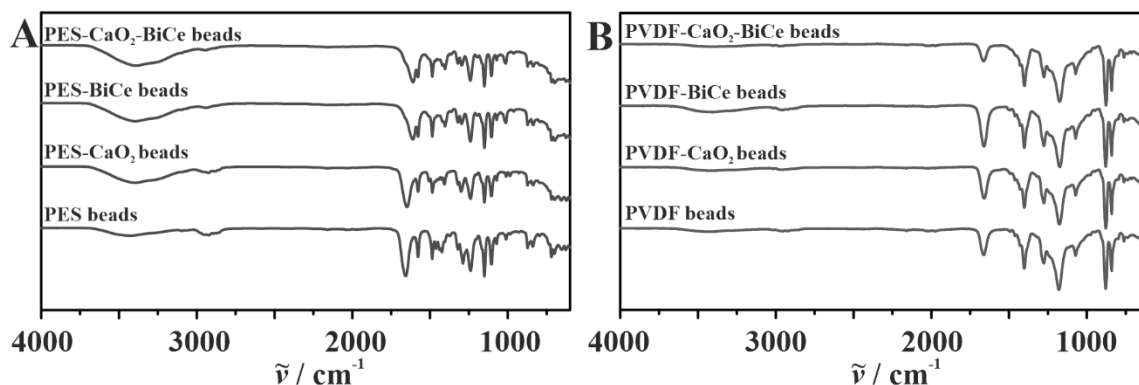
Figure 6-8. FTIR spectra of the coagulated (A) PES based composites with CaO_2 and BiCe as well as (B) PVDF based composites with CaO_2 and BiCe.

The incorporation of CaO_2 into the polymer matrix had no discernible effect on the IR spectra. Only the amount of PVP was variable, apparent from the different intensity of the band at 1500 cm^{-1}. Since PVP is simply the pore-forming component that dissolves during coagulation in aqueous solution, different amounts of PVP may be present in the polymer beads.(Figure S 6-2) The FTIR spectra of CaO_2 containing depots in Figure 6-8 show no band at 3642 cm^{-1} which is characteristic for O−H stretching vibration in $Ca(OH)_2$.[19,20] Since $Ca(OH)_2$ had not yet formed in the depot beads during the coagulation process, it can be assumed that CaO_2 was incorporated in the polymer matrix, i.e., the depot formation was successful. The release of H_2O_2 from the PES and PVDF depots was again performed using the phenol red assay. For this purpose, the composites were placed in a vial containing a phenol red/KBr mixture (Figure 6-9C+D), and the absorbance change of the supernatant at $\lambda = 590$ nm was monitored over a period of 24 hours (Figure 6-9A+B).

Pure PES and PVDF beads as well as beads containing CaO_2 and BiCe-1.5 h only showed no change in absorption spectra over a 24 h period, indicating no transformation of phenol red to bromophenol blue. Changes in color and absorption were only observed for PES-BiCe-CaO_2 and PVDF-BiCe-CaO_2 composites. Figure S6-3 shows the UV/Vis spectra after 0 and 24 h of reaction time.
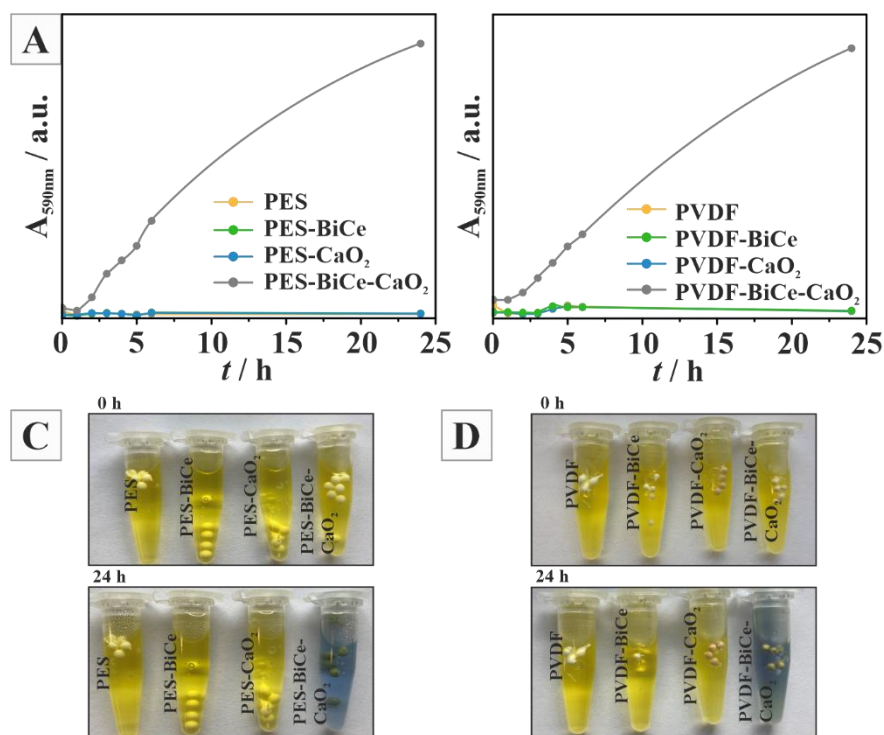
Figure 6-9. (A) Time-dependent change in absorbance at λ_{max}=590 nm in the presence of phenol red, KBr and PES, PES-BiCe, PES-CaO$_2$ and PES-BiCe-CaO$_2$ over a 24 h period. (B) Time-dependent change in absorbance at λ_{max} = 590 nm in the presence of phenol red, KBr and PVDF, PVDF-BiCe, PVDF-CaO$_2$ as well as PVDF-BiCe-CaO$_2$ over a 24 h period. C, D) Images of the phenol red assay in the presence of the composite with different composition after 0 h and 24 h.

Initially, all phenol red solutions were yellow, after 24 h of reaction time the solution color changed to a green/blue color, indicating the formation of tetrabromophenol blue. Accordingly, both BiCe-1.5 h and CaO$_2$ are required for catalysis of the oxidative bromination reaction. The result shows that H$_2$O$_2$ is released from the depot substances in PES and PVDF polymer beads. Since CaO$_2$ reacts alkaline, the application is initially limited to buffered media. Therefore, the next step was to investigate the photocatalytic generation of H$_2$O$_2$ under neutral conditions.

Synthesis of a catalyst for the photochemical generation of H₂O₂

In addition to the preparation of hydrogen peroxide-releasing depots, attempts were made to produce hydrogen peroxide photochemically. The intention was to consume the generated H_2O_2 for the BiCe-catalyzed oxidative bromination of phenol red. This approach is based on the coupling of two independent heterogeneously catalyzed reactions. The corresponding reaction course of the coupling reaction is shown schematically in Figure 6-10. Graphitized carbon nitride (g-C_3N_4) is promising photocatalyst for the generation of H_2O_2 in aqueous solution.[15,21] The first step of the process consists of the photochemical generation of H_2O_2 from water and molecular oxygen (O_2) in aqueous solution using a g-C_3N_4 catalyst.[15,21] The photogenerated H_2O_2 is used subsequently for an oxidative bromination reaction in which the substrate molecule phenol red is brominated in the presence of BiCe-1.5 h and bromide ions to form the blue dye tetrabromophenol blue.
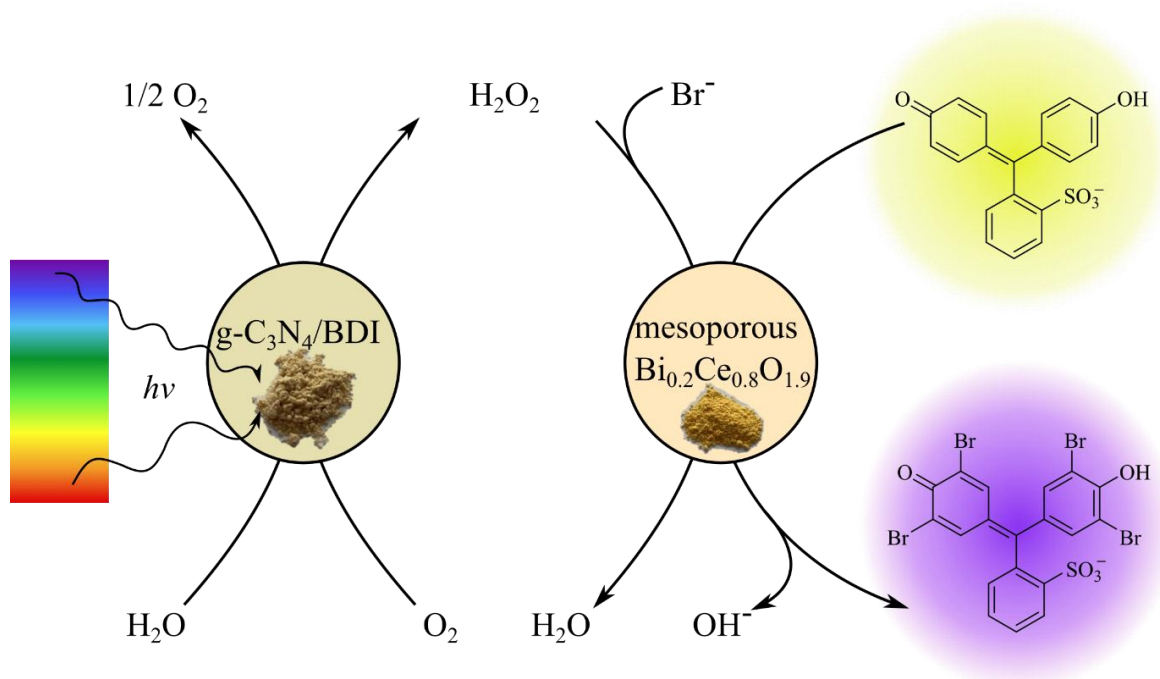
Figure 6-10. Schematic representation of the coupled catalytic reactions. The graphitized carbon nitride catalyzes the production of H_2O_2 from water and oxygen by UV irradiation. The ceria catalyst subsequently performs the bromination of the phenol red to tetrabromophenol blue in the presence of H_2O_2 and KBr.

The performance of g-C_3N_4 can be improved by incorporation of a biphenyl diimide species (BDI).[15] This modification leads to a reduction in the band gap energy and shifts it into the visual range.

The synthesis of g-C$_3$N$_4$ modified with biphenyl tetracarboxylic dianhydride (BTCDA) is shown in Figure 6-11. Melem was prepared from melamine, which was subsequently reacted with BTCDA in a ratio of 1:2.5 to yield the modified g-C$_3$N$_4$/BDI.
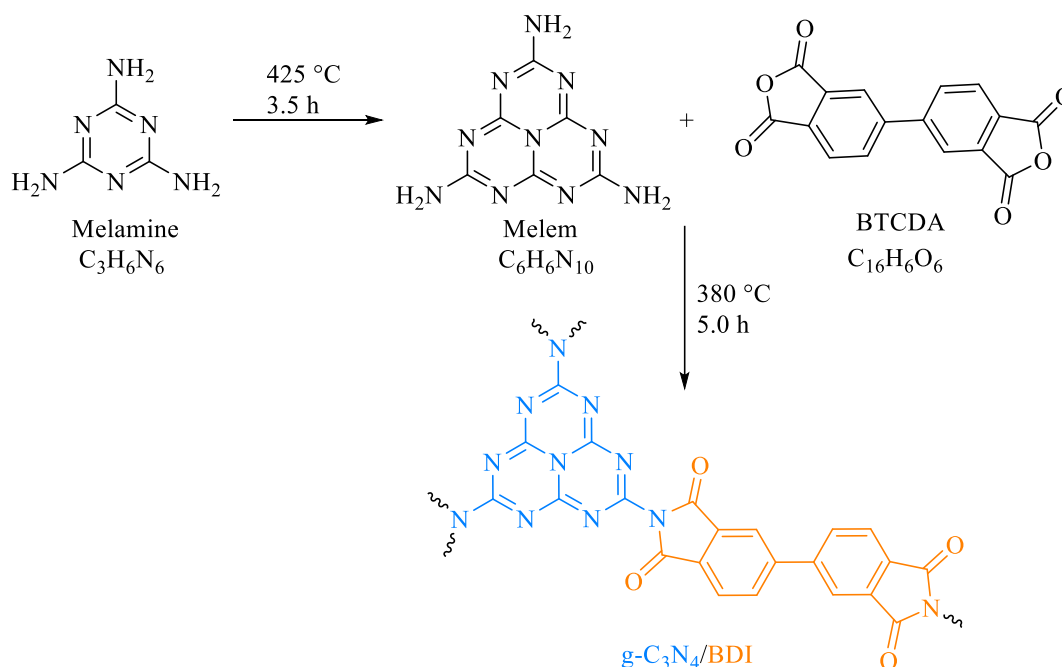
Figure 6-11. Synthesis of g-C$_3$N$_4$/BDI using melamine, melem and BTCDA as starting materials.

FTIR spectra of g-C$_3$N$_4$/BDI and all other starting materials are shown in Figure 6-12. The signals in the high wavenumber region 3100−3650 cm^{-1} are assigned to the asymmetric and symmetric N−H stretching vibrations of melamine and melem, respectively. For melem, the signal intensity of the stretching vibration is lower because there are fewer NH$_2$ groups per mole in the molecule compared to melamine. The other major signals in melamine and melem spectra in the range of 1100−1700 cm^{-1} (1424 cm^{-1} and 1577 cm^{-1}) can be associated with C−N/C=N stretching and N−H/NH$_2$ bending vibrations linked with ring deformations.[22,23] The sharp signal at 814 cm^{-1} is associated with the out-of-plane bending mode. Both, the C−N/C=N stretching and the out-of-plane bending signals are particularly characteristic of triazine structures. The FTIR spectrum of BPTCA and g-C$_3$N$_4$/BDI show the characteristic vibrational bands of the imide carbonyl groups at 1774 cm^{-1}, 1725 cm^{-1}, and 722 cm^{-1}.[24] The spectrum of the final product g-C$_3$N$_4$/BDI contains the bands of the triazine backbone and those of the BDI linker, indicating a successful synthesis. Surface area measurements revealed a very small surface area of 2.9 m^{2}g^{-1} and a zeta potential measurements a highly negative ζ potential of -22.3 mV.

Figure 6-12. FTIR spectra of melamine, melem, BTCDA and g-C₃N₄/BDI.

Photochemical H₂O₂ production

The g-C₃N₄/BDI product had a beige to slightly yellowish color, indicating an absorption in the visible range. Since photochemical excitation is crucial for photocatalytic H₂O₂ generation, the band gap energy of the product was determined. A band gap of 2.86 eV was derived, which corresponds to the energy of light with a wavelength of 434 nm. To demonstrate the photochemical generation of H₂O₂, g-C₃N₄/BDI was dispersed in Milli-Q water, sonicated for 10 min and subsequently stirred vigorously to introduce oxygen. The reaction mixture was then irradiated by two LEDs with a wavelength of 365 nm, as these have sufficient energy to excite g-C₃N₄/BDI. A quantitative determination of the H₂O₂ concentration was performed using the FOX assay ("Ferrous Oxidation - Xylenol Orange").[25–27] A FOX solution consisting of xylenol orange and Fe^{2+} ions exhibits an absorbance maximum between λ_{max} = 420–460 nm.[25] Depending on the solvent a violet colored Fe^{3+}-xylenol orange complex (Fe^{3+}-XO) with an absorbance maximum at λ_{max} = 540-600 nm is formed in the presence of Fe^{3+} ions.[25] Addition of H₂O₂ leads to an oxidation of Fe^{2+} to Fe^{3+} resulting in the formation of a violet complex. First, different amounts of H₂O₂ were added to the FOX reagent and the solutions were mixed properly.

After 15 min of reaction time, the absorbance was measured at λ_{max} = 580 nm for all concentrations to obtain a calibration curve by linear regression (Figure 6-13A).

To measure the H_2O_2 production ability of prepared g-C_3N_4/BDI, H_2O_2 concentrations for samples that were irradiated (or not irradiated, control) over a period of 4 h were calculated using the linear equation in the inset of Figure 6-13A. UV/Vis spectra of the FOX-assay in presence of g-C_3N_4/BDI are displayed in Figure 6-13B. With increasing irradiation time, an increase in absorption at 580 nm and a shift of the absorption maximum of the Fe^{3+}-XO complex to higher wavelengths were observed. This is due to an increasing Fe^{3+} concentration in solution,[26] resulting from an increasing H_2O_2 concentration. Figure 6-13C shows the concentrations of H_2O_2 in the irradiated and non-irradiated samples over a period of 4 h.
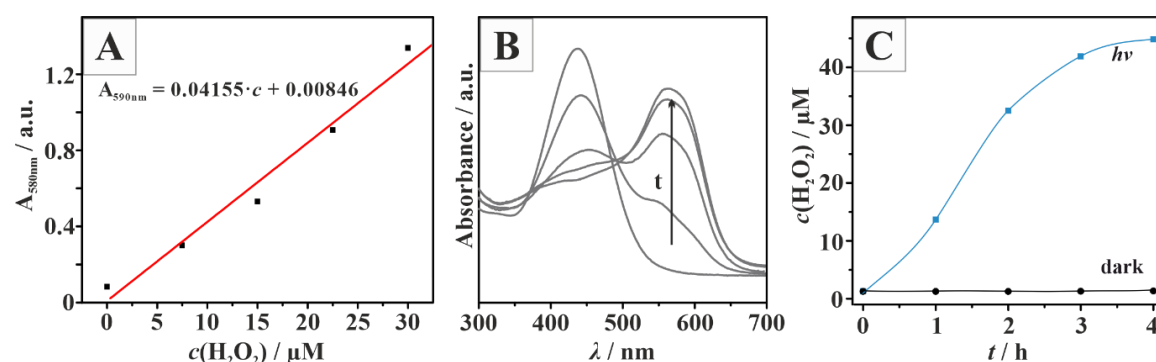
Figure 6-13. (A) Calibration line for H_2O_2 concentration determined via FOX-assay. Absorbance at λ_{max} = 580 nm was plotted against H_2O_2 concentration. Linear regression was used to determine the linear equation (inset). (B) UV/Vis spectra of the FOX assay for an irradiated g-C_3N_4/BDI sample at 0-4 h. (C) Time-dependent change in H_2O_2 concentration for an irradiated g-C_3N_4/BDI sample and a dark reference sample.

A strong increase of the hydrogen peroxide concentration was observed for a reaction time of up to 3 h, which then flattens out from 4 h resulting in an equilibrium H_2O_2 concentration of approximately 40 µM. This is due to the decomposition of H_2O_2 by the catalyst, which occurs at high H_2O_2 concentrations.[15] However, the amount of photogenerated H_2O_2 is sufficient to allow a coupling with the BiCe-1.5 h catalyzed haloperoxidase reaction. The concentration used in the haloperoxidase assay is approximately 25 µM, which is reached in the model setup between 1 and 2 h of irradiation.

Coupling reaction

Since the photochemical *in-situ* generation of hydrogen peroxide using graphitized carbon nitride was successful, this process was coupled in the next step with a haloperoxidase reaction catalyzed by BiCe-1.5 h to circumvent the external addition of H_2O_2. The g-C_3N_4/BDI and BiCe-1.5 h were spatially separated from each other by a Nadir® dialysis membrane, since the particles would agglomerate otherwise due to their different surface charges (i.e., ζ potentials), thereby forming inactive aggregates. A glass tube with holes was designed for this coupling purpose (Figure 6-14A), which was wrapped with the dialysis membrane and immersed in a beaker containing an aqueous phenol red/KBr solution and BiCe-1.5 h catalyst nanoparticles. Figure 6-14B+C show the schematic and the actual reaction setup.
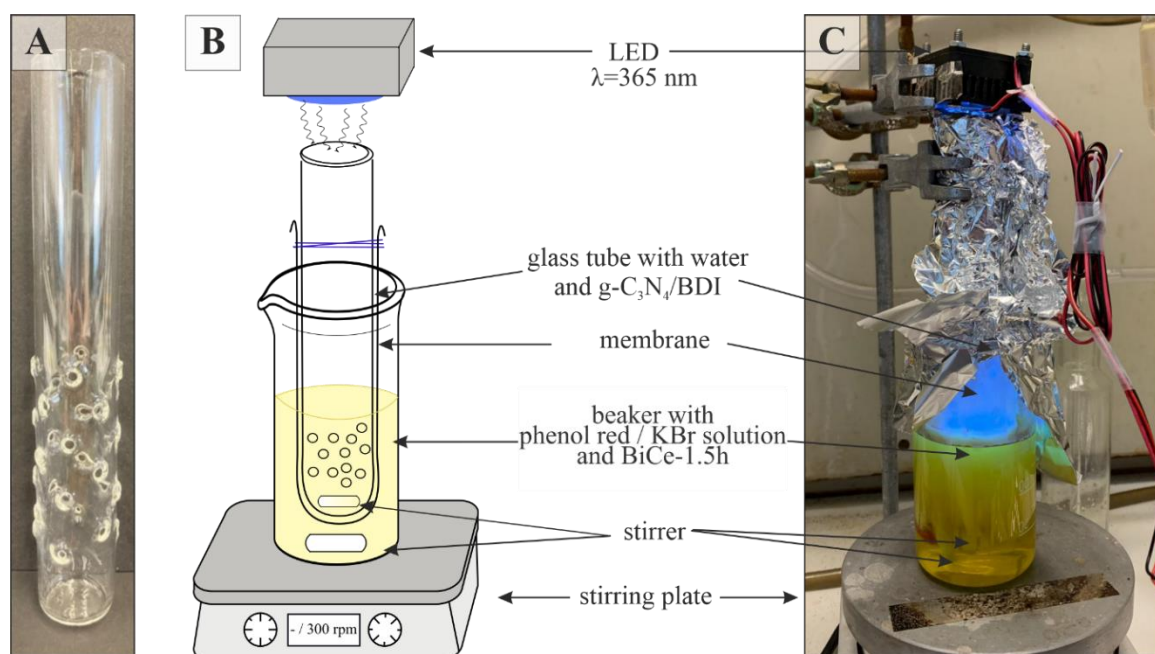
Figure 6-14. (A) Specially designed glass tube for coupling reaction. (B) Schematic overview of the reaction setup, and (C) digital image of actual reaction setup.

Milli-Q water and g-C_3N_4/BDI were added together with a magnetic stirrer into the glass tube. Acceleration of the H_2O_2 production was accomplished by irradiation of the glass tube from above with a 365 nm wavelength LED. Aliquots of the reaction medium in the outer compartment were taken every hour (1 h, 2 h, 3 h, 4 h, 5 h, 6 h, 24 h) and UV/Vis spectra were recorded. As a controls, the reactions were performed once without BiCe-1.5 h in the outer compartment, once without g-C_3N_4/BDI in the inner compartment, and once in the dark. Figure 6-15A shows the UV/Vis spectra of the dual catalysis reaction at different reaction times. Absorbance at 430 nm decreases with time indicating a decrease of the

phenol red concentration. The absorbance at 590 nm increases which is associated with the formation of tetrabromophenol blue.
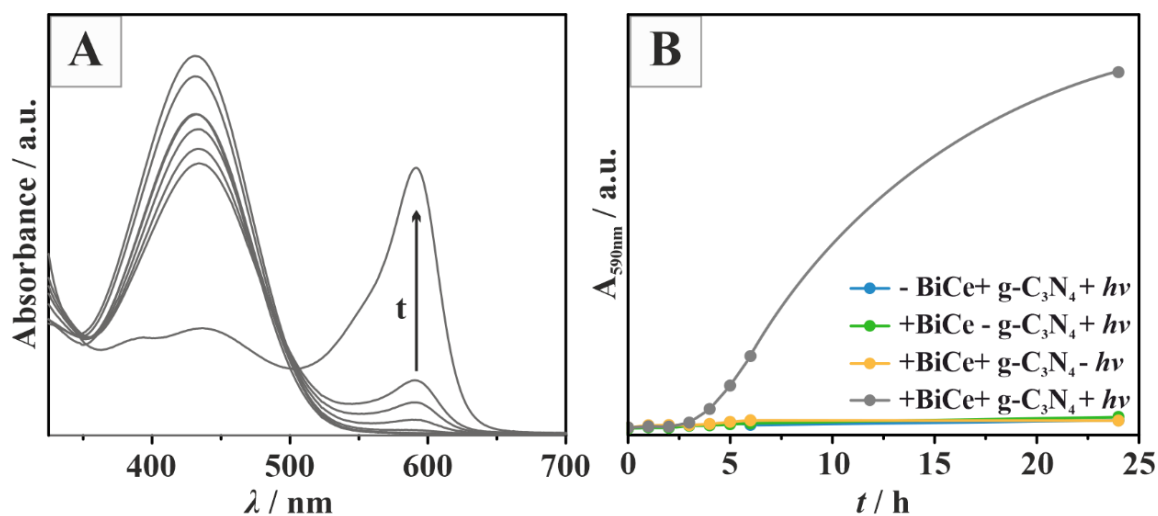
Figure 6-15. (A) Recorded time-dependent UV/Vis spectra of the coupled H_2O_2 generation/haloperoxidase reactions with g-C_3N_4/BDI, and BiCe-1.5 h under irradiation after 1 h, 2 h, 3 h, 4 h, 5 h, 6 h and 24 h. (B) Time-dependent change in absorbance at $\lambda_{max} = 590$ nm for the coupled reaction with all components (grey), without g-C_3N_4/BDI (green), without BiCe-1.5 h (blue), dark control (orange).

The reaction was carried out several times under different conditions to demonstrate that both inorganic catalysts (g-C_3N_4/BDI and BiCe-1.5 h) are needed for a successful oxidative bromination reaction. In Figure 6-15B, the absorbance at a wavelength of 590 nm is plotted against time, as this range indicates the progress of the bromination. Figure 6-15A+B shows that the absorbance increases significantly during the coupled reaction. From the third hour onwards, a low concentration of tetrabromophenol blue was observed. No absorbance change was visible in the controls. These results clearly show that (i) both inorganic catalysts (g-C_3N_4/BDI and BiCe-1.5 h) are required for the oxidative bromination reaction and (ii) that both reactions can be coupled successfully. g-C_3N_4/BDI photochemically produces H_2O_2, which reacts in the follow-up step with bromide and phenol red in the presence of BiCe-1.5 h to tetrabromophenol blue. Basically, this setup eliminates the need for external addition of H_2O_2.

6.4. CONCLUSION

Hydrothermally prepared bismuth-doped mesoporous ceria exhibits significantly higher catalytic activity in a haloperoxidase-like reaction than undoped ceria. The influence of reaction time on the catalytic properties of the nanoparticles was investigated. Correlations between the catalytic activity and surface properties such as ζ potential and surface area were examined. The BiCe-1.5 h sample showed the highest catalytic activity, and was therefore further applied in depots, and for the reaction cascade of photochemical H_2O_2 generation and haloperoxidase reaction.

To have an independent and constant supply for H_2O_2, the bromination of the phenol red was carried out in the presence of CaO_2 instead of H_2O_2. This showed a successful, although slower, conversion to tetrabromophenol blue. Aiming for a sustained H_2O_2 release, CaO_2 was incorporated successfully into different polymer matrices together with BiCe-1.5 h nanoparticles. This approach turned out to be a simple and effective procedure to release H_2O_2 slowly and steadily over a long period of time *via* a depot substance. The spatial proximity of the depot substance to the catalyst leads to the bromination of phenol red and finally to the production of a haloperoxidase mimicry compound.

Finally, an attempt was made to produce H_2O_2 *in-situ via* photocatalysis to couple two independent reactions, the photogeneration of H_2O_2 and the haloperoxidase reaction. Therefore, a heterogeneous photocatalyst, a modification of the graphitized carbon nitride g-C_3N_4/BDI, was synthesized. UV irradiation of g-C_3N_4 lead to the generation of H_2O_2 in micromolar amounts. The resulting H_2O_2 was used for the bromination of phenol red in the presence of BiCe-1.5 h and bromide ions. For this purpose, the two heterogeneous catalysts were spatially separated by a dialysis membrane. This prevented the agglomeration of the nanoparticles and at the same time ensured the exchange of the soluble reactants, which led to the formation of a successful reaction cascade.

6.5. EXPERIMENTAL SECTION

MATERIAL AND SYNTHESIS

Chemicals

Cerium nitrate hexahydrate (99.5%, CAS: 10294-41-4), bismuth nitrate-pentahydrate (98%, CAS: 10035-06-0), calcium peroxide (65%, CAS: 1305-79-9), melamine (99%, CAS: 108-78-1), and calcium acetate (CAS: 114460-21-8) were purchased from Alfa Aesar. Hydrogen peroxide (hydrogen peroxide 35% pure, stabilized (34-36%, CAS: 7722-84-1) as well as ethylene glycol (≥99%, CAS: 107-21-1) were purchased from Roth. Phenol red (CAS: 143-74-8) was purchased from Sigma-Aldrich and acetic acid glacial (HAc; 99.5%, CAS: 64-19-7) from VWR. Potassium bromide (99+%, CAS: 7758-02-3), poly(vinylpyrrolidone) (PVP, M_w = 58000 g/mol, CAS: 9003-39-8) and ammonium iron sulfate hexahydrate (99+%, CAS: 7783-85-9) from Acros Organics. Absolute ethanol (99%, CAS: 64-17-5) was purchased from Fisher Scientific, poly(ether sulfone) (PES, M_w = 58000 g/mol, CAS: 25608-63-3) from Good Fellow, poly(vinylidene fluoride) (PVDF, CAS: 24937-79-9) from Fluorochem, 1-Methyl-2-pyrrolidinone (NMP, CAS: 872-50-499) Iris Biotech GmbH, biphenyl tetracarboxylic dianhydride (BTCDA) (99%, CAS: 2420-87-3) from JK Chemicals and xylenol orange tetrasodium salt (XO, CAS: 3618-43-7) from Merck.

Synthesis of mesoporous $Bi_{0.2}Ce_{0.8}O_{1.9}$ nanoparticles. Mesoporous $Bi_{0.2}Ce_{0.8}O_{1.9}$ nanoparticles were synthesized hydrothermally in a modified procedure according to Liang *et al.*[28] For this purpose, 223 mg $Bi(NO_3)_3 \cdot 5\ H_2O$ (0.46 mmol) and 799 mg $Ce(NO_3)_3 \cdot 6\ H_2O$ (1.84 mmol) was transferred into a Teflon inlay and dissolved in 2 mL of a 1:1 mixture of water and acetic acid while stirring. 30 mL of ethylene glycol were added and stirred for another 5 min. The Teflon inlay was transferred to a metal autoclave and heated to 180 °C for different time periods (1.5 h, 2.0 h and 2.5 h). After different reaction times, the hot autoclaves were removed from the oven. The cooled solutions were centrifuged at 9000 rpm for 20 min, the nanoparticle precipitate was washed three times with Milli-Q water and dried in vacuum at 40 °C.

Synthesis of polymeric H_2O_2 depot beads. A PES stock solution consisting of 3.6 g PES, 1.4 g PVP and 15 g NMP was prepared by dissolving all components at room temperature under stirring for several hours. 2.0 g PES stock solution was then mixed with the depot substance (15 mg CaO_2) and/ or BiCe-1.5 h nanoparticles (8 mg). The freshly prepared

solutions were dropped into a H_2O/ethanol (7:3 v/v) mixture using a syringe pump, resulting in the formation of small polymer spheres by coagulation. The spheres were placed on a filter paper to dry.

PVDF stock solution consisted of 3.34 g PVDF, 1.3 g PVP and 13.93 g NMP was prepared similarly to PES stock solution. 2.00 g PVDF stock solutions were then mixed with the depot substance (15 mg CaO_2) and/ or BiCe-1.5 h nanoparticles (8 mg). The as-prepared solutions were added to water using a syringe pump, resulting in the formation of small polymer spheres by coagulation. The spheres were placed on a filter paper to dry.

Synthesis of g-C_3N_4/BDI. The synthesis of the modified g-C_3N_4/BDI was carried out according to Kofuji *et al.*[15] Melamine (3.028 g) was heated to 425 °C in a porcelain crucible for 3.5 h at a heating rate of 7 °C/min. The resulting melem (502 mg, 2.3 mmol) was mortared with 3,3',4,4'-biphenyltetracarboxylic acid dianhydride (BPTCA) (1693 mg, 5.8 mmol) for 10 min and then heated in a porcelain crucible for 5 h at 380 °C at 7°C/min. This resulted in the formation of g-C_3N_4/BDI, which displayed a light beige color.

Haloperoxidase-like reaction monitoring using the phenol red assay. The haloperoxidase-like activity of mesoporous $Bi_{0.2}Ce_{0.8}O_{1.9}$ and the composites nanoparticles were determined using the phenol red assay. The oxidative bromination reaction of phenol red (PR) to tetrabromophenol blue (TBPB) was observed spectrophotometrically.

For mesoporous $Bi_{0.2}Ce_{0.8}O_{1.9}$ a mixture of nanoparticles (25 µg mL^{-1}), PR (50 µM) and KBr (25 mM) was prepared, and the reaction was initiated by adding H_2O_2 (300 µM) or CaO_2 (300 µM), respectively. The change in absorbance at $\lambda_{TBPB} = 590$ nm was measured over a period of 10 min. The concentration of TBPB was calculated using Lambert-Beer´s law.

For CeBi-composite materials five composite beads were added to 2 mL of a PR (50 µM) and KBr (25 mM) mixture. The reaction was initiated using H_2O_2 (300 µM). The UV/Vis spectra of supernatants were measured after 0 and 24 h respectively.

For the depot materials: The depot materials were added to 2 mL of a PR (50 µM) and KBr (25 mM) mixture. The UV/Vis spectra of supernatants were measured after different reaction times.

For the coupling reaction: A beaker was filled with 100 mL of mesoporous $Bi_{0.2}Ce_{0.8}O_{1.9}$ nanoparticles (50 µg mL^{-1}), PR (50 µM) and KBr (25 mM) mixture. A glass tube with holes

encased in a membrane was placed in the beaker. The glass tube was filled with a g-C_3N_4/BDI dispersion (2 mg mL^{-1}). Then the glass tube was irradiated from above with a LED ($\lambda = 365$ nm). At different reaction times, 2 mL of the reaction mixture was taken and examined using UV/Vis spectroscopy.

FOX ('ferrous oxidation−xylenol orange') assay for H_2O_2 quantification.[25,26,29] To prepare the FOX solution, 24.5 mg of ammonium iron sulfate hexahydrate and 17.92 mg xylenol orange tetrasodium salt were first dissolved in 25 mL of a 250 mM sulfuric acid (c_{XO}=1 mM and c_{Fe} = 2.5 mM). The final FOX solution was obtained by a 1:10 dilution with Milli-Q water with c_{XO}=0.1 mM and c_{Fe}= 0.25 mM. For calibration, 100 µL of different concentrated H_2O_2 solutions were added to 1900 µL of a FOX solution. To this end, a 3 mM H_2O_2 solution was prepared as stock solution and diluted to concentrations from 0-600 µM for later calibration. (Table 6-2)

Table 6-2. H_2O_2 solutions with different concentrations prepared with a 3 mM stock solution. H_2O_2 solutions were used for the calibration curve using FOX-assay.

V(3 mM H_2O_2) / µL	V(H_2O) / µL	$c(H_2O_2)_{calibration}$ / µM	$c(H_2O_2)_{final}$ in FOX-Assay/ µM
0	200	0	0
10	190	150	7.5
20	180	300	15
30	170	450	22.5
40	160	600	30

CHARACTERIZATION

Transmission electron microscopy. A FEI Tecnai 12 TWIN microscope with LaB_6 source at 120 kV was used together with a Gatan US1000 CCD camera (16 bit, 2048 x 2048 pixels) and the Gatan Digital Micrograph software for transmission electron microscopy. Samples were prepared by dropping nanoparticle dispersions with a concentration of 1 mg/ml onto a carbon coated copper grid.

Powder X-ray diffraction. X-ray powder diffraction patterns were recorded using a STOE Stadi P diffractometer with a Dectris Mythen 1k detector in transmission mode with Mo $K\alpha 1$ radiation.

BET surface area. A 3P-Micro-300 instrument was used to determine the specific surface area. The measurements were performed with a 3P-Micro-300 instrument. Data analysis was performed using e 3P Surface Area & Pore Size Analyzer System 10.03.02 software. Nitrogen at 77.4 K was used as the analysis gas.

Zeta potentials. A Malvern Zetasizer Nano was used for ζ-potentials determination. Nanoparticle dispersions (0.5 mg/mL) were measured in disposable capillary cells (DTS1070). Data analysis was performed using Malvern Zetasizer software 8.01.4906.

UV/Vis spectroscopy. For kinetic measurements an Agilent Cary 3500 spectrophotometer was used. UV/Vis measurements of the supernatants (CeBi-composite materials, depot materials, coupling reaction) were carried out on a Cary Varian 5G UV-VIS-NIR spectrometer.

Band gap analysis. Diffuse reflectance was measured on a Cary Varian 5G UV-VIS-NIR spectrometer. The sample was prepared on Magic Scotch Tape. The band gap energy was determined by the Kubelka-Munk[30] approach *via* graphical application using the Origin8Pro software.

IR. The infrared spectra were measured on a Nicolet iS10 FT-IR infrared spectroscope from Thermo-Fisher. Data analysis was performed using the OMNIC and Origin8Pro software.

Scanning Electron Microscopy. The composite beads were attached to aluminum holders with carbon film pads. SEM images were acquired using an FEI Nova NanoSEM 630 equipped with an EDAX-Pegasus X4M instrument (for EDX measurements).

6.6.   REFERENCES

1   Scott, R. D. The Direct Medical Costs of Healthcare-Associated Infections in U.S. Hospitals and the Benefits of Prevention. *Cdc* **2009**, March, 13. https://stacks.cdc.gov/view/cdc/11550

2   Flemming, H. C.; Griebe, T.; Schaule, G. Antifouling Strategies in Technical Systems - A Short Review. In *Water Sci. Technol.* **1996**, 34 (5-6), 517–524.

3   Mattila-Sandholm, T.; Wirtanen, G. Biofilm Formation in the Industry: A Review. *Food Rev. Int.* **1992**, *8* (4) 573–603.

4   Dafforn, K. A.; Lewis, J. A.; Johnston, E. L. Antifouling Strategies: History and Regulation, Ecological Impacts and Mitigation. *Mar. Pollut. Bull.* **2011**, *62* (3), 453–465.

5   Sandy, M.; Carter-Franklin, J. N.; Martin, J. D.; Butler, A. Vanadium Bromoperoxidase from Delisea Pulchra: Enzyme-Catalyzed Formation of Bromofuranone and Attendant Disruption of Quorum Sensing. *Chem. Commun.* **2011**, *47* (44), 12086.

6   Syrpas, M.; Ruysbergh, E.; Blommaert, L.; Vanelslander, B.; Sabbe, K.; Vyverman, W.; De Kimpe, N.; Mangelinckx, S. Haloperoxidase Mediated Quorum Quenching by Nitzschia Cf Pellucida: Study of the Metabolization of N-Acyl Homoserine Lactones by a Benthic Diatom. *Mar. Drugs* **2014**, *12* (1), 352–367.

7   Herget, K.; Hubach, P.; Pusch, S.; Deglmann, P.; Götz, H.; Gorelik, T. E.; Gural'skiy, I. A.; Pfitzner, F.; Link, T.; Schenk, S.; Panthöfer, M.; Ksenofontov, V.; Kolb, U.; Opatz, T.; André, R.; Tremel, W. Haloperoxidase Mimicry by CeO 2− x Nanorods Combats Biofouling. *Adv. Mater.* **2017**, *29* (4), 1603823.

8   Frerichs, H.; Pütz, E.; Pfitzner, F.; Reich, T.; Gazanis, A.; Panthöfer, M.; Hartmann, J.; Jegel, O.; Heermann, R.; Tremel, W. Nanocomposite Antimicrobials Prevent Bacterial Growth through the Enzyme-like Activity of Bi-Doped Cerium Dioxide (Ce1−xBixO2−δ). *Nanoscale* **2020**, *12* (41), 21344–21358.

9   Herget, K.; Frerichs, H.; Pfitzner, F.; Tahir, M. N.; Tremel, W. Functional Enzyme Mimics for Oxidative Halogenation Reactions That Combat Biofilm Formation. *Adv. Mater.* **2018**, *30* (36), 1707073.

10   Więckol-Ryk, A.; Białecka, B.; Thomas, M. Application of Calcium Peroxide as an Environmentally Friendly Oxidant to Reduce Pathogens in Organic Fertilizers and Its Impact on Phosphorus Bioavailability. *Arch. Environ. Prot.* **2020**, *46* (4), 42–53.

11   Ma, Y.; Zhang, B. T.; Zhao, L.; Guo, G.; Lin, J. M. Study on the Generation Mechanism of Reactive Oxygen Species on Calcium Peroxide by Chemiluminescence and UV-Visible Spectra. *Luminescence* **2007**, *22* (6), 575–580.

12   Lin, J. C.; Tiong, S. L.; Chen, C. Y. Surface Characterization and Platelet Adhesion Studies on Fluorocarbons Prepared by Plasma-Induced Graft Polymerization. *J. Biomater. Sci. Polym. Ed.* **2000**, *11* (7), 701–714.

13 Carretier, S.; Chen, L. A.; Venault, A.; Yang, Z. R.; Aimar, P.; Chang, Y. Design of PVDF/PEGMA-b-PS-b-PEGMA Membranes by VIPS for Improved Biofouling Mitigation. *J. Memb. Sci.* **2016**, *510*, 355–369.

14 Wang, X.; Maeda, K.; Thomas, A.; Takanabe, K.; Xin, G.; Carlsson, J. M.; Domen, K.; Antonietti, M. A Metal-Free Polymeric Photocatalyst for Hydrogen Production from Water under Visible Light. *Nat. Mater.* **2008**, *8* (1), 76–80.

15 Kofuji, Y.; Ohkita, S.; Shiraishi, Y.; Sakamoto, H.; Tanaka, S.; Ichikawa, S.; Hirai, T. Graphitic Carbon Nitride Doped with Biphenyl Diimide: Efficient Photocatalyst for Hydrogen Peroxide Production from Water and Molecular Oxygen by Sunlight. *ACS Catal.* **2016**, *6* (10), 7021–7029.

16 Ge, J.; Hu, Y.; Biasini, M.; Beyermann, W. P.; Yin, Y. Superparamagnetic Magnetite Colloidal Nanocrystal Clusters. *Angew. Chem. Int. Ed.* **2007**, *46* (23), 4342–4345.

17 Libert, S.; Gorshkov, V.; Goia, D.; Matijević, E.; Privman, V. Model of Controlled Synthesis of Uniform Colloid Particles: Cadmium Sulfide. *Langmuir* **2003**, *19* (26), 10679–10683.

18 Shannon, R. D. Revised Effective Ionic Radii and Systematic Studies of Interatomic Distances in Halides and Chalcogenides. *Acta Crystallogr. Sect. A* **1976**, *32* (5), 751–767.

19 Liang, Z.; Wang, Q.; Dong, B.; Jiang, B.; Xing, F. Ion-Triggered Calcium Hydroxide Microcapsules for Enhanced Corrosion Resistance of Steel Bars. *RSC Adv.* **2018**, *8* (69), 39536–39544.

20 Khachani, M.; El Hamidi, A.; Halim, M.; Arsalane, S. Non-Isothermal Kinetic and Thermodynamic Studies of the Dehydroxylation Process of Synthetic Calcium Hydroxide Ca(OH)2. *J. Mater. Environ. Sci.* **2014**, *5* (2), 615–624.

21 Li, S.; Dong, G.; Hailili, R.; Yang, L.; Li, Y.; Wang, F.; Zeng, Y.; Wang, C. Effective Photocatalytic H2O2 Production under Visible Light Irradiation at G-C3N4 Modulated by Carbon Vacancies. *Appl. Catal. B Environ.* **2016**, *190*, 26–35.

22 Yuan, X.; Luo, K.; Zhang, K.; He, J.; Zhao, Y.; Yu, D. Combinatorial Vibration-Mode Assignment for the FTIR Spectrum of Crystalline Melamine: A Strategic Approach toward Theoretical IR Vibrational Calculations of Triazine-Based Compounds. *J. Phys. Chem. A* **2016**, *120* (38), 7427–7433.

23 Yuan, X.; Luo, K.; Liu, N.; Ji, X.; Liu, C.; He, J.; Tian, G.; Zhao, Y.; Yu, D. Cluster-Model DFT Simulations of the Infrared Spectra of Triazine-Based Molecular Crystals. *Phys. Chem. Chem. Phys.* **2018**, *20* (32), 20779–20784.

24 Chu, S.; Wang, Y.; Guo, Y.; Feng, J.; Wang, C.; Luo, W.; Fan, X.; Zou, Z. Band Structure Engineering of Carbon Nitride: In Search of a Polymer Photocatalyst with High Photooxidation Property. *ACS Catal.* **2013**, *3* (5), 912–919.

25   Bou, R.; Codony, R.; Tres, A.; Decker, E. A.; Guardiola, F. Determination of Hydroperoxides in Foods and Biological Samples by the Ferrous Oxidation-Xylenol Orange Method: A Review of the Factors That Influence the Method's Performance. *Anal. Biochem.* **2008**, *377* (1), 1–15.

26   Timabud, T.; Sanitchon, J.; Pongdontri, P. A Modified Ferrous Oxidation-Xylenol Orange Assay for Lipoxygenase Activity in Rice Grains. *Food Chem.* **2013**, *141* (3), 2405–2411.

27   Deiana, L.; Carru, C.; Pes, G.; Tadolini, B. Spectrophotometric Measurement of Hydroperoxides at Increased Sensitivity by Oxidation of Fe2+ in the Presence of Xylenol Orange. *Free Radic. Res.* **1999**, *31* (3), 237–244.

28   Liang, X.; Xiao, J.; Chen, B.; Li, Y. Catalytically Stable and Active CeO2 Mesoporous Spheres. *Inorg. Chem.* **2010**, *49* (18), 8188–8190.

29   Jiang, Z. Y.; Hunt, J. V.; Wolff, S. P. Ferrous Ion Oxidation in the Presence of Xylenol Orange for Detection of Lipid Hydroperoxide in Low Density Lipoprotein. *Anal. Biochem.* **1992**, *202* (2), 384–389.

30   López, R.; Gómez, R. Band-Gap Energy Estimation from Diffuse Reflectance Measurements on Sol-Gel and Commercial TiO2: A Comparative Study. *J. Sol-Gel Sci. Technol.* **2012**, *61* (1), 1–7.

6.7.   SUPPORTING INFORMATION
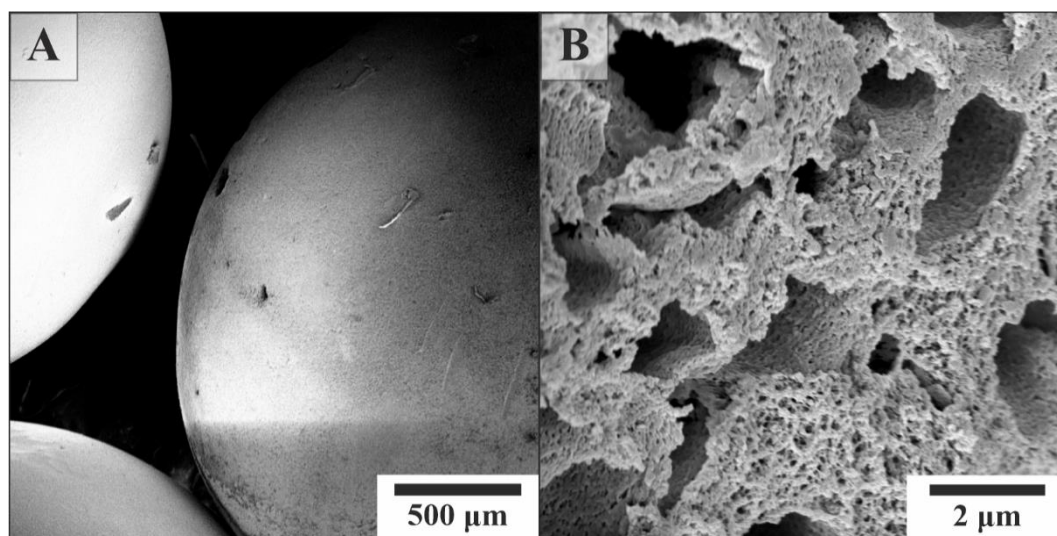
Figure S6-1. SEM image of PES beads at different magnifications.
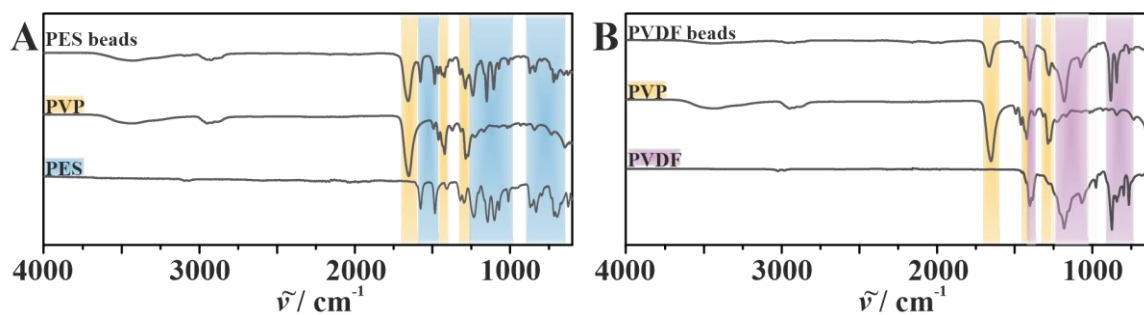
Figure S6-2. IR spectra of the starting materials PES, PVDF and PVP, as well as the resulting PES/PVDF beads after coagulation.
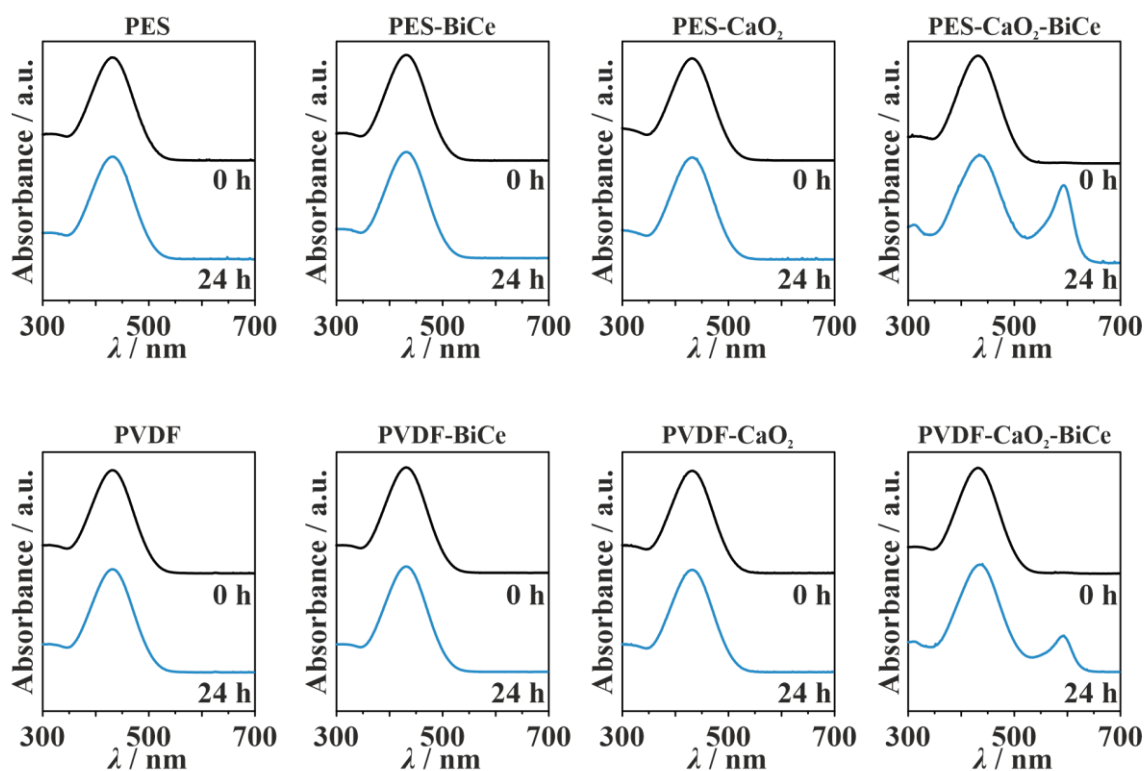
Figure S6-3. UV/Vis spectra of phenol red assay in presence of PES, PVDF, PES-BiCe, and PVDF-BiCe composites, PES-CaO$_2$ and PVDF-CaO$_2$ composites as well as PES-BiCe-CaO$_2$ and PVDF-BiCe-CaO$_2$ composites after 0 h and 24 h.

7

ADDITIONAL PROJECTS

7.1. POROUS ALGINATE-CEROXIDE HYDROGELS FOR WATER TREATMENT

-Manuscript in preparation-

Due to population growth and climate crisis, the availability of clean and cheap drinking water is a modern-day problem. Many of the world's remaining water sources are already polluted and need to be purified with new technologies. Nanotechnology based water purification systems are widely used to remove pollutants from water. In this project, a hydrogel-based system for water purification was developed. For this purpose, porous alginate-based nanomaterials were produced, which adsorb organic pollutants and can thus remove them from the water. Differently charged organic dyes were used as model pollutants. In addition, inorganic cerium oxide nanoparticles were embedded in the hydrogel matrix in order to degrade the adsorbed organic pollutants later by photocatalytic dye decomposition and render them harmless.

Personal contributions:

Project initiation, project development and coordination, initial lab work, supervision of Johannes Berg in research module.

Collaboration partners:

XXX, XXX, **Eva Pütz**, XXX, XXX, XXX, XXX

7.2. NEW CERIUM BASED STRUCTURE

Ethylene glycol based CeO_2 synthesis is widely used to generate highly dispersible and catalytic active mesoporous cerium oxide nanoparticles. When adjusting the reaction conditions a transformation from ceria nanoparticles to crystalline cerium-based coordination polymers was observed in the X-ray powder diffractograms. Automated diffraction tomography (ADT) measurements were used to solve the structure. The initial approaches of the structure solution revealed a compound with the cubic space group $Ia3d$ with the lattice parameter $a = 30.14$ Å. As the full crystal structure determination is still incomplete, more data sets must be collected, and a thermogravimetric analysis coupled with differential scanning calorimetry and mass spectrometry (TGA-DSC-MS) is needed. In particular, new ADT data have to be collected to clarify the final composition and structure of this new coordination polymer.
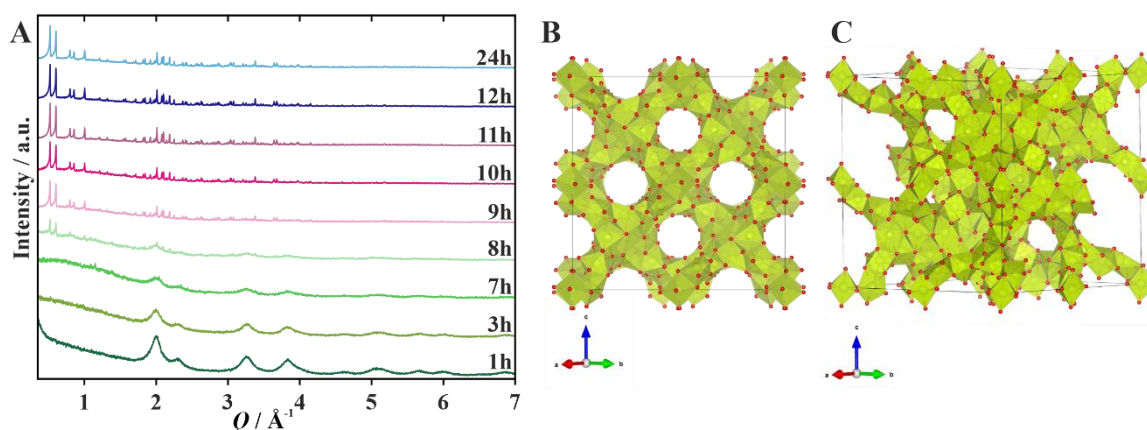
Figure 7-1. (A) PXRD patterns at different reaction times indicating a change from cerium oxide nanoparticles to a crystalline material. (B, C) Initial structure solution revealed from ADT measurements and visualized with VESTA. The oxygen atoms are shown in red and the coordination polyhedron for the cerium ions in yellow.

Personal contributions:

Project initiation, project development and coordination, initial lab work.

Collaboration partners:

Eva Pütz, XXX, XXX, XXX

8

CONCLUSION AND OUTLOOK

Marine algae protect themselves from bacterial attack by oxidatively brominating signaling molecules with the help of their haloperoxidase enzymes. This process interrupts bacterial communication and prevents the formation of biofilms. Ceria nanoparticles can mimic these natural enzymes. The aim of this work was the synthesis and optimization of ceria nanoparticles, as well as the preparation of functional nanomaterials with antibiofouling activity.

The first study investigated how the surface properties of different cerium oxides affect the catalytic performance in the oxidative bromination reaction. For this purpose, ceria nanoparticles with three different morphologies (nanorods, nanospheres and nanocubes) were prepared and their surfaces were compared in terms of Lewis acidity, ζ potential and BET surface area. Raman spectroscopy was used to investigate the stability of the surface-bound H_2O_2 substrate. The catalytic activities of the nanoparticles were determined and compared based on the oxidative bromination of the phenolic monoterpene thymol by ^1H NMR spectroscopy. A high Lewis acidity, a high product of ζ-potential and BET surface area, and a high stability of the surface-bound hydrogen peroxide contribute to an acceleration of the bromination reaction.

In the second project the surface properties BET surface area and ζ-potential were tailored simply by adjusting the reaction time. For this purpose, the growth process of mesoporous CeO_2 nanoparticles was investigated in detail using SAXS. By varying the reaction time, the BET surface area and ζ-potential could be strongly tuned in a reproducible and predictable fashion. The surface charge (ζ-potential) correlates with the Ce^{3+}/Ce^{4+} ratio at the catalyst surface, which was determined by XPS spectroscopy. Nanoparticles with high zeta potential and small Ce^{3+}/Ce^{4+} ratio were obtained at shorter reaction times, while longer reaction times resulted in nanoparticles with large BET surface area and higher Ce^{3+}/Ce^{4+} ratio. The catalytic activity of the ceria nanoparticles was investigated in the two enzyme-like reactions (haloperoxidase-like and peroxidase-like reaction). In haloperoxidase-like reactions, the nanoparticles with high zeta potential showed higher activity because the high

ζ-potential facilitated the transfer of the halide to an organic substrate. In contrast, the peroxidase-like reaction is less affected by the ζ-potential because this reaction does not involve strong electrostatic interactions. Here, the BET surface area and Ce^{3+}/Ce^{4+} ratio must be increased to facilitate electron transfer to the substrate molecule and thus provide a strong catalyst for peroxidase-like reactions.

After optimizing the ceria nanoparticles for a haloperoxidase-like reaction, the third project investigated the potential application of the nanoparticles in antifouling paints. In this context, highly dispersible nanoparticles with high ζ-potential and large BET surface area were synthesized in *n*-butyl acetate. The haloperoxidase-like activity of the nanoparticles was investigated using the phenol red assay. Additionally, biofilm tests were carried out which showed a reduction of the biofilm formation by up to 80% for the Gram-negative bacteria *Pseudomonas aeruginosa*, *Klebsiella pneumoniae*, *Methylobacterium mesophilicu*m and *Phaeobacter gallaeciensis* in the presence of the ceria nanoparticles. Quorum quenching activity of CeO_2 was confirmed using the reporter strain *A. tumefaciens* A136 confirmed. To gain insight into the processes occurring within the bacterial culture in the presence of CeO_2, LC-MS measurements of the bacterial supernatants were performed. The supernatants of the bacterial culture *Pseudomonas aeruginosa* showed that the concentration of signaling molecules (C_4-HSL and 3-oxo-C_{12}-HSL) was strongly reduced in the presence of CeO_2. Moreover, the bromide concentration in the bacterial culture decreased in the presence of CeO_2, indicating the consumption of bromide for the oxidative bromination reaction. It could be shown that the brominated signaling molecules are degraded by the bacteria and thus cannot be detected by LC-MS. However, the brominated compound HQNO (2-heptyl-4-hydroxyquinoline *N*-oxide) was detected for the first time in the presence of CeO_2, lending strong support to the oxidative bromination mechanism. HQNO is known to be responsible for biofilm formation in *Pseudomonas aeruginosa* and *Staphylococcus aureus.* To demonstrate the applicability of the haloperoxidase enzyme mimic in everyday applications the ceria nanoparticles were incorporated into polyurethane coatings and their antifouling effects were investigated. Even embedded in the coatings, the nanoparticles still showed strong biofilm inhibition and thus *quorum quenching* activity, as demonstrated by the crystal violet staining test and SEM as well as CLSM images.

In the last project, *in-situ* H_2O_2 generation was investigated to circumvent the external addition of H_2O_2 and to open additional application areas for haloperoxidase-mimetic

composites. Two different approaches were chosen. First, an H_2O_2 depot was created by embedding an H_2O_2-releasing substance together with mesoporous $Bi_{0.2}Ce_{0.8}O_{1.9}$ nanoparticles in a polymer matrix. The generation of H_2O_2 by the polymer deposit was qualitatively assessed using phenol red assays in the presence of KBr. In addition, the generation of H_2O_2 by photochemical catalysis was investigated. For this purpose, graphitized carbon nitride (g-C_3N_4/BDI) was prepared as a catalyst and its H_2O_2 generating effect was determined using the FOX assay. Irradiation of g-C_3N_4/BDI produced H_2O_2, which then contributed to the oxidative bromination of phenol red in the presence of KBr and $Bi_{0.2}Ce_{0.8}O_{1.9}$.

In summary, this work identified the activity-determining surface properties of ceria nanoparticles in terms of peroxidase and haloperoxidase-like reactions. To apply the active CeO_2 nanoparticles in antifouling applications, they were functionalized to allow a homogeneous incorporation in matrix materials. CeO_2 nanoparticles also showed significant activity in coatings and polymer matrices.

The results show that ceria-based composites are promising materials to produce biofilm inhibiting surfaces without using biocides or toxins. In particular, the biofilm formation of Gram-negative bacteria was highlighted and demonstrated using the hospital pathogens *Pseudomonas aeruginosa* and *Klebsiella pneumoniae*, as well as *Methylobacterium mesophilicum* and *Phaeobacter gallaeciensis* as examples. Unfortunately, the nanoparticles did not show any biofilm inhibitory effect on Gram-positive bacteria such as *Staphylococcus aureus*. Therefore, further research is needed to develop nanoenzymes that can also inhibit peptide-based communication of Gram-positive bacteria. Initial tests also showed an effect of the nanoparticles on fungi. Further studies need to be conducted to investigate exactly how and whether CeO_2 nanoparticles affect fungal growth, sporulation, or hyphal formation.

Bismuth substitution can increase the activity of CeO_2 nanoparticles significantly. Here, the influence of substitution level on the Lewis acidity could be investigated in more detail. In addition, bismuth-substituted cerium oxides with different morphologies were synthesized and investigated to see whether they behave similar to pure CeO_2 in terms of their properties. Further synthesis strategies must be developed to functionalize the nanoparticles specifically according to the desired applications to ensure a facile incorporation into the surrounding matrix. The influence of functionalization on catalytic activity needs additional investigation. To extend the application range of CeO_2 coatings, simultaneous embedding of CeO_2 and g-C_3N_4/BDI in coatings would be a feasible option. For this purpose, g-

C$_3$N$_4$/BDI would have to be functionalized. Its antifouling application might be extended to air/solid interfaces, such as food packaging and door handles.

9

APPENDIX

9.1. LIST OF FIGURES

9.2. LIST OF TABLES

9.3. LIST OF ABBREVIATIONS AND NOTATIONS

$[S_o]^n$ substrat concentration

A. tumefaciens A136   *Agrobacterium* tumefaciens a136

a.u.   arbitrary unit

AHL   N-acyl-homoserine lactones

AI   autoinducer

AI-1/-2   autoinducer-1/-2

BET   Brunauer/Emmett/Teller-method to determine surface area

BTCDA   biphenyl tetracarboxylic dianhydride

c   concentration

CLSM   confocal laser scanning microscopy

COSY   correlation spectroscopy

DAHSL   N-α,α-dibromoacetyl homoserine lactone

DBH   hydrolyzed *N*-α,α-dibromoacetyl homoserine lactone

DMEM   Dulbecco's modified eagle medium

EDX   energy-dispersive X-ray spectroscopy

EPS   extracellular polymeric substance

FFT   fast fourier transformation

FOX   ferrous oxidation - xylenol orange- assay for H_2O_2 quantification.

FT-IR   Fourier transform infrared spectroscopy

h   hour

HAI   healthcare-associated infections

HOX   hypohalous acid

HPO   haloperoxidase

HQNO   2-heptyl-4-hydroxyquinoline-*N*-oxide

HHQ   4-hydroxy-2-alkylquinolines

HRTEM   high-resolution transmission electron microscopy

HSL   homoserine lactone

IMO   international maritime organization

J   Couling conctant

k   reaction velocity

K. pneumonia   *Klebsiella Pneumoniae*

K_m Michaelis (-Menten) constant

LC-MS   liquid chromatography–mass spectrometry

LED	light-emitting diode
LMCT	ligand to metal charge transfer
LuxI	example of an acyl-homoserine lactone synthase
LuxR	example of an acyl-homoserine lactone receptor
M. mesophilicum	*Methylobacterium Mesophilicum*
MAS	magic angle spinning
Milli-Q water	ultrapure water
min	minute
MOF	metal-organic framework
MP	microparticle
NAD(P)H	nicotinamide adenine dinucleotide (phosphate)
NMP	n-methyl-2-pyrrolidone
NMR	nuclear magnetic resonance
NP	nanoparticle
OD_x	optical density measured at a wavelength of x nm
ONPG	ortho-nitrophenyl-β-galactoside
P. aeruginosa	*Pseudomonas Aeruginosa*
P. gallaeciensis	*Phaeobacter Gallaeciensis*
PES	polyethersulfone
PO	peroxidase
PR	phenol red
PUR	polyurethan
PVDF	poly(vinylidene fluoride)
PVP	polyvinylidene pyrilidone
PXRD	Powder X-ray diffracton patterns
Q	scattering vector
QQ	quorum quenching
QS	quorum sensing
ROR	rate of reaction
ROS	reactive oxygen species
rpm	revolutions per minute
RT	room temperature
RV	Rietveld
S. aureus	*Staphylococcus Aureus*

SAXS	small-angle x-ray scattering
S_{BET}	specific surface area
SEM	scattering electron microscopy
SOD	superoxide dismutase
t	time
TBPB	tetrabromophenol blue
TBT	tributyltin
TEM	transmission electron microscopy
TMB	3,3′,5,5′-tetramethylbenzidine
TMP	trimethylphosphine
TOF	turn over frequency
UV/Vis	ultraviolet/visible spectroscopy
V. fischeri	*Vibrio fischeri*
V-BrPO	vanadium bromoperoxidase
V-ClPO	vanadium chloroperoxidase
v_{max}	maximum reaction rate in enzyme kinetics
VOC	volatile organic compounds
wt%	weight percent
X-Gal	5-bromo-4-chloro-3-indolyl-β-d-galactopyranoside
XPS	X-ray photoemission/photoelectron spectroscopy
$\beta(Cat)$	mass concentration of catalyst
δ	chemical shift
λ	wavelength
λ_{max}	absorption maximum

9.4.   LIST OF PUBLICATIONS

[1] **E. Pütz**, XXX, XXX, XXX, XXX, XXX, XXX, XXX, XXX, XXX, Broad-Spectrum Biofilm Inhibition due to Quorum Quenching Induced by CeO_2 Containing Lacquers, 2021, in preparation.

[2] **E. Pütz**, XXX, XXX, XXX, XXX, XXX, XXX, XXX, XXX, XXX and XXX, Morphology regulated oxidative bromination of thymol with $CeO_{2\,x}$ nanocrystal enzyme mimics, 2021, in preparation.

[3] **E. Pütz**, XXX, XXX, XXX and XXX, Tuning Ceria Catalysts in Aqueous Media at the Nanoscale: How Do Surface Charge and Surface Defects Determine Peroxidase- and Haloperoxidase-Like Reactivity. 2021, in preparation.

[4] XXX, **E. Pütz**, XXX, XXX, XXX, XXX, XXX, XXX, XXX, XXX, Nanocomposite antimicrobials prevent bacterial growth through the enzyme-like activity of Bi-Doped cerium dioxide ($Ce_{1-x}Bi_xO_{2-\delta}$), *Nanoscale*, **2020**,*12*, 21344-21358.

[5] XXX, XXX, XXX, XXX, **E. Pütz**, XXX, XXX, XXX, XXX, XXX, XXX and XXX, Transparent polycarbonate coated with CeO_2 nanozymes repel Pseudomonas aeruginosa PA14 biofilms, *Nanoscale*, **2022**, *14*, 86-98.

[6] XXX, XXX, XXX, XXX, XXX, XXX, **E. Pütz**, XXX, XXX, XXX, XXX, and XXX, Selective Synthesis of Monodisperse CoO Nanooctahedra as Catalysts for Electrochemical Water Oxidation, *Langmuir* **2020**, *36*, 13804–13816.

[7] XXX, XXX, **E. Pütz**, XXX, XXX, XXX and XXX, Actuating thermo- and photo-responsive tubes from liquid crystalline elastomers, *J. Mater. Chem. C*, **2018**, *6*, 9093-9101